

ELECTROMAGNETIC AND MECHANICAL PROPERTIES OF MEDIUM β SRF
ELLIPTICAL CAVITIES

By

Crispin Contreras-Martinez

A DISSERTATION

Submitted to
Michigan State University
in partial fulfillment of the requirements
for the degree of

Physics – Doctor of Philosophy

2021

ABSTRACT

ELECTROMAGNETIC AND MECHANICAL PROPERTIES OF MEDIUM β SRF ELLIPTICAL CAVITIES

By

Crispin Contreras-Martinez

The new generation of hadron SRF linac projects to produce rare isotopes and high-intensity neutrinos require developing a new elliptical cavity design optimized for medium $\beta = 0.65$ and operating at relatively low frequency, at 650 MHz. During operation, vibration noise (microphonics) causes the cavity to deform, shifting its resonance frequency. Slight deformations of elliptical cavities can significantly detune the cavity frequency from the resonance. A frequency shift in the cavity lowers the nominal accelerating field, which can be compensated either by using additional RF power or both a dedicated fast mechanical tuner and more RF power. In addition, cavities must be designed to reduce sensitivity to microphonics. Microphonics compensation by increased RF power is not economical, especially in low-intensity linacs.

The first part of this thesis explores a cost-effective method that uses a tuner consisting of a piezoelectric actuator. The piezoelectric actuator can elastically deform the cavity to track the resonance frequency, thus allowing for efficient use of RF power towards beam acceleration. The development and testing of a new combined slow and fast tuner for the 650 MHz cavity are presented in this thesis. The slow tuning component uses a stepper motor and can compensate for frequency detuning on the order of kHz with a reaction time on the order seconds. The fast tuning component uses a piezoelectric actuator that can compensate for frequency detuning on the order of Hz and ms. A lumped circuit model to study the resonance response of the cavity in the presence of microphonics is presented. This model incorporates the experimental results of the mechanical modes of the 650 MHz cavity for the first time. Lower frequency cavities are larger and more sensitive to microphonics than the widely used 1.3 GHz elliptical cavities for the acceleration of electrons. We had an opportunity to study the microphonics properties in the cryomodule setting with eight 1.3 GHz cavities experimentally before the development of a tuner for 650 MHz cavities.

A new correlation between various cryogenic parameters and the frequency detuning of 1.3 GHz cavities is presented for multiple cavities in different cryomodules. A tuner that incorporates a piezoelectric actuator is used for the active compensation of microphonics. The piezoelectric properties of actuators for operation in a CW linac are available in the scientific literature. This thesis provides new results for piezo actuators operated at a high voltage needed for large gradient pulsed linacs. This work led to the discovery of large dielectric heating of the piezo and deviation from the dielectric heating formula found in the literature. Large heating of the piezo will result in a reduced lifetime. A discussion on why this deviation occurs is presented. A novel piezoelectric actuator was designed and built, yielding a reduction of heating by a factor of 14 at liquid helium temperatures. The properties of lithium niobate for use in SRF cavity resonance control were tested for the first time. Lithium niobate shows no heating but with a compromise of a smaller stroke. The results pave the way for future optimization of materials with larger stroke but smaller dielectric heating.

In the second part of this thesis, two resonance control algorithms were implemented on a single-cell elliptical 1.3 GHz cavity at room temperature. The proportional-integral (PI) loop algorithm was used to compensate for slow varying vibrations (less than 5 Hz). The successful implementation of this algorithm with the single-cell elliptical cavity at room temperature demonstrates that it can control liquid helium pressure variations and other slow varying vibrations of the cavity in the cryogenic environment. For vibrations above 5 Hz, the least mean square (LMS) algorithm was used. The implementation of the LMS algorithm in the FPGA successfully suppressed 2 sinusoidal vibrations by a factor of 3 with white Gaussian noise added (0.07 Hz detuning) in a matter of ms. The use of active resonance control will reduce the required cavity RF power and increase the reliability of the linac.

Para mi Papa, Mama, y toda mi familia. (To my Mom, Dad, and all my family)

ACKNOWLEDGEMENTS

I'm very thankful for everyone who has helped me along the way in completing my Ph.D. There were a lot of people who helped me along the way, in this section I will only mention a few of the people who helped me complete my work. I would first like to thank my Mom and Dad for giving me their support and always believing in me throughout this time. You two have made tremendous sacrifices so that all of us in the family could finish high school and make a better life here in the U.S.

I would like to thank my committee members Peter Ostroumov, Steve Lidia, Steve Lund, Kenji Saito, and Phil Duxbury. My committee has always provided insightful comments on my research and has helped me improve my work. Peter has always been extremely helpful during the completion of my thesis. His guidance helped me obtain two very important grants which allowed me to continue my work at Fermilab. Additionally, he has been an excellent teacher and his attention to detail was also very helpful.

At MSU, I would like to thank Scott Pratt and Kim Crosslan. Scott was extremely helpful in helping me pass the qualifying exams. Kim is a lifesaver and her invaluable help with all the paperwork that I needed to submit will always be appreciated. In the MSU SRF department, I would also like to thank Walter Hartung and John Popierlarski. Walter and John helped me set up the bead-pull experiment as well as analyze the data. In the accelerator division, I would also like to thank Alexander Plastun. Alex taught me a great deal of what I know about EM simulations in CST studio.

At Fermilab, I would like to thank Vyacheslav (Slava) Yakovlev, Yuriy Pischalnikov, Jae-Chal Yun, Warren Schappert, Roman Pilipenko, Charlie Hess, Jeremiah Holzbauer, the LLRF team, and LCLS-II team. During my time at Fermilab Slava helped me hone my skills as a physicist by providing me with physics problems that relate to my work. He is an excellent teacher and has taught me all I know about cavity resonator theory. Additionally, his feedback on my work always improved it by always focusing on physics details. Yuriy is an excellent experimentalist

and without his constant guidance, many of my experiments would have taken longer to complete. Yuriy has always provided me with methods to perform sanity checks and to not be so reliant on the results from the computer. Yuriy, JC Yun, and Charlie were also extremely helpful in setting up the piezo experiment. Yuriy and Roman taught me a tremendous amount in everything related to LabVIEW. Warren and Jeremiah helped me in all things related to signal processing and MATLAB. Warren also introduced me to the theory of resonance control and was always happy to answer any questions related to it. The FNAL and LCLS-II team at Berkeley were also helpful in setting up the system for cavity frequency detuning.

I like to thank my fellow graduate students that I met along the way who were always fun to be around: Bakul Agarwal, Victor Aguilar, John Bower, Timofey Golubev, Bryan Isherwood, Didi Luo, Derek Neben, Tenzin Ragba, David Tarazona, Chris Richards, Joe Williams, and Jonathan Wong. I would also like The MSU accelerator students for all their insightful comments whenever I presented my work during our meetings.

Lastly, I would like to thank the Accelerator Science and Engineering Training (ASET) program, the US Department of Energy, Office of Science, High Energy Physics under Cooperative Agreement award number DE-SC0018362, the DOE SCGSR program, and the Joint University-Fermilab Doctoral Program in Accelerator Physics and Technology for providing me with financial support throughout my Ph.D.

TABLE OF CONTENTS

| | |
|--|-----------|
| LIST OF TABLES | x |
| LIST OF FIGURES | xi |
| KEY TO ABBREVIATIONS | xxi |
| CHAPTER 1 INTRODUCTION | 1 |
| 1.1 A Brief History of Linacs | 1 |
| 1.2 Acceleration with Superconducting Cavities | 3 |
| 1.3 Superconducting Properties of Materials | 6 |
| 1.3.1 Free Electron Model | 6 |
| 1.3.2 Londons' Theory | 7 |
| 1.3.3 Meissner Effect | 8 |
| 1.3.4 Surface Impedance of SC in the Two-fluid Model | 8 |
| 1.3.5 BCS Theory | 10 |
| 1.3.6 Superconductor Types | 11 |
| 1.4 Best Superconductors for RF Application | 11 |
| 1.5 Motivation | 13 |
| 1.5.1 FRIB | 15 |
| 1.5.2 PIP-II | 17 |
| 1.5.3 LCLS-II | 18 |
| 1.6 Thesis Organization | 20 |
| CHAPTER 2 SUPERCONDUCTING RF CAVITIES | 21 |
| 2.1 Resonator Theory | 21 |
| 2.1.1 Lumped Circuit RLC Circuit | 23 |
| 2.1.2 Lorentz Force Detuning | 25 |
| 2.1.3 Cavity Wall Movement Model as Harmonic Oscillator | 26 |
| 2.1.4 Resonance Curve from RLC Envelope Equation | 28 |
| 2.2 Simulation of Electromechanical Coupling Model | 33 |
| 2.3 RF Power for Field Stability | 37 |
| 2.4 Summary of Chapter | 39 |
| CHAPTER 3 EXPERIMENTAL CHARACTERIZATION OF SRF CAVITY | 40 |
| 3.1 Q_0 and Frequency Measurement | 40 |
| 3.2 Bead-pull Experiment | 44 |
| 3.2.1 Lumped Circuit Model for Cavity Cells | 45 |
| 3.2.2 Cavity Cell Perturbation Model | 48 |
| 3.2.3 Measurement of Field Profile | 50 |
| 3.2.4 Bead-pull Setup | 52 |
| 3.2.5 Dumbbell Simulations for Tensile Strength | 52 |
| 3.2.6 RF Coupling | 55 |

| | | |
|---|--|------------|
| 3.2.6.1 | Effects of Antenna and Bead Length | 56 |
| 3.2.7 | Environmental Effects on Cavity Frequency | 59 |
| 3.2.8 | Tuning Ichiro Cavity | 59 |
| 3.3 | Transfer Function Measurement | 60 |
| 3.4 | Summary of Chapter | 65 |
| CHAPTER 4 MICROPHONICS STUDIES | | 66 |
| 4.1 | Sources of Microphonics | 66 |
| 4.2 | LCLS-II Microphonics Studies | 68 |
| 4.2.1 | Effects of Liquid Helium Fluctuation | 73 |
| 4.2.2 | Mechanical Harmonics Excitation in Cavity Frequency Detuning | 76 |
| 4.2.3 | Stochastic Microphonics | 79 |
| 4.2.4 | Frequency Detuning Statistics | 83 |
| 4.3 | Summary of Chapter | 87 |
| CHAPTER 5 COMBINED SLOW AND FAST TUNER | | 89 |
| 5.1 | Frequency Control of SRF Cavities | 90 |
| 5.1.1 | Double Lever Arm Tuner for 650 MHz Elliptical Cavities | 91 |
| 5.1.2 | Tuner Stiffness of 650 MHz Cavity Tuner | 93 |
| 5.1.3 | Slow Coarse Tuner | 95 |
| 5.1.4 | Fast Fine Tuner | 98 |
| 5.2 | High Voltage Operation of Piezoelectric Actuators at Cryogenic Temperature | 100 |
| 5.2.1 | Piezoelectric Effect | 101 |
| 5.2.2 | Piezoelectric Actuator Figures of Merit | 105 |
| 5.2.3 | Experimental Setup | 108 |
| 5.2.4 | Dielectric Heating | 112 |
| 5.2.5 | Self-heating Generation Model | 115 |
| 5.2.6 | Piezo Heat Generation Model Comparison | 116 |
| 5.2.7 | Heating Effects Due to the Driving Waveform | 118 |
| 5.2.8 | Effects of Heating on Resonance Control | 120 |
| 5.2.9 | Heating Effects From Unipolar and Bipolar Operation | 122 |
| 5.3 | Improvements to Heat Mitigation of Piezoelectric Actuators | 123 |
| 5.3.1 | Novel Piezoelectric Actuator Design | 123 |
| 5.3.1.1 | Cryogenic Tests Results | 126 |
| 5.3.2 | Lithium Niobate Measurements | 129 |
| 5.3.2.1 | Cryogenic Tests Results | 131 |
| 5.4 | Summary of Chapter | 132 |
| CHAPTER 6 RESONANCE CONTROL | | 135 |
| 6.1 | Resonance Control on a Copper Cavity | 135 |
| 6.1.1 | Resonance Control Algorithm | 139 |
| 6.1.2 | PI Loop Control | 139 |
| 6.1.3 | LMS Theory | 143 |
| 6.1.4 | Stability of Control Algorithm | 149 |
| 6.1.5 | Limitations of Piezo Acutators | 150 |

| | |
|----------------------------------|-----|
| 6.2 Summary of Chapter | 151 |
| CHAPTER 7 CONCLUSION | 152 |
| APPENDIX | 155 |
| BIBLIOGRAPHY | 162 |

LIST OF TABLES

| | | |
|------------|---|-----|
| Table 1.1: | AC power consideration to operate a one meter long 650 MHz superconducting and normal conducting pillbox cavities at 10 MV/m with a 1 mA beam. | 4 |
| Table 1.2: | Type-II Superconductors properties [14]. | 12 |
| Table 1.3: | Linacs with different beam currents (i_b), accelerating fields (E_{acc}), and bandwidths (Δf) of the cavity. In the table all the linacs use an elliptical cavity in the high energy section. Linacs with low beam loading in pulse and CW operation will have a small bandwidth. Linacs built are denoted by ¹ , currently being built ² , and are proposed ³ | 14 |
| Table 2.1: | Inputs to the simulation of the 650 MHz cavity. | 34 |
| Table 2.2: | Inputs to the simulation of the 650 MHz cavity lumped circuit model. The mechanical modes are obtained from the transfer function measurement done in Chapter 3. | 37 |
| Table 3.1: | Frequency sensitivity due to deformations of the mechanical resonances [22]. . . | 61 |
| Table 5.1: | 650 MHz cavity tuning properties for different geometries. | 98 |
| Table 5.2: | Figures of merit for different piezoelectric materials[87], [89]. | 108 |
| Table 5.3: | Parameters of two piezoelectric actuators used in this experiment: PZT and $LiNbO_3$ | 109 |
| Table 5.4: | Power generated by the piezo calculated from Eq. 5.11 and power generated by the piezo obtained from the fit of Eq. 5.14 at the steady state. | 117 |
| Table 5.5: | Comparison of temperature rise between the standard PICMA design piezo with the copper foam piezo with a heat sink for a 100 Hz sine wave. | 127 |
| Table 5.6: | Comparison of the standard PICMA design piezo with the copper foam piezo design without the heat sink. | 128 |

LIST OF FIGURES

| | | |
|-------------|---|----|
| Figure 1.1: | Wideröe linac with three drift tubes, each of the drift tubes is connected to the AC source. | 1 |
| Figure 1.2: | Alvarez linac with three drift tubes, the drift tubes are place inside a cavity in the TM_{010} mode. | 2 |
| Figure 1.3: | Traveling wave disc-loaded structure [4]. | 3 |
| Figure 1.4: | The Meissner effect expels the magnetic flux of in the presence of an external field at the critical temperature T_c | 9 |
| Figure 1.5: | A type-I superconductor only experiences the Meissner state where no magnetic flux enters the bulk of the material. Superconducting state is destroyed when the external magnetic field exceeds the value H_{c1} . A type-II superconductor exhibits the Meissner state, a vortex state after H_{c1} , and after H_{c2} the material becomes normal conducting. | 12 |
| Figure 1.6: | FRIB linac. | 16 |
| Figure 1.7: | Aerial view of the PIP-II linac along with the booster synchrotron and main injector ring. | 18 |
| Figure 1.8: | LCLS-II Linac layout. | 19 |
| Figure 2.1: | Circuit model of cavity system [34] | 23 |
| Figure 2.2: | The blue line depicts the cavity with zero field and the red line shows the effect of the magnetic and electric field [40]. | 25 |
| Figure 2.3: | (a) Linear and non-linear resonance curve from lumped-circuit model at 16 MV and with a LFD coefficient of $1 \text{ Hz}/(\text{MV})^2$. (b) Phase of linear and non-linear response from lumped circuit model at 16 MV and with LFD of $1 \text{ Hz}/(\text{MV})^2$ | 32 |
| Figure 2.4: | (a) Resonance curve with LFD of $1 \text{ Hz}/(\text{MV})^2$ and at different voltages. As the voltage increase the non-linearity become larger.(b) Phase with LFD of $1 \text{ Hz}/(\text{MV})^2$ driven by different voltages. | 33 |
| Figure 2.5: | Equations 2.14 and 2.21 have a positive feedback loop. The deviation from the nominal electric field will drive cavity wall movements and the wall movement of the cavity will cause detuning changing the voltage of the cavities. | 34 |

| | | |
|-------------|---|----|
| Figure 2.6: | (a) The effect on the electric field from a 2 ms RF pulse for a 650 MHz cavity with no beam and no detuning is shown. (b) The reflected and forward power are shown along with the beam current which is zero. (c) The effect of beam loading to the electric field is shown. (d) The effect of beam loading to the reverse power and forward power is shown. Simulation parameters are given in Table 2.1 | 35 |
| Figure 2.7: | Simulation parameters are the same as in Table 2.1 with the addition of the mechanical modes in Table 2.2. (a) Voltage of the cavity with 8 mechanical modes introduced in equation 2.21. The blue line depicts the voltage of the cavity and the orange the time evolution of the detuning. (b) The forward power, reflected power, and beam current are shown. The reflected power also droops due to the effect of the mechanical modes. | 36 |
| Figure 2.8: | Power provided from generator with respect to the loaded Q_L to the 650 MHz LB cavity at 11.9 MV. | 38 |
| Figure 3.1: | Schematic of signals in a cryomodule for an SRF cavity. The intermittent frequency (IF) is measured after the signal is downconverted. | 41 |
| Figure 3.2: | Field distribution of Ichero cavity prior to tuning, field flatness is $\eta_{ff} = 23\%$. The peak of the field is located at the center of the cavity cell. Note that the field is more concentrated in one region of the cavity. | 45 |
| Figure 3.3: | Lumped circuit model of multi-cell cavity, the coupling between cells is modeled by C_k and the beam tubes is modeled by C_b | 46 |
| Figure 3.4: | (a) Amplitude distribution along the cell number for a nine cell cavity based on the circuit model. Only the $6\pi/9$ to π modes are shown. (b) The dispersion curve of the 9-cell cavity, the π mode has the highest frequency. | 48 |
| Figure 3.5: | (a) Schematic of bead-pull measurement depicting the network analyzer, 9-cell Ichero cavity, stepper motor, and the controls. (b) The static tuner with the Ichiro cavity in place for tuning. | 53 |
| Figure 3.6: | The static tuner consists of plates which are used for squeezing or stretching the cell of the cavity. A motor is used to control for the fine steps. | 53 |
| Figure 3.7: | Three different style of rods were used in the experiment. Initially there was a large block of niobium and the rods were cut at different angles. The angles were 0, 45, and 90 degrees. Tensile strength for niobium, the plot depicts the values for high grade (HG) niobium of RRR=492 and low grade(LG) niobium of RRR= 30 [58]. | 54 |

| | |
|---|----|
| Figure 3.8: COMSOL simulation of : (a) Force applied to the cell is 2 kN ,the pressured calculated is within the elastic regime.(b) The force applied to the cell is 3.2 kN, the pressure is then enough for inelastic deformation of high grade niobium. | 55 |
| Figure 3.9: COMSOL simulation of : (a) Frequency with respect to force applied to the cell. (b) Frequency with respect to the displacement of the cavity cell due to the force applied. | 55 |
| Figure 3.10: (a) BNC antenna length used to couple to the cavity π mode.(b) Fishing line and bead (in this case a needle). | 56 |
| Figure 3.11: (a) SWR with respect to the antenna length, the length was varied by 5 mm. (b) SWR with respect to the antenna length, the length was varied by 1 mm. | 57 |
| Figure 3.12: Phase difference from the forward power to the transmitted power of the cavity with respect to the pickup antenna lengths. | 58 |
| Figure 3.13: Phase difference from the forward power to the transmitted power of the cavity with respect to the needle length. | 58 |
| Figure 3.14: (a) Initial field flatness at was at 23.58 % (b) Final field flatness at 98.4% | 60 |
| Figure 3.15: 650 MHz cavity with tuner installed. | 61 |
| Figure 3.16: First six natural mechanical frequencies of the cavity-helium vessel system simulated in ANSYS [22]. | 62 |
| Figure 3.17: Transfer function measurement setup consists of a master oscillator, an analog phase detector, and the piezo with an amplifier. | 63 |
| Figure 3.18: Transfer function results driven with the piezo actuator for the 650 MHz cavity. The main resonance occurs at 215 Hz. | 64 |
| Figure 3.19: (a) Time series of voltage measured from the piezo actuator. The top plot is the signal from the cavity and the bottom is the signal from the piezo actuator.(b) FFT of time-series from the piezo actuator. | 64 |
| Figure 4.1: Phases of helium with respect to temperature and pressure [63]. | 67 |
| Figure 4.2: CMTF testing facility at Fermilab. | 69 |
| Figure 4.3: Cryogenic flow schematic of a 1.3 GHz LCLS-II cryomodule [18]. | 70 |

| | | |
|--------------|--|----|
| Figure 4.4: | (a) Histogram of 8 cavities, the red lines indicate the specification of the peak detuning.(b) Spectrogram of cavity shows narrowband frequencies which change in amplitude and frequency in time. | 71 |
| Figure 4.5: | Results for cryomodule 6 after passive mitigation techniques were implemented. (a) Histogram of 8 cavities, the red lines indicate the specification of the peak detuning.(b) Spectrogram of cavity shows narrowband frequencies which change in amplitude and frequency in time. | 72 |
| Figure 4.6: | Cavity 1 frequency df/dp in Hz/torr. | 73 |
| Figure 4.7: | Frequency detuning for cryomodule 15 for different dates. The sampling rate from helium pressure sensor is 1 Hz. (a) 30 minute time series of the detuning for cavities 1 through 3 superimposed with the pressure of the liquid helium. (b) 4 hour data capture showing cavities 4 and 5 superimposed with the liquid helium pressure. This data was taken a day after (a). | 74 |
| Figure 4.8: | (a) 30 minute cavity frequency detuning for cryomodule 15 superimposed with liquied helium pressure. (b) 30 minute cavity frequency detuning for cryomodule 17. | 75 |
| Figure 4.9: | Cavity frequency detuning for cryomodule 17. (a) Spectrogram of cavity frequency detuning for cavity 7, there is a correlation between 373 Hz source frequency modulation and the variation of the helium pressure. (b) Spectrograms of cavities 2, 5, 6,and 7 display the same frequency modulation but at a different frequency each. | 75 |
| Figure 4.10: | Cavity Frequency data for cryomodule 15. (a) Spectrograms of cavity 7 at demonstrating the harmonics of the 18 Hz source. (b) Helium supply pressure for the 2.2 K and 5 K lines. | 76 |
| Figure 4.11: | Cryogenic data for cryomodule 15. (a) Liquid level probe reading measured in percentage of probe being submerged in liquid helium.(b) Liquid helium flow rates for supply lines at 2, 5, and 40 K. | 77 |
| Figure 4.12: | Data for cryomodule 15. (a) Frequency detuning of cavity 5 of a 4 hour data acquisition.(b) Inlet pressure of the helium supply lines at 2.2 K and at 5 K temperatures. | 78 |
| Figure 4.13: | Cryomodule 15 data. (a) Liquid level readings of the downstream and upstream positions given in percentages of probe submerged in liquid helium. The left axis shows the values for the downstream level and the right axis shows the upstream level. (b) The flow rate of the 2, 4,and 40 K are shown. The left hand axis shows the values for the 2 and 5 K flow while the right axis shows the flow rate for the 40 K flow. | 78 |

| | |
|--|----|
| Figure 4.14: Autocorrelation for simulated signals. (a) White Gaussian noise. (b) Sinewave with white Gaussian noise added. (c) Signal with two different sinusoids (beats). (d) Sinusoidal Gaussian. | 80 |
| Figure 4.15: Data for cryomodule 15. (a) Cavity 1 detuning spectrogram with a 15 Hz narrowband vibration that turns on randomly. (b) Cavity 8 detuning spectrogram with a 15 Hz narrowband vibration. | 81 |
| Figure 4.16: Autocorrelation of frequency detuning for CM 14 cavity 1 with different bandpass filter bandwidth.(a) Bandwidth of 1 to 12 Hz, (b) 12 to 25 Hz, (c) 25 to 100 Hz, and (d) above 100 Hz. | 81 |
| Figure 4.17: Data for cryomodule 8. (a) Spectrogram of cavity 8, the 15.5 and 20.5 Hz display stochastic behavior. (b) The inlet pressure for helium show a slow amplitude modulation. | 82 |
| Figure 4.18: Autocorrelation of frequency detuning for CM 8 cavity 1 with different bandpass bandwidths.(a) Bandwidth of 1 to 12 Hz,(b) 12 to 25 Hz, (c) 25 to 100 Hz, and (d) above 100 Hz. | 83 |
| Figure 4.19: Simulated distributions for different signals: (a) two tones at 29 Hz and 29.5 Hz; (b) two tones at 20 and 30 Hz; (c) sine wave at 20 Hz; and (d) Gaussian pulse with sine wave at 30 Hz. | 84 |
| Figure 4.20: Results for CM 15: (a) Histogram of 8 cavities, the red lines indicate the specification of the peak detuning. (b) RMS detuning for all 8 cavities. | 85 |
| Figure 4.21: (a) Histogram of cavity 1 in CM 15 with Gaussian fit. (b) Histogram of cavity 4 in CM 15 with Gaussian Fit. Note that this distribution deviated from the Gaussian fit. | 85 |
| Figure 4.22: Results for CM 14: (a) Histogram of 8 cavities, the red lines indicate the specification of the peak detuning. (b) RMS detuning for all 8 cavities, main contribution is from 15 Hz. | 86 |
| Figure 4.23: (a) Contribution to the RMS detuning from vibrations less than 20 Hz. (b) Contributions to the RMS detuning from vibrations between 20 and 100 Hz. | 87 |
| Figure 4.24: Contributions to the RMS detuning from vibrations above 100 Hz but less than 500 Hz. | 87 |
| Figure 5.1: Jacketed 650 MHz cavity with double lever tuner mounted. | 91 |
| Figure 5.2: Schematic of the 650 MHz cavity double lever tuner. The lengths are for the different pivoting points. | 92 |

| | |
|---|-----|
| Figure 5.3: (a) Dial indicators on the tuner arms measure the displacement. (b) Load cell to record the forces on the tuner side. | 94 |
| Figure 5.4: (a) Force on the 650 MHz cavity with respect to the deformation. (b) Lead-screw displacement with respect to the displacement of the tuner arm. | 95 |
| Figure 5.5: (a) Lever tuner attached to the 650 MHz PIP-II cavity. The motor is shown which is responsible for slow and coarse tuning. (b) The longitudinal view of the tuner, this shows the two piezos which are located in the tuner arm. | 96 |
| Figure 5.6: Frequency of the 650 MHz $\beta_G = 0.9$ cavity after cool down to 2 K. | 97 |
| Figure 5.7: Results for 650 MHz $\beta_G = 0.90$ cavity. (a) Small step hysteresis (b) Long step hysteresis | 97 |
| Figure 5.8: PI PICMA piezo capsule used in the 650 MHz tuner. | 98 |
| Figure 5.9: Hysteresis of two piezo capsules at 2 K on the 650 MHz cavity. The maximum voltage used was 100 V with 20 V increments. At 100 V the piezo can shift the frequency of the cavity by -1.97 kHz. | 99 |
| Figure 5.10: Hysteresis of a piezo capsule before and after the application of a 7 kN force was applied. | 99 |
| Figure 5.11: PZT piezo failure after bipolar operation at 77 K, the electrode is destroyed [86] | 100 |
| Figure 5.12: Cross-sectional view of a perovskite crystal unit of a ferroelectric material (PZT). Each of the circles denotes the ion and charge. | 102 |
| Figure 5.13: The total energy of the system with respect to the polarization is shown. In the paraelectric phase where the elastic energy term is dominant only one minimum is observed which corresponds to polarization of zero. The ferroelectric phase has two minimums with positive and negative polarization. | 103 |
| Figure 5.14: (a) The polarization (P) and strain curve (S) is shown with respect to the applied electric field. (b) The initial direction of the dipole domains is random and is change with a strong electric field. Note that each of the states is labeled by a letter and corresponds to the position on the polarization and strain curves [88]. | 104 |
| Figure 5.15: Orthogonal system to describe the properties of a polarized piezo ceramic. Axis 3 is the direction of polarization [81]. | 106 |

Figure 5.16: (a) Tower with the Dewar (b) and, Tower that holds the can which enclosed the piezos. All the instrumentation is wired from the can to the outside. (c) The inside of the can contains two piezo encapsulations with four Cernox RTDs. 110

Figure 5.17: (a) The piezo element consists of two stacks glued together. The cernox RTD is located at the center of the piezo stacks. (b) The piezo stacks are place into a stainless steel encapsulation. (c) The piezo is then preloaded with Belleville washers, the washers are put on top of the piezo element and screwed into place. A geophone is mounted on top of the piezo encapsulation. 111

Figure 5.18: Schematic of data acquisition 111

Figure 5.19: Cross section view of simulation of piezo heating in the experimental setup done in CST studio. 112

Figure 5.20: (a) Temperature inside and outside the piezo ceramic after being driven by a 100 Hz sine wave at $V_{pp}=100$ V on a single stack. The decay is occurs when the piezo is turned off. (b) Temperature rise of the temperature sensors on the copper disk and on the inside of the second piezo. 113

Figure 5.21: Dissipation factor and capacitance measured with an LCR meter with respect to decreasing temperature on the piezo. Note that the voltage used to measure these parameters is $V_{pp}=1$ V. 114

Figure 5.22: (a) Temperature rise of piezo driven by a $V_{pp}=100$ V sine wave with different frequencies. (b) Temperature rise of piezo driven by a 100 Hz sine wave at different voltages. 115

Figure 5.23: Fit of Eq. 5.14 for temperature rise of piezo driven by $V_{pp}=100$ V at 100 Hz sine wave. 117

Figure 5.24: (a) Piezoelectric actuator being driven with 3 different waveforms with the same peak-to-peak voltage and frequency. The square wave gives the largest temperature rise followed by the triangular wave and lastly the sine wave. In the case of the copper temperature for the triangular waveform a helium liquid level drop caused an increase in temperature. (b) Frequency spectrum of the three different waveforms with fundamental frequency of 100 Hz. 119

Figure 5.25: (a) Piezoelectric actuator being driven with 3 different waveforms all at $V_{pp} = 100V$. The tones waveform is composed of the sum of three sinusoids with frequency of 25 Hz, 50 Hz, and 100 Hz. The amplitude of each of the sum is equal and their sum is equal to the $V_{pp} = 100V$. (b) Frequency spectrum of the tones waveform, each of the frequencies was given equal weight. 120

| | |
|---|-----|
| Figure 5.26: Voltage of geophone during the trial at 100 Hz at $V_{pp}= 100$ V. The voltage of signal from the geophone can be relate to its velocity from the stimulation from the piezo. | 121 |
| Figure 5.27: (a) Temperature rise at $V_{pp}= 50$ V in both unipolar and bipolar mode, the results are consistent with each other.(b) The time constant from for each of the trials are similar. | 122 |
| Figure 5.28: Thermal conductivities of different materials which are used in the piezo actuator. | 124 |
| Figure 5.29: (a) Cross-section of standard piezo design with only two contact points. The encapsulation is also shown. (b) New copper foam design with copper plates used to contact the copper foam. Encapsulation of the new design is shown. | 125 |
| Figure 5.30: Design model of the copper foam piezo actuator design. | 125 |
| Figure 5.31: (a) Schematic of piezo setup, this setup up uses two heat sinks where one is attached directly to the piezo. (b) Actual piezo setup. | 126 |
| Figure 5.32: The piezos were cooled with liquid helium. (a) The standard PICMA design piezo modulated with 100 Hz sine wave with varying voltages. (b) Piezo with heat sink modulated with a 100 Hz sine wave with varying voltages. The temperature rise is smaller in the new design. | 127 |
| Figure 5.33: The capacitance and dissipation factor are measured with an LCR for the lithium niobate piezo at 1 kHz at $V_{pp}= 1$ V. | 130 |
| Figure 5.34: Temperature increase of the piezo being driven by a 200 Hz sine wave at 500 Vpp while cooled at 77K. No significant temperature rise was observed. | 131 |
| Figure 5.35: The piezo was cooled with liquid helium. The modulation at 200 Hz at $V_{pp} = 1000$ V resulted in a 0.1 K in temperature on the outside encapsulation. | 132 |
| Figure 6.1: Setup of a single cell copper cavity for resonance control. The left side is driven by a piezo simulating the microphonics disturbance and the right side is driven by a piezo for compensation. | 136 |
| Figure 6.2: Resonance control algorithm setup, a master oscillator (MO) is used to drive the cavity. The forward and reverse power are measured from the dual directional coupler. The envelope of the reverse power is measured with a crystal detector. | 137 |
| Figure 6.3: (a) Transfer function of copper cavity. (b) The harmonics of the system arise when the transfer function is taken. The main diagonal line is due to the stimulation of the piezo and the adjacent lines are the harmonics. | 138 |

| | |
|---|-----|
| Figure 6.4: Temperature and frequency variation of the copper cavity. | 140 |
| Figure 6.5: Compensation with integral gain only with frequency offset in the cavity. | 140 |
| Figure 6.6: (a) Signal of the phase detector and control signal. The phase between them is close to 0 degrees. (b) A phase shift of 180 degrees was also implemented but the frequency detuning got worse. | 141 |
| Figure 6.7: (a) Time series signal of the cavity frequency detuning with a 10 Hz vibration from the disturbance piezo. A proportional gain $K_p = 45$ and integral gain of $K_I = 15$ was used to dampen the 10 Hz vibration. (b) Histogram of the peak to peak values of the cavity detuning. | 142 |
| Figure 6.8: (a) FFT of cavity detuning with PI algorithm on and off, the gains were $K_p = 45$ and $K_I = 15$. (b) Integrated RMS frequency detuning with PI algorithm on and off. | 143 |
| Figure 6.9: LMS algorithm schematic, the control $u(t)$ has a filter weight update based on the frequency shift of the cavity. | 144 |
| Figure 6.10: Cavity detuning with a 10 Hz vibration is damped with different learning rates μ . The large the μ value the faster the damping of the 10 Hz occurs. | 146 |
| Figure 6.11: (a) Control using PI and LMS algorithms with no white noise added to the disturbance piezo. (b) Control using PI and LMS algorithms with white noise on the disturbance piezo. | 146 |
| Figure 6.12: (a) Piezo control voltage (left) and cavity frequency detuning (right). The disturbance piezo voltage is doubled changing the cavity frequency detuning. (b) A closer look at the point where the piezo disturbance signal is doubled, the piezo control signal adapts to this change by increasing the voltage. | 147 |
| Figure 6.13: a) Piezo control and cavity detuning signal, the disturbance piezo signal phase is changed from 0 to 180 degrees. (b) A closer look at the control signal shows that the phase also changes to adapt and dampen the vibration. | 148 |
| Figure 6.14: (a) Cavity frequency detuning with the LMS algorithm turn on and off with 10 and 80 Hz vibrations. (b) Histogram cavity frequency detuning with the LMS algorithm on and off. | 148 |
| Figure 6.15: Integrated RMS cavity frequency detuning with the LMS algorithm on or off. The vibrations damped are 10 and 80 Hz. | 149 |
| Figure 6.16: (a) Control signal for the PI loop control at $K_p = 37$ and $K_I = 50$ for 10 Hz vibration (b) Control signal with LMS algorithm on for a 10 Hz vibration. | 150 |

Figure 6.17: (a) LMS control with different learning rates μ . (b) Zoom in showing vibration harmonics from the 10 Hz. 150

Figure .1: The amplitude and phase of the harmonic oscillator with different Q values.
(a) Amplitude of the harmonic oscillator with respect to the driving frequency.
(b) Phase of the harmonic oscillator with respect to the driving frequency. . . . 157

Figure .2: (a) Amplitude plot of Duffing equation with instability hysteresis. The x-axis is given by the normalized frequency Ω . (b) Phase plot with instability hysteresis. 158

Figure .3: The Amplitude and frequency response of the Duffing oscillator is shown with a damping coefficient of $\alpha = 0.02$. The left leaning curves show a softening spring system with β being negative and the right leaning curves show a hardening system with β . (a) Amplitude of the resonance curve for the Duffing oscillator. (b) Phase of the Duffing oscillator. 160

KEY TO ABBREVIATIONS

MSU Michigan State University

NSCL National Superconducting Cyclotron Laboratory

SRF Superconducting Radio Frequency

Linac Linear Accelerator

FNAL Fermi National Accelerator Laboratory

FRIB Facility for Rare Isotopes

LCLS-II Light Coherent Light Source II

SNS Spallation Neutron Source

Eu-XFEL European X-ray Free-electron Laser

LLRF Low-level Radio Frequency

PZT Lead Zirconate Titanate

CW Continuous Wave

PIP-II Proton Improvement Plan II

LHe Liquid Helium

LN2 Liquid Nitrogen

ILC International Linear Accelerator

CHAPTER 1

INTRODUCTION

1.1 A Brief History of Linacs

About 30 percent of Nobel prizes in physics are awarded due to the use of particle accelerators [1]. A particle accelerator delivers energy to a charged particle beam via the application of an electric field. When the particle beam reaches the desired energy it is either collided with another particle beam or with a target. The first accelerators built in the 20th century were linear accelerators (linacs) that used an electrostatic field to accelerate particles. In an electrostatic accelerator, the main limitation occurs due to electrical breakdown which occurs at a few MVs. With higher energies needed to probe for new physics, a new acceleration method was needed. During the 1920s a new method was developed which used alternating fields with a frequency range of 1-800 MHz. Alternating the polarity of the accelerating structures helped improved the electrical breakdown by pushing the field threshold higher. Additionally, using an alternating polarity allowed to used multiple resonators which used the same accelerating voltage thus multiplying the energy of the particle by the amount of resonators used.

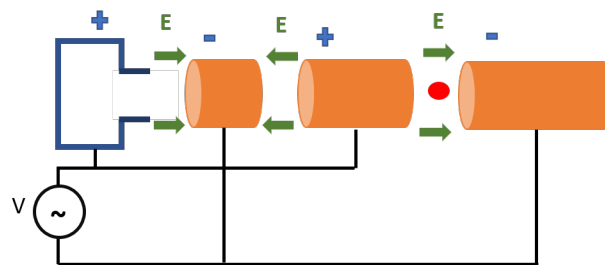


Figure 1.1: Wideröe linac with three drift tubes, each of the drift tubes is connected to the AC source.

In 1924, Gustav Ising proposed the first accelerator that used alternating fields for acceleration giving rise to all modern-day accelerating structures [2]. This accelerator consisted of a vacuum tube with multiple concentric drift tubes which functioned as a Faraday cages. Fig. 1.1 shows

the schematic of the setup, the beam is accelerated through multiple gaps and as the field changes polarity it continues through the drift tube to prevent deceleration. This experimental setup was later demonstrated by Rolf Wideröe in 1927 at Aachen, Germany [3]. In this experiment, an RF voltage of 25 kV from a 1-MHz oscillator was applied to a single drift tube between two grounded electrodes. A beam of potassium was accelerated through this setup reaching the final beam energy of 50 keV. This design kept evolving with time with multiple drift tubes being used to reach higher energies. The second development for linear acceleration was due to Luis Alvarez, this design used a resonant RF cavity for acceleration. The resonant cavity consists of several drift tubes and each of the gaps is in phase with each other as opposed to the Wideröe type resonator. The first Alvarez cavity resonator with drift tubes linac design was 1 m in diameter and 12 m long with a resonant frequency of 200 MHz, this design accelerated protons from 4 to 32 MeV. The kinetic energy needed to reach 99 % of the speed of light for an electron is 2.62 MeV and for a proton it is 6.65 GeV. For accelerating the electron or other particle to relativistic speed the Wideröe and Alvarez cavity resonator with drift tubes would not be suitable since it's limited to velocity between $0.05 < \beta = v/c < 0.4$.

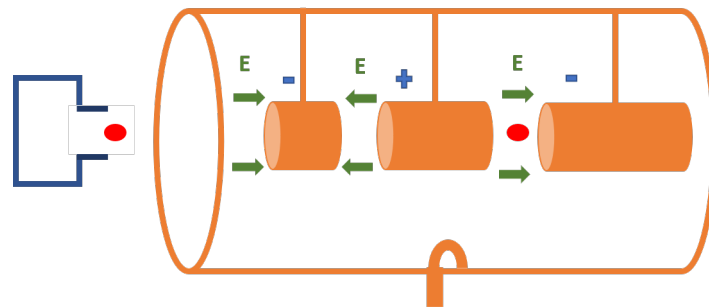


Figure 1.2: Alvarez linac with three drift tubes, the drift tubes are placed inside a cavity in the TM_{010} mode.

Coupled resonator structures are used to accelerate relativistic particles in the velocity range of $0.4 < \beta < 1$. A coupled resonator structure reduces the phase velocity of the RF wave due to the periodic elements. This reduction in phase velocity is optimized to match the velocity of the particle for synchronism in acceleration. Additionally, this coupled resonator structure only uses one power source compared to multiple individually driven resonators. There are many designs for

coupled-resonator structures in this section only one will be discussed. One of the first structures to be used was a disc-loaded traveling waveguide. Fig 1.3 shows the shape of the structure which consists of several disks each separated by $d=\beta\lambda/2$, λ is the wavelength from the resonant frequency of the structure. The disks are placed to slow the phase velocity to match the particle velocity for

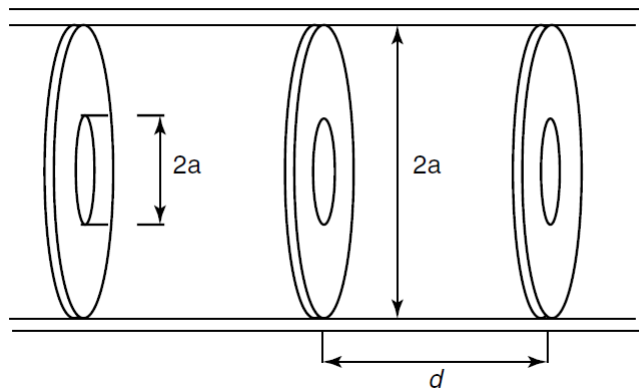


Figure 1.3: Traveling wave disc-loaded structure [4].

optimal synchronization. This structure was first put into place in the SLAC tunnel which is 3 km long. The SLAC linac accelerated positrons and electrons up to 50 GeV in the 1980s [4]. A standing wave structure can also be used for the acceleration of relativistic particles, the geometry is the same but the coupling is different. For relativistic acceleration, all modern SRF linacs use an iris-loaded geometry. The geometry of the cavities has changed and now takes on an elliptical shape to reduce the surface peak fields. Additional reasons why this geometry was chosen will be discussed in the next section. These developments and the addition of the RF Quadrupole (RFQ) form the basis of all modern linear accelerators [4].

1.2 Acceleration with Superconducting Cavities

The first cavities used in linacs were all made from normal conducting materials such as copper. To reach high accelerating gradients normal conducting cavities are operated in pulse operation with a low duty cycle (1 to 10 %) to prevent the cavity from overheating. As will be discussed later the cavity's beam aperture radius depends on its frequency. The transverse dimension of a cavity

is roughly inversely proportional to the resonant frequency. Most cavities at room temperature and in the relativistic regime operate at 10 GHz or higher frequency since their shunt impedance or efficiency is higher in this regime. The limit of normal conducting cavities is the ability to maintain a high duty cycle which in modern linacs is essential to reach large beam power to produce secondary beams. Table 1.1 shows a comparison of two pillbox cavities one meter long operated in CW mode at 650 MHz with a 1 mA beam passing through it. The parameters listed on the table will be discussed further in Chapter 2 of this thesis. The materials used for comparison are copper for the normal conducting cavity and niobium for the superconducting cavity. These are the two materials most commonly used in modern-day linacs.

Table 1.1: AC power consideration to operate a one meter long 650 MHz superconducting and normal conducting pillbox cavities at 10 MV/m with a 1 mA beam.

| Parameters | Units | Superconducting | Normal Conducting |
|----------------------------|------------|-----------------------|---------------------|
| R_s (Surface Resistance) | m Ω | 20×10^{-6} | 6.56 |
| Q_o | | 1.28×10^{10} | 3.91×10^4 |
| r/Q_o | Ω | 195.9 | 195.9 |
| P_C | kW | 40×10^{-3} | 13.05×10^3 |
| P_{RF} | kW | 10 | 13.09×10^3 |
| Refrigeration | kW | 29.8 | - |

One of the main differences between a normal conducting and superconducting cavity is the surface resistance (R_s) which differs roughly by five orders of magnitude. The power dissipated on the walls ($P_c = \frac{V_c^2}{(r/Q_o)Q_o}$) of a one meter long superconducting cavity at 10 MV/m is 40 W which is much smaller compared to 13.05 MW in a copper cavity. For the copper cavity, this power dissipation is enough to melt the copper. Note that in general a room temperature cavity will be optimized to increase the shunt impedance by making the bore radius smaller. This can increase the shunt impedance by 4 to 6 times. But even with this improvement the power dissipate on the wall is still large. The power delivered to the beam is more efficient in a superconducting cavity since

only 40 W are dissipated on the cavity walls. The RF power needed to maintain an accelerating gradient of 10 MV/m and with a beam current of 1 mA for a superconducting cavity the pillbox cavity is 10 kW compared to 13.09 MW in a copper cavity. Note that the RF power includes the power lost on the cavity walls and power imparted to the beam. In terms of RF power consumption, a superconducting cavity is a better option.

For a proper comparison, the power needed to maintain both cavities in operation must also include the power needed to support the cavity operation at 2 K, the result of this calculation is shown in Table 1.1. Niobium reaches the superconducting state at 9.2 K and is cooled to 4.2 K or 2 K depending on the cavity type. The cryogenic AC wall power was obtained by using the refrigerator efficiency which for a large plant is $\eta_f = 0.2$ and the Carnot cycle efficiency using $\eta_c = \frac{2}{300-2} = 0.0067$ [5]. This gives a wall power to heat removal efficiency of 746 W/W leading to a total power of 29.8 kW to operate the cavity at 2 K. The total power consumption of operating the SRF cavity is 39.8 kW while the copper cavity is 13.09 MW not taking into account the cooling of the copper cavity. Again, even considering the power needed for cooling the superconducting cavity it is clear that an SRF cavity is better for CW operation.

In modern linacs the design of cavities has changed from pillbox cavities to elliptical cavities in the range of $\beta = v/c > 0.6$. This has led to improvements in r/Q_o , reduction of surface peak fields that can be sustained on the cavity walls thus leading to higher accelerating fields [5]. In general normal conducting cavities have a smaller beam aperture radius compared to SRF cavities, this is to increase the r/Q_o to reduce the heat load on the cavity walls. In hadron and high beam current linacs a smaller beam aperture results in large wakefields which are detrimental to the beam [6]. Thus, a larger beam aperture will result in less beam loss leading to less activation. An SRF cavity is ideal for high power and CW operation of linacs which can be used to accelerate hadrons or electrons.

1.3 Superconducting Properties of Materials

A superconducting material exhibits three features, the first is a drop of DC resistance to zero at a specific temperature known as the critical temperature (T_c) where the material undergoes a phase change. The second feature is the ability to behave as a perfect diamagnet with zero magnetic field inside the material when the critical temperature is reached. Lastly, a superconductor can also behave as if there were a gap in the energy of width 2Δ centered about the Fermi energy in the set of allowed one-electron levels [7]. The superconducting state can arise from pure metals, metal alloys, and ceramics. The critical temperature for superconductors can vary from $325\mu K$ [8] for polycrystalline rhodium (Rh) at ambient pressure to 250 K for LaH_{10} at 170 GPa [9]. Superconductivity for certain materials also depends on the pressure applied to them. The pressure can range from ambient pressure to 170 GPa, for applications in accelerators a material with low pressure is desired such as the helium pressure of 23 torr in the cryomodule. This section will give a brief overview of each of these features of a superconductor and why niobium was chosen as the material to build the cavities.

1.3.1 Free Electron Model

Electrical resistance can be understood via the free electron model which dictates that the valence electrons of atoms are the conductors of electricity. The heating of the conductor RF current is caused by the electron scattering of the lattice imperfections such as missing atoms, interstitial atoms, and chemical impurities. Electrons get also scattered by phonons which are the lattice vibrations caused by thermal motion. As the temperature goes down the number of phonons goes down and the dominant term for the resistance is caused by the metal's impurity.

In the classical theory, the conductivity is given by

$$\sigma = \frac{ne^2\tau}{m} \quad (1.1)$$

where n is the number of electrons per unit volume, τ is the average time between collisions, and m is the electron mass. The mean free path from the electron collisions is obtained from the classical

equipartition energy theorem and given by $l = \nu\tau$. At low temperature, the main contribution to resistance is due to the metals' impurities quantified by the residual resistance ratio (RRR). The RRR is the ratio of the resistivity of the metal at 300 K to the resistivity at 0 K ($RRR = \frac{\rho_{300K}}{\rho_{0K}}$). In a metal, heat is transported by electrons and phonons. The main mechanism for heat transport at low temperature is done by the valence electrons since the number of phonons goes down following the relation for the number of phonons $\propto T^3$ [10].

1.3.2 Londons' Theory

The first theory to explain the occurrence of superconductivity in metallic materials was given by the London brothers [11]. In 1934 Gorter and Casimir [12] developed the two-fluid model which describe the flow of electrons as coexisting fluids. The two types of fluids are called the normal electron responsible for the Joule Heating effect and the superelectron (later to be called Cooper pairs) which moves without resistance. Based on the two-fluid model the London brothers derived the equations which describe low resistance and the perfect diamagnetism in superconductivity. The superelectron flow can be modeled in a perfect conductor. When an electric field is applied to the metal the electrons obey the equation

$$\frac{d\mathbf{v}}{dt} = -\frac{e}{m}\mathbf{E} \quad (1.2)$$

using the current density $\mathbf{j}_s = -n_s e\mathbf{v}$, where n_s is the density of the superelectrons, the above equation is rewritten as

$$\frac{d\mathbf{j}_s}{dt} = \frac{n_s e^2}{m}\mathbf{E} \quad (1.3)$$

this equation is known as the first London equation. The Londons expressed the electromagnetic field in terms of a vector potential \mathbf{A} as $\mathbf{B} = \nabla \times \mathbf{A}$ and $E = -\frac{\partial \mathbf{A}}{\partial t}$. This lead to the expression of current density in terms of the vector potential \mathbf{A} as

$$\mathbf{j}_s = -\frac{n_s e^2}{m}\mathbf{A} \quad (1.4)$$

Using Ampere's law $\nabla \times \mathbf{B} = \mu_0 \mathbf{j}_s$ leads to the Helmholtz equation

$$\nabla^2 (\mathbf{B}) = \frac{1}{\lambda_L^2} \mathbf{B} \quad (1.5)$$

For a 1D case the solution for this equation is

$$\mathbf{B}_x(x) = B_0 e^{-x/\lambda_L} \quad (1.6)$$

where $\lambda_L^2 = \frac{m}{n_s e^2 \mu_0}$ is the London penetration depth and B_0 is the applied field. This shows that the applied magnetic field will decay exponentially as it moves into the bulk material showing that a magnetic field is not present inside. The penetration depth is inversely proportional to the square root of the superelectron density n_s which changes with temperature. As the temperature increases, n_s decreases and the flux penetration increases.

1.3.3 Meissner Effect

The Meissner effect is a phenomenon where a superconducting material in the presence of an external magnetic field expels the magnetic flux abruptly from the inside of the conductor when the material is cooled below the critical temperature T_c . Figure 1.4 shows how the effect of the Meissner effect arises after the critical temperature is reached. The London equations predict that the current density and the magnetic field in a superconductor only exist within the penetration depth λ_L .

1.3.4 Surface Impedance of SC in the Two-fluid Model

A superconductor dissipates energy in the presence of AC fields. The reason for this is high-frequency fields penetrate a thin surface layer and induces oscillations in the electrons which have a small mass. The two-fluid model can be used to understand which component gives rise to the surface impedance. The two-fluid model posits that there is a normal conducting (σ_n) component as well as superconducting component (σ_s), where conductivity of the components is $\sigma_s \gg \sigma_n$. In normal conducting materials, the surface resistance is given by the skin depth δ and conductivity σ

$$R_s = \frac{1}{\delta \sigma} \quad (1.7)$$

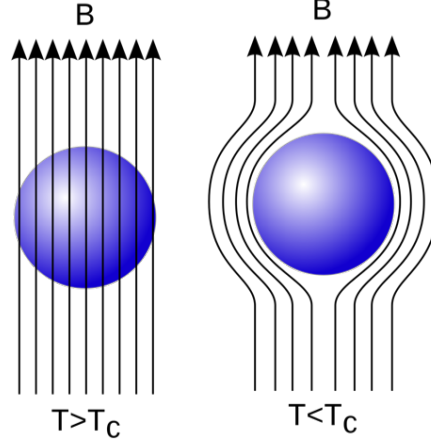


Figure 1.4: The Meissner effect expels the magnetic flux of in the presence of an external field at the critical temperature T_c .

The normal current in the material obeys Ohm's law

$$J_n = \sigma_n E_0 e^{-i\omega t} \quad (1.8)$$

while the superconducting component receives an acceleration $m_s \dot{v}_s = -2eE_0 e^{-i\omega t}$ yielding the supercurrent density

$$J_s = i \frac{2n_s e^2}{m_e \omega} E_0 e^{-i\omega t} = i \frac{1}{\mu \lambda_L^2 \omega} E_0 e^{-i\omega t} \quad (1.9)$$

the complex conductivity is obtained:

$$\sigma = \sigma_n + i\sigma_s \quad (1.10)$$

The RF magnetic field penetrates a superconductor much less than a normal conductor by the London penetration length λ_L . The surface resistance is given by the real part of the complex surface impedance

$$R_s = \text{Re} \left(\frac{1}{\lambda_L \sigma} \right) = \frac{1}{\lambda_L} \frac{\sigma_n}{\sigma_n^2 + \sigma_s^2} \quad (1.11)$$

Since $\sigma_s^2 \gg \sigma_n^2$ at RF frequencies the surface resistance can be simplified to $R_s \approx \sigma_n / (\lambda_L \sigma_s^2)$.

Therefore, the surface resistance is due to the normal conducting components in this case electrons.

The number of electron can be obtain by using the Maxwell-Boltzmann distribution which give $n_n \propto e^{-E/k_B T}$ where E is the energy. The normal conductivity is then given by

$$\sigma_n \propto l e^{-E/k_B T} \quad (1.12)$$

Using the value of the conductivity of the superconducting component $1/\sigma_s^2 = \mu^2 \lambda_L^4 \omega^2$ and plugging in to the surface resistance above yields

$$R_s \propto \lambda_L^3 \omega^2 l e^{-E/k_B T} \quad (1.13)$$

From the two-fluid model the surface resistance is shown to depend on exponential on temperature and proportional to the square of the RF frequency. The results from BCS will be shown in the next section.

1.3.5 BCS Theory

The first complete microscopic theory of superconductivity was published in 1957 by Bardeen, Cooper, and Schrieffer [13]. The theory shows that two electrons can interact with each other via a phonon. When an electron passes through a lattice it will polarize it by attracting the positive ions and these excess positive ions then attract a second electron. This interaction is known as a Cooper pair and occurs when two electrons with equal and opposite momentum as well as spin interact given by (\mathbf{p}, \uparrow) and $(-\mathbf{p}, \downarrow)$. While electrons are fermions that obey the Fermi-Dirac statistics due to their 1/2 spin, a Cooper pair obeys the Bose-Einstein statistics meaning all the pairs can occupy the same quantum state. The extension of the Cooper pair wavefunction is given by the coherence length ξ which BCS theory predicts as

$$\xi_{BCS} = \frac{\hbar v_F}{\pi \Delta} \quad (1.14)$$

where v_F is the Fermi-velocity and $\Delta = 1.764 k_B T_c$ is the energy band gap. The energy gap forms due to the formation of the Cooper pairs and is dependent on temperature.

The BCS surface resistance for a superconductor is given by [14]

$$R_{BCS} = \frac{\mu_0^2 \lambda_L^3 \sigma \Delta \omega^2}{k_B T} \ln \left(\frac{2.246 k_B T}{\hbar \omega} \right) \exp \left(-\frac{\Delta}{k_B T} \right) \quad (1.15)$$

where the product $\sigma \lambda \propto l(1 + \xi_{BCS}/l)^{3/2}$. The surface resistance depends on the temperature T, the bandgap energy Δ , the frequency of the RF field f, the mean free path l , and the coherence length

ξ_{BCS} . In addition to the BCS resistance experimental results show that the surface resistance has the following relation

$$R_s = R_{BCS} + R_0 \quad (1.16)$$

where R_0 is known as the residual resistance. In literature the residual resistance is attributed to the dissipation caused by trapped vortices oscillating under the RF field, lossy oxides or metallic hydrides on the surface, grain boundaries, generation of hypersonic or localized electron surface states [14]. Typical values from residual resistance can range from 5 to 15 n Ω [15]. The BCS resistance for a 650 MHz cavity at 2 K is 2.2 n Ω .

1.3.6 Superconductor Types

There are two types of superconductors, type-I which exhibits the Meissner state and type-II which in addition to the Meissner state exhibits a vortex state. The general theory of how these two types of superconductors arise is given by the Ginzburg-Landau (GL) theory [16]. The critical fields where the RF currents start breaking the Cooper pairs can be calculated from this theory. The relationship between the magnetic field and temperature with respect to the superconductor type is shown in Fig. 1.5. The superconducting type is defined by the GL parameter $\kappa_{GL} = \lambda_L / \xi_{BCS}$. For type-I superconductor this value is $\kappa_{GL} < 1/\sqrt{2}$, the transition from the Meissner state to the normal state occurs at H_c . For type-II superconductors the value is $\kappa_{GL} > 1/\sqrt{2}$, the magnetic field at which the material leaves the Meissner state is $H_{c1} = \frac{\pi\hbar/e}{4\pi\lambda_L^2} (\ln\kappa_{GL} + 0.5)$ and critical field where it goes from the vortex state to normal conductor is $H_{c2} = \frac{\pi\hbar/e}{2\pi\xi_{BCS}^2}$.

1.4 Best Superconductors for RF Application

For accelerator application using SRF cavities the right superconducting material should provide five properties. The first is a low surface resistance and low residual resistance. The second property is a higher lower critical magnetic field H_{c1} where the Meissner state is destroyed due to the penetration vortices. The third is a high H_{c2} which gives the SRF breakdown once the material

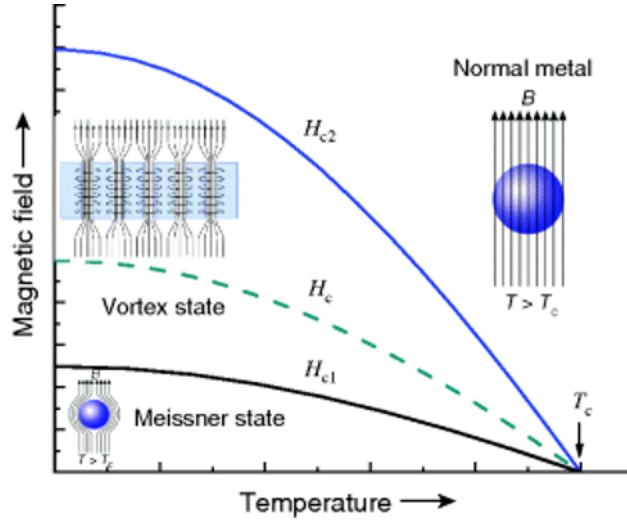


Figure 1.5: A type-I superconductor only experiences the Meissner state where no magnetic flux enters the bulk of the material. Superconducting state is destroyed when the external magnetic field exceeds the value H_{c1} . A type-II superconductor exhibits the Meissner state, a vortex state after H_{c1} , and after H_{c2} the material becomes normal conducting.

goes normal conducting. The fourth is a high thermal conductivity to transfer the RF dissipated power through the cavity wall. The fifth property is to provide good mechanical properties and malleability to minimize crack formation during manufacturing [14]. Pure niobium (Nb) is the best

Table 1.2: Type-II Superconductors properties [14].

| Material | T_c [K] | H_{c2} [mT] | H_{c1} [mT] | λ_L [nm] |
|----------|-----------|---------------|---------------|------------------|
| Nb | 9.2 | 200 | 170 | 40 |
| Nb_3Sn | 18 | 540 | 40 | 85 |
| NbN | 16.2 | 230 | 20 | 200 |
| MgB_2 | 40 | 320 | 20-60 | 140 |

candidate meeting these criteria. Nb has the highest critical field H_{c1} for the phase transition into the vortex state. In the vortex state, the material experiences higher resistance due to the magnetic vortices. Additionally, the penetration of the magnetic field is much lower compared to the other materials. For NbN and MgB_2 the London penetration depth is 4 and 3 times larger compared to Nb. Non-superconducting properties of the materials for SRF cavities are also important. For example, the thermal conductivity of Nb_3Sn is three orders of magnitude lower than for Nb at 2 K.

This means that Nb_3Sn is more prone to overheating. Additionally, Nb is very malleable compared to other metals which makes for easier production. Nb_3Sn is also very brittle which makes it harder to shape the cavities. Efforts are underway to develop methods to mitigate limitations of Nb_3Sn to exploit the higher T_c [17]. Niobium is also used as an alloy for steel to yield better strength, due to this applicability niobium can be readily found whereas other materials must be manufactured or they are not as abundant. For these reasons niobium makes a suitable choice for the manufacturing of SRF cavities.

1.5 Motivation

The new generation of SRF linacs used for the production of rare isotopes, high-intensity neutrinos, and x-rays should provide relatively low intensity CW or pulse beams. Low intensity linacs (low beam loading) require less input RF power for the cavity to accelerate the beam. This results in the condition that the loaded quality factor remains high and the resonance bandwidth being narrow, typical half-bandwidth range from 10 Hz for the LCLS-II [18] and 30 Hz for the PIP-II Linac [19].

Table 1.3 shows a comparison of different linacs that are built, currently being built, and proposed with different beam currents and modes of operation. These small bandwidths make the cavities susceptible to an RF power trip if the cavity deviates by more than half the bandwidth from its resonant frequency. SRF cavities are manufactured from thin sheets of niobium ranging from 2-4 mm in thickness to provide more efficient cooling and to reduce cost of bulk material but provide sufficient mechanical rigidity. The thin cavity walls make them susceptible to mechanical deformation causing a shift in the resonant frequency. The 650 MHz 5-cell elliptical which will be used for the PIP-II project has a frequency deformation sensitivity of 240 Hz/ μm [19]. For this cavity a 62.5 nm mechanical deformation will cause it to shift more than 15 Hz from the resonant frequency. This shift will make the cavity unable to provide synchronous acceleration. A more detailed discussion is presented in chapter 2 on methods to mitigate the cavity's deformation. This problem can be solved by using a larger power source which are more expensive and add

Table 1.3: Linacs with different beam currents (i_b), accelerating fields (E_{acc}), and bandwidths (Δf) of the cavity. In the table all the linacs use an elliptical cavity in the high energy section. Linacs with low beam loading in pulse and CW operation will have a small bandwidth. Linacs built are denoted by ¹, currently being built ², and are proposed ³.

| Project | Linac Type | Particle | f | E_{acc} | i_b | Δf |
|---------------------------------|------------------|----------|--------|-----------|-------|------------|
| | | | MHz | MV/m | mA | Hz |
| Wideband CW | | | | | | |
| ARIEL ¹ [20] | Nuclear Physics | e- | 1300 | 10 | 10 | 650 |
| Narrowband CW | | | | | | |
| CEBAF Upgrade ³ [21] | Nuclear Physics | e- | 1497 | 20 | .43 | 37 |
| LCLS-II ² [18] | Material Science | e- | 1300 | 16 | 0.062 | 10 |
| FRIB ² [22] | Nuclear Physics | ion | 644 | 17.5 | .33 | 20 |
| PIP-II ² [19] | Neutrino Physics | p | 650 | 18.8 | 2.6 | 30 |
| Wideband Pulsed | | | | | | |
| Eu-XFEL ¹ [23] | Material Science | p | 1300 | 23.6 | 5 | |
| ESS ² [24] | Material Science | p | 704.42 | 19.9 | 62.5 | 550 |
| SNS ¹ [25] | Material Science | p | 805 | 15.9 | 26 | 300 |
| ILC ³ [26] | Higgs Factory | e-,e+ | 1300 | 40 | 7.6 | 140 |

cost to operation. A cost effective method is to use a piezoelectric actuator to compensate for the mechanical detuning of the cavity. This approach has been demonstrated in various SRF linacs such as SNS [25] and EuX-FEL [27]. A voltage is applied to piezoelectric actuator which compresses the cavity to change the frequency. The theory of the piezoelectric actuator and resonance control algorithm will be discussed in chapter 5 and 6 respectively.

In Table 1.3 all the linacs listed use or will use elliptical cavities. The methods used for resonance control are applicable to any cavity shape. Narrowband linacs need piezoelectric actuators and a resonance control algorithm to avoid a cavity RF trip due to the loss of resonance. In the case of wideband linacs, resonance control algorithms are being pursued to reduce the amount of RF power used during operation. This thesis will discuss the piezoelectric actuator technology which will be used for three different linacs: FRIB, PIP-II, and LCLS-II which all fall in the class of narrowband CW linacs. Data for microphonics will also be presented based on the capture for the LCLS-II cryomodules. The following sections will present an overview of the scientific goals for each of

the linacs as well as the discussion of the layout and particle sources.

1.5.1 FRIB

The FRIB linac, under construction at MSU, will be the world's most powerful radioactive beam facility, making nearly 80% of the isotopes predicted to exist for elements below uranium. The linac will be operated in CW and capable of producing 400 kW beams for all elements from uranium having a maximum energy of 200 MeV/nucleon to protons reaching an energy of 500 MeV [28]. FRIB will have unique capabilities and will offer opportunities to answer fundamental questions about the inner workings of the atomic nucleus, the formation of the elements in the universe, and the evolution of the cosmos [29].

The linac layout resembles a paper clip as shown in Figure 1.6, it will feature a room temperature 0.5 MeV/u front-end followed by an SRF section consisting of 4 classes of niobium cavities [28]. In a heavy ion accelerator the ions such as uranium must undergo charge stripping which gets rid of electrons in the outer shell of the nucleus. This is done since the charge to mass ratio (q/A) is small, the energy gain of a heavy ion can be written as $(q/A) \times E$ where E is the electric field. As the (q/A) increases the ion acceleration becomes more efficient. The front end contains an Electron Cyclotron Resonance (ECR) ion source which is used to produce relatively high charge state ions. After the ions leave the ECR ion source they go through the Low Energy Beam Transport (LEBT) which contains the Radiofrequency Quadrupole (RFQ) which is made up of copper. The ions then enter linac segment 1 which contains Quarter-wave Resonators (QWR) of $\beta_{opt} = 0.041$ and $\beta_{opt} = 0.085$ both made of niobium and operate at 4.2 K. During this linac segment, the ions undergo charge stripping which is done by intercepting the beam with a liquid-lithium sheet. Linac segments 2 and 3 contain half-wave resonators (HWR) of $\beta_{opt} = 0.29$ and $\beta_{opt} = 0.53$ also made of niobium and operate at 2 K which accelerate the beam to 200 MeV/nucleon. The 200 MeV/nucleon beam will then strike a solid carbon disk target which will produce a secondary beam via fragmentation containing rare isotopes. The secondary beam will go through a fragment separation section which will select the desired ions which are then delivered to the nuclear experiments.

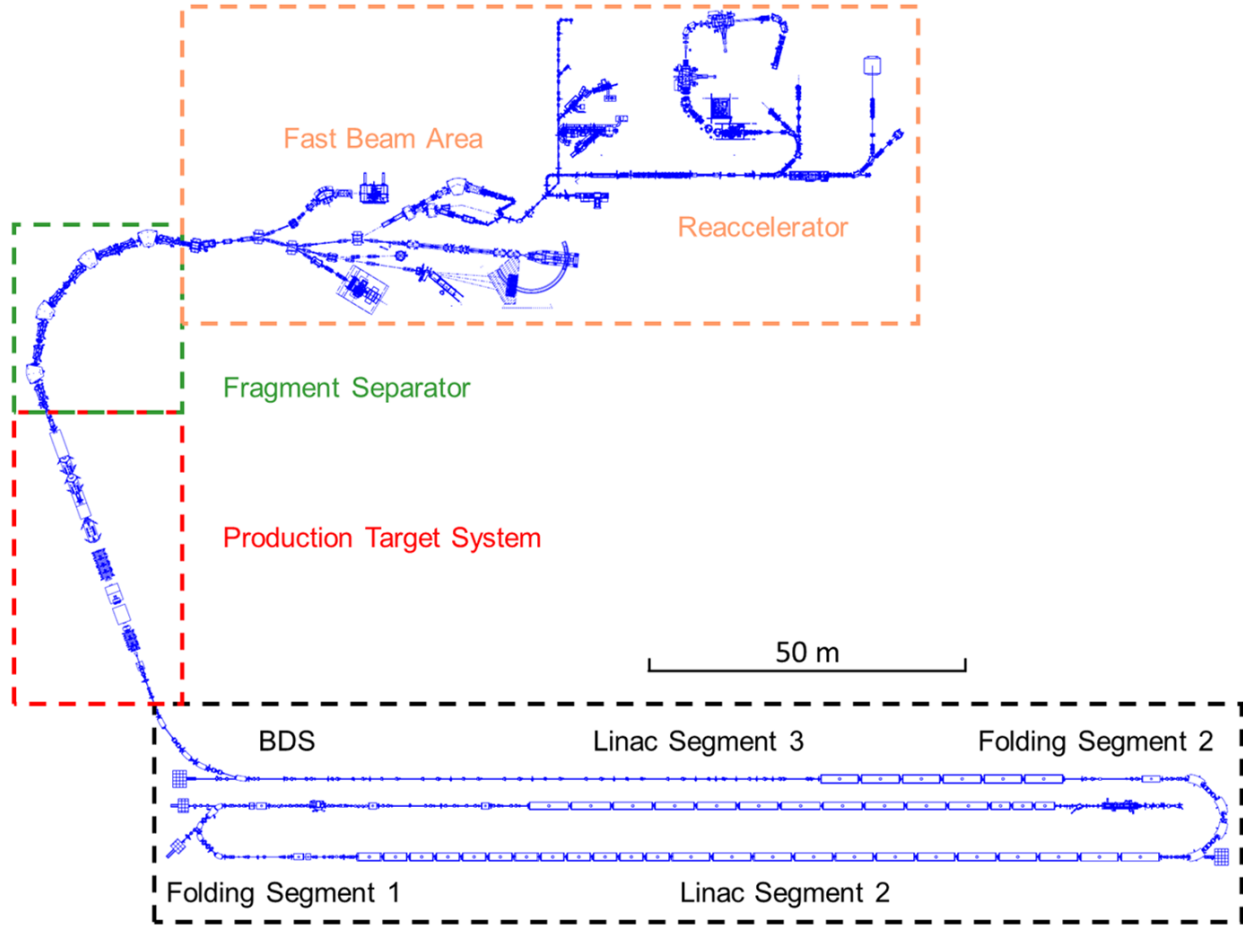


Figure 1.6: FRIB linac.

Although the current FRIB configuration will be the most powerful ion beam linac, a higher beam energy of 400 MeV/u will produce even more isotopes which will give scientists more opportunities to study rare isotope behavior. This is due to a higher charge stripping for uranium and large cross sections at higher energy. A detailed explanation can be found in the design report [30]. FRIB will undergo an energy upgrade by installing additional cryomodules in the space left in the linac tunnel [22]. The cryomodules will use $\beta = 0.61$ 5-cell 644 MHz elliptical cavities made of niobium and operated at 2 K. This upgrade will raise the energy from 200 MeV/nucleon to 400 MeV/nucleon. In this upgrade section the cavities will use dynamic (slow and fast) tuner design for the 644 MHz cavity based on the work at FNAL for the 650 MHz for the PIP-II cavities and research in the frame of this thesis. The tuner will consist of a piezoelectric actuator for fast

and fine frequency combined with a motor for slow and coarse frequency tuning. In CW operation the tuner will be used for compensation of microphonics.

1.5.2 PIP-II

The PIP-II superconducting linac is being constructed inside the main Tevatron ring and will upgrade Fermilab's accelerator complex. It will provide a beam for the Mu2e (Muon-to-Electron), Muon g-2, and DUNE experiments, each of these experiments seek to discover physics beyond the standard model. The Mu2e experiments seek to discover the conversion of muons to electrons without the emission of neutrinos. The Muon g-2 experiment will measure the anomalous magnetic dipole moment of a muon to a precision of 0.4 parts-per-million. The high precision measurement will be compared to theoretical predictions to test the current theory. Any deviation would point to possible undiscovered subatomic particles. The primary science goal of DUNE will be to carryout a comprehensive program of neutrino oscillation measurements. The search for charge parity violation in neutrino oscillation may give insight in to the origin of the matter-antimatter asymmetry in the universe.

The PIP-II warm front-end consist of an H^- ion source, the LEBT, RFQ, and a Medium Energy Beam Transport (MEBT) [19]. The H^- beam originates from a DC ion source and transported through the LEBT to a CW normal conducting RFQ where it is bunched and accelerated to 2.1 MeV leading to the MEBT section. The superconducting linac starts immediately downstream of the MEBT and will accelerate the beam from 2.1 MeV to 800 MeV. This linac section will consists of five classes of SRF cavities made of niobium. After the MEBT, the beam continues into the Half-wave Resonator with $\beta_{opt} = .112$. It then enters two types of single spoke resonators 1 (SSR1) at $\beta_{opt} = 0.22$ and SSR2 at $\beta_{opt} = 0.475$, and finally it goes into two types of elliptical cavities the low beta (LB) cavity at $\beta_{opt} = 0.65$ and the high beta (HB) cavity at $\beta_{opt} = 0.97$. The beam then will be injected into the booster synchrotron at 800 MeV and will exit with a beam energy of 8 GeV. Lastly the beam goes into the main injector ring resulting in a proton beam energy of 120 GeV and power of 1.2 MW. The proton beam will hit a target producing a secondary kaon beam which

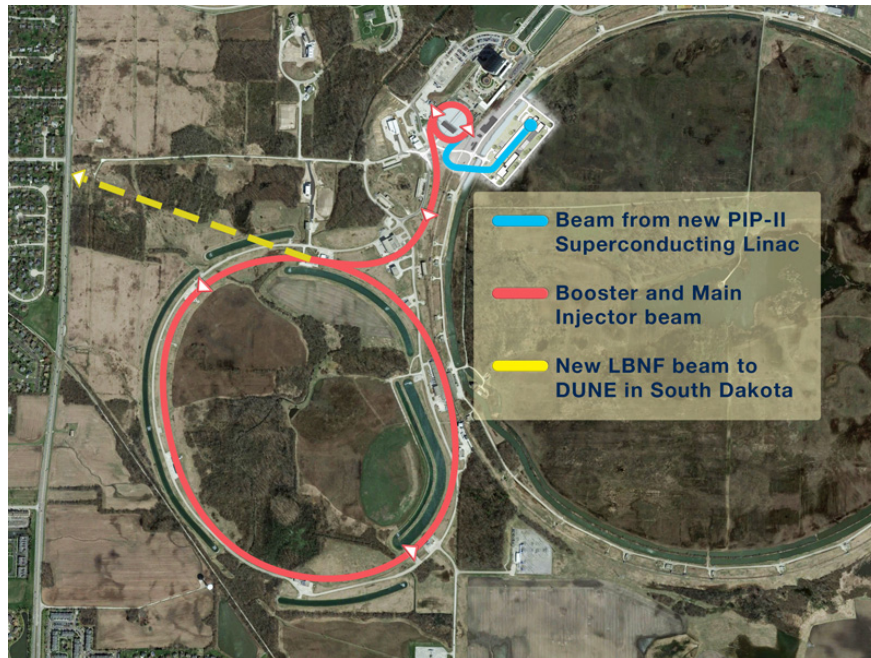


Figure 1.7: Aerial view of the PIP-II linac along with the booster synchrotron and main injector ring.

decays into neutrinos. The neutrino beams travels 800 miles through the earth from Fermilab to an underground detector in Sanford South Dakota.

The PIP-II linac will operate in CW with low beam loading which leads to narrowband cavities. The main source of detuning on the cavities will be from microphonics. There will be two different type of tuners, one for the SSR1 and SSR2 cavities, and one for the LB and HB elliptical cavities. Both types of tuners will be lever tuners consisting of a slow and course frequency tuning as well as a fast and fine frequency tuning. The tuners for the HB and LB cavities will be discussed extensively in this thesis.

1.5.3 LCLS-II

The LCLS-II is a next generation X-ray free-electron laser (FEL) time-resolved microscope that can view structure and function in the material and the chemical world down to the fundamental length and time scales of individual molecules and atoms [18]. The LCLS-II linac will use SRF cavities made of niobium operated in CW to accelerate electrons to 4 GeV to produce ultrashort

X-rays pulses from 100 to 1 fs. This will allow scientist to study nanoscale material dynamics, dynamics of energy and charge (processes like photosynthesis and other chemical reactions), and biological functions in real time.



Figure 1.8: LCLS-II Linac layout.

The electrons are produced in a normal conducting RF gun with a CsTe photo-cathode. A UV laser is used to produce 500 pC at 1 MHz from the CsTe cathode [18]. The electron beam exits the RF gun with an energy of 750 keV and proceeds to the CW 1.3 GHz buncher cavity with two emittance compensating solenoids. The electron beam then makes its way into the SRF linac composed of 4 different sections: L0, L1, L2, and L4. L0 has one cryomodule with eight 1.3 GHz TESLA 9-cell SRF cavities, this section accelerates the beam from 0.75 MeV to 100 MeV. L1 has two 1.3 GHz cryomodules which accelerate the beam from 100 MeV to 250 MeV. This section includes three 3.9 GHz linearizer cryomodules which also provide the first bunch compression. The L2 section has twelve 1.3 GHz cryomodules which accelerate the beam from 250 MeV to 1.5 GeV and generates the second stage of bunch compression. The L3 has twenty 1.3 GHz cryomodules which accelerate the beam from 1.5 GeV to the final energy of 4 GeV. The beam is then sent to undulators, an undulator is a periodic structure of dipole magnets. Electrons traversing through the undulator undergo oscillations which lead to coherent emission of X-rays.

The LCLS-II linac will be operated in CW with very low beam loading, for the 1.3 GHz cavities the half-bandwidth is 10 Hz. The main source of detuning is caused by microphonics. All SRF cavities use a frequency tuner composed of a slow and coarse frequency tuning as well as fast and

fine frequency tuning. Nineteen 1.3 GHz cryomodules and three 3.9 GHz cryomodules were tested in Fermilab. The results of microphonics for the 1.3 GHz cavities will be discussed in Chapter 4.

1.6 Thesis Organization

In Chapter 2, the theory of SRF cavities will be discussed. The lumped-circuit model of the cavity will be derived from Maxwell's equations. The effects of the Lorentz force detuning will be discussed based on the circuit model. The lumped circuit model is used to study the effects of microphonics in a cavity.

Chapter 3 will discuss the measurement setup of the cavity. The algorithm used to calculate the detuning will be discussed as well as the instrumentation. A section is devoted to measurements of the transfer function of the cavity-tuner system which is used to measure the mechanical eigenmodes of the system. Lastly, a bead-pull measurement of the cavity will be discussed.

In chapter 4 measurements of the vibrational noise coupling to the cavity, known as microphonics, will be presented and discussed. Chapter 5 deals with the slow and fast tuner which uses a motor and piezoelectric actuator for compensation of microphonics. A section is devoted to the studies of piezoelectric actuator reliability and the study of heating under a high voltage regime. To conserve power and avoid a cavity RF trip a resonance control algorithm is needed to compensate for microphonics.

Chapter 6 will present the resonance algorithm which will be used, the results from implementing this algorithm on a single cell elliptical cavity at room temperature. The appendix will discuss a harmonic oscillator as well as the non-linear case. The appendix provides a set of equation to predict the hysteresis of the resonance curve.

CHAPTER 2

SUPERCONDUCTING RF CAVITIES

The harmonic oscillator can model the behavior of an RF cavity. Cavity wall movements will be model as a harmonic oscillations and the electromagnetic field component will be modeled as an RLC circuit which can be derived from Maxwell's equation. The harmonic oscillator resonance curve, the resonance curve phase, and the time dependent solution are derived. These equations are used to characterize the system.

2.1 Resonator Theory

The amplitude of the accelerating gradient of the cavity is modeled as a harmonic oscillator derived from Maxwell's equations. This derivation was shown by Condon [31] and Bethe [32]. The form of the derived equation is similar to the RLC circuit, the RLC circuit model is then used to characterize the cavity model. During operation, the cavity experiences vibration noise known as microphonics and is characterized by slow frequencies less than 200 Hz. Since the cavity is operated at high frequency, the slow variations are separated from the high frequency components to obtain the field envelope equation. The envelope equation is used to study the effects of microphonics. Additional figures of merits of the cavity are derived from this equation such as the quality factors for different components.

Starting with Maxwell's equations given by

$$\nabla^2 \mathbf{E} - \frac{1}{c^2} \frac{\partial^2 \mathbf{E}}{\partial t^2} = -\mu_o \frac{d\mathbf{J}}{dt} \quad (2.1)$$

The current density \mathbf{J} in Eq. 2.1 has three components, the ohmic losses on the cavity walls, the losses from the coupling ports which excite the cavity, and the beam current. The cavity can be excited by an infinite number of modes. Generally in designing a cavity, only one mode is of interest. This mode has to have the lowest frequency and have a longitudinal electric field along the axis to accelerate the beam. In a cylindrical resonator this mode is know as the TM_{010} . The

electric field can be expanded in a complete set of eigenmodes as shown by Slater [33]

$$\mathbf{E} = \sum_n e_n(t) \mathbf{E}_n(\mathbf{r}) \quad (2.2)$$

where $e_n(t)$ are the time variations and $\mathbf{E}_n(r)$ are the spatial variations. The normalization for this complete set is

$$\int E_m \cdot E_n dV = 2\delta_{mn} \frac{\sqrt{U_m U_n}}{\epsilon_0} \quad (2.3)$$

where $U_m = \frac{\epsilon_0}{2} \int |E_m|^2 dV$ is the total energy per mode. Plugging in the complete set of eigenmodes, the normalization, and the Helmholtz equation $\nabla^2 E_n = -(\frac{\omega_n}{c})^2 E$ into Eq. 2.1 leads to

$$\ddot{e}_n + \omega_n^2 e_n = \frac{1}{2U_n} \frac{d}{dt} \left(\int \mathbf{J} \cdot \mathbf{E}_n dV \right) \quad (2.4)$$

This equation shows the time variation of the electric field for the respective mode n .

One component of \mathbf{J} is the surface currents on the cavity walls which causes ohmic losses. This gives rise to the intrinsic quality factor Q_n of the cavity. For the accelerating mode of the cavity this is denoted by Q_0 with the form of

$$Q_n = \omega_n \frac{U_n}{P_{loss}} = \omega_n \frac{\frac{\epsilon_0}{2} \int |E_n|^2 dV}{\frac{R_s}{2} \int |H_n|^2 dV} \quad (2.5)$$

where R_s is the surface resistance. The intrinsic quality factor can also be rewritten as

$$Q_n = G_n / R_s, \quad G_n = \omega_n \frac{\epsilon_0 \int |E_n|^2 dV}{\int |H_n|^2 dV} \quad (2.6)$$

where G_n is known as the geometric factor since the parameter only depends on the geometry of the resonator. The intrinsic quality factor is an important parameter to obtain the cryogenic load. From the result of Eq. 2.6 the intrinsic quality factor can be improved by increasing the geometric factor and lowering the surface resistance. Typical values for an intrinsic quality factor of an SRF cavity are on the order of 10^{10} . The second component of \mathbf{J} is the current density which is used to couple the forward power to the cavity and also to probe the field of the cavity. This is done with two different ports, the power lost in these ports is denoted by $P_{ext,n}$ and the quality factor is given by $Q_{ext,n} = \omega_n \frac{U_n}{P_{ext,n}}$. The total quality factor seen by the generator is given by

$$Q_{L,n} = \left(\frac{1}{Q_n} + \frac{1}{Q_{ext,n}} \right)^{-1} \quad (2.7)$$

and it is known as the loaded quality factor which is the total damping seen by the generator. The last component of the current density is given by the beam current and it's put together with the generator current for cavity excitation. Adding the effect of the current to Eq. 2.4 the equation becomes

$$\ddot{e}_n + \frac{\omega_n}{Q_{L,n}} \dot{e}_n + \omega_n^2 e_n = \gamma_n \dot{I} \quad (2.8)$$

where γ_n is a constant and I is the remaining terms in the integral.

2.1.1 Lumped Circuit RLC Circuit

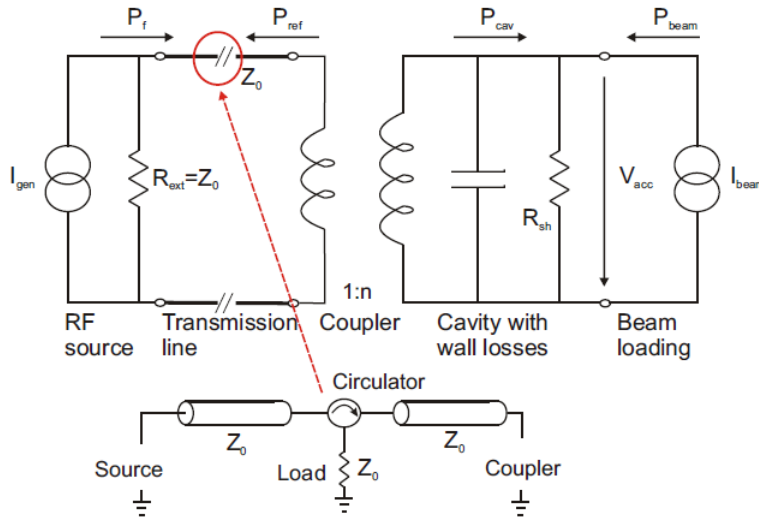


Figure 2.1: Circuit model of cavity system [34].

The form of Eq. 2.8 is similar to the form of a driven LCR circuit model which is shown in Fig. 2.1, the equation is given by

$$\ddot{\mathbf{V}}(t) + \frac{\omega_0}{Q_L} \dot{\mathbf{V}}(t) + \omega_0^2 \mathbf{V}(t) = \omega_0 \frac{R_L}{Q_L} \dot{\mathbf{I}}(t) \quad (2.9)$$

where $\omega_0 = \frac{1}{\sqrt{LC}}$, Q_L is the same as in Eq. 2.7, and $R_L = \left(\frac{1}{R} + \frac{1}{Z_{ext}} \right)^{-1}$. This equation describes the voltage \mathbf{V} excited by an RF source. The excitation by the RF source is modeled by a current source \mathbf{I} matched to the waveguide connecting the source to the input coupler antenna. The terms are bold since they are complex values. R represents the shunt impedance of the cavity and Z_{ext} is

the external load. The shunt impedance is defined by $P_{loss} = V^2/r$ where r is the shunt impedance of the real cavity. The relation of the circuit and real cavity is given by

$$\frac{r}{Q_0} = \frac{2R}{Q_0} = \frac{V^2}{\omega_0 U} \quad (2.10)$$

Note that in this relation the shunt impedance is not dependent on the surface resistance. The beam is modeled as a current with a negative sign since it is extracting energy from the cavity. The coupling to the cavity is modeled as a transformer and denoted by the coupling factor

$$\beta = \frac{R}{Z_{ext}} = \frac{R}{N^2 Z_0} = \frac{P_{ext}}{P_{loss}} \quad (2.11)$$

where N is for the transformer ratio and Z_0 is the impedance of the coaxial line. With this definition R_L can be rewritten as

$$R_L = \frac{R}{1 + \beta} \quad (2.12)$$

and the loaded quality factor Q_L as

$$Q_L = \frac{Q_0}{1 + \beta} \quad (2.13)$$

For SRF cavities with $Q_0 \gg Q_L$ the coupling factor β is in the order of 10^3 to 10^4 . The typical values of the loaded quality factor Q_L range from 3×10^6 to 3×10^7 . The loaded Q_L is measured during testing of the cavity and defines the overall bandwidth of the RF mode, it will be shown later how this is related to the beam current.

Equation 2.9 gives the voltage \mathbf{V} on the time scale of the RF driving frequency which for this thesis is 650 MHz. The perturbations that couple to the cavity are much slower on the order of 100 Hz. This equation can be modified to represent the time dependence of field envelope by plugging the following two equations into Eq. 2.9: $\mathbf{V}(t) = \mathbf{V}_c(t)e^{i\omega_{RF}t}$ and $\mathbf{I}(t) = \mathbf{I}_g(t)e^{i\omega_{RF}t}$ where I_g and V_c are the slow terms for the cavity voltage and the generator current respectively. The substitution results in the envelope equation

$$\dot{\mathbf{V}}_c + \left(\omega_{\frac{1}{2}} - i\Delta\omega \right) \mathbf{V}_c = R_L \omega_{\frac{1}{2}} (2\mathbf{I}_g - \mathbf{i}_b) \quad (2.14)$$

where $\omega_{\frac{1}{2}} = \frac{\omega_0}{2Q_L}$ is the half-bandwidth of the cavity, a derivation of this formula is shown in the appendix. The detuning of the cavity with respect to the RF generator is $\Delta\omega = \omega - \omega_{RF}$.

The current driving the cavity has two components. The current from the RF generator \mathbf{I}_g and the current from the beam \mathbf{I}_b . Note that the terms \mathbf{V}_c , \mathbf{I}_g , and \mathbf{i}_b are complex and incorporate amplitude and phase information. The frequency detuning of the cavity occurs from the deformation of the cavity walls. Equation 2.14 can be used to model the behavior of the cavity in an FPGA [35]–[38]. This model can be used for cavities in either a pulsed or a CW linac.

2.1.2 Lorentz Force Detuning

The cavity walls experience mechanical deformation leading to frequency detuning from three different sources: Lorentz force detuning, microphonics, and the piezoelectric actuator. The Lorentz force detuning (LFD) results from the interaction of the RF magnetic field in the cavity and the wall currents on the cavity resulting in a Lorentz force. The force density in an electromagnetic field is given by $\mathbf{f} = \rho\mathbf{E} + \mathbf{J} \times \mathbf{B}$ which can be used to derive the Lorentz force detuning pressure on the cavity wall as shown by J. Tückmantel, $P_{LFD} = \mu_0|H_0|^2 - \epsilon_0|E_0|^2$ [39]. The interaction with the electric field causes the elliptical cavity iris wall to bend inwards while the magnetic field causes the equator of the cavity to bend outwards as shown in Fig. 2.2. From a design point of view, the only way to mitigate LFD is to make the cavity stiffer, this can be done with stiffening rings or with the tuner which will be discussed later.

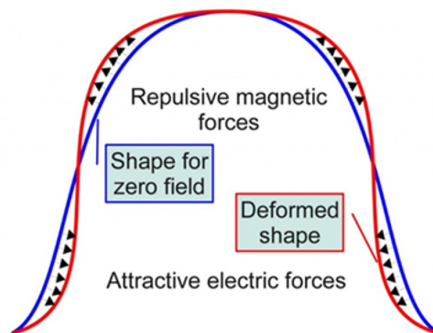


Figure 2.2: The blue line depicts the cavity with zero field and the red line shows the effect of the magnetic and electric field [40].

The frequency shift can be related to the energy as shown for the harmonic oscillator using the adiabatic theorem in the next section. This same relationship can be derived directly from Maxwell's

equations by adding perturbations to the material inside the cavity (ϵ, μ) or perturbations of cavity shape. The result of adding a perturbation to the cavity shape is given by

$$\frac{\Delta\omega}{\omega_0} \approx \frac{\int(\mu_0|H_0|^2 - \epsilon_0|E_0|^2)dV}{\int(\mu|H_0|^2 + \epsilon|E_0|^2)dV} \quad (2.15)$$

where the denominator is the energy of the cavity and in the numerator the term in the integrand is the radiation pressure P_{LFD} . This equation is known as Slater's Perturbation theorem [33] and is used to calculate the frequency shift based on a known volume deformation of the cavity or a change in the dielectric properties inside the cavity. The frequency shift from LFD is given by $\Delta f = k_L E_{acc}^2$ where k_L is the LFD coefficient with units of $Hz/(MV/m)^2$. This frequency shift is known as the static LFD, the dynamic LFD occurs from the interaction of external vibrations with the cavity.

2.1.3 Cavity Wall Movement Model as Harmonic Oscillator

The cavity wall mechanical deformations are modeled with second-order differential equations where each equation gives the behavior of a mechanical mode. External vibrations excite mechanical modes of the cavity-tuner system, the vibrations then interact with the Lorentz force yielding the dynamic LFD. Due to this interaction instabilities occur in the cavity's electric field characterized by discontinuities analogous to the amplitude behavior of the Duffing oscillator. The behavior of the Duffing oscillator is presented in the appendix. These instabilities were first observed in normal conducting resonators in the 1960s in the Soviet Union [41]. The stability conditions were derived by comparing the rate of energy transfer from the electromagnetic mode to the mechanical mode and incorporating the rate of dissipation of energy of the mechanical mode [42]. This analysis is only applicable to normal conducting cavities where the decay time of the electromagnetic mode is much less than the period of the mechanical mode.

The work done by Schulze [43] extended the analysis of the instabilities to an arbitrary decay time in the electromagnetic mode and period of the mechanical oscillation to make relevant SRF cavities. This work made the first mention and demonstrated the effectiveness of using ponderomotive effects

to damp mechanical modes. The derivation of the second-order differential equation to describe the interaction of the dynamic LFD and the cavity's mechanical modes is based on the work of Schulze [43], Delayen [44], Karliner, et al [45]. The cavity is modeled with an infinite number of mechanical modes of vibration represented by a complete infinite set of orthonormal displacement functions $\phi_\mu(\vec{r})$. The actual displacement of the cavity wall, $\xi(\vec{r})$, and the forces on the wall, $F(\vec{r})$, can be expanded into the functions $\phi_\mu(\vec{r})$:

$$\xi(\vec{r}) = \sum q_\mu \phi_\mu(\vec{r}), \quad q_\mu = \int \xi(\vec{r}) \cdot \phi_\mu(\vec{r}) dS \quad (2.16)$$

$$F(\vec{r}) = \sum F_\mu \phi_\mu(\vec{r}), \quad F_\mu = \int F(\vec{r}) \cdot \phi_\mu(\vec{r}) dS \quad (2.17)$$

where q_μ is the amplitude of the mechanical mode μ whose equation of motion is

$$\frac{d}{dt} \frac{\partial L}{\partial \dot{q}_\mu} - \frac{\partial L}{\partial q_\mu} + \frac{\partial \Phi}{\partial \dot{q}_\mu} = F_\mu \quad (2.18)$$

where $L=T-U$ is the Lagrangian, T is the kinetic energy, U is the potential energy, and Φ is the power dissipation. They are defined as

$$U = \frac{1}{2} \sum c_\mu q_\mu^2, \quad T = \frac{1}{2} \sum c_\mu \frac{\dot{q}_\mu^2}{\Omega_\mu^2}, \quad \Phi = \sum \frac{c_\mu}{\tau_\mu} \frac{\dot{q}_\mu^2}{\Omega_\mu^2} \quad (2.19)$$

where c_μ is the elastic constant, Ω_μ is the mechanical frequency, and τ_μ is the decay time of the mechanical mode μ . Plugging these equations into the Lagrange equation 2.18 leads to the harmonic oscillator equation describing the cavity wall deformations:

$$\ddot{q}_\mu + \frac{2}{\tau_\mu} \dot{q}_\mu + \Omega_\mu q_\mu = \frac{\Omega_\mu^2}{c_\mu} F_\mu \quad (2.20)$$

To relate the mechanical deformation to the frequency detuning, the adiabatic theorem is used. The adiabatic theorem for a harmonic oscillator states that the action $\frac{U}{\omega}$ can be assumed to be constant if the changes in frequency are slow enough. U is the energy and ω is the cavity frequency. The change in energy can be related to the change in frequency using the adiabatic theorem as $\frac{\Delta\omega}{\omega} = \frac{\Delta U}{U}$. The frequency shift caused by the mechanical mode μ is directly proportional to q_μ and the force F_μ due to the radiation pressure being proportional to the square of the amplitude of the

voltage V_c . The harmonic oscillator equation 2.20 can be expressed in the terms of the frequency shift of the mode which is

$$\Delta\ddot{\omega}_\mu + \frac{2}{\tau_\mu}\Delta\dot{\omega}_\mu + \Omega_\mu^2\Delta\omega_\mu = -k_\mu\Omega_\mu^2V_c^2 + m(t) + p(t) \quad (2.21)$$

The constant k_μ is the Lorentz coefficient for that mode and represents the coupling of that mode between the RF field and the mechanical mode μ . The term $m(t)$ is an additional driving term from external vibrations and microphonics. The $p(t)$ is the piezo driving term. Notice that the voltage of the cavity is a driving term for the frequency shift of the cavity. The total frequency shift measured is the sum of all the modes

$$\Delta\omega(t) = \sum \Delta\omega_\mu(t) \quad (2.22)$$

The static Lorentz force frequency shift is given by $\Delta\omega_0 = -V^2 \sum k_\mu$. The static Lorentz coefficient, also known as LFD constant, is then given by $k_L = \sum k_\mu$ and produces a frequency shift of $\Delta f = k_L E_{acc}^2$. Typical values range from 0.8 to 3 Hz/(MV/m)² for elliptical cavities with frequency shifts at 25 MV/m of 500 Hz and 1875 Hz respectively. Equations 2.14 and 2.21 are used to simulate the behavior of the cavity which will be shown in the next section.

2.1.4 Resonance Curve from RLC Envelope Equation

When the cavity experiences the Lorentz force detuning the resonance curve starts to deviate from the linear regime. The non-linear resonance curve has a branch with an instability and it forms a hysteresis with a width setup by the jump-up and jump-down frequencies. In this section the jump-up and jump-down frequencies will be derived with their respective amplitude from the envelope equation of the RLC circuit. This set of equations are used to find the instability branch of the resonance curve analogous to the Duffing oscillator which will be discussed in the appendix. Starting from Eq. 2.14, the resonance and phase curves of the cavity are obtained in the steady-state where the derivative is zero. The voltage amplitude is given $|V_c| = \frac{(\omega_{1/2}V_g)}{\omega_{1/2} + (\Delta\omega)^2}$ where V_g is the generator voltage and the phase is $\tan \phi = \frac{\omega_{1/2}}{\Delta\omega}$. For the non-linear resonance

curve the detuning $\Delta\omega$ is replaced by $(\epsilon - 2\pi k_L V^2)$ which contains the effects of the LFD. This substitution of the detuning variable was also employed by Landau [46] for a harmonic oscillator. The resonance equation is now $V_c^2 \left((\epsilon - 2\pi k_L V_c^2)^2 + \omega_{1/2}^2 \right) = \omega_{1/2}^2 V_g^2$. Substituting $x = (V_c/V_g)^2$ into the equation and putting all the terms on one side yields :

$$0 = (2\pi k_L V_g^2)^2 x^3 - 2(2\pi k_L V_g^2) \epsilon x^2 + (\epsilon^2 + \omega_{1/2}^2) x - \omega_{1/2}^2 = f(x, \epsilon) \quad (2.23)$$

The function $f(x, \epsilon)$ will have three different roots which are used to calculate the jump frequencies. This function is dependent on two variables, x is related to the voltage of the cavity and ϵ the detuning. Note that both variables depend on each other, a change in voltage will shift the frequency. Similarly, a frequency shift will change the cavity voltage. When finding the roots, one of the variables will be kept constant. The real roots from this equation give the stable component of the resonance curve while the imaginary roots give the unstable component. This equation has a minimum real root x_1 with a corresponding detuning of ϵ given by Eq. 2.23, the quadratic equation relative to detuning is :

$$x_1 \epsilon^2 - 2(2\pi k_L V_g^2) x_1^2 \epsilon + \left[(2\pi k_L V_g^2)^2 x_1^3 + \omega_{1/2}^2 (x_1 - 1) \right] = 0 \quad (2.24)$$

and the solution for the detuning at this minimum x value is

$$\epsilon_{1,2} = 2\pi k_L V_g^2 x_1 \pm \omega_{1/2} \sqrt{1/x_1 - 1} \quad (2.25)$$

Once the root x_1 of the cubic equation 2.23 is known it can be simplified to a second-order polynomial:

$$(2\pi k_L V_g^2)^2 x^2 + (2\pi k_L V_g^2) \left((2\pi k_L V_g^2) x_1 - 2\epsilon \right) x + \left[\epsilon^2 + \omega_{1/2}^2 + (2\pi k_L V_g^2) \left((2\pi k_L V_g^2) x_1 - 2\epsilon \right) x_1 \right] \quad (2.26)$$

This second-order polynomial will later be used to derive the jump frequencies.

The real roots can be obtained by considering equation 2.23 as $f(x, \epsilon)$ and at the jump frequencies the function is discontinuous leading to $\frac{dx}{d\epsilon} \rightarrow \infty$. Using this method the value of the LFD coefficient k_L needed to reach the non-linear resonance curve will be calculated. The

derivative of x (voltage squared) with respect to the detuning yields:

$$\frac{dx}{d\epsilon} = -\frac{\partial f/\partial \epsilon}{\partial f/\partial x} = -\frac{-4\pi k_L V_g^2 x^2 + 2\epsilon x}{3(2\pi k_L V_g^2)^2 x^2 - 8\pi k_L V_g^2 \epsilon x + \epsilon^2 + \omega_{1/2}^2} \quad (2.27)$$

The discontinuity results when the denominator is zero. The quadratic equation from the denominator equating zero is

$$3(2\pi k_L V_g^2)^2 x^2 - 8\pi k_L V_g^2 \epsilon x + \epsilon^2 + \omega_{1/2}^2 = 0 \quad (2.28)$$

In order to get the real roots with respect to x from the quadratic equation the discriminant for the roots must be greater $(4\pi k_L V_g^2 \epsilon_{cr})^2 - 3(2\pi k_L V_g^2)^2 (\epsilon_{cr}^2 + \omega_{1/2}^2) \geq 0$. Any real root will yield stable points in the resonance curve. This leads to the important result where the critical values needed to reach the non-linear resonance curve can be calculated. The detuning is given by

$$\epsilon_{cr} = \sqrt{3}\omega_{1/2} \rightarrow \Delta f_{cr} = \pi\sqrt{3}\frac{f_0}{Q_L} \quad (2.29)$$

gives the detuning value for a stable resonance curve. The root when the discriminant is zero is

$$x_{cr} = \frac{V_{cr}^2}{V_g^2} = \frac{2}{3} \frac{\epsilon_{cr}}{2\pi k_L V_g^2} \rightarrow V_{cr}^2 = \frac{2}{\sqrt{3}} \frac{\omega_{1/2}}{2\pi k_L} \quad (2.30)$$

gives the critical voltage. Upon substituting the value of V_{cr}^2 to equation 2.23, three real roots can be obtained if the following is satisfied:

$$\omega_{1/2}^2 V_g^2 = \frac{2}{\sqrt{2}} \frac{\omega_{1/2}}{2\pi k_L} \left[\left(\sqrt{3}\omega_{1/2} - 2\pi k_L \frac{2}{\sqrt{3}} \frac{\omega_{1/2}}{2\pi k_L} \right)^2 + \omega_{1/2}^2 \right] = \frac{8}{3\sqrt{3}} \frac{\omega_{1/2}^3}{2\pi k_L} \quad (2.31)$$

This equation yields the LFD coefficient that will result in a non-linear resonance curve $k_{cr,L}$. Any LFD coefficient that is greater than the critical value will yield a non-linear resonance curve.

$$k_{cr,L} = \frac{4}{3\sqrt{3}} \frac{f_0}{Q_L V_g^2} \quad (2.32)$$

Note that critical LFD coefficient $k_{cr,L}$ is dependent of the voltage square of the cavity and bandwidth.

This set of equations are used to determine the general shape of the resonance of the curve. The maximum value is given by the points $(\Delta f_{max}, V_{max})$ and the two points which limit the hysteresis are $\Delta f_{u,d}, V_{u,d}$ where the u and d denote the jump-up and jump-down points. The maximum point can be found by setting equation 2.27 equal to zero ($\frac{dx}{d\epsilon} = 0$) which occurs when the numerator is $4\pi k_L V_g^2 x - 2\epsilon = 0$. When this is satisfied then the maximum voltage and the frequency at this point is given by

$$\Delta f_{max} = k_L V_{max}^2 \quad \text{and} \quad V_{max} = V_g \quad (2.33)$$

The jump-up and jump-down frequencies are obtained from equations 2.23 and 2.28. From equation 2.28 the result $\epsilon^2 + \omega_{1/2}^2 = -3(2\pi k_L V_g^2)^2 x^2 + 8\pi k_L V_g^2 \epsilon x$ and substituting this into equation 2.23 leads to

$$\epsilon_{1,2} = \frac{4\pi k_L V_g^2 x_{1,2}^3 + \omega_{1/2}^2}{4\pi k_L V_g^2 x_{1,2}^2} \quad (2.34)$$

Now substituting this expression into equation 2.28, the polynomial for x is then

$$x^4 - x^3 + \frac{\omega_{1/2}^2}{4(2\pi k_L V_g^2)^2} = 0 \quad (2.35)$$

The first root of this equation is only slightly less than the value of $x=1$. Therefore assuming $x_1 = 1 - \Delta x_1$ leads to $\Delta x_1 = \frac{\omega_{1/2}^2}{4(2\pi k_L V_g^2)^2}$ so that the jump-down amplitude is given by

$$V_d = V_g \sqrt{x_1} \approx V_g \left(1 - \frac{\omega_{1/2}^2}{8(4\pi k_L V_g^2)^2} \right) \quad (2.36)$$

and the jump-down frequency

$$\epsilon_d = 2\pi k_L V_g^2 x_1 + \frac{\omega_{1/2}^2}{4\pi k_L V_g^2 x_1^2} \quad (2.37)$$

Knowing root x_1 reduces the degree of the equation 2.35 to

$$x^3 + (x_1 - 1)x^2 + x_1(x_1 - 1)x + x_1^2(x_1 - 1) = 0 \quad (2.38)$$

Once the root is found which should be less than one and real, equation 2.34 can be then used for the jump-up frequency. The jump-up frequency and voltage are given by

$$V_u = V_g \sqrt{x_2}, \quad \epsilon_u = 2\pi k_L V_g^2 x_2 + \frac{\omega_{1/2}^2}{4\pi k_L V_g^2 x_2^2} \quad (2.39)$$

where x_2 is the second root.

The effects of the LFD on the resonance curve are shown in figures 2.3 and 2.4 for a 650 MHz elliptical cavity. Figure 2.3 shows the amplitude and the phase of the cavity with a linear and non-

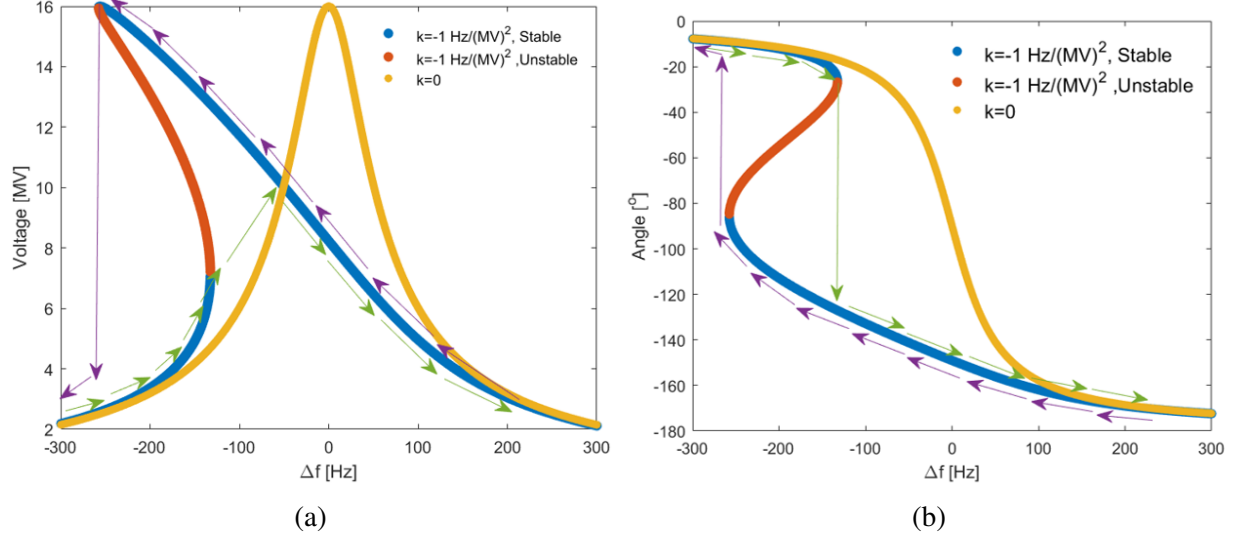


Figure 2.3: (a) Linear and non-linear resonance curve from lumped-circuit model at 16 MV and with a LFD coefficient of $1 \text{ Hz}/(\text{MV})^2$. (b) Phase of linear and non-linear response from lumped circuit model at 16 MV and with LFD of $1 \text{ Hz}/(\text{MV})^2$.

linear system. For the non-linear system, the blue line shows the stable region while the unstable is shown by the orange line. The LFD coefficient used for this simulation is $k_L = 1 \text{ Hz}/(\text{MV}/m)^2$ and the loaded quality factor is $Q_L = 8 \times 10^6$. This behavior is similar to the Duffing equation where there is a region on the resonance curve which is unstable. The jump-up and jump-down frequencies derived earlier give the hysteresis of the system. This is denoted by the green and purple arrows which give the amplitude depending of the frequency sweep. The unstable region can be made unreachable, by increasing the driving frequency until the jump-up frequency is reached the voltage will jump to the jump-up voltage which is a lower value than the maximum value. Decreasing driving the frequency far from the resonance will drop the voltage at the jump-down frequency. This instability can be resolved by using a piezoelectric actuator for resonance control.

The non-linearity of the resonance curve arises from the size of the electric field E_{acc} . At small accelerating gradient values, the resonance curve and the phase resemble the linear case. Starting at $E_{acc} = 9 \text{ MV}/M$ for the 650 MHz cavity the instability is observed shown in the 2.4 in red. As

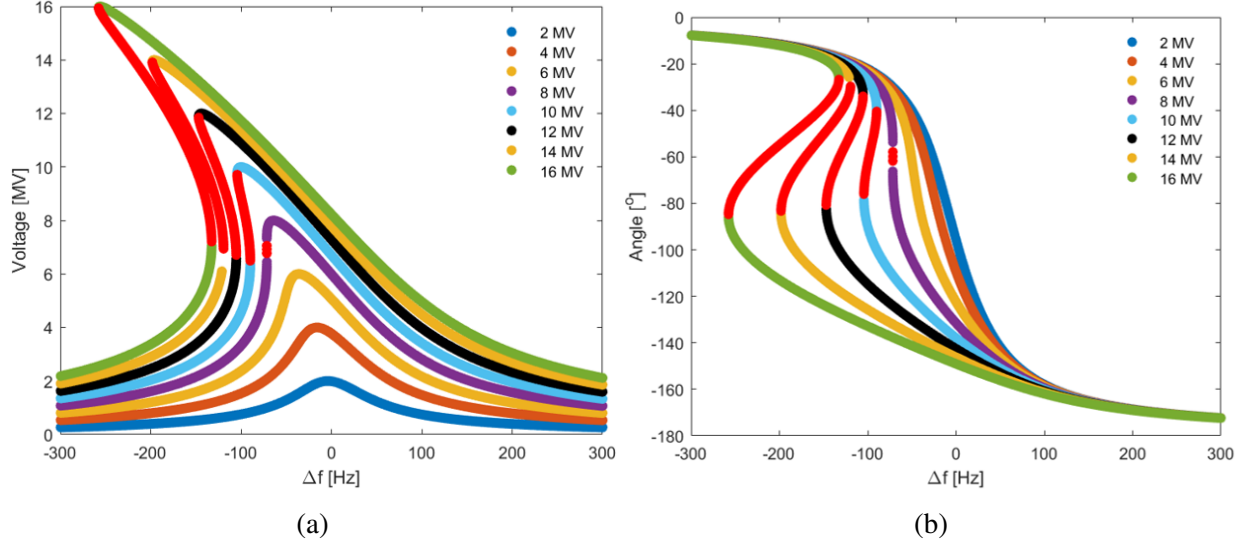


Figure 2.4: (a) Resonance curve with LFD of $1 \text{ Hz}/(\text{MV})^2$ and at different voltages. As the voltage increase the non-linearity become larger.(b) Phase with LFD of $1 \text{ Hz}/(\text{MV})^2$ driven by different voltages.

the electric field increases the non-linearity increases by increasing the size of the unstable region and the hysteresis. This behavior is important in resonance control of linacs which operate in a low beam-loading regime since the bandwidth is smaller. This will be discussed further in the next section.

2.2 Simulation of Electromechanical Coupling Model

The lumped circuit model from Eq. 2.14 and the frequency detuning from the cavity wall deformation from Eq. 2.21 are used to simulate the behavior of the cavity under external perturbations such as microphonics or from LFD. This set of coupled equations is solved using the Euler method via a MATLAB script. The simulations consist of a 650 MHz cavity operated in pulsed and CW mode. The script can simulate the behavior of any type of elliptical cavity with the figures of merit as inputs. The goal of these simulations is to study the behavior of the forward, reflected, and transmitted power signals which are used to calculate the cavity frequency. The perturbations studied in these simulations will include the effects of microphonics, LFD, and beam acceleration. This set of equations are coupled to each other, where the perturbations to the electric field drive deformations on the cavity walls as shown in Eq. 2.21. The frequency detuning of the cavity will

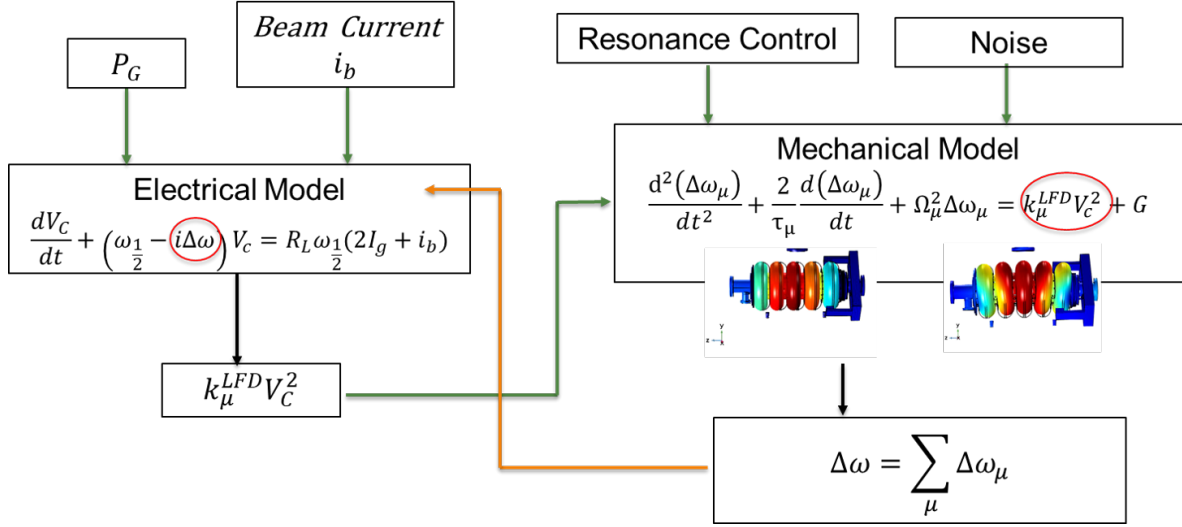


Figure 2.5: Equations 2.14 and 2.21 have a positive feedback loop. The deviation from the nominal electric field will drive cavity wall movements and the wall movement of the cavity will cause detuning changing the voltage of the cavities.

then cause a decrease in the cavity voltage. A diagram depicting the positive feedback from these two equations is shown in Fig. 2.5.

During pulse mode operation the cavity goes through three stages. These three stages are simulated with the MATLAB script for the 650 MHz cavity. The parameters for this simulation are given in Table 2.1. The first stage is the filling time, during this process the cavity is supplied

Table 2.1: Inputs to the simulation of the 650 MHz cavity.

| Parameters | Values |
|----------------------|-----------------|
| r/Q_o [Ω] | 341 |
| Q_L | 8×10^6 |
| V_c [MV] | 25 |
| L_{eff} [m] | 1.03 |
| i_b [mA] | 2 |

with RF power to reach the nominal gradient. The second stage is the region where the beam is accelerated, this is called the flat-top stage. The last stage is the decay of the field when the power is turned off. This three-stage process is repeated based on the macro-pulse cycle of the beam passing

through the cavity.

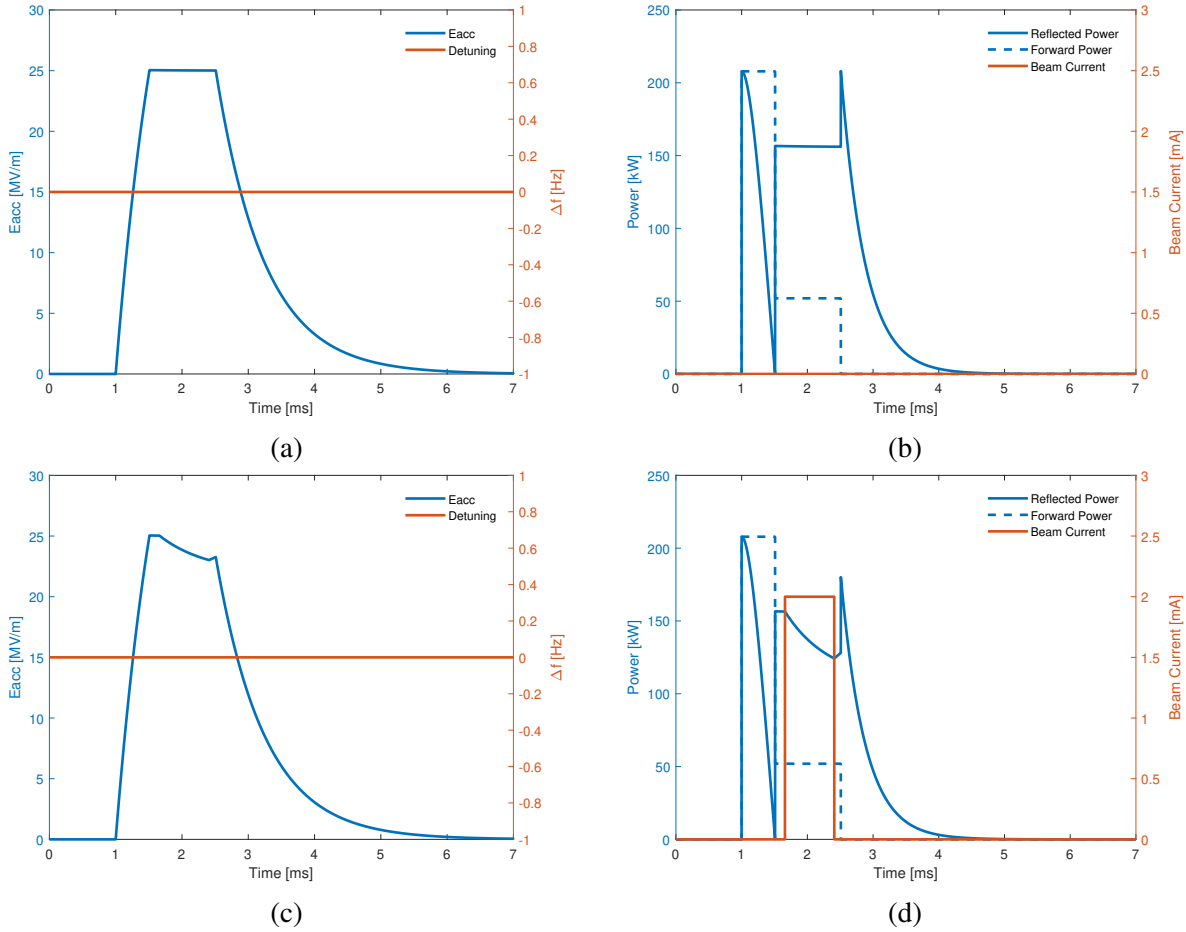


Figure 2.6: (a) The effect on the electric field from a 2 ms RF pulse for a 650 MHz cavity with no beam and no detuning is shown. (b) The reflected and forward power are shown along with the beam current which is zero. (c) The effect of beam loading to the electric field is shown. (d) The effect of beam loading to the reverse power and forward power is shown. Simulation parameters are given in Table 2.1.

In the case where the cavity experiences no frequency detuning, each stage can be described by an analytical expression. During the filling time the voltage behavior is given by $V_c = R_L 2I_g \left(1 - e^{-\frac{t}{\tau}}\right)$ where the time constant is $\tau = \frac{1}{\omega_{1/2}} = \frac{2Q_L}{\omega_0}$. The filling time is given by $t_{fill} = \tau \ln(2)$ where τ is the time constant of the cavity. The flat-top region from the simulation is shown in Fig. 2.6 (a), the duration in this simulation is 1 ms. In this case there is no beam and to achieve the flat top the forward power is reduced as shown in 2.6 (b). The cavity voltage in this region is $V_c = R_L I_g$, this is known as the accelerating voltage. In the last stage, the RF power is turned off yielding an

exponential decay from the cavity voltage $V_c = R_L I_g e^{-\frac{t}{\tau}}$. The simulation results for the effects with a 2 mA beam are shown in Figures 2.6 (c) and (d). The LFD effects are ignored in this simulation and only the effects of the voltage and power levels are given. In an open-loop system, the voltage drops due to the extraction of energy from the beam. Since Q_L is coupled to the beam the reverse power drops due to impedance matching of the cavity and generator. The nominal gradient is kept constant by adding more RF power to the cavity or by deforming the cavity via a piezoelectric actuator.

The modified result for the frequency detuning simulation due to deformations on the cavity walls and LFD is shown in Fig. 2.7. In this simulation, the effects of the beam were not considered. This simulation is for the system in open-loop and includes 8 different mechanical modes of the 650 MHz cavity which were measured with the piezo actuator. More details on the measurement of the mechanical modes are discussed in Chapter 3. Parameters for the modes are given in Table

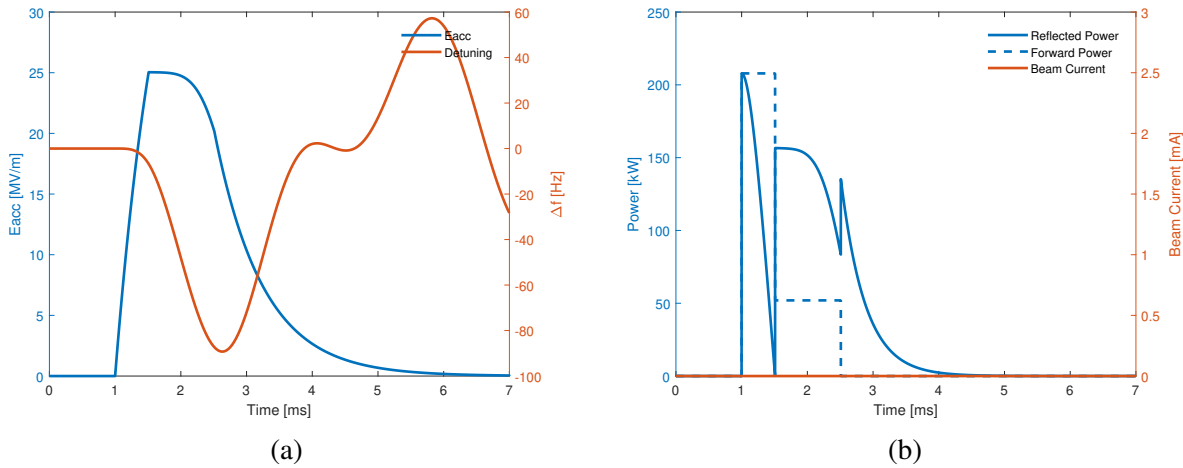


Figure 2.7: Simulation parameters are the same as in Table 2.1 with the addition of the mechanical modes in Table 2.2. (a) Voltage of the cavity with 8 mechanical modes introduced in equation 2.21. The blue line depicts the voltage of the cavity and the orange the time evolution of the detuning. (b) The forward power, reflected power, and beam current are shown. The reflected power also droops due to the effect of the mechanical modes.

2.2, this include the frequency f_m of the mode, the quality factor Q_m , and the coupling k_L . During the filling time of the cavity, the frequency begins to change due to the Lorentz force deforming the cavity. The detuning continues throughout the flat-top stage due to the mechanical modes of the cavity. These perturbations cause the cavity field to decrease along with the frequency. When the

Table 2.2: Inputs to the simulation of the 650 MHz cavity lumped circuit model. The mechanical modes are obtained from the transfer function measurement done in Chapter 3.

| Mode | $f_m [Hz]$ | Q_m | $k_{L,m} [Hz/V]$ |
|------|------------|-------|------------------|
| 1 | 157 | 5.1 | 54 |
| 2 | 181 | 5.1 | 113 |
| 3 | 188 | 10.6 | 70 |
| 4 | 215 | 10.1 | 239 |
| 5 | 291 | 9.8 | 35 |
| 6 | 329 | 7.9 | 34 |
| 7 | 381 | 4.5 | 37 |
| 8 | 411 | 6.3 | 22 |

RF power is turned off the frequency increases and goes to the initial value prior to the filling stage. The cavity frequency change due to these perturbations alters the impedance mismatch decreasing the reflected power. An estimate of the power necessary to maintain the nominal accelerating gradient is given in the next section.

2.3 RF Power for Field Stability

One approach to reduce the effects of frequency detuning is by increasing the RF power going to the cavity. Adding more power to the cavity will increase the accelerating gradient. The beam intensity of the linac determines the minimum power and bandwidth of operation of the cavity. The loaded Q_L is represented as $Q_L = \left(\frac{1}{Q_0} + \frac{1}{Q_{ext}} + \frac{1}{Q_{beam}} \right)^{-1} \approx \frac{V_c}{i_b R / Q_0}$ since the Q_{beam} ¹ for the beam is much smaller than the intrinsic Q_0 and the external quality factor Q_{ext} . Equation 2.40 derived from the lumped circuit model is used to calculate the power needed from the generator to maintain a constant accelerating field when a cavity is detuned. Note that this equation is only valid when $\beta \gg 1$. This equation introduces the phase of the beam denoted by ϕ_b . The power needed to

¹Note that the Q_{beam} relation is different from the definition of the quality factor which is proportional to energy/dissipation. In this case this was added to show the dependance of Q_L with respect to the beam current.

maintain an accelerating gradient of 11.46 MV/m in the 650 MHz low beta (LB) elliptical cavity is shown in Fig. 2.8 with respect to the loaded Q_L . The parameters used for this plot are the beam current $i_b = 2mA$, the shunt impedance $r/Q_o = 341\Omega$, the voltage $V_c = 11.9MV$, and the phase $\phi_b = 0$.

$$P_g = \frac{V_c^2}{4(r/Q_o)Q_L} \left(\left(1 + \frac{(r/Q_o)Q_L i_b \cos(\phi_b)}{V_c} \right)^2 + \left(\frac{\Delta f}{f_{1/2}} + \frac{(r/Q_o)Q_L i_b \sin(\phi_b)}{V_c} \right)^2 \right) \quad (2.40)$$

More RF power is needed to maintain the accelerating gradient constant when it decreases due

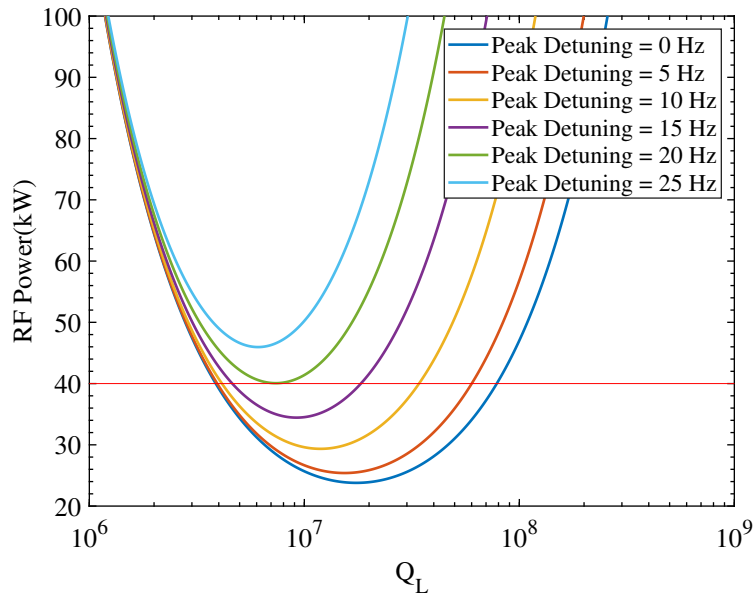


Figure 2.8: Power provided from generator with respect to the loaded Q_L to the 650 MHz LB cavity at 11.9 MV.

to cavity detuning. Figure 2.8 shows RF power curves which are parabolic and corresponding to different levels of detuning. These plots have a minimum power corresponding to the impedance match of the RF power generator to the cavity with a beam being accelerated. The minimum RF power of each curve shifts to a lower Q_L with an increasing level of detuning. The Q_L decreases since the coupling β increases due to more power lost in the coupler. As Q_L decreases from the minimum RF value of the curve the cavity bandwidth increases thus allowing for a larger detuning. In the case of an increasing Q_L from the minimum RF value the coupling decreases which lowers the bandwidth.

In an ideal case where no detuning occurs the total power needed to accelerate the beam and to account for joule heating on the cavity walls is 24 kW. The 650 MHz cavity has a 40 kW source, this puts a limit of 20 Hz peak detuning on the cavity which can keep a constant accelerating gradient since there is only an 16 kW overhead. The piezoelectric actuator along with resonance control algorithms can be used to minimize the power overhead and use less RF power. With a piezoelectric actuator and resonance control algorithm, the entire linac can save several 100s of kW. Additionally, the resonance control algorithm will prevent the cavities from losing RF power.

2.4 Summary of Chapter

A model of the frequency and accelerating gradient behavior of an SRF cavity can be used as a testbed for resonance control algorithms, providing an estimate of the RF power consumption, and modeling the behavior of microphonics. The time-dependent voltage of the cavity was derived from Maxwell's equation yielding a similar form as the equation for an RLC circuit. The cavity wall deformations caused by microphonics are modeled as a harmonic oscillator. The behavior of the cavity's forward, reflected, and transmitted power with microphonics and LFD was presented. This model is very useful for predicting properties of resonance control. Features were evaluated with reference to PIP-II SRF cavities and results are in agreement with expectations. The lumped-circuit model also provides an estimate for the maximum detuning that can be sustained and the loaded quality factor value needed to minimize the RF power consumption. In a cavity with low beam intensity and a large gradient a ponderomotive instability occurs. This behavior is akin to that of the Duffing equation where the system shows a hysteresis at the instability region. The amplitude of the system will change depending on the direction of the sweep. A set of equations were derived to calculate the frequency at which these jumps occur. The instability can be corrected with a piezoelectric actuator.

CHAPTER 3

EXPERIMENTAL CHARACTERIZATION OF SRF CAVITY

The performance of the cavities is tested prior to installation in the cryomodule. The measurements consist of obtaining field flatness of the cavities, the intrinsic quality factor of the cavities Q_0 , and the transfer function which gives the mechanical eigenmodes of the cavities. The field-flatness and transfer function measurements are conducted at room temperature while the Q_0 is measured at 2 K. When the cavity is tested in the cryostat or in the cryomodule the transfer function is measured again. In this chapter, two elliptical cavities will be discussed. The field flatness tuning was conducted on a 9-cell 1.3 GHz Ichiro cavity [47]. The field flatness methods implemented on this cavity are similar to other elliptical cavities. The 5-cell 650 MHz PIP-II cavity was used to measure the mechanical modes using the piezoelectric actuator. These modes were used for the simulation discussed in Chapter 2.

3.1 Q_0 and Frequency Measurement

The cavity can be characterized by three signals: the forward power, the reflected power, and the transmitted power. The intrinsic quality factor Q_0 is measured using the decay of the transmitted power [5]. The intrinsic quality factor is used to estimate the heat load on the cryogenic system. The frequency of the cavity is measured with the forward and transmitted power. Additionally, the transmitted power is used to measure the accelerating gradient of the cavity. The frequency and the accelerating gradient of the cavity are monitored to provide the optimal beam acceleration. The reflected power is used as a calibration and to measure optimal coupling to the cavity.

A schematic of the signal topology of the cavity in a cryomodule testing environment is shown in Fig. 3.1. The cavity is excited by an RF generator at the π mode resonant frequency of the cavity. This signal is then amplified to get to the nominal gradients of the cavity via an RF amplifier. A circulator is used to prevent the reflected power from the cavity from damaging the amplifier and generator. The forward and reflected power signals are measured after the circulator via a dual

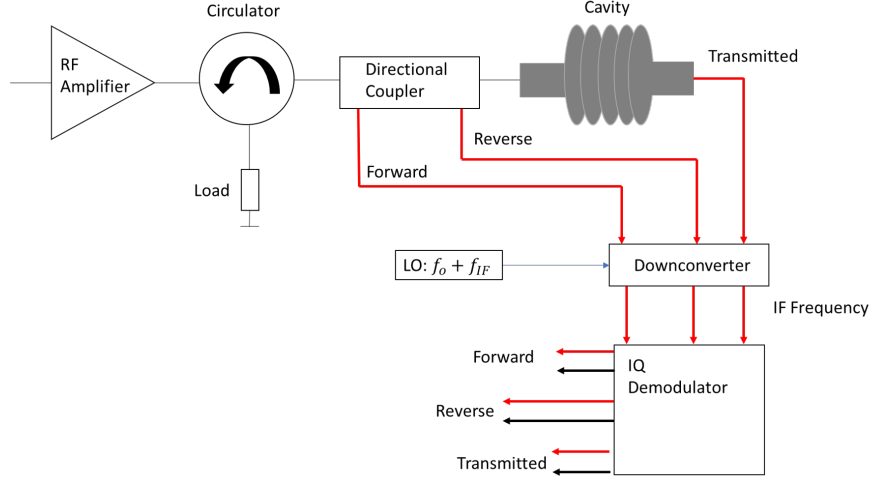


Figure 3.1: Schematic of signals in a cryomodule for an SRF cavity. The intermittent frequency (IF) is measured after the signal is downconverted.

directional coupler. Lastly, the transmitted power is measured from the cavity port.

The intrinsic quality factor Q_0 can be measured by obtaining the decay time of the stored energy when the power is turned off. The stored energy in the cavity behaves as

$$\frac{dU}{dt} = -P_L = -\frac{\omega_0 U}{Q_L} \quad (3.1)$$

where P_L is the loaded power and the solution to the equation yields $U(t) = U_0 e^{-\frac{\omega t}{Q_L}}$ with $U_0 = U(t = 0)$. The energy stored is related to the power transmitted to the cavity. The time constant then relates to the loaded quality factor Q_L which includes the ohmic losses on the cavity walls as well as the losses on the ports. From this relation, the intrinsic quality factor is obtained from the time decay constant of the stored energy

$$Q_0 = (1 + \beta)\omega_0\tau_L \quad (3.2)$$

where β is the coupling of the cavity to the RF generator. The coupling of the cavity to the RF generator is calculated using the forward and reflected power. The reflection coefficient $\Gamma = \frac{\beta-1}{\beta+1}$ when no detuning is present. The relationship of the forward power (P_f) to the reflected power

$P_r = \Gamma^2 P_f$ are used to obtain the coupling relation:

$$\beta = \frac{1 \pm \sqrt{P_r/P_f}}{1 \mp \sqrt{P_r/P_f}} \quad (3.3)$$

The upper sign is used when the cavity is overcoupled $\beta > 1$ and the lower sign is used when the cavity is undercoupled $\beta < 1$. Note that the equation above only holds when the frequency detuning of the cavity is zero. The cavity can be determined to be overcoupled or undercoupled by using RF input rectangular pulses to excite the cavity. The shape of the reflected power determines the cavity's coupling [5]. The accelerating gradient E_{acc} is calculated with the equation [48]

$$E_{acc} = \frac{\frac{2\beta}{1+\beta} \sqrt{\frac{r}{Q} \omega_0 \tau_L P_f}}{L} \quad (3.4)$$

where the $\frac{r}{Q}$ is the shunt impedance of the cavity determined from simulation and L is the active length of the cavity. Q_0 measurements are made with respect to E_{acc} ranging from 1 MV/m to the nominal accelerating gradient. The method described above for measuring the Q_0 is for critical coupling $\beta = 1$ cavities. Higher coupling needs to include the error in measurement of the intrinsic quality factor Q_o which depends on the coupling β of the cavity. An analysis of the factor contributing to this error is given in Holzbauer et al. [49] and Frolov [50]. These papers take into account the errors from the circulators and the dual directional coupler.

The cavity frequency is calculated from the phase difference of the forward and transmitted power of the cavity. The relationship between the phase and frequency shift is given by

$$\tan(\phi) = 2Q_L \frac{\Delta f}{f_0} \quad (3.5)$$

where ϕ is the phase difference of the forward and transmitted power. The loaded quality factor can be determined from the time decay constant τ_L as shown earlier. The cavity frequency shift Δf is only valid in the linear region of $\tan(\phi)$. Additionally, the resonant frequency of the cavity f_0 must not have large fluctuations (several kHz) and the loaded quality factor Q_L must not change by a large percentage (more than 10 %). A large change in the loaded quality factor will produce a larger error in frequency shift calculation Δf of the cavity. During operation with beam acceleration, the

resonant frequency and Q_L will only have small fluctuation. Thus, the frequency shift Δf equation will yield accurate measurements when the cavity in steady state. In the case of pulse operation where the accelerating gradient changes rapidly another equation can be used, this is discussed in [51].

During beam operation, the low-level RF (LLRF) system must maintain an amplitude shift to a tolerance of better than 0.01 % and a phase better than 0.01 degrees to provide optimal beam acceleration [52]. The cavity's accelerating gradient, phase, and frequency are calculated using the forward and transmitted power. The resonant frequency of the cavities is high at 650 MHz (ILC type 1.3 GHz), to preserve the envelope and phase of these waveforms the sampling must be double this frequency. Additionally, these signals are used to calculate the control algorithms for the LLRF controls to maintain a stable gradient by changing the RF power. This high frequency sampling from a field-programmable gate array (FPGA) can be costly. Thus, a method know as downconversion is implemented which preserves the amplitude and phase of the original signals but at a smaller frequency. Downconversion is a multiplication of an RF signal with a low noise reference signal to generate an intermediate signal at a smaller frequency [34]. Assuming two sinusoidal signals

$$V_{RF}(t) = A_{RF} \sin(\omega_{RF}t + \phi_{RF}), \quad V_{LO}(t) = A_{LO} \sin(\omega_{LO}t + \phi_{LO}) \quad (3.6)$$

where the V_{RF} is the signal from the cavity and V_{LO} is the signal from the local oscillator (LO). The intermediate output signal is given by

$$V_{IF}(t) = \frac{1}{2} A_{RF} A_{LO} [\cos((\omega_{LO} - \omega_{RF})t + (\phi_{LO} - \phi_{RF})) - \cos((\omega_{LO} + \omega_{RF})t + (\phi_{LO} + \phi_{RF}))] \quad (3.7)$$

A low pass filter is then implemented to get rid of the high frequency component of V_{IF} . This leads to simplification of the intermediate signal as

$$V_{IF} \approx \frac{1}{2} A_{RF} A_{LO} \cos(\omega_{IF}t + \Delta\phi) \quad (3.8)$$

where $\omega_{IF} = \omega_{LO} - \omega_{RF}$ and $\Delta\phi = \phi_{LO} - \phi_{RF}$. As an example, consider the RF frequency from the cavity power signals to be 650 MHz and the LO oscillator frequency is 652 MHz. In this

case the intermediate frequency (IF) will be 2 MHz. At 2 MHz the sampling frequency is more manageable for an FPGA and thus results in a less expensive FPGA board. The downconversion method can also be used to determine the frequency offset of the cavity by setting the LO frequency to 650 MHz, the signal multiplied will thus give the phase difference [53]. The work in this thesis calculates the frequency using the phase difference of the forward and transmitted power since no beam is accelerated during the trials. This will still lead to accurate frequency measurements.

3.2 Bead-pull Experiment

A multicell cavity is a structure with multiple resonators coupled together via an iris opening to maximize the acceleration of the beam. A multicell cavity will give rise to different electromagnetic modes, the mode use for acceleration is the π mode which is the one that will be tuned. In the monopole mode the number of modes that can be excited is equal to the number of cells. The experimental procedure of tuning the cavity to field-flatness will be done with a 9-cell 1.3 GHz Ichiro ILC type cavity. This cavity was used since it was the only cavity available at the time. The tuning method obtained from this study can be implemented on any elliptical cavity. The bead-pull experiment is conducted after the fabrication of a bare niobium cavity, after bulk etching, heat treatment, and light etching for the final surface finish. The purpose of SRF cavity surface etching is to prevent field emissions. This etching removes a layer of the cavity surface which is what causes the shift in frequency and field-flatness. The bead-pull field distribution measurement is done with a bead passing through the axis of the cavity. A typical field distribution after manufacturing and cavity wall processing is shown in Fig. 3.2. This is the field distribution is from the Ichiro cavity, in this case the field distribution is higher from 200 to 700 mm compared to 700 to 1200 mm. This measurement is then used to provide a uniform field by mechanically compressing or stretching the cavity's cell to. The field uniformity is known as the field flatness which is measured as a percentage given by the formula [54]:

$$\eta_{ff} = \left(1 - \frac{E_{z,max} - E_{z,min}}{\langle E_z \rangle} \right) \times 100 \quad (3.9)$$

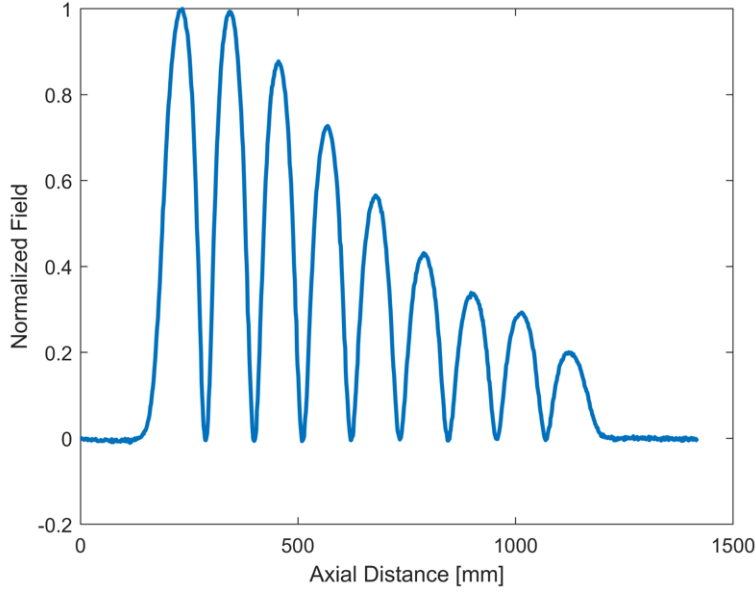


Figure 3.2: Field distribution of Icheru cavity prior to tuning, field flatness is $\eta_{ff} = 23\%$. The peak of the field is located at the center of the cavity cell. Note that the field is more concentrated in one region of the cavity.

where E_z is the field in the longitudinal direction of the cavity. $E_{z,max}$ is the maximum field of all the cells and $E_{z,min}$ it the minimum field of all the cells. The average of all the field peaks is taken and given by $\langle E_z \rangle$. The field flatness of an elliptical cavity is set to be tuned at $\geq 98\%$ by compressing or stretching the cavity cells. A field flatness of 98% will increase the accelerating voltage, reduce the electric and magnetic fields on the surface since the peak of the field in the cell sets the limit. A reduced electric and magnetic field on the surface prevents the occurrence of multipacting and field emission on the cavity surface which hinders the cavity performance.

3.2.1 Lumped Circuit Model for Cavity Cells

The electric field distribution of an N-cell cavity is modeled with a lumped-circuit model with an N number of LC circuit resonators. Each of the resonators is coupled via a capacitor. The validity of this model describing the behavior of coupled resonators was demonstrated by Knap [55]. The coupling of resonators via a small hole is shown from Maxwell's equation and derived by Bethe [32] demonstrates the validity of modeling the coupling via a capacitor. The N-cell cavity can be excited with a total of N electromagnetic monopole modes. Each of these modes has a different field

distribution, the modes are named based on the phase difference of the field from the neighboring cell. The first mode is known as the π/N mode and the last is the π mode. The electromagnetic mode of the cavity used for beam acceleration will be discussed in this section. The circuit model is shown in Fig. 3.3, the coupling between cells is provided by the capacitance C_k and the beam tubes are modeled as a capacitance C_b . The capacitance C is used to model the electric field region of the cavity cell while the inductor L is used to model the magnetic region of the cavity cell. In

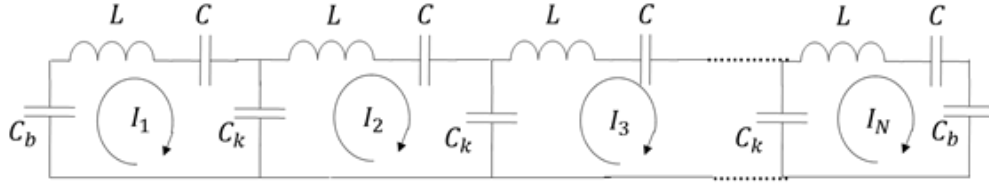


Figure 3.3: Lumped circuit model of multi-cell cavity, the coupling between cells is modeled by C_k and the beam tubes is modeled by C_b .

this model, the resistance of the each cell is taken to zero since $Q_0 \gg 1$. Applying Kirchhoff's current law leads to the following equations

$$(1 + k + \gamma)I_1 - kI_2 = \Omega I_1 \quad (3.10)$$

$$-kI_{j-1} + (1 + 2k)I_j - kI_{j+1} = \Omega I_j, \quad 1 < j < N \quad (3.11)$$

$$-kI_{N-1} + (1 + k + \gamma)I_N = \Omega I_N \quad (3.12)$$

where $k = C/C_k$ is the coupling between cells and $\gamma = C/C_b$ models the effects of the beam tubes. The normalized frequency is given by $\Omega = \omega^2/\omega_0^2$ and the frequency of each cell is $\omega_0 = 1/\sqrt{LC}$. The j subscripts is to enumerate the cavity cells and N is the total number of cells of the cavity. The effects of the beam tubes from γ can be taken into account using the amplitude of the π -mode

of the cavity which is given by

$$V^N = \frac{1}{\sqrt{N}} \begin{pmatrix} 1 \\ -1 \\ 1 \\ \vdots \end{pmatrix} \quad (3.13)$$

Applying this equation into to Eq. 3.10 leads to the relation $\gamma = 2k$. The general \mathbf{A} matrix then becomes:

$$\mathbf{A} = \begin{pmatrix} 1+3k & -k & 0 & \cdots & 0 \\ -k & 1+2k & -k & & \vdots \\ 0 & & \ddots & & 0 \\ \vdots & & & -k & 1+2k & -k \\ 0 & \cdots & 0 & -k & 1+3k \end{pmatrix} \quad (3.14)$$

that only depend on the coupling of the cells. This system of equations can be written as

$$\mathbf{A}\mathbf{v} = \Omega\mathbf{v} \quad (3.15)$$

The solution to Eq. 3.15 is given by

$$v_j^m = \sqrt{(2 - \delta_{mN})/N} \sin \left[m\pi \left(\frac{2j-1}{2N} \right) \right] \quad (3.16)$$

where δ_{mN} is the Kroneker delta, j is the cell number, and m is the mode of the cavity. The total number of modes is equal to the number of cells of the cavity N . The eigenvalues for the equation are given by

$$\Omega^m = \left(\frac{f_m}{f_0} \right)^2 = 1 + 2k \left[1 - \cos \left(\frac{m\pi}{N} \right) \right] \quad (3.17)$$

which is the normalized frequency of the mode. Equations 3.16 and 3.17 are used to determine which eigenmode is used to accelerate the beam. A 9-cell cavity is modeled in Fig. 3.4 below. The

mode used to accelerate the beam needs to have a uniform amplitude. This property is observed in the $6\pi/9$ ($m=6$) and the π ($m=9$) modes. The modes are named after the phase difference of the amplitude between the cells. The $6\pi/9$ resembles the behavior of the " $\pi/2$ " mode where some of the cells have zero amplitude. Since both $6\pi/9$ and π mode can be used for beam acceleration a discussion on which mode is more favorable will be done in the next section.

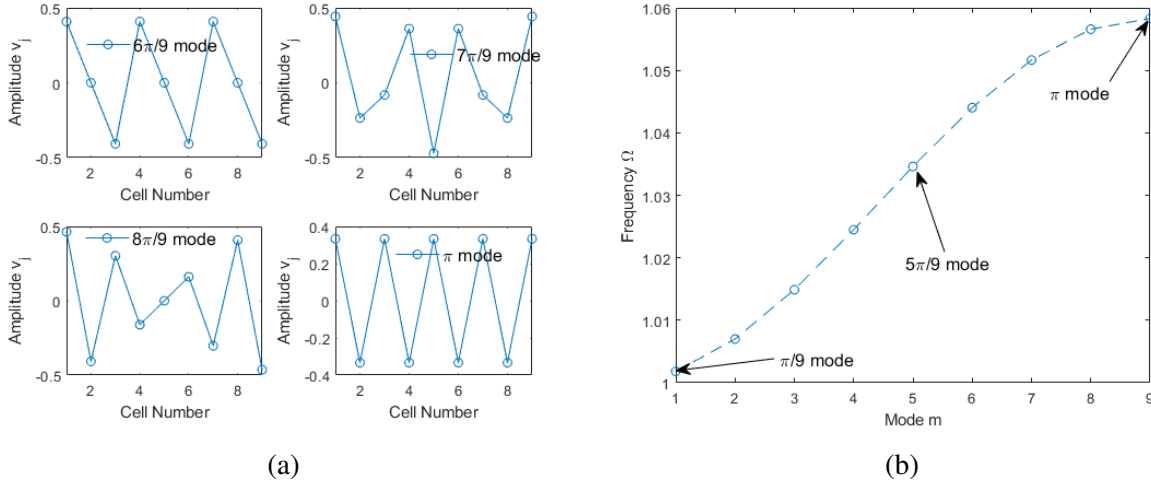


Figure 3.4: (a) Amplitude distribution along the cell number for a nine cell cavity based on the circuit model. Only the $6\pi/9$ to π modes are shown. (b) The dispersion curve of the 9-cell cavity, the π mode has the highest frequency.

3.2.2 Cavity Cell Perturbation Model

The out-of-tune model was adapted from Padamsee [5] and Schmuser [56] which uses eigenvalue perturbation. The perturbation model will yield an algorithm to find the appropriate squeezing and stretching of the cavity cells to obtain a uniform field distribution. Additionally, from the perturbation model, the optimal electromagnetic mode will be determined.

The cavity with a non-uniform field can be modeled as a small perturbation of the capacitance:

$$C_j = \frac{C}{1 + e_j} \quad (3.18)$$

where e_j is the small perturbation equivalent to a cell deformation and j denote the cell number. This perturbations is equivalent to a single cell being mechanically deformed in the cavity. Equation 3.15

is modified as

$$(\mathbf{A} + \mathbf{E})\mathbf{v}' = \Omega'\mathbf{v}' \quad (3.19)$$

where $E_{ij} = \delta_{ij}e_j$ and \mathbf{v}' is the perturbed eigen vector. Using a first order non-degenerate perturbation approach the eigenvalues and eigenvectors can be obtained [56]. The eigenvalue are

$$\delta\Omega^{(m)} = \Omega'^{(m)} - \Omega^{(m)} = \sum_j v_j^{(m)} e_j v_j^{(m)} \quad (3.20)$$

The eigenvectors are modified via

$$\delta\mathbf{v}^{(m)} = \mathbf{v}'^{(m)} - \mathbf{v}^{(m)} = \sum_{n \neq m} \frac{1}{\Omega^{(m)} - \Omega^{(n)}} \sum_j v_j^{(m)} e_j v_j^{(n)} \mathbf{v}^{(n)} \quad (3.21)$$

This set of equations are used to measure the field flatness.

The sensitivity to the capacitance perturbation which translates to a deformation of the cavity cell is different for each mode. The modes which can be used for acceleration of the beam are the $\pi/2$ mode and the π mode since the amplitude is uniform. The sensitivity for the amplitude perturbation for the π and $\pi/2$ mode are shown in [55]. For the $\pi/2$ mode the shift is

$$|\delta\mathbf{v}^{(N/2)}| \sim \frac{|\Delta\Omega|}{\Omega^{N/2} - \Omega^{N/2-1}} \sim N \frac{|\Delta\Omega|}{k} \quad (3.22)$$

where k is the coupling between cells. For the π mode the amplitude shift due to error is

$$|\delta\mathbf{v}^{(N)}| \sim \frac{|\Delta\Omega|}{\Omega^N - \Omega^{N-1}} \sim N^2 \frac{|\Delta\Omega|}{k} \quad (3.23)$$

These equations show that the $\pi/2$ mode is less sensitive to cavity cell deformations since it only depends on N while the π mode depends on N^2 . Thus the $\pi/2$ mode is more stable when deformations of the cells are present. This becomes important when there is a large number of cells (more than 9) in the cavity. The reason why the $\pi/2$ mode is not used in an SRF cavity is that the empty coupling cells (where the field is zero) are prone to multipacting. The processing of multipacting is difficult since there is no field in the coupling cell. Additionally, a cavity with different coupling cells is difficult to manufacture. Therefore, although the $\pi/2$ mode cavity is more stable in the presence of cavity cell deformations the π mode is used in an SRF cavity due to easier multipacting processing and ease of manufacturing.

During the bead-pull experiment the field perturbation $\delta\mathbf{v}^{(m)}$ is measured and not the individual cell perturbation e_j . There is a transformation which can be used to find the perturbation given by

$$\delta\mathbf{v}^{(m)} = \mathbf{H}\mathbf{e} \quad (3.24)$$

where \mathbf{H} is given by

$$H_{lk}^{(m)} = \sum_{j \neq m} \frac{v_l^{(j)} v_k^{(j)} v_k^{(m)}}{\Omega^{(m)} - \Omega^{(j)}} = \sum_{j \neq m} \frac{v_l^{(j)} v_k^{(j)} v_k^{(m)}}{2k[\cos(j\pi/N) - \cos(m\pi/N)]} \quad (3.25)$$

with these equation the perturbation can be measured. In the next section the details of the field measurement will be discussed.

3.2.3 Measurement of Field Profile

The field flatness is measured with a metal bead as it moves on the axis of the cavity. The field flatness can be measured for each of the modes of the cavity but the one of interest is the π mode.

The perturbation induced by the bead can be found via the Slater perturbation theorem

$$\frac{\delta f_{bead}}{f_0} \approx -\frac{\epsilon_0 \Delta V_{bead}}{4} \frac{|\mathbf{E}'|^2}{U} \quad (3.26)$$

where ΔV_{bead} is the volume change from the bead. Only the electric field is taken into account since the magnetic field is zero at the axis for the π mode. The prime on the electric field indicates that it is perturbed. Representing the Slater perturbation theory in terms of the lumped-circuit model 1st order perturbation gives:

$$\delta f'^{(N)} = \frac{1}{2} \frac{f'^{(N)}}{\Omega'^{(N)}} \left(v_j'^{(N)} \right)^2 e_{bead} \quad (3.27)$$

where the prime indicates the perturbed value and N is for the π mode. In order to use the first-order perturbation equation the amplitudes $v_j'^{(N)}$ must be rewritten in terms of the unperturbed case $v_j^{(N)}$.

This can be done by adding an error to the unperturbed case as following

$$\left(v_j'^{(N)} \right)^2 = \left(v_j^{(N)} \right)^2 \left(1 + \frac{\delta v_j^{(N)}}{v_j^{(N)}} \right)^2 \approx \left(v_j^{(N)} \right)^2 \left(1 + \frac{2\delta v_j^{(N)}}{v_j^{(N)}} \right) \quad (3.28)$$

This equation can then be substituted into Eq. 3.27 yielding

$$\delta v_j^{(N)} = \left[\frac{\delta f_j'^{(N)}}{\left(v_j^{(N)}\right)^2} \frac{2\Omega_j'^{(N)}}{e_{bead} f_j'^{(N)}} - 1 \right] \frac{v_j^{(N)}}{2} \quad (3.29)$$

This form of the equation can be simplified further into terms that can be measured using the average of the frequency shift:

$$\langle \delta f' \rangle = \frac{1}{N} \sum_j \delta f_j'^{(N)} = \frac{1}{2N} \frac{f_j'^{(N)}}{\Omega_j'^{(N)}} e_{bead} \sum_j \left(v_j'^{(N)}\right)^2 = \frac{1}{2N} \frac{f_j'^{(N)}}{\Omega_j'^{(N)}} e_{bead} \quad (3.30)$$

the summation term goes to one since the amplitudes are normalized. The amplitude shift can now be represented in terms of measured frequency shift as follows:

$$\delta v_j^{(N)} = \left[\frac{\delta f_j'^{(N)}}{\langle \delta f' \rangle} - 1 \right] \frac{v_j^{(N)}}{2} \quad (3.31)$$

From equation $\delta \mathbf{v}^{(m)} = \mathbf{H} \mathbf{e}$ the perturbation \mathbf{e} can almost be obtained. The \mathbf{H} matrix cannot be inverted since it has a vanishing determinant since of the N equations (from Eq. 3.24) only N-1 are independent. This makes sense since from the bead-pull measurement there is no way to tell which of the cells of the cavity has the right amplitude ($e_j=0$). It's also possible that all cells are wrong and need to have an adjustment to get the field flat. This can be resolved by assuming that an arbitrary cell, say number N, is correct. Then $e_N = 0$ and the N-th column of the matrix \mathbf{H} is taken out which leads to the reduced matrix \mathbf{H}_r . The error from the cells can be obtained by reduced vectors giving

$$\mathbf{e}_r = (\mathbf{H}_r)^{-1} \delta \mathbf{v}_r \quad (3.32)$$

Using \mathbf{e}_r for tuning will lead to an error in the Nth cell and also change the frequency of the π mode f_π . This can be avoided if all the errors $e_{r,j}$ can be shifted by their average yielding

$$e_{c,j} = - (e_{r,j} - \langle \mathbf{e}_r \rangle) \quad \text{for } j = 1, \dots, (N-1) \text{ and } e_{c,N} = \langle \mathbf{e}_r \rangle \quad (3.33)$$

The frequency correction that is needed to remove the error in cell j is

$$\delta f_{corr,j} = \frac{\epsilon_{c,j} f_\pi}{2N} \quad (3.34)$$

The last step is to apply a frequency shift to all cells if another frequency is desired:

$$\delta f_{\mu} = \frac{f_{desired} - f_{measured}}{N} \quad (3.35)$$

therefore cell j needs to be altered by $\delta f_{corre,j} + \delta f_{\mu}$. The desired frequency can be the warm frequency needed to reach the correct value at 2 K.

3.2.4 Bead-pull Setup

An Ichiro (ILC type) 9-cell 1.3 GHz cavity has been used for measurements and field flatness tuning. Similar tuning techniques are applied to all PIP-II and FRIB elliptical cavities prior to the cold testing or installation into the cryomodule. The setup shown in Fig. 3.5 consists of a bead, a fishing line to place the bead on, a motor to move the bead, a network analyzer, and lastly the static tuner. The network analyzer (NWA) measures the $S_{21} = V_2^-/V_1^+$ phase, where V_1^+ is the incident at wave port 1 and the outgoing wave at port 2 is V_2^- . The S_{21} signal is then recorded by the computer via the NWA. The phase from the forward and transmitted power is related to the frequency shift as in Ref. [57]

$$\Delta\phi = \arg(S_{21}) = \tan^{-1} \left(\frac{-(f/f_0 - f_0/f)}{1 + \beta_1 + \beta_2} \right) \approx -2Q_L \frac{\Delta f}{f_0} \quad (3.36)$$

A MATLAB script is used to control the speed of the bead via the motor. The static tuner consists of plates which are used to squeeze the cell (decrease the frequency) or stretch the cell (increase the frequency) as shown in Fig 3.6. The movement of the plates are controlled via a motor.

3.2.5 Dumbbell Simulations for Tensile Strength

The field flatness of the cavity is corrected by squeezing or stretching the cells. In order for the deformation effect to be permanent the pressure applied to the cell must be greater than the yield stress. A material undergoes three stages of deformation when it's under pressure. The first stage is known as the elastic behavior which occurs until the yield stress is applied. Once the pressure is released from the material it will deform to it's original configuration. When pressure is applied

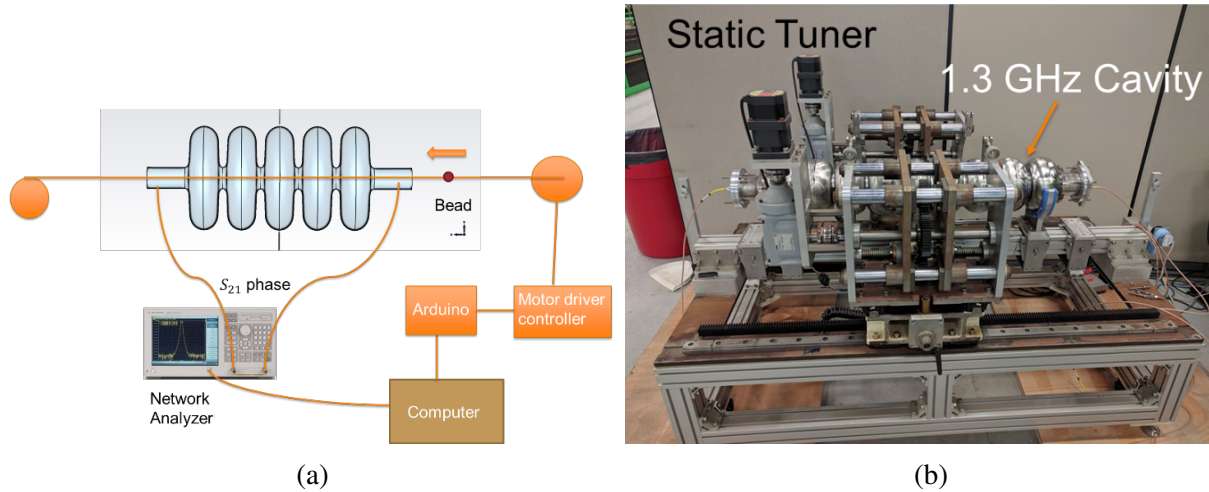


Figure 3.5: (a) Schematic of bead-pull measurement depicting the network analyzer, 9-cell Ichero cavity, stepper motor, and the controls. (b) The static tuner with the Ichiro cavity in place for tuning.

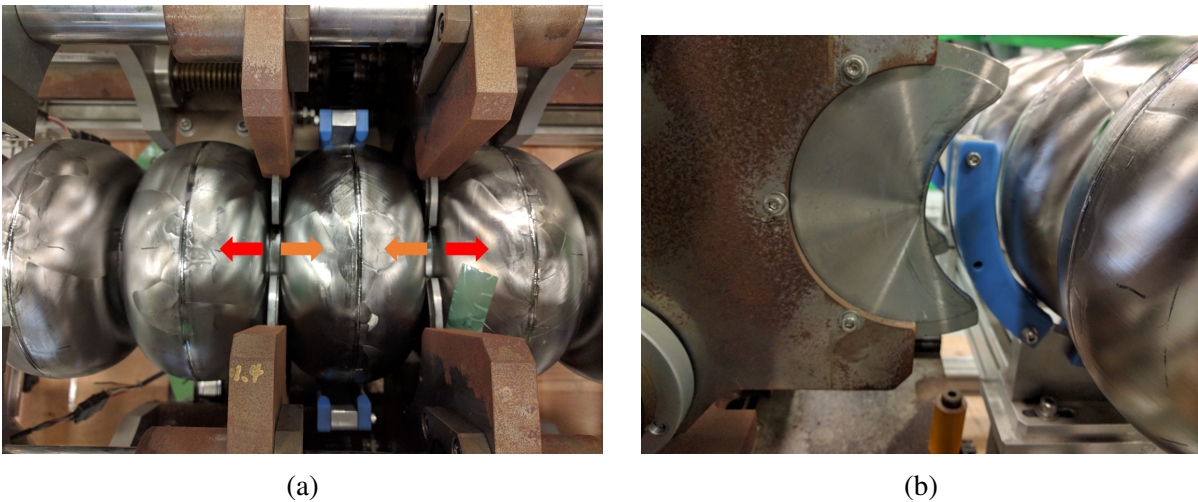


Figure 3.6: The static tuner consists of plates which are used for squeezing or stretching the cell of the cavity. A motor is used to control for the fine steps.

above the yield stress the material undergoes an inelastic deformation where the material will not back to its original configuration. This is the region that must be used to tune the cavity. The last region occurs when the ultimate strength is reached, at this point the material will break. During tuning the deformation must remain below this limit. Simulations were performed to estimate the region of inelastic deformation based on the frequency shift. The dumbbell configuration was used to model the cavity, this configuration consists of two cell iris connected together as shown in Fig. 3.8. The dumbbell simulations were done using COMSOL Multiphysics [59] to estimate

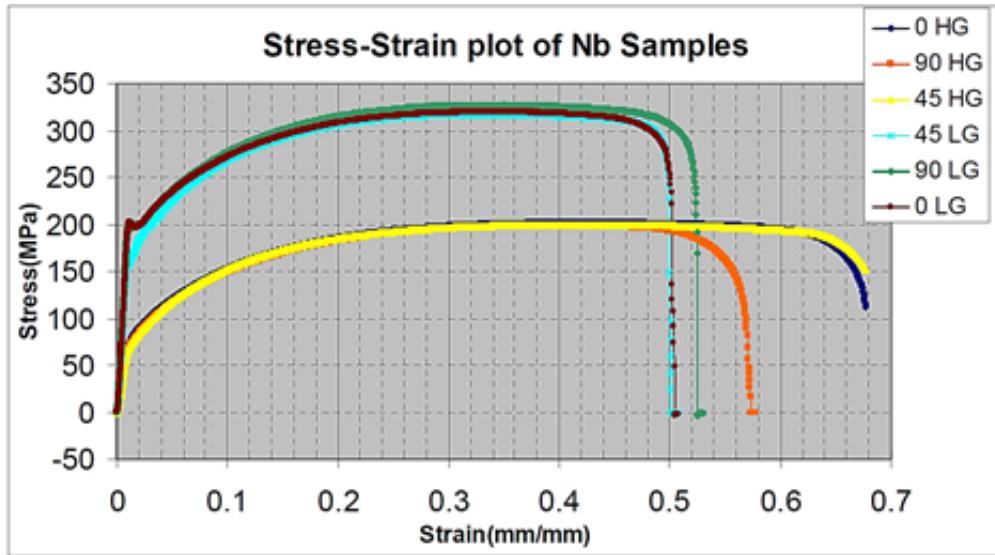


Figure 3.7: Three different style of rods were used in the experiment. Initially there was a large block of niobium and the rods were cut at different angles. The angles were 0, 45, and 90 degrees. Tensile strength for niobium, the plot depicts the values for high grade (HG) niobium of RRR=492 and low grade(LG) niobium of RRR= 30 [58].

the frequency shift for each of the stages of the deformation of niobium. The results are shown in Fig. 3.8 in terms of the calculated applied pressure. The elastic and inelastic regions are based on the curve given in Fig. 3.7, for HG niobium the material begins to inelastically deform with a pressure of 70 MPa. The figure on the left shows that a 2 kN force is not enough to inelastically deform the cavity cell since the pressure is below 70 MPa. The start of the inelastic deformation occurs after a force of 3.2 kN is applied, the pressure on the cell goes above 70 MPa.

The relationship between the force applied and the frequency shift of the cavity can be calculated based on these results. The results are given in Fig. 3.9 for the frequency with respect to force applied and the frequency with respect to the displacement these forces produce. The results indicate that in order for the cell to be inelastically deformed the frequency shift should be greater than 600 kHz. This corresponds to a displacement of 0.15 mm. The maximum yield of the cell occurs when the shift in frequency is greater than 1.6 MHz, this is a region that will be avoided. These simulations serve as an estimate of the frequency shift range where the stretching and squeezing of the cell must remain for the deformation to be inelastic and to avoid breaking the cavity cell.

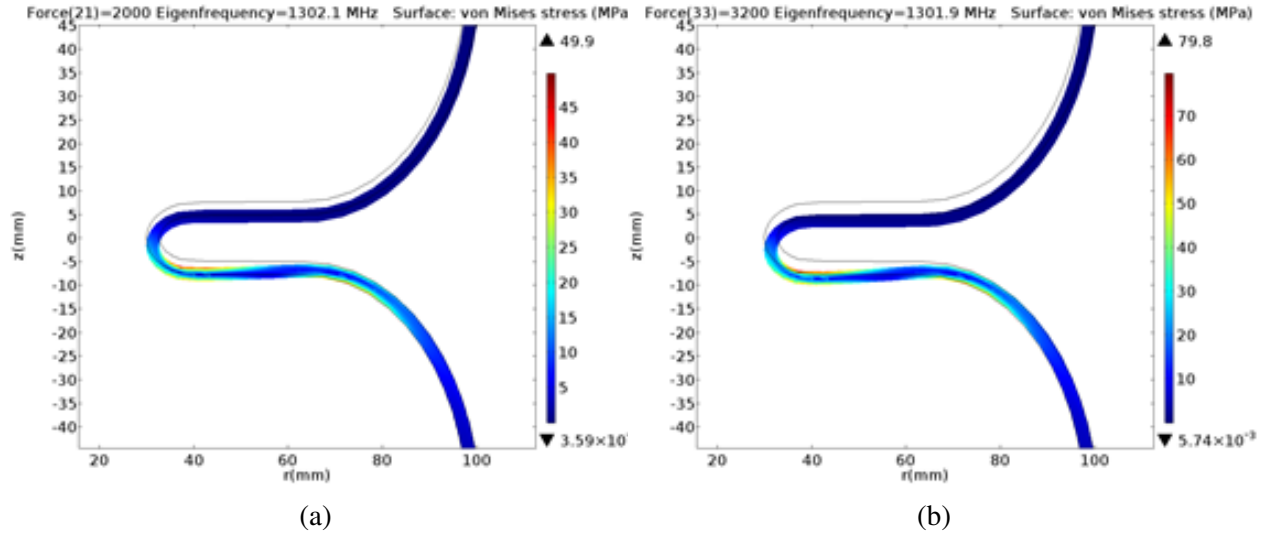


Figure 3.8: COMSOL simulation of : (a) Force applied to the cell is 2 kN ,the pressured calculated is within the elastic regime.(b) The force applied to the cell is 3.2 kN, the pressure is then enough for inelastic deformation of high grade niobium.

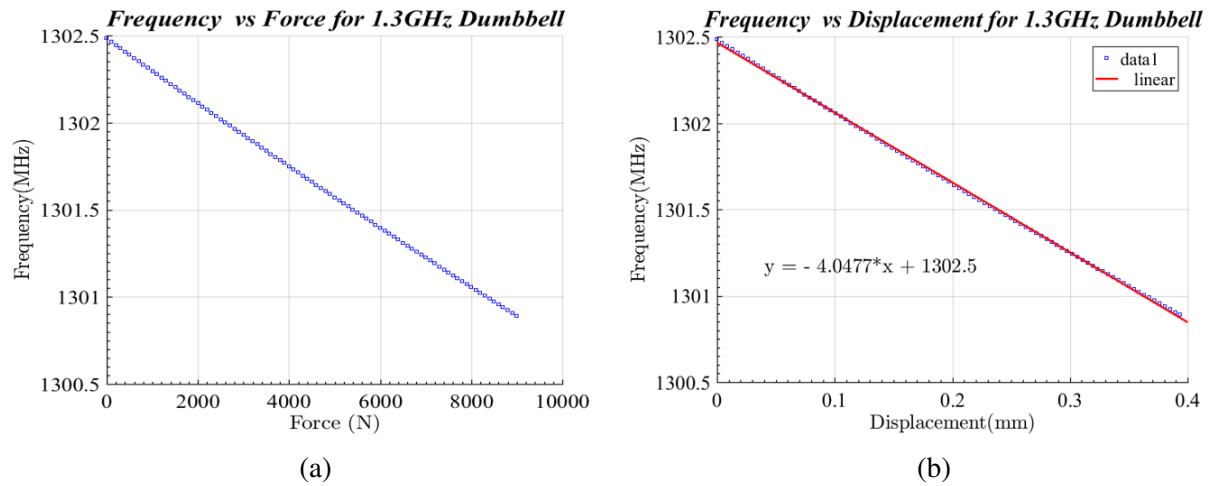


Figure 3.9: COMSOL simulation of : (a) Frequency with respect to force applied to the cell. (b) Frequency with respect to the displacement of the cavity cell due to the force applied.

3.2.6 RF Coupling

The bead-pull field profile measurements are done with an NWA and two RF couplers which are monopole antennas. One antenna excites the cavity while the other picks up the transmitted signal. The choice of the input RF coupler antenna length is essential to reduce error from the reverse power and avoid perturbing the field. Additionally, the cavity bandwidth depends on the antenna length, an appropriate antenna length is needed to determine the bead size. The needle and the

antenna are shown in Fig. 3.10. The next sections will discuss the effects of the antenna and bead length on the field profile.

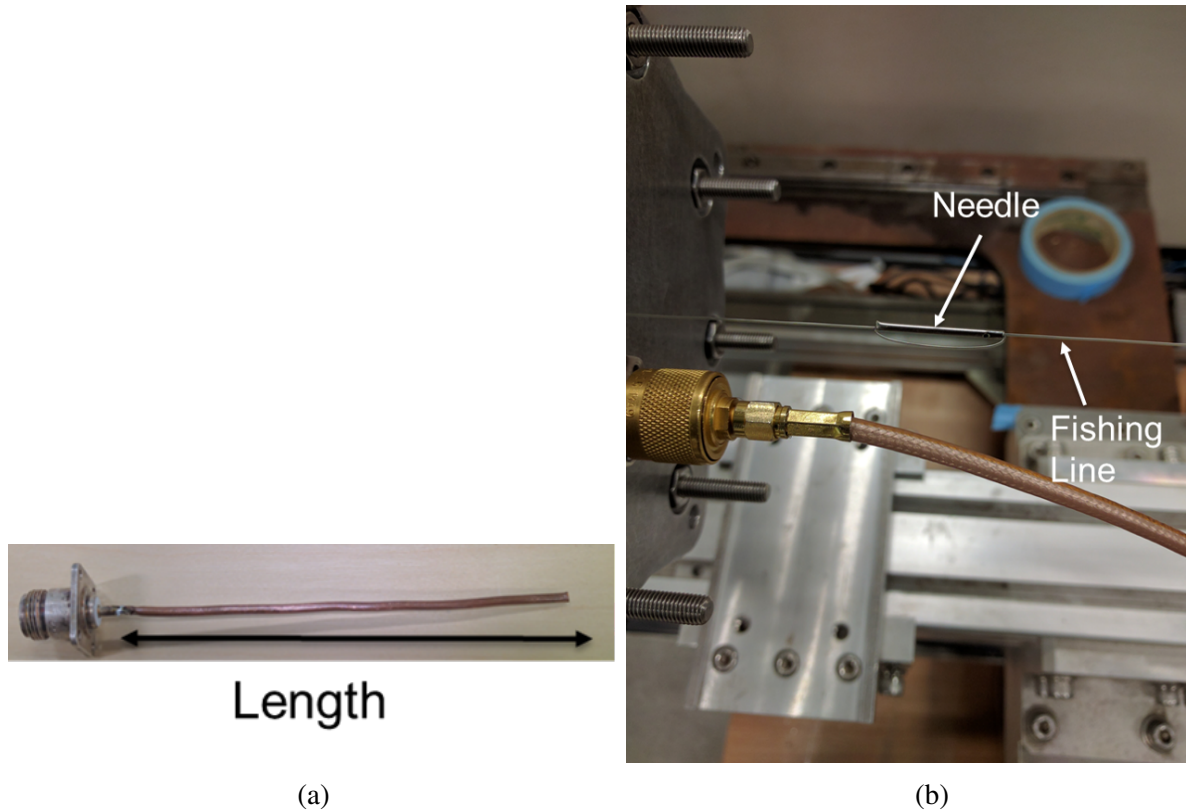


Figure 3.10: (a) BNC antenna length used to couple to the cavity π mode.(b) Fishing line and bead (in this case a needle).

3.2.6.1 Effects of Antenna and Bead Length

The input antenna coupling is measured via the NWA by using the standing wave ratio (SWR). The SWR is given by

$$SWR = \frac{1 + |\Gamma|}{1 - |\Gamma|} \quad (3.37)$$

where $\Gamma = (\beta - 1)/(\beta + 1)$ defined earlier. For the undercoupled case with $\beta < 1$, the SWR is $1/\beta$. For the overcoupled case with $\beta > 1$ the $SWR = \beta$. Lastly for the critically coupled case with $\beta = 1$ the $SWR = 1$. The SWR was measured with the NWA using S_{11} measurements. The SWR was minimized by taking several measurements at different antenna lengths. The first trial was done to find the minimum value of SWR shown in Fig. 3.11 (a). To the left of the minimum of the plot, the

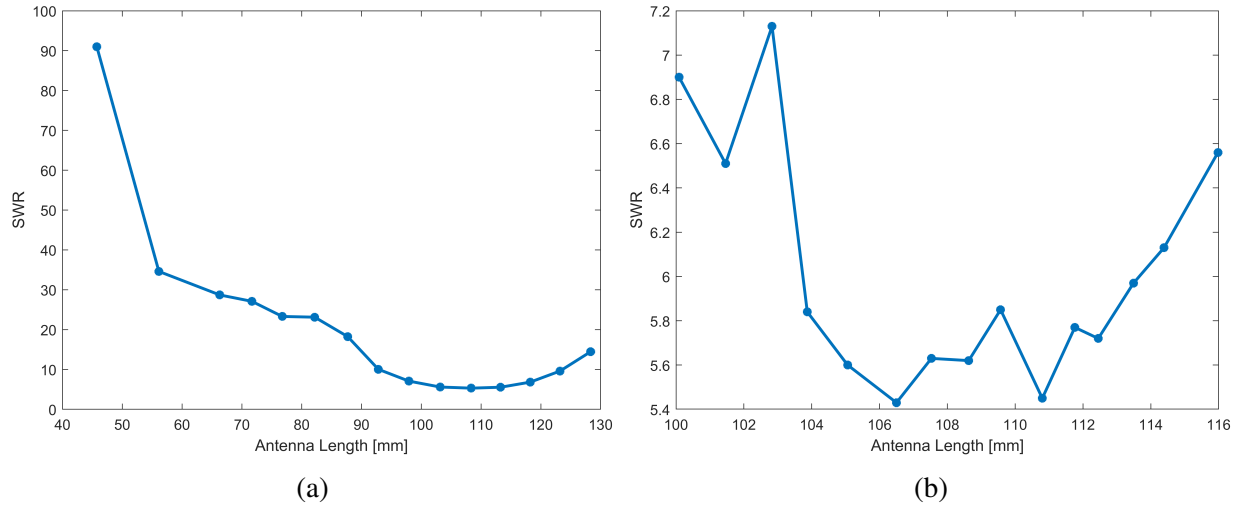


Figure 3.11: (a) SWR with respect to the antenna length, the length was varied by 5 mm. (b) SWR with respect to the antenna length, the length was varied by 1 mm.

cavity will be under-coupled and to the right of the minimum, it is over-coupled. The second trial was performed to get a more precise antenna length and minimum value, the results are shown in Fig. 3.11 (b). The antenna length was reduced to 106.5 mm to minimize the reflected power. Note that the critically coupled case was not reached.

The input antenna length chosen to minimize the SWR has a distorting effect on the field distribution shown in Fig. 3.12. The field measurements also show that the field between the cavity irises does not go to zero at the length that minimizes the SWR. These issues are eliminated by reducing the length of the antenna. An optimum antenna length of 85 mm or less minimize the perturbation of the field profile and consistently measures the field as zero at the cavity irises. The antenna should also be long enough so that the coupling is low to minimize the reflected power. An antenna length was set at 67 mm to compromise between reducing the SWR and the perturbation of the field profile.

The field profile of the cavity is measured with a stainless steel needle that rides on the fishing line on the axis of the cavity. The field perturbation due to the needle needs to be small, this was optimized by measuring the field profile at different needle lengths as shown in Fig. 3.13. A long needle produces a large distortion on the field profile causing a phase shift larger than the bandwidth of the cavity. Additionally, the field at the cavity iris location does not go to zero. As the length of

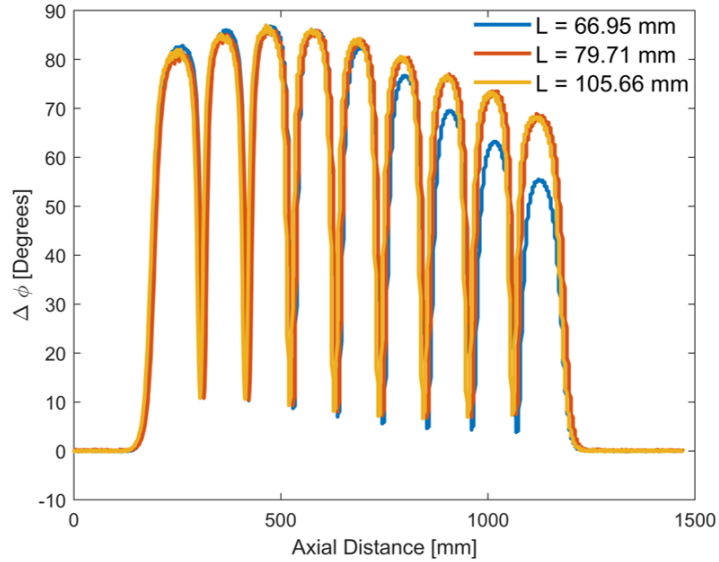


Figure 3.12: Phase difference from the forward power to the transmitted power of the cavity with respect to the pickup antenna lengths.

the needed decreases, the noise of the system becomes dominant causing peaks of the fields to be distorted. This distortion at the peaks will cause an error in calculating the appropriate tuning. The optimal needle length was found to be 6 mm, at this length there was no noise on the field profile and the phase shift stayed within the cavity bandwidth.

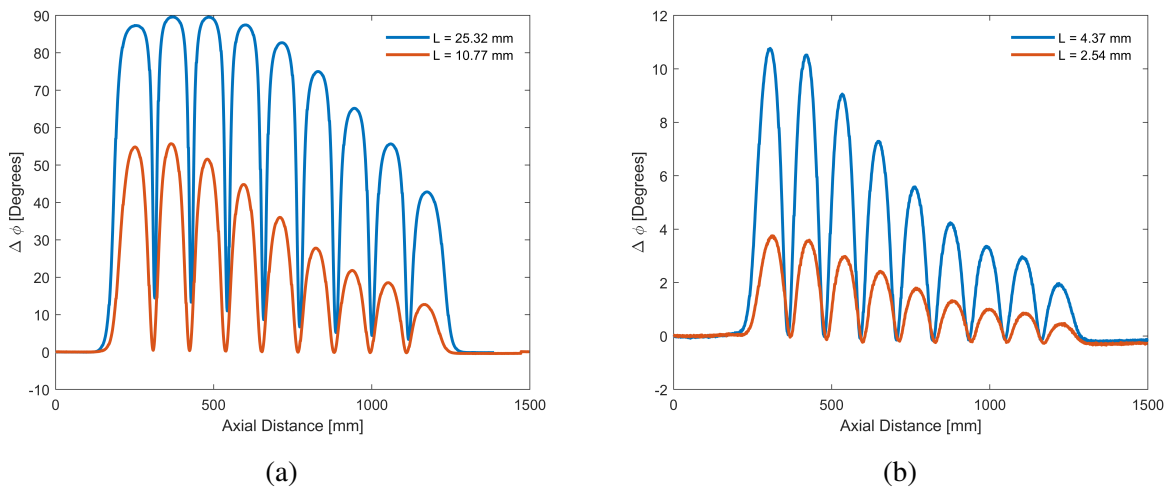


Figure 3.13: Phase difference from the forward power to the transmitted power of the cavity with respect to the needle length.

3.2.7 Environmental Effects on Cavity Frequency

In addition to having a uniform field profile, the frequency set at room temperature must take into account the thermal contraction when cooled to 2 K and when the cavity accelerating volume is set to vacuum. When the cavity is being tuned at room temperature and under atmospheric pressure the frequency of the cavity will be susceptible to temperature shifts, humidity, and small pressure fluctuations. The measured frequency from the calculated will differ by [60]

$$f_{meas} = \frac{f_{calc}}{[1 + \alpha(T - T_0)]\sqrt{\epsilon}} \quad (3.38)$$

where $\alpha = 7.3 \times 10^{-6} K^{-1}$ is the thermal expansion coefficient of niobium at room temperature. The permittivity of air is denoted by ϵ and f_{calc} is the calculated frequency. The permittivity can be modeled as [60]

$$\epsilon = \epsilon_{nc} + (0.72\Delta p + 3.8\Delta T + 2\Delta\phi) \times 10^{-6} \quad (3.39)$$

where $\epsilon_{nc} = 1.000646$, Δp is the change in pressure, ΔT change in temperature, and $\Delta\phi$ the change in humidity. When tuning the cavity the temperature has the largest effect. Humidity and pressure should be recorded for accurate measurements. For example, if the cavity's initial frequency is recorded at 1298 MHz and sometime later in the day it's recorded again but with a $\Delta T = 2K$ the frequency will now be at 1297.981 MHz. This 2 K temperature shift results in a frequency shift of 19 kHz. Therefore it is necessary to conduct the cavity tuning in a stable environment that provides constant temperature, humidity, and pressure regulation.

3.2.8 Tuning Ichiro Cavity

The method to estimate the amount a cavity cell needs to be squeezed or stretched was discussed in section 3.2.3. After the field is measured the maximum values are calculated for each of the cells. The equation 3.24 is used, the amplitude pertubance is measured from equation 3.31 and the \mathbf{H}_r is populated based with the equation 3.25. Once these terms from these equations are known the correction frequency can be calculated from equation $\delta f_{corr,j} = \frac{e_{c,j} f \pi}{2N}$. If the $\delta f_{corr,j}$ is positive the cell needs to be stretched and if $\delta f_{corr,j}$ is negative the cell will be compressed. If

the frequency shift $\delta f_{corr,j}$ is smaller than the shift needed to reach the inelastic deformation then it will be skipped. The results for the tuning procedure are shown in Fig. 3.14. The initial field flatness of the cavity was 23.58 % and after 4 iterations a field flatness of 98.4 % was reached. The

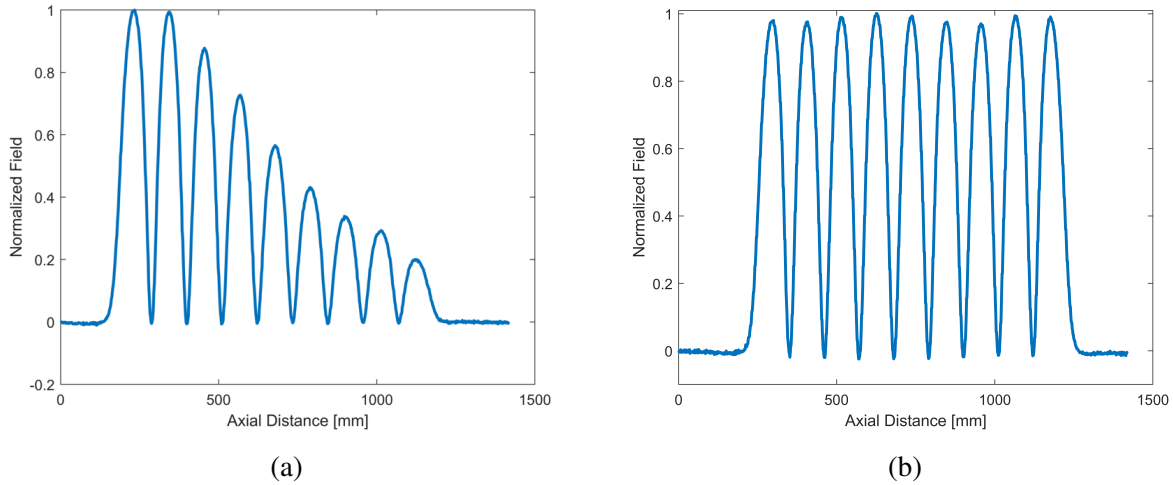


Figure 3.14: (a) Initial field flatness at was at 23.58 % (b) Final field flatness at 98.4%

methods used for this cavity can be applied to any elliptical cavity.

3.3 Transfer Function Measurement

The transfer function measurement of the cavity-tuner system is necessary to characterize the mechanical modes of the system. The transfer function is measured with a piezoelectric actuator. A sine wave is used to drive the piezo and the response of the cavity detuning is recorded. This measurement yields the mechanical modes to which the cavity-tuner system is most sensitive. Results from this measurement are used to model the cavity behavior in the circuit model in Chapter 2. In this section, the first results of the transfer function for the 650 MHz cavity were obtained at room temperature (see Fig. 3.15).

The mechanical modes of an elliptical cavity consist of 2 different types: the longitudinal modes and transverse modes. The longitudinal modes of the cavity consists of the cavity cells deforming longitudinally like an accordion. The other type of modes are the transverse modes where the motion of the cavity is in the transverse direction of the cavity axis. The two types of

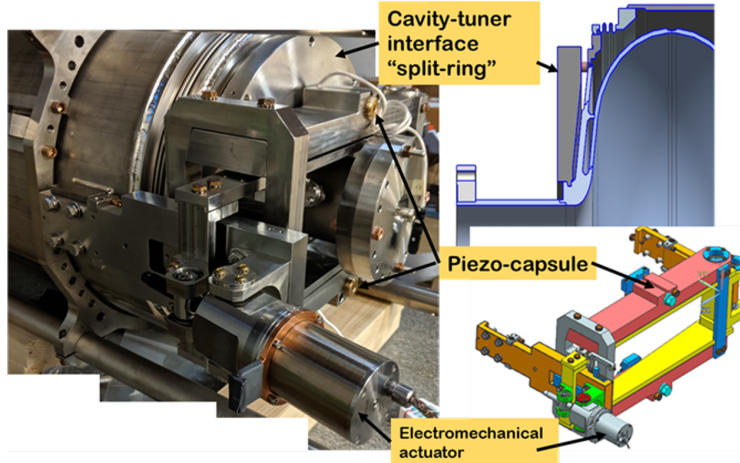


Figure 3.15: 650 MHz cavity with tuner installed.

mode are depicted in Fig. 3.16. These modes were modeled using ANSYS for the 644 MHz cavity which has similar parameters to the 650 MHz cavity [22]. The color in the plots indicates the normalized level of deformation where red is a large deformation and blue a smaller deformation. The frequency detuning sensitivity for each mode is given by Tab. 3.1. The detuning of the cavity is larger when a longitudinal (accordion) mode is excited by external vibration noise compared to the transverse mode. The longitudinal mode has a sensitivity of 37.2 kHz/mm compared to the largest transverse mode sensitivity of -0.52 kHz/mm. This is due to the end cell deformations and because the deformation is along the radius of the cell.

Table 3.1: Frequency sensitivity due to deformations of the mechanical resonances [22].

| Mode | $f_m [Hz]$ | $\Delta f / \Delta r$ [kHz/mm] |
|----------------|------------|--------------------------------|
| Vessel | 35.8 | -0.15 |
| Cavity 1 | 71.8 | -0.26 |
| Cavity 2 | 90.5 | -0.45 |
| Accordion | 94 | 37.2 |
| Vessel Rocking | 116 | -0.52 |
| Twist | 123 | -0.02 |

A schematic of the hardware and signal topology to measure the transfer function is shown in

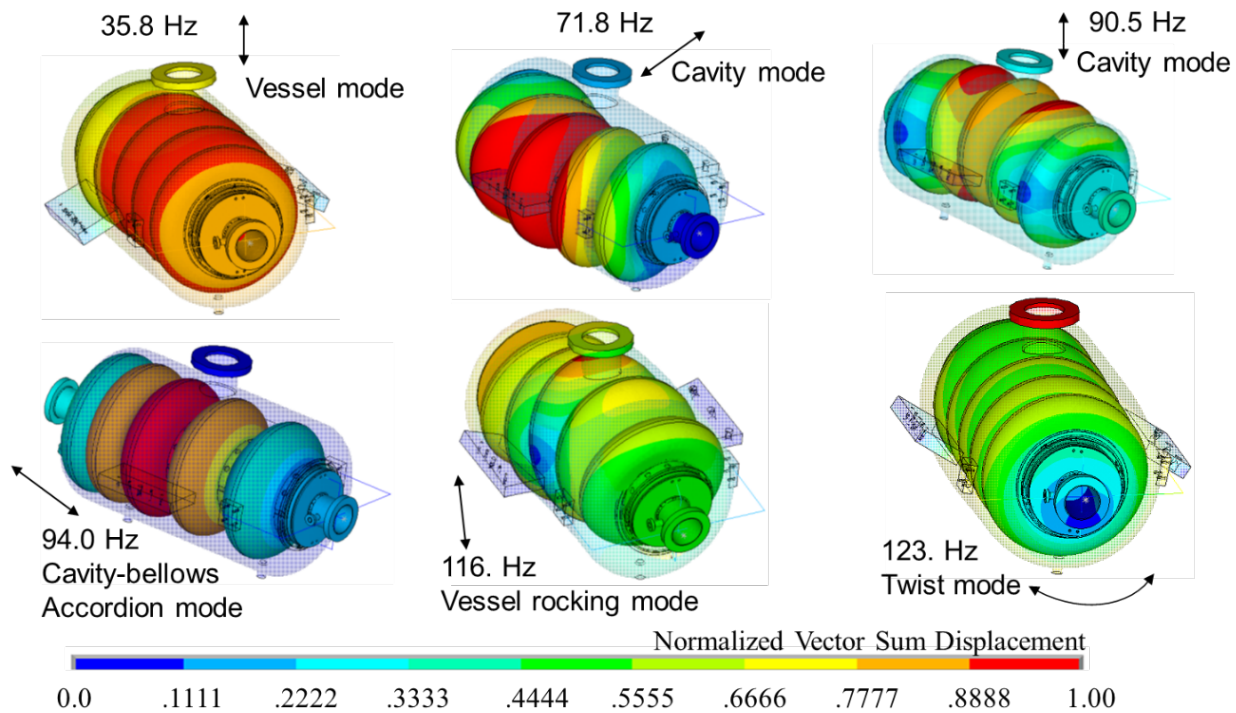


Figure 3.16: First six natural mechanical frequencies of the cavity-helium vessel system simulated in ANSYS [22].

Fig. 3.17. An RF analog signal generator known as a master oscillator (MO) is used to produce the input signal to excite the cavity in the π mode which occurs at 648 MHz at room temperature. The MO signal is fed through a power splitter to produce two signals. One of the signals is the forward power to the cavity fed through the beampipe flange. The second signal from the power splitter was sent to input A of the AD8032 Analog Phase Detector (APD) [61]. A second cavity antenna on the opposite beampipe flange provided the transmitted power which was sent to input B of APD. The output signal of the APD is proportional to the phase shift between forward and transmitted power, this was digitized with NI-PXI-4472 14-bit ADC [62]. Calibration of the APD detector was done by applying DC voltage to the piezo and measuring the response. The piezo voltage response was measured previously with a network analyzer with a sensitivity of 36 Hz/V on the cavity. This technique provided the relation between APD output signal in mV to cavity detuning in Hz.

The transfer function is measured with a piezoelectric actuator which is driven by a sine wave. A LabVIEW program was written to generate a stimulus sine waveform with a bias of 15 V and

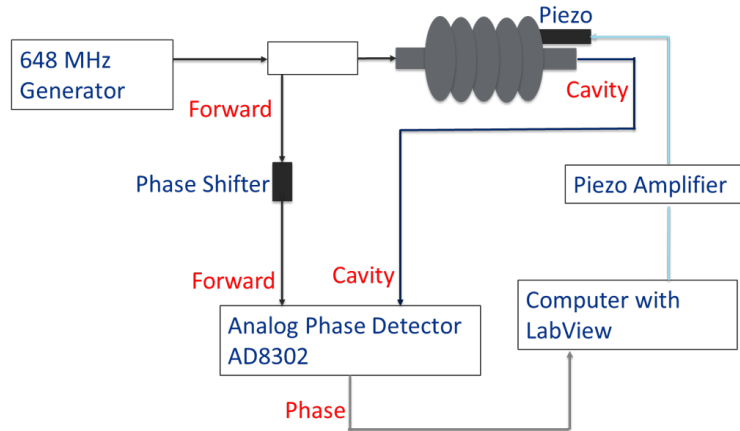


Figure 3.17: Transfer function measurement setup consists of a master oscillator, an analog phase detector, and the piezo with an amplifier.

amplitude peak-to-peak of 30 V. The frequency sine waveform driving the piezo was swept from 1 Hz to 500 Hz. The piezo driving waveform has 2 intervals for each of the frequencies to allow the decay of each driving frequency before moving to the next. The first interval is 3 seconds long where the piezo is on followed by a 3-second interval when voltage is 0 V. The cavity-tuner system transfer function of the 650 MHz cavity measured at room temperature is presented in Fig. 3.18. The system has the first resonance at 157 Hz and strongest at 215 Hz. The 215 Hz resonance is due to a longitudinal mechanical mode since it produces the largest response. A vibration of 100 Hz or less on the cavity will produce constant response. No mechanical mode can be observed in this region. The transfer function measurement demonstrates that the structural design requirement is met since no mechanical resonance lies below 100 Hz. This is important since most vibrational sources occur below 100 Hz as will be shown in Chapter 4.

The transfer function measurements driven by the piezo are then complemented by using the piezos as sensors. The vibration generation on the cavity was done by lightly tapping the cavity's beam pipe flange (opposite to the tuner side) with a rubber hammer. Fig. 3.19 shows the responses as measured by APD and piezos during 10 seconds where the cavity was lightly tapped 9 times with the hammer. By comparing transfer functions presented in Fig. 3.18 and Fig. 3.19 it is shown that the main resonance peaks fall on the same frequency. The frequency spectrum measured by

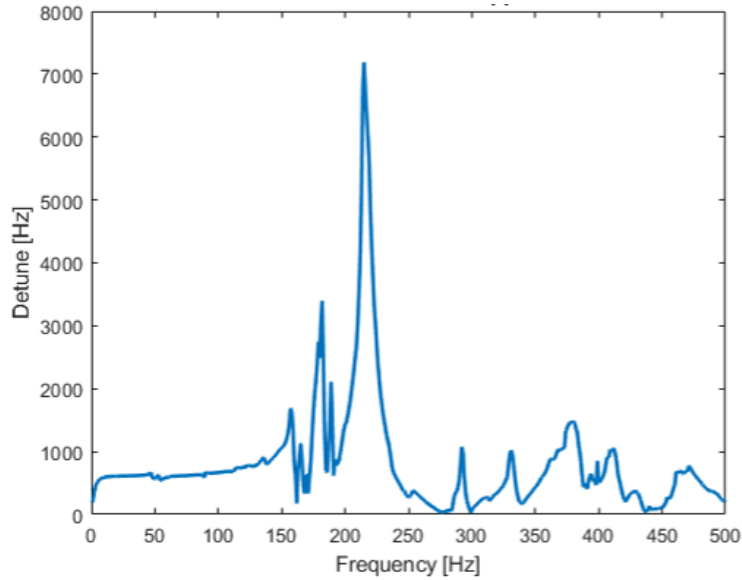


Figure 3.18: Transfer function results driven with the piezo actuator for the 650 MHz cavity. The main resonance occurs at 215 Hz.

piezo sensors demonstrates that there is a good correlation with peaks at the range of 150 to 250Hz to the signal measured from the APD. At the same time, the piezos measured some strong peaks below 100Hz (20 Hz, 45 Hz, 55 Hz, and 85 Hz) that were not observed in the spectrum measured with the APD system. This was attributed to the low vibrational frequency resonances which are transversal mechanical modes rather than longitudinal mechanical modes of the cavity.

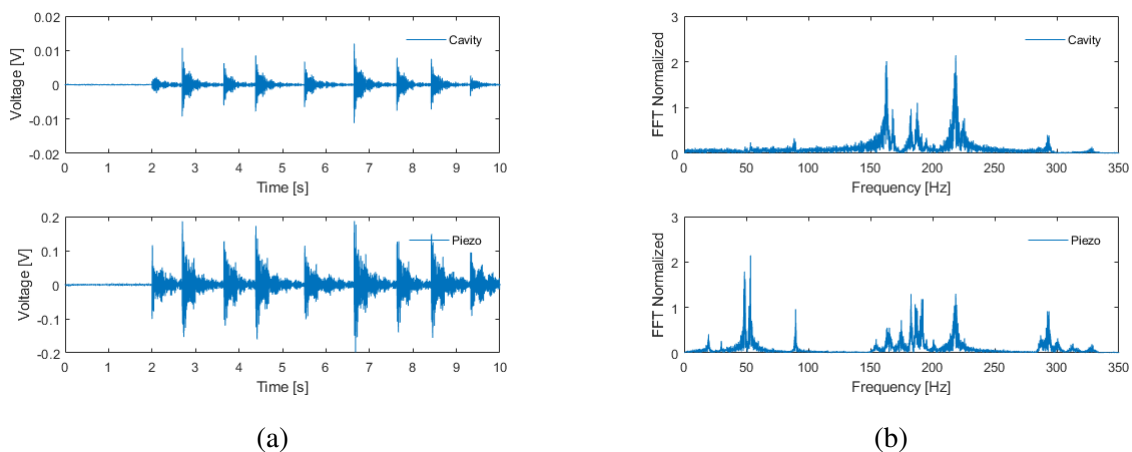


Figure 3.19: (a) Time series of voltage measured from the piezo actuator. The top plot is the signal from the cavity and the bottom is the signal from the piezo actuator. (b) FFT of time-series from the piezo actuator.

3.4 Summary of Chapter

Three different signals such as the forward, reflected, and transmitted power were used to characterize the elliptical cavity properties. These signals are used to measure the intrinsic quality factor and the cavity frequency. Before an elliptical cavity is placed in a cryomodule for operation the field must be uniform. This is achieved by measuring the field via the bead-pull method and deforming the cavity cells until a uniform field is reached. In this chapter, a perturbation method to obtain a uniform field by estimating the cell deformation yielded an improvement of field flatness from 28 % to 98 %. A COMSOL simulation was used to estimate the safe range and the range in which the deformation is inelastic. During operation, the cavity will experience microphonics. The first experimental results for the mechanical modes of the PIP-II 650 MHz cavity were presented. These measurements are needed to find sensitive mechanical modes of the cavity-tuner system. The results show that no mechanical modes are found below 100 Hz. The main mechanical mode is longitudinal and occurs at 215 Hz. These results can be used in the cavity lumped circuit model to obtain the behavior when microphonics are present.

CHAPTER 4

MICROPHONICS STUDIES

Cavities are prone to deformation due to their thin walls (ranging from 2-4 mm) from vibrational noise known as microphonics. Stiffening rings and a stiffer tuner mitigate these deformations, all the cavities discussed in this chapter implemented these methods. Despite implementing these changes, the microphonics noise is still present and inducing frequency detuning. Since the 650 MHz cavities were still being built and tested, the microphonics on the LCLS-II cryomodules were studied. The elliptical cavities used in the LCLS-II cryomodules are 9-cell and 1.3 GHz. The LCLS-II linac will operate with a low-intensity beam requiring less RF power which results in narrowband cavities. Although the cavity types are different, for different applications, the effects from the cryogenics and pumps near the cryomodule will be similar for most cryomodules. A MATLAB script was written to do the signal processing of the cavity frequency and analyze the cryogenic parameters for 12 cryomodules (96 cavities).

4.1 Sources of Microphonics

Vibrational noise known as microphonics can couple to the cavity and cause frequency detuning. Microphonics can be attributed to pumps, internal and external vibrations in the cryomodule, pressure variation in the helium bath, and thermoacoustic oscillations (TAOs) in the helium supply lines. Vacuum pumps can not be turned off since they maintain the vacuum of cavity volume and the insulating region outside the cavity vessel. Likewise, external vibrations can be difficult to pinpoint and impossible to mitigate. Frequency detuning due to the helium bath pressure variation is mitigated with stiffening rings. The stiffening rings on the cavity results in a frequency pressure sensitivity in the range of 5.33 Hz/Torr to 75 Hz/Torr. The typical variation in the liquid helium bath pressure in a large cryogenic plant for a linac ranges from 0.06 to .13 Torr at 2 K.

An important aspect to the contribution of microphonics is the effect of a heat source in the liquid helium, such as when RF power is supplied to the cavity. In the cryomodule setting helium

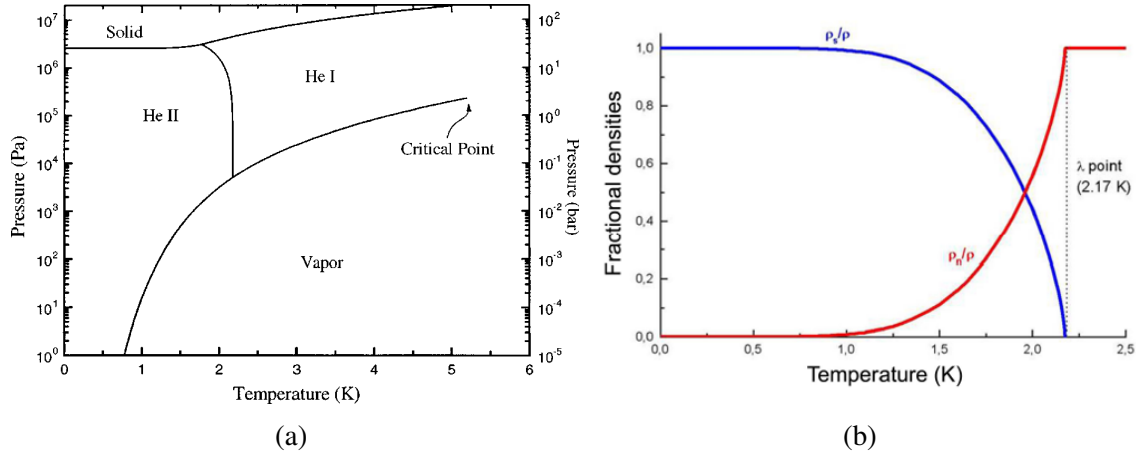


Figure 4.1: Phases of helium with respect to temperature and pressure [63].

will experience three phases shown in Fig. 4.1 below. The He-I and He-II are both liquids, the other phase is a gas. There are two important phase transitions of helium, one is the critical transition where both HE-I a liquid, and a gas can coexist. This occurs at a temperature above 5 K and 100 kPa. The second phase transition occurs at 2.17 K and 5.048 kPa known as the lambda point. At this temperature and pressure, both liquids and gas can coexist. As the temperature is decreased and kept at the same pressure the liquid helium will transition to He-II. He-II is a phase used to cool the cavity and it's considered a liquid. The temperature and the pressure of the liquid helium cooling the cavity are 2 K and 23 Torr (3.06 kPa). He-II is known as a superfluid that has small or zero viscosity. During this phase transition, the thermal conductivity of He-II also increases drastically from He-I which is why it is used to cool down the cavity.

He-I is considered a normal fluid, and when a heat source is applied to it will start to bubble. This bubbling will contribute to vibrations in the helium vessel. He-II dissipates heat differently, instead of bubbling the heat is transferred in the form of waves analogous to a sound wave in the air, this phenomenon is known as second sound. Since the viscosity is negligible the superfluid also experiences less flow restriction due to obstacles such as bends from a pipe. Although, the He-II is an inviscid fluid the flow of heat can still experience disturbances. The two-fluid model posits the He-II to be a mixture of normal-fluid atoms and superfluid atoms with densities ρ_n and ρ_s , all the entropy is carried by the normal-fluid atoms. The interaction between these two fluids can

create turbulence (Quantum turbulence) which can result in changes in the speed of second sound [64]. The velocity distribution from this turbulence gives a non-Gaussian distribution compared to a Gaussian distribution from classical turbulence. As will be shown later this Gaussian-like distribution with tail ends is also observed in the distribution of detuning of the cavities.

To characterize the microphonics of the cavity environment frequency measurements are taken since the cavity is the most sensitive sensor available in the cryomodule. The cavity frequency measurements will yield the severity of the frequency detuning as well as the RMS detuning and the spectra of the noise. The spectra can be used to calculate the contribution to the overall detuning of each frequency. If a specific frequency contributes largely to the total detuning passive mitigation techniques should be taken. One passive mitigation technique is to use vibration measurements with geophones or accelerometers around the cryomodule setting to pinpoint the frequency observed in spectra of the cavity. Once a source is identified steps should be taken to mitigate it if possible. The microphonics spectra will also be analyzed for correlations with other parameters such as helium flow and supply pressure. The results from other labs such as BESSY indicate that the microphonics spectrum is not time-invariant (noise source changes frequency and amplitude) [53]. In the next section, the microphonics spectrum for the LCLS-II cryomodules will be shown and discussed.

4.2 LCLS-II Microphonics Studies

The LCLS-II is an X-ray FEL linac that uses 9-cell 1.3 GHz SRF cavities. A collaboration between SLAC, Fermilab, Lawrence Berkeley National Lab (LBNL), and Thomas Jefferson Lab (JLab) was made so that Fermilab and JLab would conduct the cryomodule (CM) tests at their respective facilities, and finally after qualifying the cryomodules, ship them to SLAC in California. The study of microphonics for the LCLS-II cryomodules was done at Fermilab in the cryomodule testing facility (CMTF) facility [65] shown in Fig. 4.2. The cryomodule is roughly 13 m long and contains eight SRF cavities, a magnet, and a beam position monitor (BPM). The cavities are cooled down to 2 K with liquid helium, the schematic of the cryogenic flow needed to get to this temperature is shown in Fig. 4.3. Two thermal intercepts are surrounding the cavities which are at



Figure 4.2: CMTF testing facility at Fermilab.

4.6 and 40 K to reduce the overall heat load at 2 K. A higher heat load at 2 K results in higher costs. The supply liquid helium is 2.3 K with a pressure of 3 bar (2250 Torr). Then undergoes a pressure change through a Joule-Thomson(JT) valve to reach 2 K. During this pressure change the liquid helium undergoes a phase transition from a normal liquid to a superfluid [63]. When the cavity has a heat load the temperature and liquid level are regulated with another JT valve. The entire helium vessel of the cavities is filled with liquid helium to reach the 2-phase helium pipe. The 2-phase pipe contains 2 K liquid and vapor, the vapor forms from the heat load of the cavities. The 2 K vapor is then transported to the cryogenic plant to be reused. Each of these cryogenic lines affects the cavity detuning since they produce a vibration.

The microphonics study was made possible by a joint effort of of the cryogenics group, LLRF group, and resonance control group at FNAL. The LLRF at CMTF allows the capture of all eight cavities simultaneously and synchronously for an extended period [66]. During testing of the prototype cryomodule (pCM) a source of microphonics that caused large stochastic frequency detuning on the cavities was observed. This noise was attributed to thermoacoustic oscillations

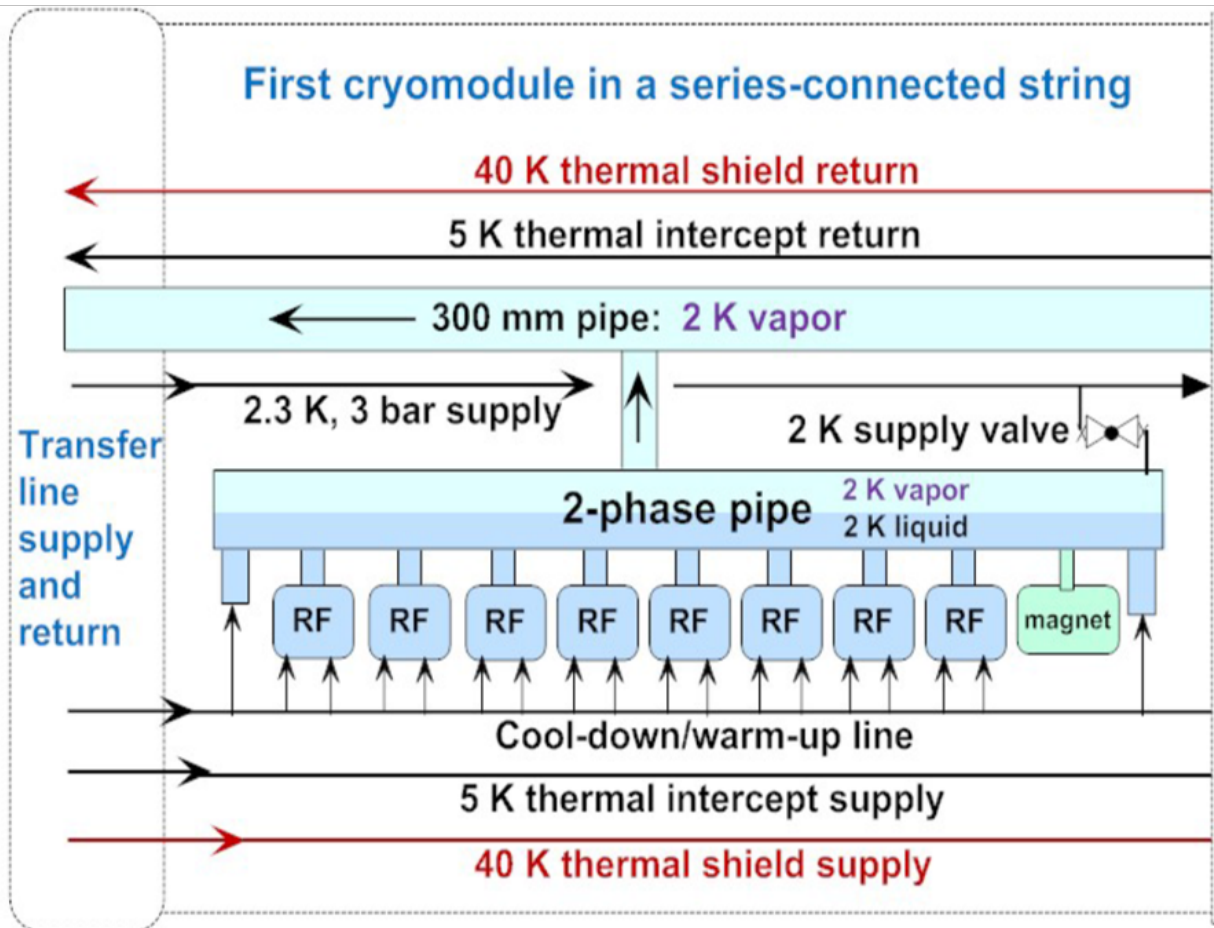


Figure 4.3: Cryogenic flow schematic of a 1.3 GHz LCLS-II cryomodule [18].

(TAO) after various tests were performed and the results of this determination are shown by Hansen et al. [67]. A TAO occurs in a cryogenic tube when a thermal gradient is formed within the tube [68]. This thermal gradient drives an acoustic oscillation where the cold cryogenic fluid moves to the warm end and expands forcing the fluid back to the cold end. The frequencies which can occur from this phenomena are in the 10-100 Hz range [69]. The effect of TAOs on the cavity detuning is shown in the spectrogram in Fig. 4.4. The spectrogram gives the Fourier transform result in 3 dimensions with the vertical being the frequency, the horizontal time, and the color bar shows the intensity. The spectrogram plot is characterized by narrowband frequency lines that change in frequency value and intensity over time. This behavior demonstrates that the sources are not time-invariant and are stochastic. The majority of the microphonics source frequencies were less

than 100 Hz. The histogram of the detuning of the cavities is large as shown in Fig. 4.4. For most of the cavities, the histogram has a Gaussian distribution, the cavities that deviate from this distribution have additional noise which is not Gaussian. Note that the requirements for operation are a peak detuning of 10 Hz set by the power source [18]. Under these conditions, there would not be enough power to maintain the gradient of the cavities since the frequency is above the 10 Hz peak limit.

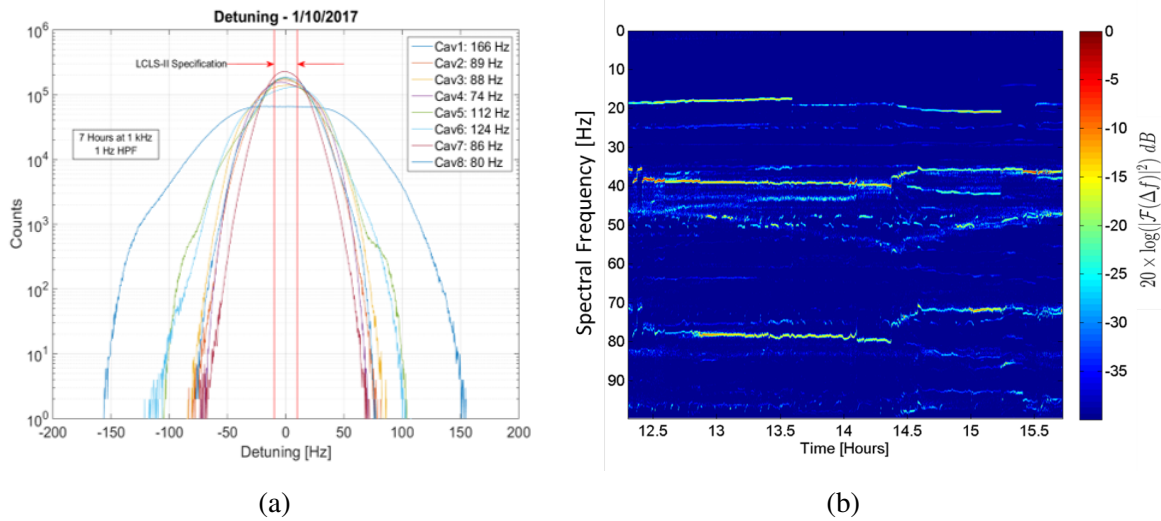


Figure 4.4: (a) Histogram of 8 cavities, the red lines indicate the specification of the peak detuning.(b) Spectrogram of cavity shows narrowband frequencies which change in amplitude and frequency in time.

The frequency detuning of the cavities was reduced by applying two different modifications to the cryogenic valves. The cryogenic valves were modified by adding wiper rings along the valve stem to dampen oscillations. The valves were also reconfigured to change the helium supply line by altering where the input connects. These techniques are described in detail by Hansen et al [67]. The histogram above shows that the frequency detuning of cavity 1 is larger than the others. This was due to the rigid connection of cavity 1 to the gate valve. Later, this rigid connection was replaced with bellows. This and other changes are discussed at length in Refs. [70]–[72]. These changes result in a substantial decrease in frequency detuning of all eight cavities as shown in Fig. 4.5. The histograms of all the cavities have a Gaussian distribution with an RMS detuning of less than 2 Hz, to bring them within specification. From cryomodule 6 on all the cavities are within

peak detuning specification and all the frequency lines in the spectrogram are mostly stable.

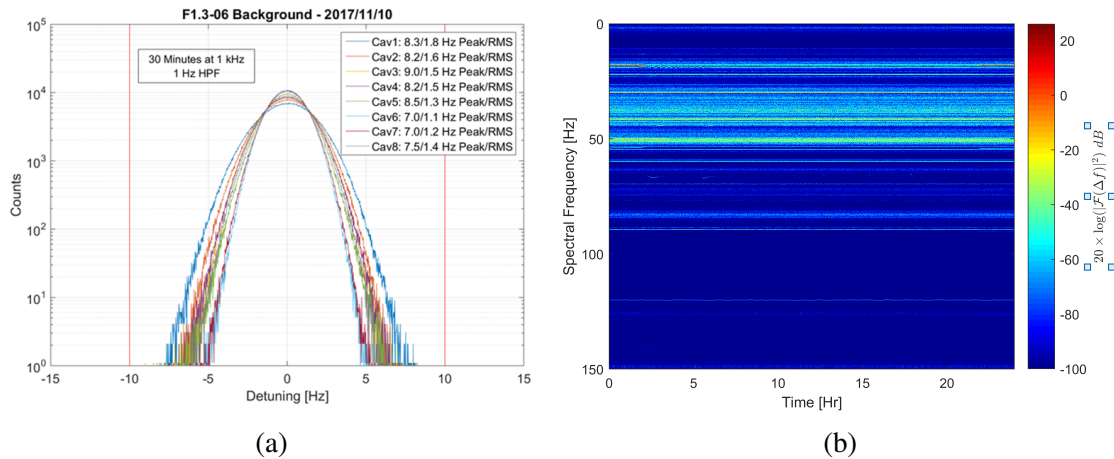


Figure 4.5: Results for cryomodule 6 after passive mitigation techniques were implemented. (a) Histogram of 8 cavities, the red lines indicate the specification of the peak detuning.(b) Spectrogram of cavity shows narrowband frequencies which change in amplitude and frequency in time.

Implementing these changes yielded a peak detuning below 10 Hz and an RMS detuning of less than 2 Hz for each cavity. All the cryomodules displayed similar microphonic sources, such as a 30 Hz source attributed to the Kinney vacuum pump. There were events where some of the cavity's peak detuning exceeded the 10 Hz limit while others were within the limit, this occurred in the same cryomodule. While the peak detuning exceeded the 10 Hz limit the values were in the range of 11-30 Hz, smaller than before the passive mitigation techniques were implemented. The data also shows that the microphonics noise spectrum changed throughout the day in the same cryomodule. In the next section, the data from cryomodules with cavities that exceed the 10 Hz limit will be presented, this will include the use of histograms of the frequency detuning and a cumulated mean square value calculated from the spectral density function. This value will be called the integrated RMS detuning and is interpreted as the area under the curve of the spectral density function obtained from an FFT. When plotted over a frequency range the detuning frequency source which contributes the most will be characterized by a jump. These plots will be discussed in more detail in the next section. Each of the cryomodules is numbered based on the production and date tested. The prototype cryomodule is known as a pCM while the rest are given a number, the next being CM 2 up to CM 19, which was the last cryomodule tested at CMTF in Fermilab.

During the qualification of the cryomodule, the frequency detuning is measured after the cooldown going from 293 K to 2 K. The detuning of all eight cavities is recorded and studied via histograms, integrated frequency detuning, and spectrograms. Additionally, the correlation between frequency detuning and cryogenic parameters is explored. The data acquisitions span different stages of the cryomodule testing starting from initial cooldown, data acquired days after the initial cooldown, and data at the nominal voltage. The data is presented by frequency excited on the cavities, first smaller frequencies will be discussed followed by higher frequencies.

4.2.1 Effects of Liquid Helium Fluctuation

The smallest frequency excitations of the cavity occur due to the helium pressure variation in the cavity's liquid helium vessel, the correlation between these two parameters will be shown for different cryomodules. This effect has been observed by other labs such as Bessy [53] and CBETA [73]. A JT valve maintains the liquid level in the 2 K two-phase pipe and an external pump maintains the vapor pressure at 23 Torr to maintain it at 2 K. These two different mechanisms can give rise to the liquid helium pressure variation. The frequency pressure sensitivity (df/dp) measurements for the cavities yield a value 75 ± 5 Hz/torr shown in Fig. 4.6.

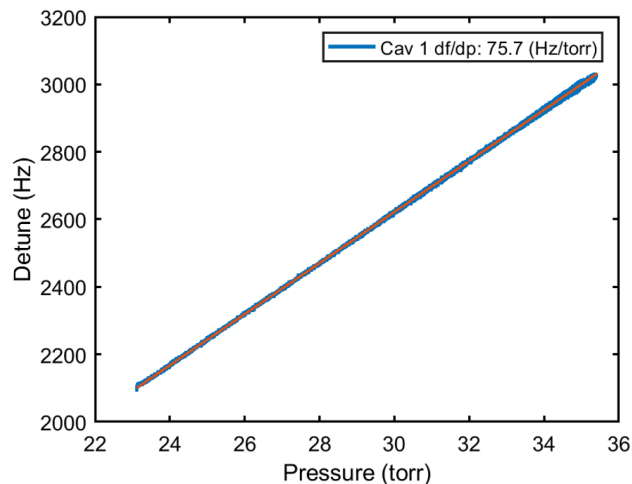


Figure 4.6: Cavity 1 frequency df/dp in Hz/torr.

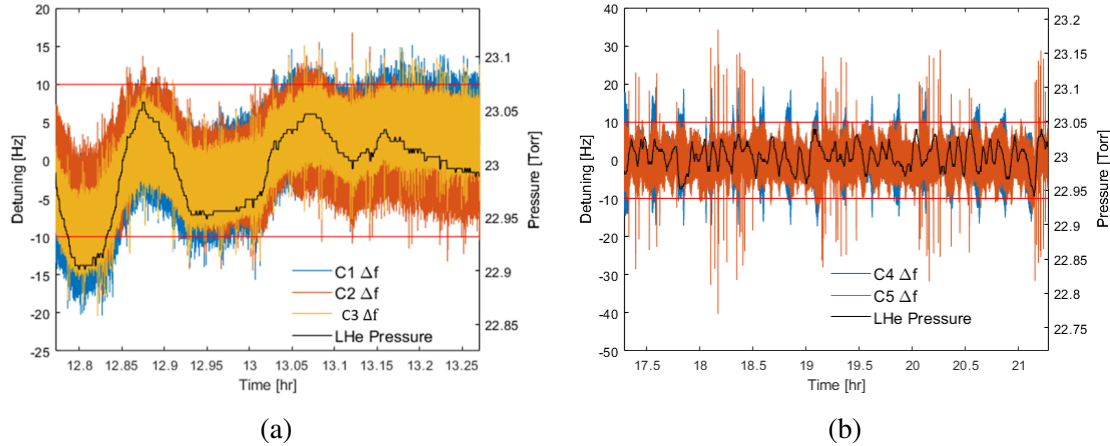


Figure 4.7: Frequency detuning for cryomodule 15 for different dates. The sampling rate from helium pressure sensor is 1 Hz. (a) 30 minute time series of the detuning for cavities 1 through 3 superimposed with the pressure of the liquid helium. (b) 4 hour data capture showing cavities 4 and 5 superimposed with the liquid helium pressure. This data was taken a day after (a).

The cavity frequency and helium pressure correlation is shown in Fig. 4.7 for CM 15 for different days. The variation of the helium pressure matches the trend of the frequency detuning. In this plot, the DC offset was removed by subtracting the average of the signal and the red lines indicate the 10 Hz limit of the cavity. The time series of the detuning of CM 15 is a 30-minute data capture with a sampling frequency of 1 kHz. This same sampling frequency is used for all other cryomodules. Only two or three cavity frequency detunings are plotted for better visibility of the signals, but all 8 are recorded simultaneously and display similar behavior. Note that the helium pressure is measured at the downstream end of the liquid level of the 2 K two-phase pipe, this pressure is assumed to be the same at all of the cavities. The sampling frequency for the pressure data from the sensor is 1 Hz, this sampling frequency is the same for the other cryogenic parameters presented henceforth.

The amplitude and frequency of the helium pressure can vary by day as shown in Fig. 4.7 (b) for CM 15 on a different date compared to Fig. 4.7 (a). For Fig. 4.7 (b) the helium pressure variation is higher than Fig. 4.7 (a). The frequency detuning on Fig. 4.7 (b) has also more impulses compared to Fig. 4.7 (a). Similar results were obtained for CM 14 and CM 17 shown in Fig. 4.8. The helium pressure variation from these plots ranges from 55 mTorr to 156 mTorr. Note that the helium pressure fluctuation frequency is different for CM 14,15 and 17 as shown Fig. 4.7 and Fig. 4.8.

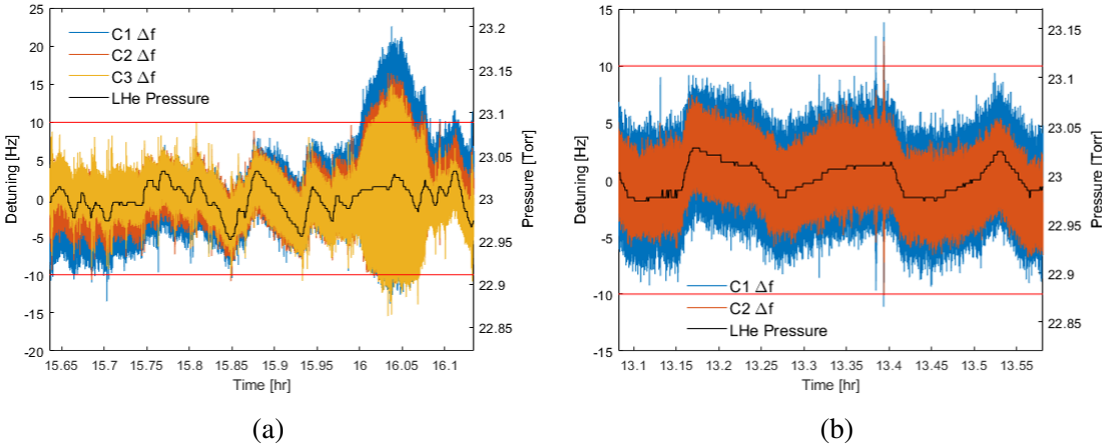


Figure 4.8: (a) 30 minute cavity frequency detuning for cryomodule 15 superimposed with liquied helium pressure. (b) 30 minute cavity frequency detuning for cryomodule 17.

When the helium pressure variation is small the cavities experience fewer events that are past the 10 Hz limit. The regulation of the JT valve and the 2 K two-phase pump appear to play a role in the variability.

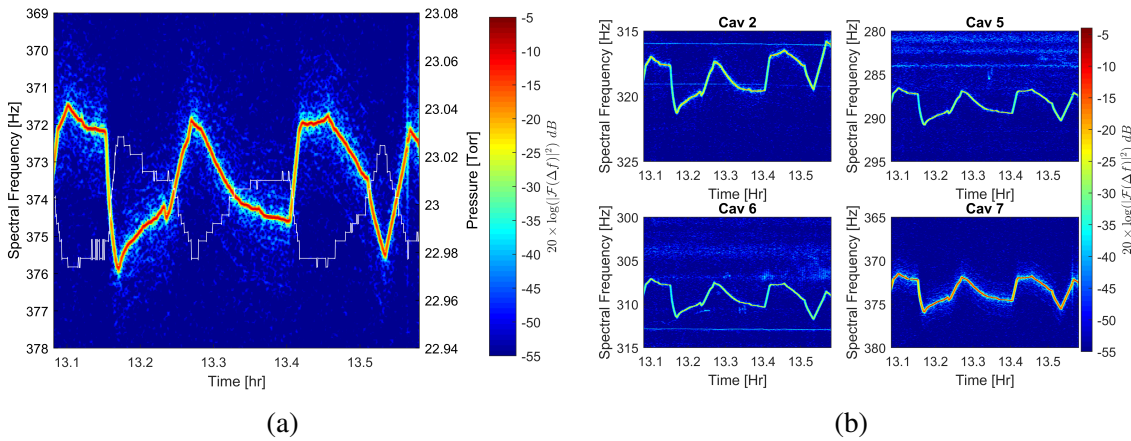


Figure 4.9: Cavity frequency detuning for cryomodule 17. (a) Spectrogram of cavity frequency detuning for cavity 7, there is a correlation between 373 Hz source frequency modulation and the variation of the helium pressure. (b) Spectrograms of cavities 2, 5, 6, and 7 display the same frequency modulation but at a different frequency each.

Higher frequency excitations on the cavity can sometimes be correlated with the helium pressure. The correlation between a 370 Hz source frequency modulation and the liquid helium pressure is shown Fig. 4.9 (a) for CM 17. The frequency modulation of the 370 Hz source is opposite of the helium pressure variation but the shifts occur simultaneously. The peak detuning of all cavities was

small and few events were outside the 10 Hz limit. Although cavity 7 is the only one affected by the 370 Hz vibration the signal is observed in all cavities at different frequencies, as shown in Fig. 4.9 (b). The signal is weak at cavities 1 and 8. The relation between small frequency excitations can also lead to mechanical harmonic excitations in the frequency detuning of the cavity. This will be discussed next.

4.2.2 Mechanical Harmonics Excitation in Cavity Frequency Detuning

The data from Fig. 4.7 (a) shows an 18 Hz narrowband frequency plotted in a spectrogram shown in Fig. 4.10 . This 18 Hz line is the fundamental frequency of harmonics 36, 54, and 90 Hz that arise in all cavities. At approximately hour 13 on the plot, a distortion appears in all the harmonics. This distortion shows a strong correlation with the supply pressure of the 2.2 and 5 K helium lines

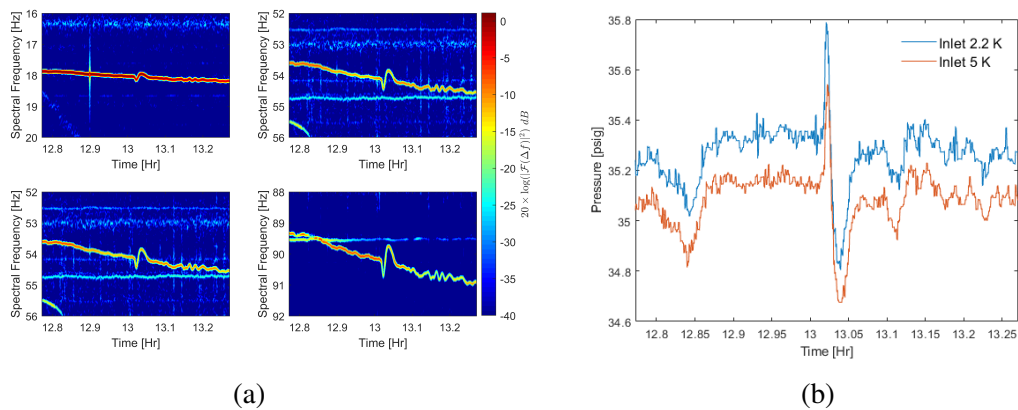


Figure 4.10: Cavity Frequency data for cryomodule 15. (a) Spectrograms of cavity 7 at demonstrating the harmonics of the 18 Hz source. (b) Helium supply pressure for the 2.2 K and 5 K lines.

shown in Fig. 4.10 (b) as being opposite of the cavity frequency detuning. The effects can also be seen on the 5 K helium flow rate sensor shown in Fig. 4.11. This sensor reads out the flow rate of helium in grams g/s. This shift in supply line pressure and flow rate did not have any effect on the liquid level sensors located at the downstream and upstream positions of the cryomodule. The liquid level reading shown in the same figure shows the percentage of liquid covering the probe,

the difference in liquid levels is due to the tilt of the cryomodule. The amplitude and frequency modulation increase with higher-order mechanical harmonics (eg. 90 Hz).

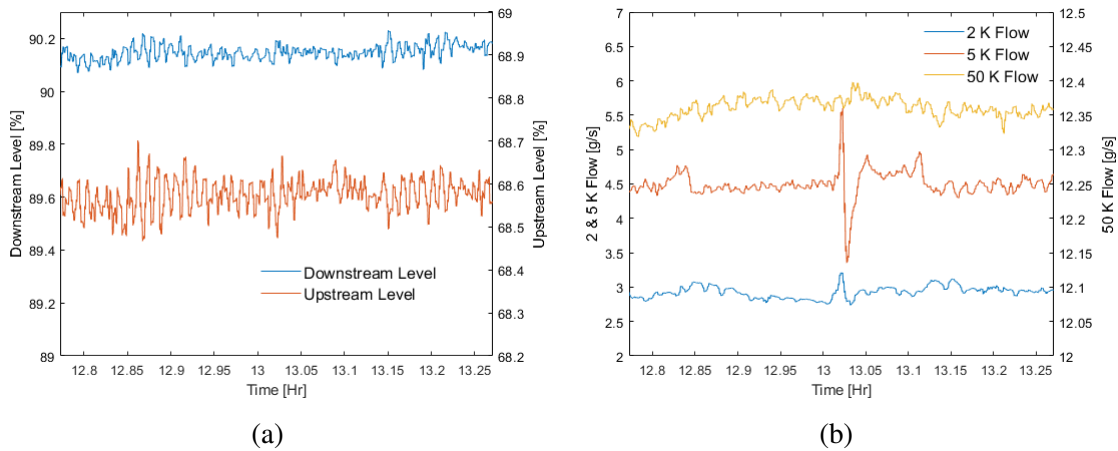


Figure 4.11: Cryogenic data for cryomodule 15. (a) Liquid level probe reading measured in percentage of probe being submerged in liquid helium.(b) Liquid helium flow rates for supply lines at 2, 5, and 40 K.

On the same cryomodule, but on a different day, a 23 Hz fundamental frequency creates a harmonic of 46 Hz vibration which detunes only cavities 4, 5, and 6. The line shown in 4.12 (a) is sinusoidal and has multiple lines near it, this behavior resembles the inlet pressure of the 2.2 K and 5 K helium transfer lines as shown in Fig. 4.12 (b). Additionally, there is a strong correlation between the frequency detuning modulation observed in the time series of only cavity 4 and of the inlet pressure. The frequency modulation of the 23 and 46 Hz lines is double the amplitude modulation frequency of the inlet pressure. The multiple line behavior on the spectrogram can be explained by the short impulses on the times series of the detuning data (see Fig. 4.7 (b)), these short impulses give rise to multiple frequencies. The inlet pressure behavior is periodic but the pulses on the frequency detuning time series are too narrow for correlation. The 5 K and 2 K helium flow rates show the same periodic behavior as the inlet pressure as shown in Fig. 4.13 but again the variation does not correlate to the narrow pulses on the cavity frequency detuning time series. The excitation of harmonics of the cavities can be attributed to instability in the cryogenic lines. These can be seen in the inlet pressures and flow rate of helium. While a small frequency source won't cause large detuning higher-order harmonics can lead to higher detuning. A small frequency

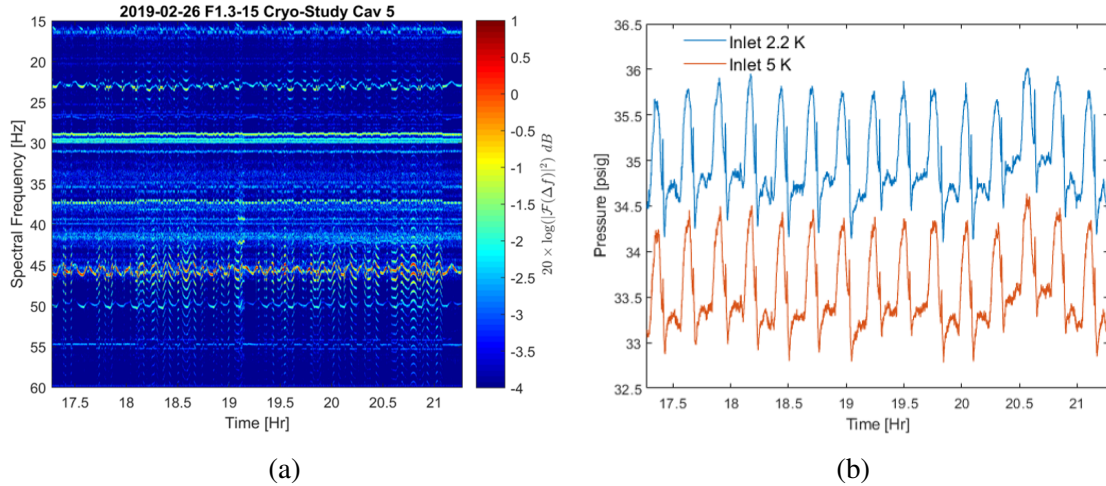


Figure 4.12: Data for cryomodule 15. (a) Frequency detuning of cavity 5 of a 4 hour data acquisition.(b) Inlet pressure of the helium supply lines at 2.2 K and at 5 K temperatures.

source won't cause large detuning but if higher-order harmonics are excited a larger detuning is possible.

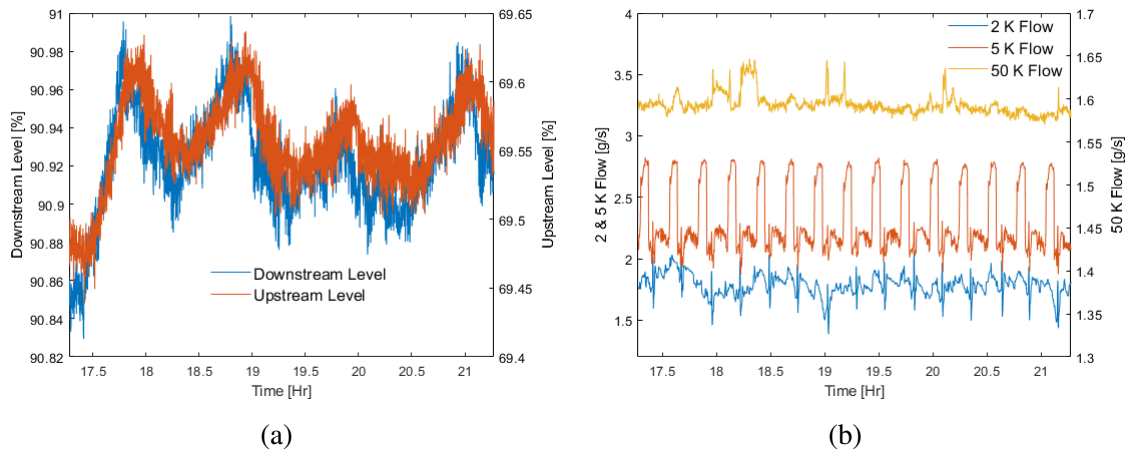


Figure 4.13: Cryomodule 15 data. (a) Liquid level readings of the downstream and upstream positions given in percentages of probe submerged in liquid helium. The left axis shows the values for the downstream level and the right axis shows the upstream level. (b) The flow rate of the 2, 4, and 40 K are shown. The left hand axis shows the values for the 2 and 5 K flow while the right axis shows the flow rate for the 40 K flow.

The harmonics observed in the frequency detuning can be acoustic or mechanical. The mechanical harmonics can occur from the eigenmodes of the metal structure such as the cavity string assembly, the cryomodule, and the 2 K two-phase pipe. The wavelength of the wave traveling in the metal can be estimated using the equation $\lambda = v/f$ where v is the speed of sound in the metal

and f is the frequency being excited. The cryomodule is made out of stainless steel and the cavity is made out of niobium. The speed of sound in stainless steel is 6 km/s and for niobium, it is 3.48 km/s. The fundamental frequencies of the harmonics were 18 and 23 Hz. For an 18 Hz vibration in stainless steel a wavelength of 333 m can be excited in the metal and for niobium a wavelength of 193 m can be excited on the metal. The 18 Hz source cannot excite harmonics on the metals since the wavelength exceeds the dimension of the entire cryomodule which is 13 m long. The speed of sound of saturated helium vapor at 2 K is 226 m/s, the wavelength is 12.5 m for an 18 Hz source. In a pipe with both ends open, the length is given by $L = n\lambda/2$ where n is the harmonic order, for $n=1$ the length is 6.25 m. For a pipe with one end open, the length is $L = n\lambda/4$, for $n=1$ the length is 3.125 m. The length of a pipe to create harmonics with these lengths are within the dimensions of the cryomodule. Thus the harmonics observed in the frequency have a high probability of coming from the acoustic waves in helium.

4.2.3 Stochastic Microphonics

The control of the system can be impacted whether the system is stochastic or deterministic. A deterministic source is easier to control than a stochastic which can be challenging to control. White Gaussian noise which is found in the microphonics signal appears stochastic. In a system which has pure white Gaussian noise the system outputs are not correlated. This means that each output is independent of each other and random. A system can be classified as stochastic based on its distribution and with autocorrelation. The autocorrelation (R_{xx}) of a signal can be interpreted as a measure of the similarity of the signal with its time-shifted version of itself, this is given by

$$R_{xx}(\tau) = \int_{-\infty}^{\infty} x(t)x(t - \tau)dt \quad (4.1)$$

where $x(t)$ is the signal and τ is the delay. The autocorrelation of four different simulated signals are shown in Fig. 4.14. The results of an autocorrelation for a white Gaussian noise shown in 4.14 (a) is a Dirac delta function demonstrating that there is no correlation with the signal past a time lag of 0. For a deterministic signal, such as a sine waveform with white noise added,

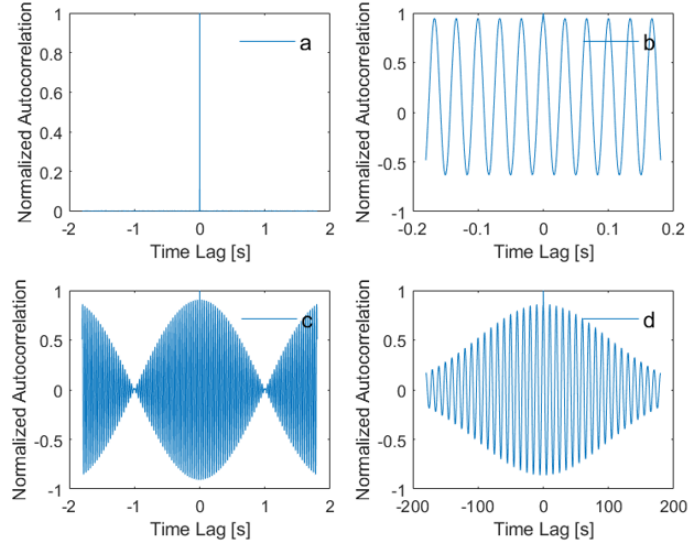


Figure 4.14: Autocorrelation for simulated signals. (a) White Gaussian noise. (b) Sinewave with white Gaussian noise added. (c) Signal with two different sinusoids (beats). (d) Sinusoidal Gaussian.

the autocorrelation shows that the signal is correlated with itself at a certain periods as shown in Fig. 4.14 (b). The autocorrelation for a signal with two tones is shown in Fig 4.14 (c) which shows a modulation the correlation function. Lastly, the autocorrelation for a for a gaussian pulse given by $1/\sqrt{2\pi\sigma}exp(-0.5(t^2/\sigma^2))sin(\omega t)$ is shown in Fig. 4.14 (d). The results from these simulated signals will be used to classify the signal from the frequency detuning of the cavities.

The microphonics noise coupling to the cavities can be stochastic. Such behavior was observed in a 30 min capture for CM 14 after cooldown. The detuning times series for cavities 1, 2, and 3 display narrow pulses and then one large pulse on all cavities as shown in Fig. 4.8(a). The narrow pulses don't have a periodicity and the amplitude varies by the cavity number. The pressure variation in the liquid helium has a peak-to-peak of 70 mTorr. There is no correlation between the narrow pulses and the liquid helium pressure in the helium vessel. The large frequency detuning observed in the time-series plot is due to a 15 Hz vibration which occurs simultaneously for all cavities. This 15 Hz vibration turns on for 15 minutes and then disappears as shown in the spectrogram for cavity 1 in Fig. 4.15(a). The inlet pressure for the 2.2 and 5 K helium lines show no correlation with the 15 Hz line turning on or off, the plot is shown in Fig. 4.15. The liquid levels and the flow rate

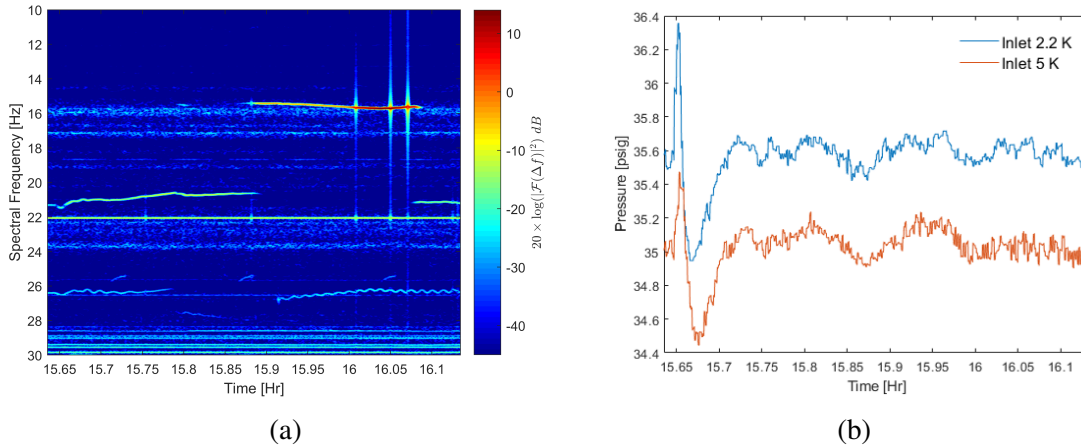


Figure 4.15: Data for cryomodule 15. (a) Cavity 1 detuning spectrogram with a 15 Hz narrowband vibration that turns on randomly. (b) Cavity 8 detuning spectrogram with a 15 Hz narrowband vibration.

parameters don't display any correlation with the behavior of the 15 Hz source. This 15 Hz vibration causes large frequency detuning in all cavities but is short-lived. The 15 Hz source appears in other cryomodules but this level of detuning was not observed. Thus, no cryogenic instabilities were correlated with the 15 Hz source. A bandpass filter was used to study the autocorrelation of cavity

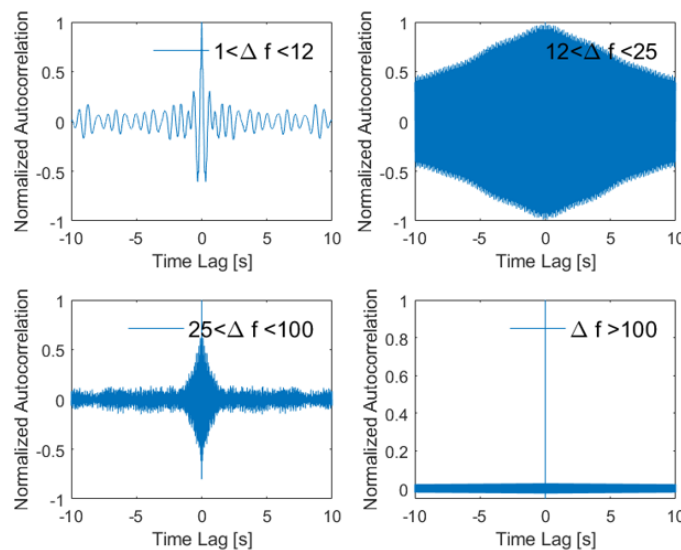


Figure 4.16: Autocorrelation of frequency detuning for CM 14 cavity 1 with different bandpass filter bandwidth.(a) Bandwidth of 1 to 12 Hz, (b) 12 to 25 Hz, (c) 25 to 100 Hz, and (d) above 100 Hz.

1 from the results shown above. The signal was divided into four different bandwidths one at low

frequency and the last at high frequency. The results of the autocorrelation are shown in Fig. 4.16. The bandpass for the signal below 12 Hz and for signal above 100 Hz are quasi-stochastic since the similarity is small after a lag of 0 but not zero. For vibrations above between 12 Hz and 100 Hz the frequency detuning is deterministic for short periods of time but become random after a long time.

In this same frequency range, a similar stochastic vibration was observed in CM 8. There are two frequencies, one at 15.5 Hz and the other at 20.5 Hz. Both of these frequencies are not stable and turn on and off randomly. There was no correlation with the inlet helium pressure amplitude modulation shown in Fig. 4.17(b). Additionally, the helium flow rates and helium levels did not correlate with the vibrational sources. The autocorrelation at different bandpass bandwidths is

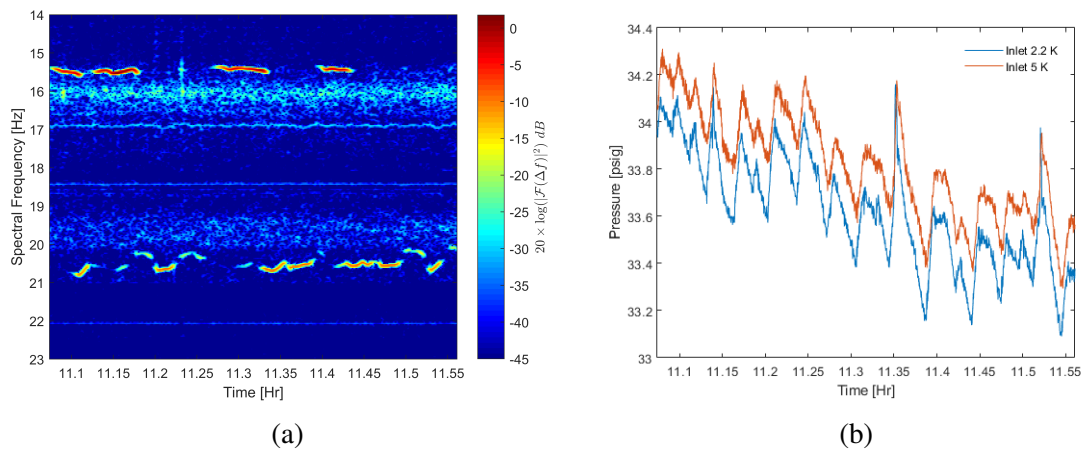


Figure 4.17: Data for cryomodule 8. (a) Spectrogram of cavity 8, the 15.5 and 20.5 Hz display stochastic behavior. (b) The inlet pressure for helium show a slow amplitude modulation.

shown in Fig. 4.18. The low and high frequency again show quasi-stochastic behavior. In the frequency range between 12 Hz and 100 Hz the autocorrelation shows a modulation which is attributed to two frequency very close together. A vibration of 29 and 29.5 Hz was observed in all cavities and all cryomodules but at different strength in each. These two vibration frequencies are close to each other giving rise to the modulation of the autocorrelation. The vibration can be attributed to the kinney vacuum pump and a mechanical mode of the cavity and power coupler. In this case, the frequency detuning was not as severe as in CM 14. In the next section, a summary of the detuning statistics will be discussed.

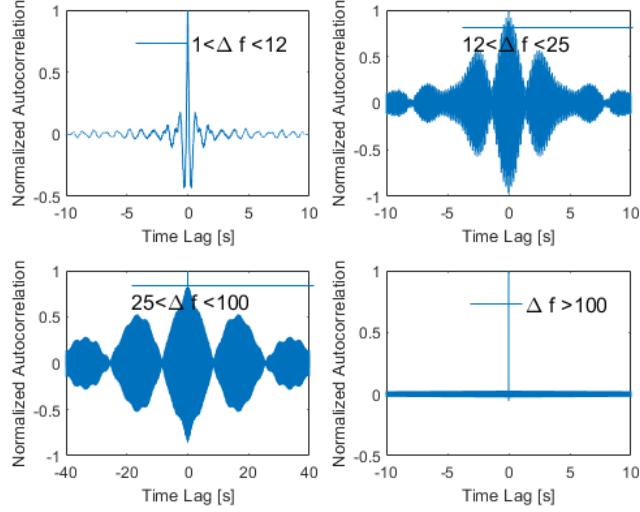


Figure 4.18: Autocorrelation of frequency detuning for CM 8 cavity 1 with different bandpass bandwidths.(a) Bandwidth of 1 to 12 Hz,(b) 12 to 25 Hz, (c) 25 to 100 Hz, and (d) above 100 Hz.

4.2.4 Frequency Detuning Statistics

The effects of the vibrations in the frequency detuning signal can also be observed in the frequency detuning distribution plots. If the distribution is Gaussian, the number of peak events past the 10 Hz limit can be calculated based on the standard deviation. A summary of the detuning of all the cavities in 12 cryomodules will be discussed in this section. This will be done by comparing the distribution of a simulated signal and the frequency detuning of the cavities.

A simulated sinusoidal signal with white Gaussian noise added gives a bimodal distribution as shown in Fig. 4.19 (a), (b), and (c). In a sine wave with Gaussian amplitude given by

$$\frac{1}{\sqrt{2\pi}\sigma} \exp(-0.5(t^2/\sigma^2)) \sin(\omega t) \quad (4.2)$$

the peak of the distribution is Gaussian but the side lobes are much larger (Fig. 4.19 (d)). The results from these distributions can be used to estimate the type of vibrational noise affecting the cavities. A non-Gaussian distribution has a vibration that can be compensated for with passive mitigation techniques or with resonance control. The goal of the resonance control algorithm is to reproduce a Gaussian distribution with a small standard deviation so that peak frequency detuning events become rare during operation.

The frequency detuning measurements for all cavities yield quasi-Gaussian distributions. The 4

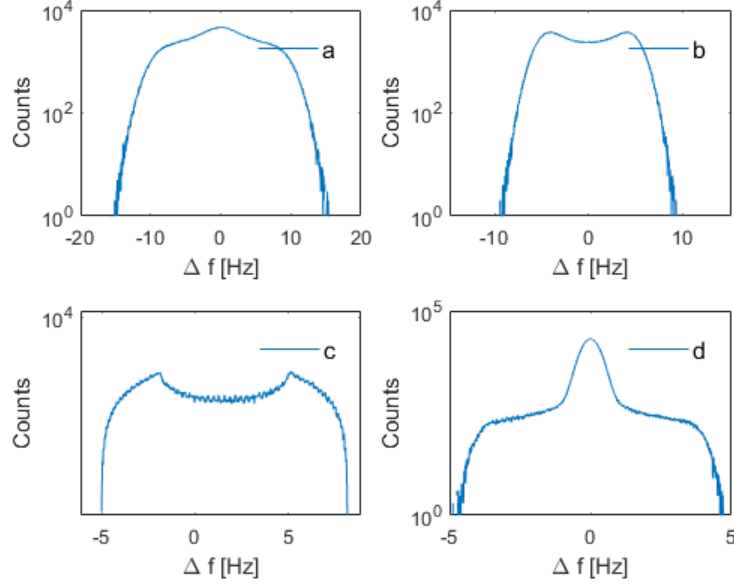


Figure 4.19: Simulated distributions for different signals: (a) two tones at 29 Hz and 29.5 Hz; (b) two tones at 20 and 30 Hz; (c) sine wave at 20 Hz; and (d) Gaussian pulse with sine wave at 30 Hz.

hour histogram for the data from 4.7(b) is shown in Fig. 4.20 (a). The distributions of the frequency detuning have different widths and peak detuning. The RMS value can be related to the standard deviation $\delta f_{RMS}^2 = \langle \Delta f \rangle^2 + \sigma^2$. The RMS detuning is the same as the standard deviation since the average detuning is zero after a high pass filter removes the DC offset. The RMS detuning for CM 15 cavities spans from 1.3 Hz to 3.2 Hz (the 3.2 Hz RMS value belongs to cavity 4). The variation of the RMS detuning is due to the different vibrations that couple to the cavity. Each of the contributions is shown in Fig. 4.20 (b) and is calculated by

$$\Delta f_{RMS}(f) = \sqrt{\sum |\mathcal{F}[\Delta f(t)]_i|^2} \quad (4.3)$$

where $\Delta f_{RMS}(f)$ is the integrated frequency detuning spectrum up to the index of Fourier components $\mathcal{F}[\Delta f(t)]_i$. Each contribution from the vibration is given by an increment in the integrated RMS detuning. For this data 61 % to 85 % of the RMS detuning was due to vibrations sources below 100 Hz.

The deviations from Gaussian distribution for cavities 1 and 4 are due to the tail ends as shown in Fig. 4.21. The deviation from the Gaussian distribution in cavity 4 is due to the 41 Hz vibration. This can be seen from the time-series data and the spectrogram shown earlier. The reason for this

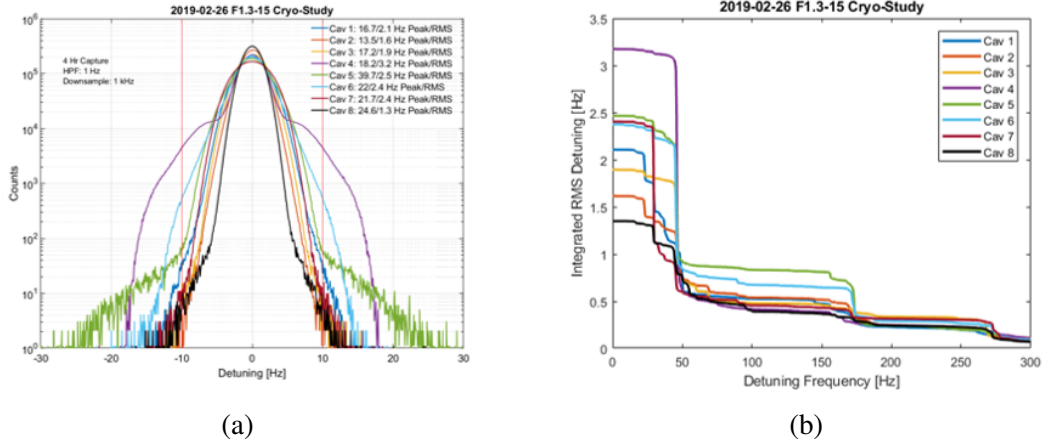


Figure 4.20: Results for CM 15: (a) Histogram of 8 cavities, the red lines indicate the specification of the peak detuning. (b) RMS detuning for all 8 cavities.

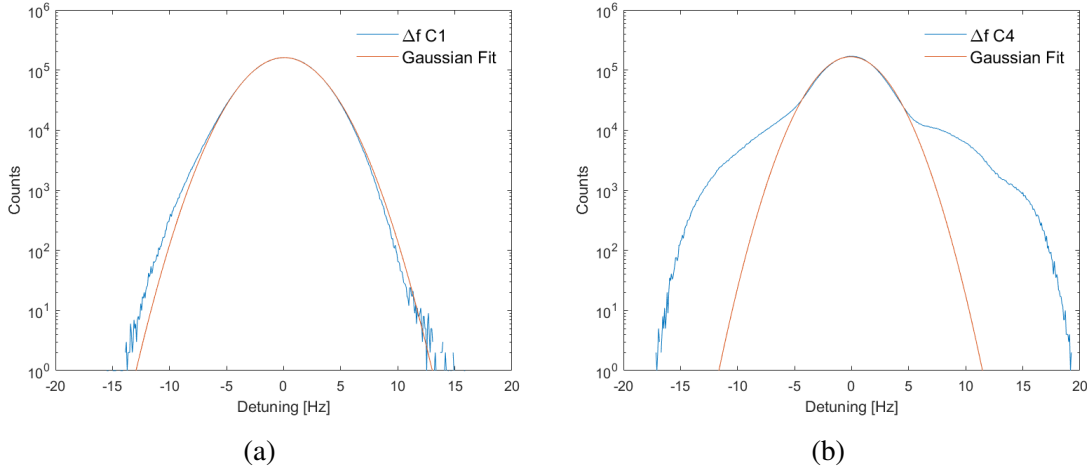


Figure 4.21: (a) Histogram of cavity 1 in CM 15 with Gaussian fit. (b) Histogram of cavity 4 in CM 15 with Gaussian Fit. Note that this distribution deviated from the Gaussian fit.

change is due to narrowband monotonic frequency waveforms. The results for Fig. 4.22 is due to a sinusoidal Gaussian pulse as shown in Fig. 4.19 (d) and can also be seen from the time-series detuning data. The peak detuning relation to the RMS detuning for CM 15 during this capture can range from $\Delta f_{peak} = 7\sigma$ to $\Delta f_{peak} = 19\sigma$. If the distribution is purely Gaussian the expected fraction inside the range $\mu \pm x\sigma$ is given by

$$\text{erf}(x/\sqrt{2}) = \frac{2}{\sqrt{\pi}} \int_0^{x/\sqrt{2}} e^{-t^2} dt \quad (4.4)$$

where x is the number of standard deviations away from the mean and $\text{erf}(x)$ is the error function. If

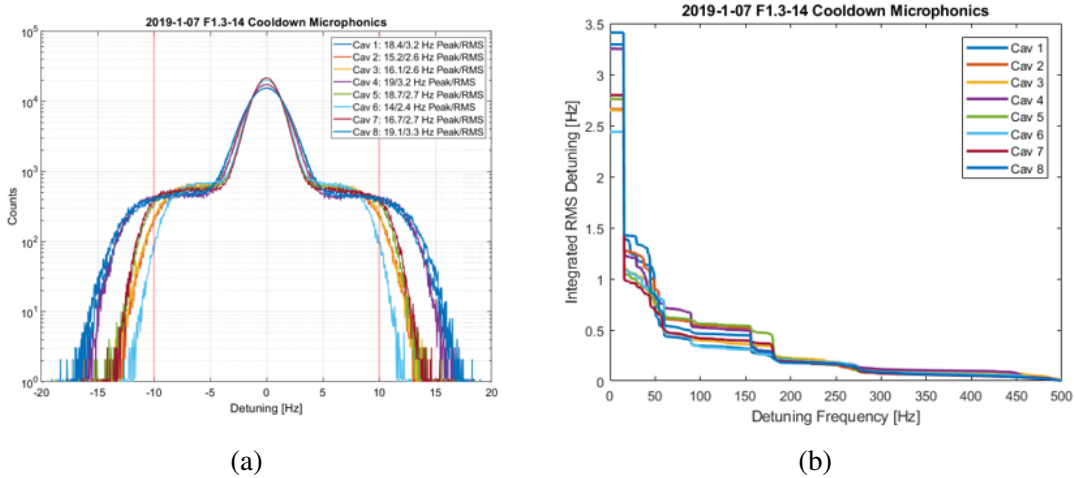


Figure 4.22: Results for CM 14: (a) Histogram of 8 cavities, the red lines indicate the specification of the peak detuning. (b) RMS detuning for all 8 cavities, main contribution is from 15 Hz.

the peak detuning is $\Delta_{peak} = 6\sigma$ the probability of this event occurring would be one in 5.06×10^8 . At a sampling of 1 kHz and an RMS detuning of 1.67 Hz, a peak detuning greater than 10 Hz would occur every 6 days. A smaller RMS detuning value leads to less likelihood of a 10 Hz peak detuning.

The analysis of the RMS detuning for all cavities in 12 cryomodules shows that on average 70 % of the vibration sources coupling to the cavity are below 100 Hz. The rest comes from vibration frequencies above 100 Hz. The results for all cavities and all 12 cryomodules is shown in Figures 4.23 and 4.24. The data was processed with a 1 Hz high pass filter and sampling frequency of 1 kHz. The length of the data captured is 30 min but for CM 15 it is 4 hours and for CM 12 it is 2 hours. The results are divided into three sections: one is vibration frequencies below 20 Hz, second is vibration frequencies between 20 Hz and 100 Hz, and lastly vibration frequencies above 100 Hz. The plots give the fraction of contribution to the RMS detuning for each of the three sections. One outlier from the data occurred in cavity CM18, the main contribution from this source was due to a 241 Hz vibration. This vibration source was due to an issue with the piezo amplifier which was later resolved.

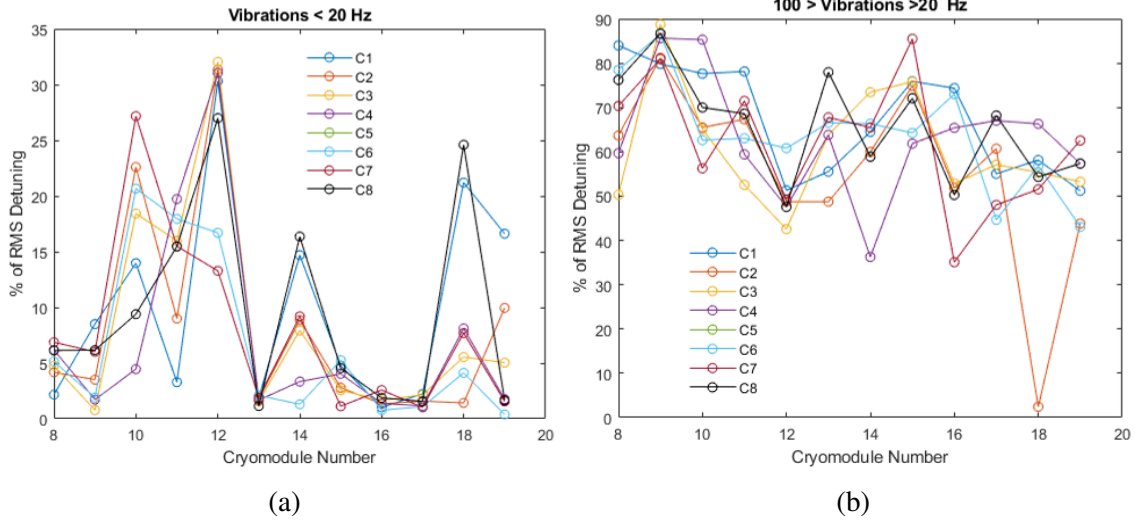


Figure 4.23: (a) Contribution to the RMS detuning from vibrations less than 20 Hz. (b) Contributions to the RMS detuning from vibrations between 20 and 100 Hz.

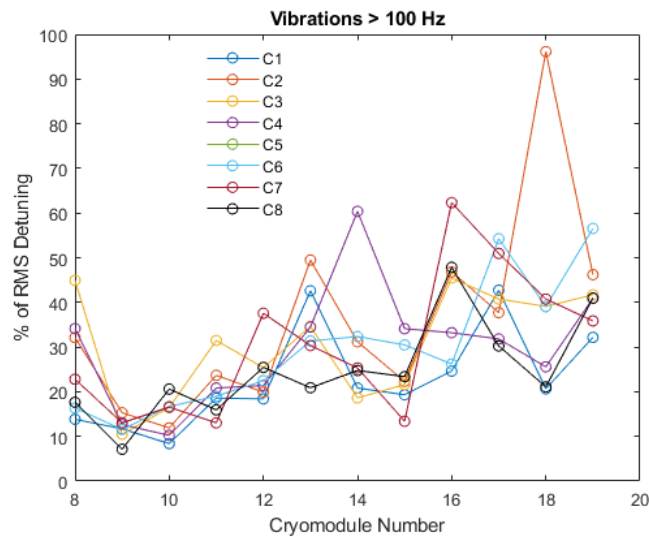


Figure 4.24: Contributions to the RMS detuning from vibrations above 100 Hz but less than 500 Hz.

4.3 Summary of Chapter

In low beam intensity linacs, microphonics can couple to the cavity leading to detuning and decreasing the accelerating gradient as well as resulting in an RF trip. The effects of microphonics on cavity frequency detuning were studied for the LCLS-II project cryomodules tested at FNAL. Passive mitigation techniques were implemented which included modifying the cryogenic valve

plumbing to reduce the effect of TAOs. Modifications were implemented to the cavity string structure to damp the vibrational effects.

Despite these passive mitigation techniques the cavities still experience frequency detuning caused by residual microphonics. An analysis of the frequency detuning of 96 cavities along with multiple cryogenic parameters was made for 12 cryomodules. The results discussed in this chapter demonstrate that cryogenic parameters such as liquid helium flow rate and liquid helium pressure variation affect the frequency detuning. Helium pressure variation is the main detuning contribution for vibrations below 10 Hz. On average, 70 % of vibrations contributing to detuning are below 100 Hz. In this range, it was shown that these vibrations are controllable since they are deterministic based on the autocorrelation of the signal. Above 100 Hz, the vibrations are stochastic and require a non-linear controller. The results from this analysis will be used as the basis for the simulation of microphonics noise in real-time. The resonance control algorithm implementation developed for SRF cavities in Chapter 6 will then mainly focus on targeting vibration frequencies below 100 Hz. The majority of vibration frequencies below 100 Hz are found to be linear and relatively stable in time.

CHAPTER 5

COMBINED SLOW AND FAST TUNER

The SRF cavity tuner has three roles. It is needed for active microphonics compensation. It is also used for moving the cavities to the nominal frequency after cool down to 2 K. Lastly, it is used for protecting the cavity during pressure tests. This chapter will present the first results of the tuner operation for the 650 MHz elliptical cavity at room temperature and when cooled down to 2 K. There are two components to the tuner, one is the slow and coarse component consisting of a stepper motor. The slow and coarse component is used to compensate for the frequency shift of the cavity due to length contraction during cooldown. The fast and fine tuner component consists of two piezo actuator capsules. The piezoelectric actuators are used to compensate for the effects of microphonics as well as LFD. For active microphonics compensation, the tuner maintains the frequency of the cavity at the nominal accelerator operating frequency. This will ensure that the gradient and phase of the cavity is kept at nominal value. Minimizing the detuning of the cavity with a fast tuner will reduce the overall RF power needed to compensate for the detuning as well as reducing the number of RF trips.

The properties and operation of the lead zirconate (PZT) actuator for resonance control of a CW linac are well studied for small piezo voltage operation and the results are found in the scientific literature [74]. A high voltage operation of the piezo actuator is needed for resonance control of a pulsed linac due to the larger frequency shift caused by LFD. The frequency shift in a pulsed linac can range from 500 Hz to 1 kHz. This chapter will present the results of the studies of a PZT actuator operated at high voltage. High dielectric heating was observed in the PZT actuators in this high voltage regime. The large dielectric heating produced large temperature fluctuations on the ceramic body. To compensate for this large heating, a novel piezo design was developed which helped reduced heating. Additionally, a piezoelectric material made from lithium niobate ($LiNbO_3$) was tested for the first time for resonance control of an SRF cavity.

5.1 Frequency Control of SRF Cavities

The RF accelerating field and its phase in the cavity are dependent on resonant frequency detuning. As the detuning increases, the accelerating gradient of the cavity decreases. Three techniques were developed to keep the cavity at resonance thus maintaining the same accelerating gradient. The first is related to the acceleration of high-intensity beams which requires the RF power for the beam loading compensation and to increase the beam power. Higher RF power decreases Q_L and increases the bandwidth of the cavity as well as the accelerating gradient of the cavity. The increase in bandwidth allows the cavity to be operated in presence of microphonics, LFD, and other external noise. In low-intensity linacs, this increase in RF power is costly and is also limited by the RF power supply. The bandwidth of the cavity is limited by the amount of power the RF source can deliver. If the microphonics or LFD detuning exceeds this bandwidth set by the power supply limit, then the cavity will trip due to the amplitude or phase of the resonance being out of tolerance. The latter can result in operation downtime in the linac.

A second method to reduce RF power and maintain the accelerating gradient is to use a variable reactance circuit. The detuning of the cavity caused by microphonics and LFD results in a change of the input reactance. The offset reactance at the cavity input can be matched with a fast reactive tuner. A promising method is to use ferroelectric ceramics that can vary capacitance over a range of 10 ns rate and that can sustain large power dissipation as shown in [75]. The ferroelectric ceramic is used in the RF coupling element, with the varying capacitance the reactance of the input can be matched to that of the cavity. This technology is still in its infancy and more work needs to be done for them to be deployed in a linac.

The third, and most widely used method, is done by changing the geometry of the cavity with a mechanical deformation. The cavity frequency is changed by elastically compressing or stretching the cavity. The stretching and compression are done via a stepper motor for slow and coarse tuning. The fast reaction tuning is done with piezoelectric actuators. The majority of the SRF linacs such as SNS, Eu-XFEL, LCLS-II, and ESS employ a tuner system with piezoelectric actuators located inside a cryomodule at insulating vacuum and at cryogenic temperatures. The successful operation

of these tuning systems contributed to the use of similar methods for the PIP-II cavities which will use a double lever tuner for the elliptical cavities.

5.1.1 Double Lever Arm Tuner for 650 MHz Elliptical Cavities

The 650 MHz elliptical cavity is equipped with a double lever tuner which consists of two different lever arms. One of the arms has a stepper motor for slow and coarse tuning. The other arm uses a piezoelectric actuator for fast and fine frequency tuning. There are two different lever tuner arms to minimize the force on the motor but at the same time amplify the force that the motor applies to the cavity. The tuner is mounted on the cavity's helium vessel and located inside the insulating vacuum space of the cryomodule as shown in Fig. 5.1. The tuner consists of two lever arms of

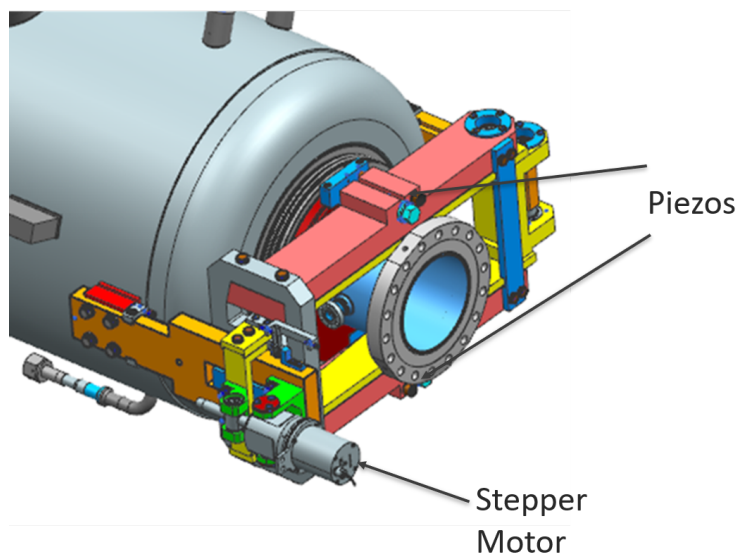


Figure 5.1: Jacketed 650 MHz cavity with double lever tuner mounted.

different lengths and pivot points. The slow and coarse component is driven by a stepper motor consisting of a planetary gearbox and a lead screw. The lead screw moves the motor arm (yellow in Fig. 5.2) pivoting about bearing 1 and moves bearing 2 resulting in movement of the main lever arm (pink in Fig. 5.2). The piezo actuators are located in the main lever arm to contact the cavity to deform it. A voltage is applied to the piezo actuator to elongate it and thus compress the cavity

which changes the frequency. The schematic model of the double lever arm tuner for the 650 MHz cavity is shown in Fig. 5.2.

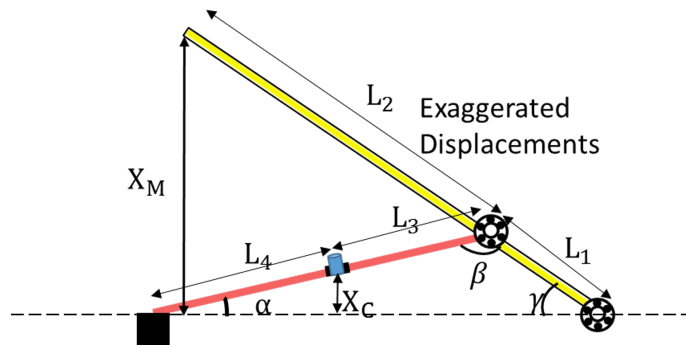


Figure 5.2: Schematic of the 650 MHz cavity double lever tuner. The lengths are for the different pivoting points.

The tuner's motor arm displacement, X_M , to the main arm displacement making contact with the cavity, X_C , can be calculated from the geometry of the tuner. The length of the pivot points are obtained from the Fig. 5.2. Using Fig. 5.2 the following equations are obtained from the geometry:

$$\sin(\gamma) = \frac{X_M}{L_1 + L_2}$$

$$\frac{L_3 + L_4}{\sin(\gamma)} = \frac{L_1}{\sin(\alpha)}$$

$$X_C = L_4 \sin(\alpha)$$

The ratio of the displacement on the motor arm (X_m) to the displacement of the cavity (X_C) is then

$$\frac{X_M}{X_C} = \left(\frac{L_3 + L_4}{L_1} \right) \left(\frac{L_1 + L_2}{L_4} \right) = 18.07 \quad (5.1)$$

A displacement on the motor arm will be 18 times longer than the displacement on the cavity. The displacement ratio will change when a load such as a cavity with non-negligible stiffness is placed at the point of contact. The ratio of the force applied at the tuner lead screw to the cavity contact is obtained by considering the torque of the arms in equilibrium. The ratio of the force on the cavity (F_C) to the force on the tuner arm (F_M) is found to be

$$\frac{F_C}{F_M} = \left(\frac{L_3 + L_4}{L_1} \right) \left(\frac{L_1 + L_2}{L_4} \right) = 18.07 \quad (5.2)$$

These two formulas give the mechanical advantage of the tuner. Large displacement on the lever arm gives small displacement on the cavity contact point. This also means that a small force at the tuner lead screw is amplified 18 times at the cavity contact point.

For the PIP-II elliptical cavities, a coarse tuning range of 200 kHz is required after cool down to bring the cavity frequency to 650 MHz. Using this frequency shift of 200 kHz, equations (5.1) and (5.2), the cavity stiffness of 4.9 kN/mm, and the tuning sensitivity of cavity the force on the motor and piezos can be calculated. The force on the motor is $F_M = 179 \text{ N}$ and for all the piezos at this point $F_{piezo} = 1.85 \text{ kN}$. Each piezo capsule then receives half the force, resulting in a force of 927 N since there are two capsules in parallel. Each piezo has an internal preload of 800 N and each piezo will experience 33.7 N when all of them are operated at 100 V. The total force on a single piezo capsule is then 1.7 kN, which is less than half of the blocking force (maximum force provided by the piezo, 4 kN). The coarse tuning for the planned FRIB cavity is the same as the PIP-II cavity. The only difference is the cavity stiffness which is half of the PIP-II cavities.

5.1.2 Tuner Stiffness of 650 MHz Cavity Tuner

The cavities experience deformations from liquid helium pressure fluctuation, LFD, and microphonics. To mitigate these deformations stiffening rings are used. In addition to stiffening rings, a stiffer tuner will also reduce the effects of LFD and liquid helium pressure fluctuations according to simulations [76]. The stiffness of the tuner for the 650 MHz cavity was measured for the first time. The tuner stiffness is made by applying a force to the tuner arms and measuring their displacement due to the force. The measurements of the prototype tuner, given in [77], yielded a tuner stiffness of 20 kN/mm. These measurements were done with a mock cavity, with this tuner stiffness the effects of the Lorentz force detuning would be 650 Hz for the LB 650 MHz cavity. The deformations of the tuner in the arms were measured and also the effects on the mock cavity. These measurements motivated improvement the ANSYS model which resulted in a modified design of the tuner. The measurements which are shown next demonstrate an improved tuner stiffness of 40 kN/mm. With this tuner stiffness, the Lorentz force detuning at 16 MV/m is 490 Hz.



(a)



(b)

Figure 5.3: (a) Dial indicators on the tuner arms measure the displacement. (b) Load cell to record the forces on the tuner side.

The cavity stiffness and the tuner stiffness were calculated using a load cell which records the force and two dial indicator measuring the displacement of the two tuner lever arms. The setup of the system is shown in Fig. 5.3 where the load cell is placed in the position of the stepper motor. A force is applied to the tuner arm and load cell by using a screw held together by two spherical balls. As the screw is turned the screw expands onto the tuner arm and the motor tuner plate. The force on the cavity is 18 times greater than the one measured at the load cell as shown from the kinematic ratio in Eq. 5.2. Using this ratio the cavity stiffness was calculated at 12.8 kN/mm show in Fig.5.4 (a). Note that this also includes the stiffness of the split rings which are used to make contact with the piezos and tuner, a full description of the split rings is given in Ref. [78]. The tuner stiffness was calculated by using the cavity stiffness and using the displacement of the tuner arm. The tuner stiffness is given by

$$K_T = K_c \frac{\eta}{x_{arm} - \eta} \quad (5.3)$$

where η is the kinematic ratio of the lever arm without load which is 18. The arm displacement is x_{arm} . Thus using the results from Fig. 5.4(b) the tuner stiffness can be calculated to be 40 kN/mm. This value is in agreement with the ANSYS simulation result. This is the highest possible stiffness value that can be obtained from this design without having to modify the tuner or the helium vessel as discussed in Ref. [79].

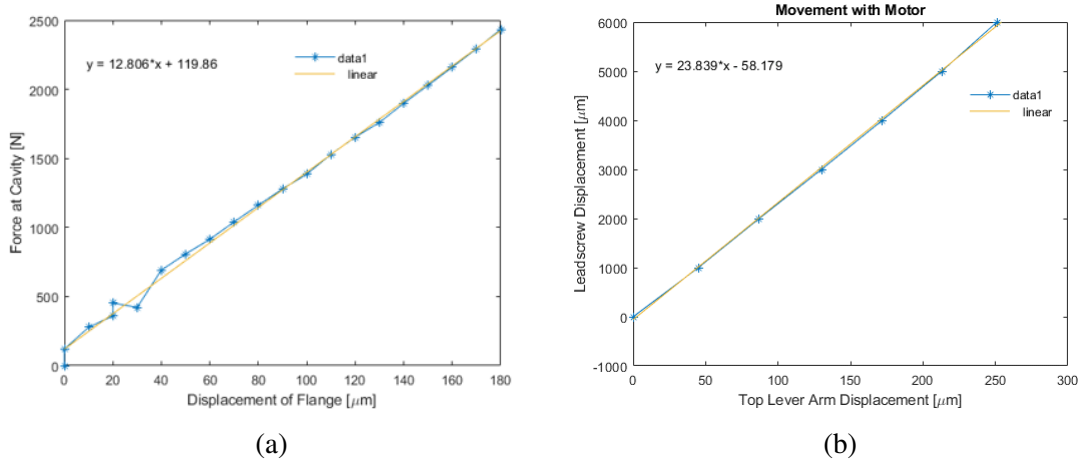


Figure 5.4: (a) Force on the 650 MHz cavity with respect to the deformation. (b) Leadscrew displacement with respect to the displacement of the tuner arm.

5.1.3 Slow Coarse Tuner

The slow coarse component of the lever arm tuner consists of a Phytron stepper motor [80]. The Phytron stepper motor has been tested in ultra-high vacuum and at cryogenic temperature in the cryomodule environment. Accelerated lifetime tests done at Fermilab demonstrate that this stepper motor should not fail after prolonged use such as the operation of 25 years which is the lifetime of a typical Linac [80]. The cavity in the cryomodule with beam and high power is expected to produce field emissions and other radiation which can be detrimental to the stepper motor. The results of an irradiation hardness test with a dose level of $5 \cdot 10^8$ Rad (expected from LCLS-II operation during the lifetime of linac) demonstrate that the stepper motor should survive under these conditions since no performance degradation was observed [74]. Thus, the Phytron stepper motor is expected to sustain operation for the lifetime of the linac for PIP-II and FRIB upgrade.

The stepper motor consists of a threaded rod that drives a nut attached to the motor arm. To complete one whole turn on the spindle the motor moves 10 ksteps. One whole turn on the spindle is equal to a 1 mm linear translation of the motor arm. The stepper motor can deliver up to 1.3 kN of force, in the lever arm tuner this can be amplified as shown in Eq. 5.2. The tuner was tested on the 650 MHz $\beta_G = 0.9$ helium vessel dressed cavity shown in Fig. 5.5. The cavity-tuner system was placed in a cryostat at the Muon Detector Building (MDB) in Fermilab where the tests were carried

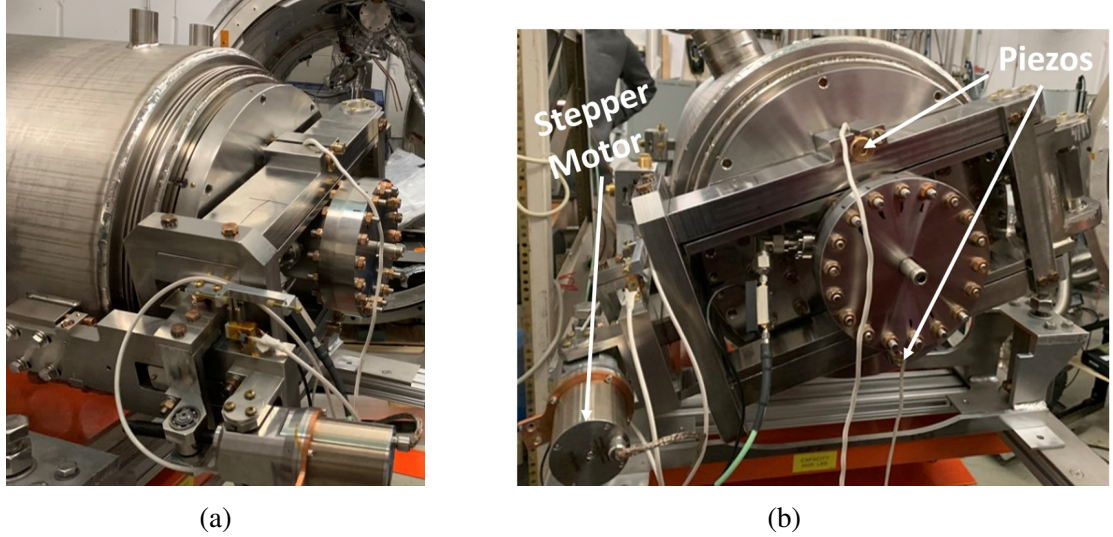


Figure 5.5: (a) Lever tuner attached to the 650 MHz PIP-II cavity. The motor is shown which is responsible for slow and coarse tuning. (b) The longitudinal view of the tuner, this shows the two piezos which are located in the tuner arm.

out. Once the cavity is cooled to 2 K the frequency will not be exactly at 650 MHz. The value of the frequency is set up after the field-flatness inelastic tuning so that it is slightly higher than the 650 MHz value for the tuner to be engaged with the cavity since the tuner can only compress which lowers the frequency. The frequency of the cavity at 2 K before tuning was 650.06 MHz, a total of 100 ksteps were required to compress the cavity to 650 MHz which is shown in Fig. 5.6. An additional 100 ksteps were implemented to check the range of the tuner and verify that no limit switches are tripped during the movement. The hysteresis of the stepper motor was tested by first operating it in small step increments and then in large step increments as shown in Fig. 5.7. In the short-range hysteresis with increments of 200 steps the difference between the compression and relaxation sweep is 30 Hz. The sensitivity of the tuner in this range is .58 Hz/step. At the long-range with a span of 100 ksteps the sensitivity is 0.57 Hz/step and the difference between the compression and relaxation movement is 500 Hz. These values demonstrate that the stepper motor can tune the cavity to 650 MHz and has a compression large range. The same tuner will be used for the 650 MHz $\beta_G = 0.61$ and $\beta_G = 0.92$ which have a lower cavity stiffness of 4 kN/mm. It is expected that the tuner sensitivity will be much higher for these cavities due to the smaller cavity stiffness. The properties of the other elliptical cavities are shown in Table 5.1. The forces from

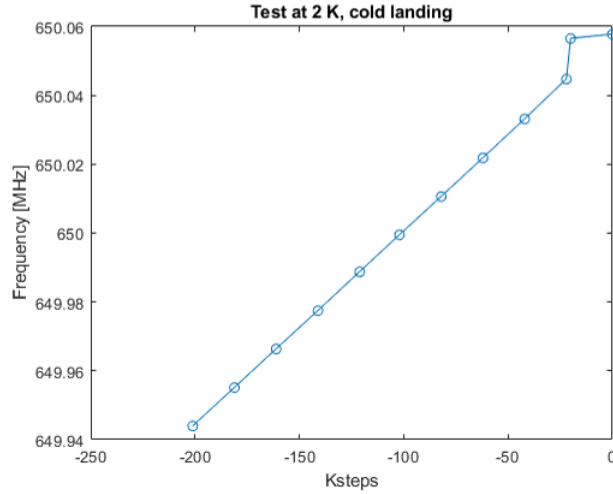


Figure 5.6: Frequency of the 650 MHz $\beta_G = 0.9$ cavity after cool down to 2 K.

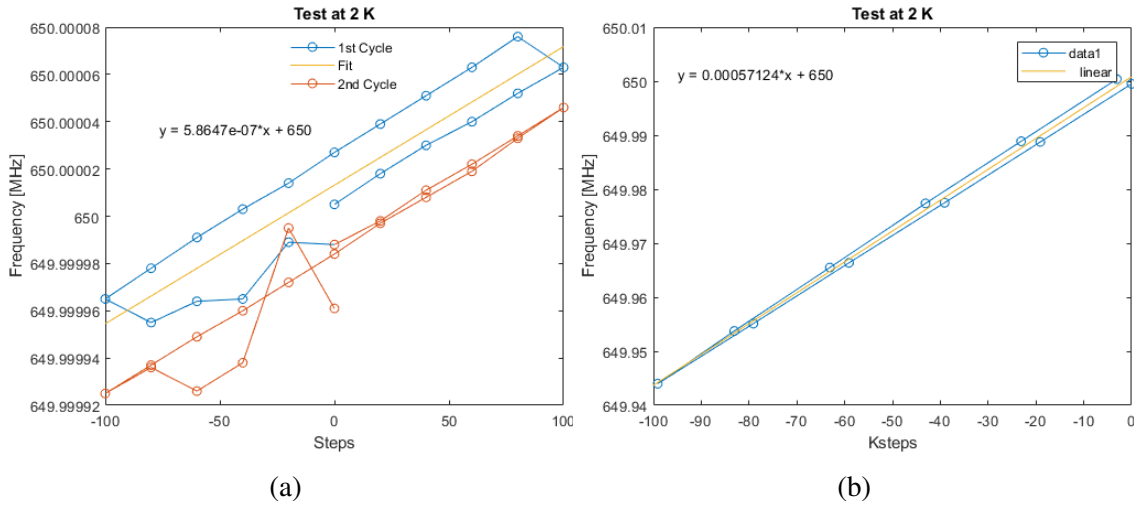


Figure 5.7: Results for 650 MHz $\beta_G = 0.90$ cavity. (a) Small step hysteresis (b) Long step hysteresis

the $\beta_G = 0.9$ cavity on the piezo are also expected to be much higher at 7 kN compared to the 2.5 kN of the other cavity models. If a large force is applied to the piezo, then there is a change for depolarization. The results after compressing the piezo by 7 kN on the piezo displacement will be shown in the next section.

Table 5.1: 650 MHz cavity tuning properties for different geometries.

| | $\beta = 0.61$ | $\beta = 0.9$ | $\beta = 0.92$ |
|-----------------------------|----------------|---------------|----------------|
| Cavity Stiffness [kN/mm] | 4 | 12.8 | 4 |
| Tuning Sensitivity [kHz/mm] | 240 | 180 | 160 |
| Force per Capsule [kN] | 1.67 | 7.11 | 2.5 |
| Piezo Sensitivity [Hz/V] | 64.8 | 36 | 43.2 |
| Full Range (20% RT) [kHz] | 12.8 | .72 | .864 |

5.1.4 Fast Fine Tuner

The piezoelectric actuators are used for fast and fine frequency tuning control of microphonics. The piezoelectric actuators are designed and fabricated by Physik Instrumente (PI) per FNAL specifications. The design consists of two $10 \times 10 \times 18\text{mm}^3$ PICMA lead zirconate titanate (PZT) ceramic glued together and encapsulated in a stainless steel cylindrical shell [81]. Fig. 5.8 shows the piezo encapsulation with the two PZT ceramics. The accelerated lifetime test demonstrates that the piezo can sustain 2×10^{10} pulses with a peak-to-peak amplitude of $V_{pp} = 2\text{ V}$ which equivalent to 25 years of operation of the LCLS-II linac. A low voltage is needed since the frequency detuning can range from 5 to 30 Hz as shown in Chapter 4. The irradiation hard test at 5×10^8 rad with

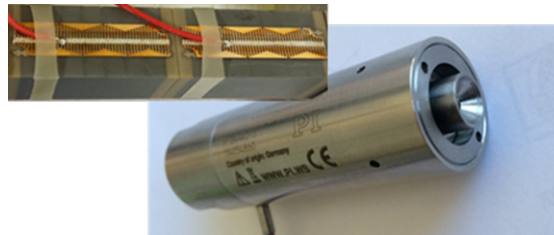


Figure 5.8: PI PICMA piezo capsule used in the 650 MHz tuner.

gamma radiation demonstrated a decrease of stroke displacement of 10 percent [74]. This decrease in displacement stroke will still be able to provide a frequency shift that can cancel microphonics. The effects of neutron irradiation in PZT piezo were studied by the CARE project in France showing

small degradation [82]. The reliability of this piezo model is well demonstrated and for this reason this piezo was selected for the 650 MHz tuners.

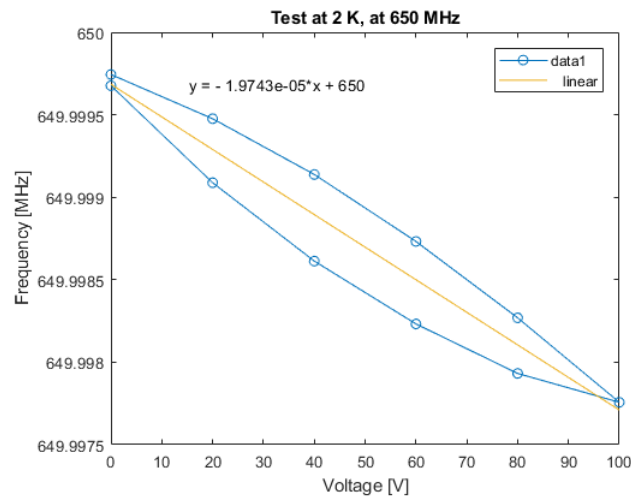


Figure 5.9: Hysteresis of two piezo capsules at 2 K on the 650 MHz cavity. The maximum voltage used was 100 V with 20 V increments. At 100 V the piezo can shift the frequency of the cavity by -1.97 kHz.

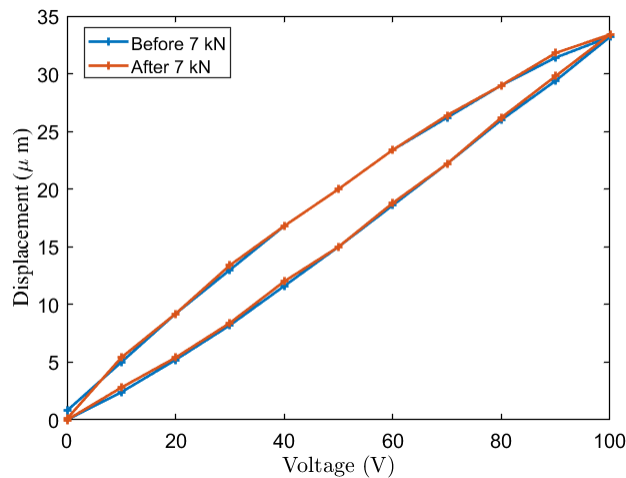


Figure 5.10: Hysteresis of a piezo capsule before and after the application of a 7 kN force was applied.

The piezo actuator can expand by $34 \mu\text{m}$ when 100 V is applied at room temperature. The tuner will consist of two piezo capsules which make contact with the cavity. The piezo displacement was studied on the 650 MHz cavity at 2 K with results shown in Fig. 5.9. At 100 V on both

piezo capsules, the cavity frequency shift was -1.97 kHz. If only a single piezo capsule was used at 100 V the frequency shift would only be half the value obtained. The $\beta_G = 0.9$ cavity has a stiffness of 12 kN/mm. It is expected that the load on the piezos will be 7 kN, which is high, and nearing the blocking force. A test was performed on the piezo displacement before and after a 7 kN force was applied to check for effects in depolarization. A 7 kN force is applied to the piezo and then released. Results shown in Fig. 5.10 demonstrate that this does not affect the piezo stroke displacement. Therefore, this piezo will be able to work under the stress of this higher stiffness cavity and not depolarize.

5.2 High Voltage Operation of Piezoelectric Actuators at Cryogenic Temperature

Linacs with a high accelerating gradient, operated in a pulsed mode, require a large operating piezoelectric voltage for resonance control. This is due to the LFD which causes a large frequency shift and is compensated with an active piezoelectric-tuning system. In CW operation the detuning of the cavity can range from 10 Hz to 100 Hz as was presented in Chapter 4. The detuning for a pulsed linac is on the order of -500 to 3 kHz [83], [84], and [85]. To compensate for this larger detuning the piezo must operate at higher voltage. In this high voltage range, the piezo is expected to warm up drastically due power dissipation in an insulated vacuum. Additionally, the piezo has a small thermal conductivity contributing to the heating. What prompted this investigation was the result of the piezo operation for the FLASH project which results in a piezo failure [86]. That

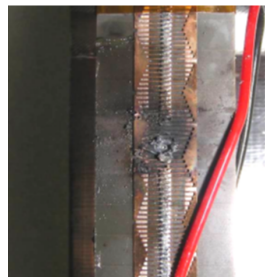


Figure 5.11: PZT piezo failure after bipolar operation at 77 K, the electrode is destroyed [86]

piezo was operated at high bipolar voltage (-100 to 100 V) operation at 77 K. This resulted in

burned electrodes as shown in Fig. 5.11. In this section, an overview of the theory of piezoelectric materials will be discussed as well as characterization of the dielectric properties (capacitance, dielectric losses), the piezoelectric actuator stroke from geophone measurements, and thermal properties such as heating. Results obtained in the temperature range of 20K to 300K will be presented and discussed.

5.2.1 Piezoelectric Effect

The piezoelectric effect (from the Greek “piezen”, meaning to press) was first discovered by Pierre and Jacques Curie in 1880. They discovered that electric charges arise when mechanical forces are applied to materials like tourmaline, quartz, topaz, cane sugar, and Rochelle salt. With appropriate electrodes covering the material an electric voltage can be measured which is related to the mechanical deformation. A year later Gabriel Lippmann deduced the inverse piezoelectric effect based on thermodynamics. He speculated that a non-symmetric crystal would deform when submitted to an electric field. This phenomenon is known as the inverse piezoelectric effect. The inverse piezoelectric effect was then confirmed by the Curie brothers. Since the time of their discovery, the piezoelectric effect has had numerous applications in a wide range of fields and industries. A particular application relevant to SRF cavity resonance control is the use of piezoelectric sensors and linear actuators which have displacements in the nm to μm range. The accuracy of displacement (increments in nm range), fast response time (on the order of μs), and no remnant magnetic field, all make piezoelectric actuators ideal for the application of resonance control in SRF cavities.

The piezoelectric effect is due to the occurrence of electric dipole moments in the material caused by an asymmetry of the atomic structure of the lattice as shown in Fig. 5.12. In total, there exist 32 groups of crystals that are based on crystallographic symmetry. This group is divided into two classes one which has center symmetry (11) and the other without (21) [87]. Of the 21 crystals with non-center symmetries 20 are piezoelectric. In this geometry, the positive ion is offset from the center. This gives the unit cell an overall charge thus forming a dipole moment. The

piezoelectric class can be further divided into two classes, one is the ferroelectric and the other the paraelectric. All ferroelectric materials exhibit the piezoelectric effect. A ferroelectric material exhibits a spontaneous polarization (two in opposite directions) which occurs below the Curie temperature T_c , this is known as the ferroelectric phase. The phase above the Curie temperature is known as the paraelectric phase where the asymmetry disappears and the piezoelectric effect is not observed or is significantly decreased. Below the Curie temperature, the polarization of the material can be changed with an electric field. The ferroelectric material also exhibits hysteresis in polarization and strain with the respect to the applied electric field.

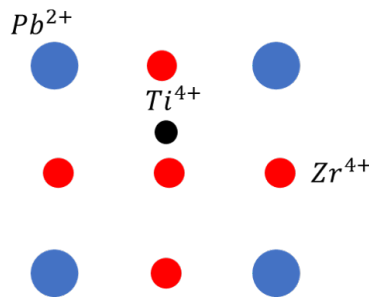


Figure 5.12: Cross-sectional view of a perovskite crystal unit of a ferroelectric material (PZT). Each of the circles denotes the ion and charge.

The origin of the spontaneous polarization in a ferroelectric material can be explained by the lattice vibrations of the material. The phase transition from paraelectric to ferroelectric can be modeled using the electric field from a dipole and interaction of the ions as springs, this discussion is based on the results from K. Uchino [87]. The complete behavior of the spontaneous polarization in a ferroelectric is described using the Ginzburg-Landau theory of phase transition. As the temperature decreases the phonon mode in which the center ion moves becomes dominant. Using Fig. 5.12 as a reference, the ion which is moving and thus causing the dipole moment is the center (color black) with charge positive charge. The two different polarizations (with opposite directions) arise from the dipole moment energy and elastic energy of the ion and surrounding lattice ions. Once the dipole is set up an electric field is generated by

$$E_{loc} = \left(\frac{\gamma}{3\epsilon_0} \right) P \quad (5.4)$$

where γ is known as the Lorentz factor and P is the polarization. The dipole moment is given by

$$\mu = \left(\frac{\alpha\gamma}{3\epsilon_0} \right) P \quad (5.5)$$

where α is the ionic polarizability of the ion. The dipole moment energy is given by $W_{dip} = -N\mu \cdot E_{loc}$, where N is the number of dipoles. The elastic energy is given by $W_{elas} = N \left(\frac{k}{2}x^2 + \frac{k'}{4}x^4 \right)$ where k and $k'(>0)$ are the spring constants modeling the interaction of the center ion with respect to neighboring ions and x is the displacement of the center ion. The displacement x is related to the polarization by $P = Nqx$. The total energy $W_{tot} = W_{dip} + W_{elas}$ is given by

$$W_{tot} = \left(\frac{k}{2Nq^2} - \frac{N\alpha\gamma^2}{9\epsilon_0^2} \right) P^2 + \left(\frac{k'}{4N^3q^4} \right) P^4 \quad (5.6)$$

The total energy with respect to polarization gives minimum energy. In the case of the paraelectric

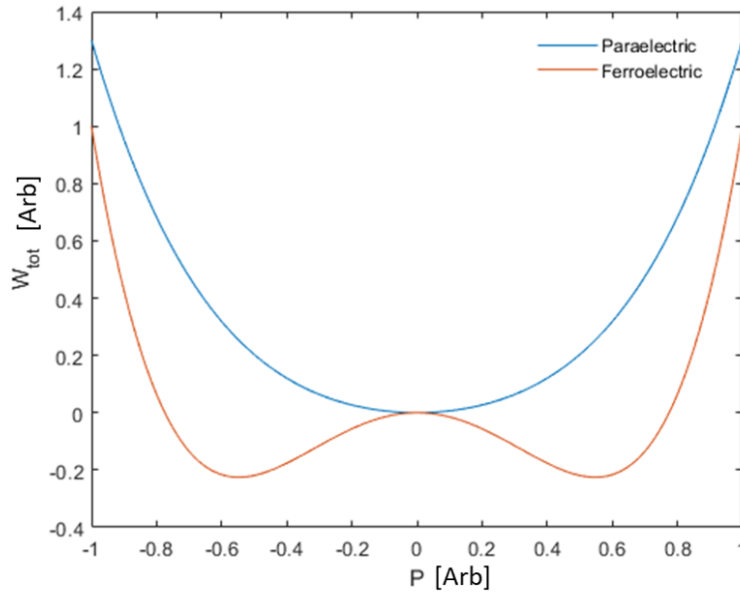


Figure 5.13: The total energy of the system with respect to the polarization is shown. In the paraelectric phase where the elastic energy term is dominant only one minimum is observed which corresponds to polarization of zero. The ferroelectric phase has two minimums with positive and negative polarization.

phase where the temperature is $T > T_c$ both the P^2 and P^4 constants are positive and only one minimum is observed at the polarization of 0. When the dipole moment energy becomes dominant

at a temperature $T < T_c$ the constant term of P^2 becomes negative causing two minimums that correspond to the two polarizations in a ferroelectric: one which is positive and the other negative. The behavior of this equation for the ferroelectric and paraelectric phase is shown in Fig 5.13.

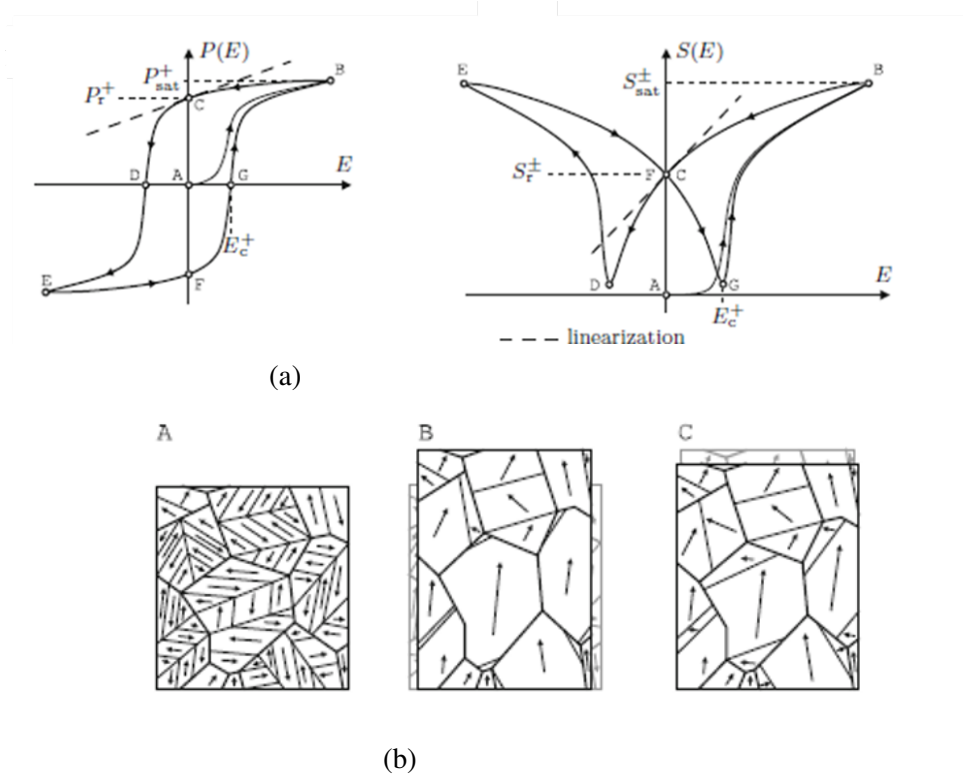


Figure 5.14: (a) The polarization (P) and strain curve (S) is shown with respect to the applied electric field. (b) The initial direction of the dipole domains is random and is change with a strong electric field. Note that each of the states is labeled by a letter and corresponds to the position on the polarization and strain curves [88].

So far, the microscopic behavior of the piezoelectric material has been discussed. At the macroscopic level, ferroelectric materials split the dipoles into groups known as Weiss domains to minimize depolarizing fields and mechanical stresses [88]. Each of these domains has a dipole and in the volume of the material they are oriented randomly. In most cases, a ferroelectric polarization process is required to imprint the macroscopic asymmetry by proper orientation of these domains. The process is shown in Fig. 5.14 where the strain and polarization plots with respect to the applied field are given. The initial domain structure of the material is given by A in Fig. 5.14, an electric field is applied until it reaches the critical value known as the coercive field which is several kV/mm.

The coercive field limit causes reorientation of the dipole moments. To keep the operating voltage within practical limits, the PZT actuators are constructed from thin layers of the PZT ceramic which can range from $20 \mu\text{m}$ to $100\mu\text{m}$. Each layer in the whole actuator is connected electrically in parallel. Thus, the total displacement is given by the sum of all the strain from the individual layers. During the polarization process the favorable orientation to the polarity field direction grows while those in the unfavorable direction shrink. The polarization process leaves a remnant polarization, this is shown in part C of the figure above. During the operation of the piezoelectric actuator it is important to not exceed the coercive field value since this will result in depolarization. As the temperature decreases the coercive field needed to depolarize the material increases, this is due to the dipole phonon mode becoming more dominant since the thermal phonons decrease. The properties presented in this section will be quantified in the next section where the figures of merit will be given.

5.2.2 Piezoelectric Actuator Figures of Merit

The piezoelectric material has several figures of merit which are the piezoelectric strain constant d_{im} where the indices are $i,j=1,2,\dots,6$, and $m=1, 2, 3$; piezoelectric voltage constant g_{mn} ; electromechanical coupling k_{mn} where $n= 1, 2, 3$; Curie Temperature T_c ; the blocking force F_B ; and the dissipation factor $\tan(\delta)$ and the capacitance C of the material. The axis of polarization are given by the indices m and n , they are depicted in Fig. 5.15. In this chapter, the dissipation factor and capacitance will be studied to model the heating of the actuator made of PZT operated at high voltage.

The interaction between the piezoelectric strain constant d_{mn} , voltage constant g_{mn} , and electromechanical coupling k_{mn} can be described by using the piezoelectric equations. The magnitude of the induced strain \mathbf{S} by an external electric field \mathbf{E} is given by [87]

$$S_i = s_{ij}^E T_j + d_{im} E_m \quad (5.7)$$

where the indices are $i,j=1,2,\dots,6$, $m=1,2,3$, and s_{ij} is the compliance tensor which is the inverse

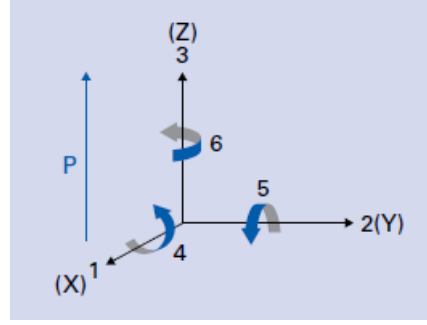


Figure 5.15: Orthogonal system to describe the properties of a polarized piezo ceramic. Axis 3 is the direction of polarization [81].

of Young's modulus and T_j is external stress. The stiffness of the material can be obtained from Young's modulus and will also affect the blocking force value. The blocking force is the maximum force generated by the material and is achieved when the displacement of the actuator is zero. The tensors and matrices of the equation above can be populated based on the geometry of the crystal each geometry and the values for tensors and matrices is discussed by Uchino [87]. The piezo actuators that are used in this thesis are rectangular prism and polarized in the z direction. The indices are then $m=n=3$, from now on this indices will be used to describe the direction of the piezo parameters. Note that the strain is not only affected by the external stress but also by the electric field on the material. The units for the piezoelectric strain constant d_{mi} can be given in charge per force (pC/N) or distance over voltage (pm/V). A large strain constant d is desired for a material that will be used in actuator applications. The converse effect where the piezoelectric material is used a sensor is described by using the electric displacement equation below:

$$D_m = d_{mi}T_i + \epsilon_{mk}^T E_k \quad (5.8)$$

where E_k is the electric field and T_i is the external stress on the material. The variable $k=1,2,3$ and the other indices are the same as before. In this equation stress also affects the electric displacement value. A large strain constant d_{im} is again desired to yield a good sensor. The strain constant d_{im} can be related to the piezoelectric voltage constant g_{mn} when the stress is $\mathbf{T}=0$ in Eq. 5.2.2 and $E_3=0$ in the polarization equation $P_3 = d_{33}T_3 + \epsilon_{33}E_3$, this yields $g_{33} = \frac{d_{33}}{\epsilon_{33}}$ where the indices indicate the direction of polarization in this case z as shown in Fig. 5.15. The units for the voltage

constant are Vm/N, this can be used to calculate the field based on the external stress without an electric field. Note that this equation is an approximation and can only be used at low fields and low stress.

The energy conversion from the electrical input energy to mechanical energy, stored energy, and losses play an important role in the operation of the piezo. The electromechanical coupling is used to calculate the ratio of stored mechanical energy to input electrical energy for an actuator or stored electrical energy to input mechanical energy for a sensor. The k_{33} parameter can be calculated using the piezoelectric constant d_{33} , the compliance s_{33} , and the permittivity ϵ_{33} leading to the result is given by [87]

$$k_{33}^2 = \frac{d_{33}^2}{\epsilon_{33}s_{33}} \quad (5.9)$$

note that this is in the direction of polarization z in the longitudinal direction of piezo. Not all the mechanical stored energy is used due to mechanical load, the energy transmission coefficient is defined by $\lambda_{max} = (\text{Output mechanical energy})/(\text{Input electrical energy})$ or $\lambda_{max} = (\text{Output electrical energy})/(\text{Input mechanical energy})$. The energy transmission coefficient can be related to the electromechanical coupling by

$$\lambda_{max} = \left[\frac{1}{k_{33}} - \sqrt{\frac{1}{k_{33}^2} - 1} \right]^2 \quad (5.10)$$

For small k_{33} , $\lambda_{max} \approx \frac{k_{33}^2}{4}$ and for large k_{33} , $\lambda_{max} \approx \frac{k_{33}^2}{2}$. The energy transmission coefficient is limited by the value of the k_{33} . The overall efficiency of the system is defined by $\eta = (\text{Output mechanical energy})/(\text{Consumed electrical energy})$ for an actuator. The consumed electrical energy takes into account the energy loss due to heating. The loss due to heating is given by the equation

$$\dot{Q}_G = \frac{\pi}{4}(C \tan \delta) f V_{pp}^2 \quad (5.11)$$

where C is the capacitance of the piezo; $\tan \delta$ is the dissipation factor; f is the driving frequency of the piezo; and V_{pp} is the peak-to-peak voltage drive of the piezo. Equation 5.11 only holds for a low voltage less than $V_{pp} \leq 10$ V for piezoelectric material made of PZT.

The piezoelectric figures of merit can be used to find an ideal material candidate for resonance control of SRF cavities. The blocking force F_B , the piezoelectric strain constant d_{33} , and the voltage constant g_{33} should all be large. A comparison of the piezoelectric figures of merit for different materials is shown in Table 5.2. These are the 4 main materials in production for piezoelectric actuators, note that the PZT material has the largest strain constant d_{33} which results in large displacement with respect to the applied voltage. The downside to this large stroke displacement is that the relative permittivity is large, this factor contributes to the heating of the piezo since the capacitance and dissipation factor depend on the permittivity. In cavities with a small bandwidth and large LFD a large voltage is needed for resonance control. Larger voltage can cause excessive heating on the ceramic. The heating properties of the PZT piezo actuators are studied in the next section.

Table 5.2: Figures of merit for different piezoelectric materials[87], [89].

| Parameter | Quartz | $BaTiO_3$ | PZT 5H | $LiNbO_3$ |
|----------------------------|--------|-----------|--------|-----------|
| d_{33} [pC/N] | 2.3 | 190 | 593 | .06 |
| g_{33} [10^{-3} Vm/N] | 57.8 | 12.6 | 19.7 | .23 |
| k_{33} | 0.09 | 0.38 | 0.50 | .17 |
| ϵ_{33}/ϵ_0 | 5 | 1700 | 3400 | 29 |
| T_c [C] | | 120 | 194 | 1150 |

5.2.3 Experimental Setup

The majority of the SRF linacs such as SNS, Eu-XFEL, LCLS-II, and ESS employ a tuner system with piezoelectric actuators located inside a cryomodule (CM) at insulating vacuum. There are two reasons why this configuration is chosen, one is to maximize the stroke displacement of the piezo by being closer to the cavity. Additionally, a humidity-free environment increases the overall lifetime of the piezo by preventing voltage breakdown due to water creeping into the ceramic [90].

A PZT piezo actuator operated at high voltage is expected to heat up drastically due to the low thermal conductivity of the ceramic and for being in a vacuum with only two contacts to dissipate heat.

To replicate these conditions, the experiment was conducted at a specialized facility constructed at FNAL for testing instrumentation inside an insulating vacuum at cryogenic temperature [74]. Two piezo actuators one made from lithium niobate $LiNbO_3$ and the other from PZT were tested, their properties are given in Table 5.3 below. Liquid nitrogen (77 K) and liquid helium (4 K) were

Table 5.3: Parameters of two piezoelectric actuators used in this experiment: PZT and $LiNbO_3$.

| | PIC 050 | PIC 255/252 |
|--|-----------|-------------|
| Material | $LiNbO_3$ | PZT |
| Length [mm] | 36 | 18 |
| Cross-section [mm ²] | 100 | 100 |
| Stroke (300 K) [μ m] | 3 | 18 |
| Stiffness [N/ μ m] | 195 | 200 |
| Blocking Force (300 K) [N] | 585 | 3600 |
| Curie Temperature [K] | 1423 | 623 |
| Density ρ [g/cm ⁻³] | 5 | 7.80 |
| Relative Permittivity ϵ_{33}/ϵ_0 | 28.7 | 1750 |

used to cool down the setup. The liquid nitrogen cool down was used to ensure that the setup was working correctly but also yielded useful data. The operation in the cavity is done at 2 K but in this case 4 K was used since it is only a difference of 2 K. Two piezo capsules each consisting of two $10 \times 10 \times 18$ mm stacks glued together were placed on top of a thick copper disk which acted as the base for vibrating piezo and as a heat sink. Each double piezo stack was preloaded with Belleville washers inside a capsule made from a thin stainless steel tube. The copper disk was connected to a copper braid which contacted the liquid via a copper rod. This setup ensured that the copper disk would reach temperatures close to the liquid. The copper disk along with the piezo capsules was

enclosed in a can as shown in Fig. 5.16 (a) and kept under vacuum at 10^{-3} Torr. A total of four

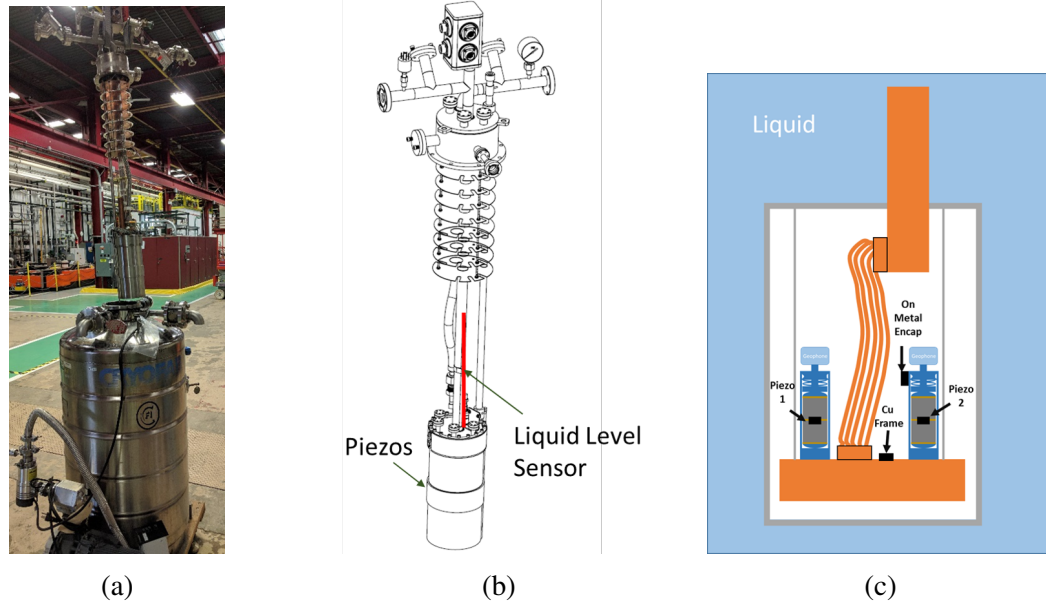


Figure 5.16: (a) Tower with the Dewar (b) and, Tower that holds the can which enclosed the piezos. All the instrumentation is wired from the can to the outside. (c) The inside of the can contains two piezo encapsulations with four Cernox RTDs.

Cernox temperature sensors were used. One was placed on the copper plate, the second one was placed on the side of the piezo capsule encasing. The other two sensors were placed in the middle of the two piezo stacks. The location of the temperature sensors is shown in Fig. 5.16 and 5.17. The temperature sensors for the piezos were placed in the middle of the stacks for three reasons. The primary reason was that most of the heat is concentrated in this region. The second reason was to avoid the possibility of the sensor falling off during operation since the piezo is expanding and contracting. Placing it in the middle allowed only one 10x10x18 mm stack to be fully operational while the other stack which made contact with the RTD sensor was not operated. The last reason was to avoid frictional heating of the sensor due to the piezo rubbing against it during operation. Once the RTD sensors were attached, both stacks were placed inside a stainless steel encapsulation and stress preloaded with Belleville washers.

To verify that the piezos were being stimulated by a sine wave voltage a geophone was mounted on top of the encapsulations as shown in Fig. 5.17 (c). The liquid helium level of the Dewar was also monitored for the tests using a resistance probe. The data was collected via the data acquisition

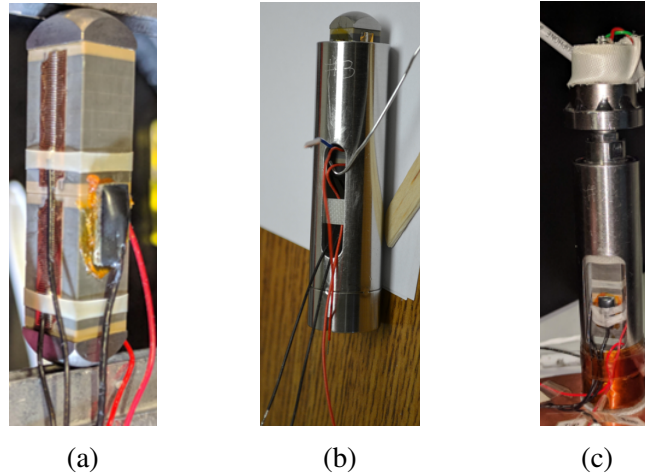


Figure 5.17: (a) The piezo element consists of two stacks glued together. The cernox RTD is located at the center of the piezo stacks. (b) The piezo stacks are placed into a stainless steel encapsulation. (c) The piezo is then preloaded with Belleville washers, the washers are put on top of the piezo element and screwed into place. A geophone is mounted on top of the piezo encapsulation.

(DAQ) module NI PXI-1031. This DAQ was also used for driving the piezo with a sine wave pulse. The schematic of this setup is shown in Fig. 5.18. The Lakeshore meter relayed the resistance of the Cernox sensors which was then calculated to give temperature based on the calibration curve of the RTD sensors. The Agilent 4264B LCR meter was used to measure the capacitance of a stack as well as the dissipation factor. The pulse used for this measurement had a frequency of 1 kHz and 1 V peak-to-peak amplitude.

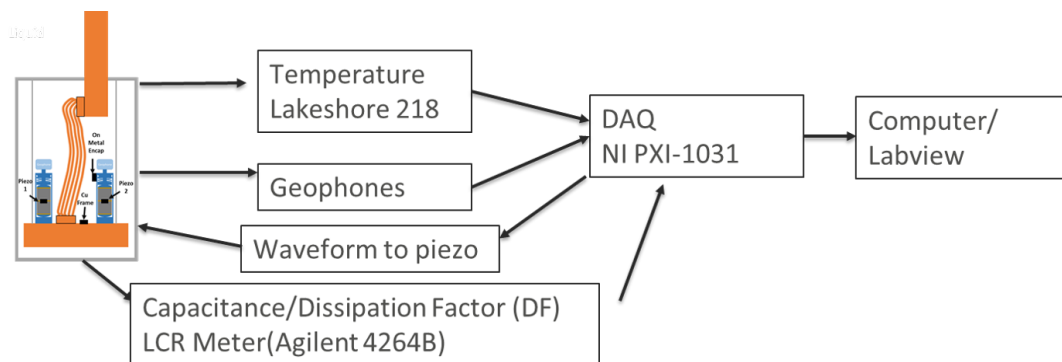


Figure 5.18: Schematic of data acquisition.

5.2.4 Dielectric Heating

For the operation of narrow bandwidth and high LFD cavity the piezo needs a high voltage waveform for resonance control. The study of dielectric heating of the piezoelectric material is important since large temperature fluctuations can affect the coercive field (the critical field that changes the polarization of the material). Additionally, the effects of large temperature fluctuations can cause stress on the ceramic which can result in piezo failure. The first material to be discussed is PZT since this is the most widely used material for actuators due to the large stroke it provides. At room temperature, the Physik Instrumente (PI) piezo actuator can operate from -20 V to 120 V (unipolar operation). Below 77 K the voltage range of operation can go down to -100 V. Bipolar operation of the piezo actuator is defined in the range of -100 to 100 V and the unipolar operation when the voltage is only positive. The displacement stroke of the piezo can be doubled when the piezo is operated in the bipolar regime, but the heating must be monitored to ensure the temperature will not go above 77 K. It is also important to calculate the heat load of the piezo due to the proximity

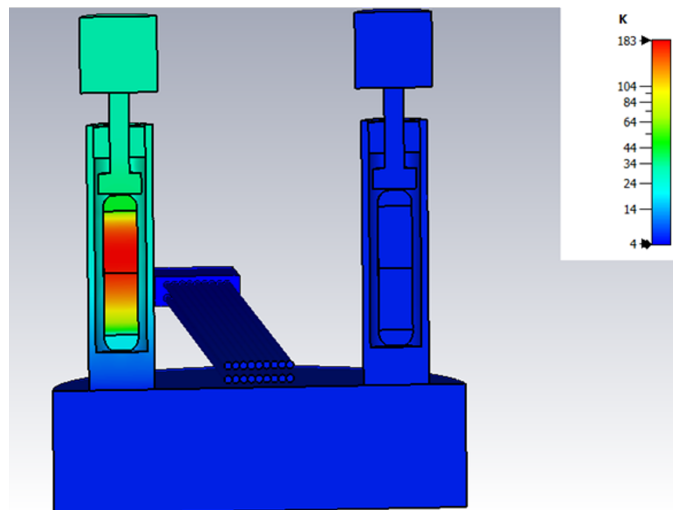


Figure 5.19: Cross section view of simulation of piezo heating in the experimental setup done in CST studio.

of the cavity to prevent heat flow there. The heating on the piezo arises from dielectric heating and the low thermal conductivity of the PZT ceramic. The thermal conductivity for PZT at 70 K is $0.07 \text{ Wm}^{-1}\text{K}^{-1}$ and at 15 K is reduced to $0.01 \text{ Wm}^{-1}\text{K}^{-1}$ [91]. This small thermal conductivity

presents a problem for heat dissipation since the piezo is in a vacuum and only has two contact points within the encapsulation for heat dissipation. A simulation done in CST studio [92] for the temperature gradient based on 1 W power (equivalent to the modified dielectric heating equation at $V_{pp}=100$ V and 100 Hz) being dissipated on the piezo is shown in Fig. 5.19. The figure shows that the majority of the heat is concentrated in the middle of both stacks. The results are based on the thermal equilibrium reached after the 1 W dissipation is applied for a long time.

The temperature rise time series for the trial of a 100 Hz unipolar sine wave at $V_{pp}= 100$ V is shown in Fig. 5.20. This trial consists of driving the piezo for 1.5 hours until temperature saturation is reached. The piezo is driving waveform is then turn off. This trial produced the largest temperature rise of 91 K reaching 110 K from 20 K. If the piezo had been operated in the bipolar mode with a voltage less than -20 V a depolarization would have occurred since the 77 K threshold was surpassed. The temperature on the outside of the stainless steel capsule also rose rapidly showing that there is large heat dissipation but not enough to cool down the piezo. This large heat flow is also enough to be detected by the temperature sensors on the copper disk and inside of the second piezo shown in Fig. 5.20 (b). The equilibrium temperature on the piezo is 110 K and 2 hours are needed to reach it. During the cooldown the capacitance and dissipation

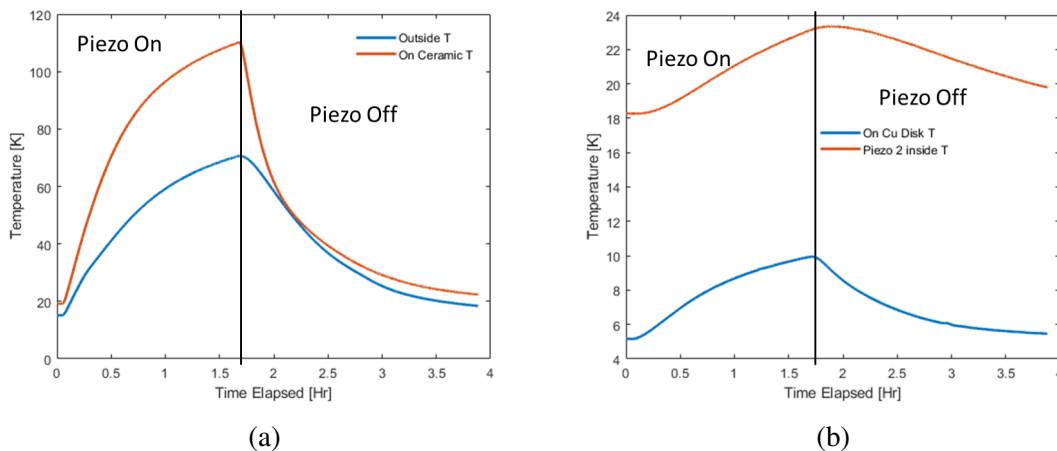


Figure 5.20: (a) Temperature inside and outside the piezo ceramic after being driven by a 100 Hz sine wave at $V_{pp}= 100$ V on a single stack. The decay is occurs when the piezo is turned off. (b) Temperature rise of the temperature sensors on the copper disk and on the inside of the second piezo.

factor were measured with the LCR meter, the results are shown in Fig. 5.21. The voltage for this measurement was 1 V_{pp} and the frequency was 1 kHz. As the piezo cools down the capacitance and dissipation decrease showing their temperature dependence. These results show that as the piezo heats up increasing the temperature, the capacitance and dissipation factor also increase creating positive heating feedback.

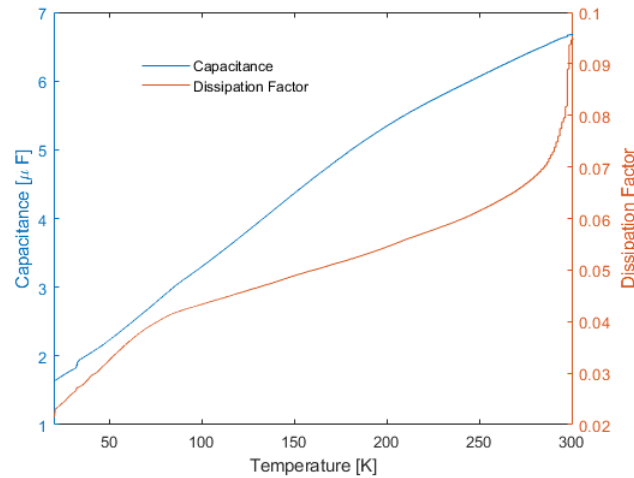


Figure 5.21: Dissipation factor and capacitance measured with an LCR meter with respect to decreasing temperature on the piezo. Note that the voltage used to measure these parameters is $V_{pp} = 1$ V.

The heating of the piezoelectric actuator can be estimated using Eq. 5.11. The first trials were done with both liquid nitrogen and liquid helium. To characterize the heating, only the liquid helium results will be shown first and the results for the other trials will be discussed in the next sections. The heating estimated from this equation is proportional to the temperature rise $\dot{Q}_G \propto \Delta T$. The trials for a $V_{pp} = 100$ V sine wave with different frequencies show that the temperature rise is indeed linear with respect to the driving frequency which is in agreement with the Eq. 5.11 as shown in Fig. 5.22. The plots show the temperature rise from 20 K, for Fig. 5.22(a) the piezo was driven by a $V_{pp} = 100$ V sine wave with different frequencies. This trial was done with the copper foam piezo which will be discussed later. Based on the dielectric heating equation the temperature rise was expected to follow a quadratic trend with respect to the driving voltage. As the piezo was operated at a higher voltage a deviation of temperature was observed. When the piezo was stimulated at

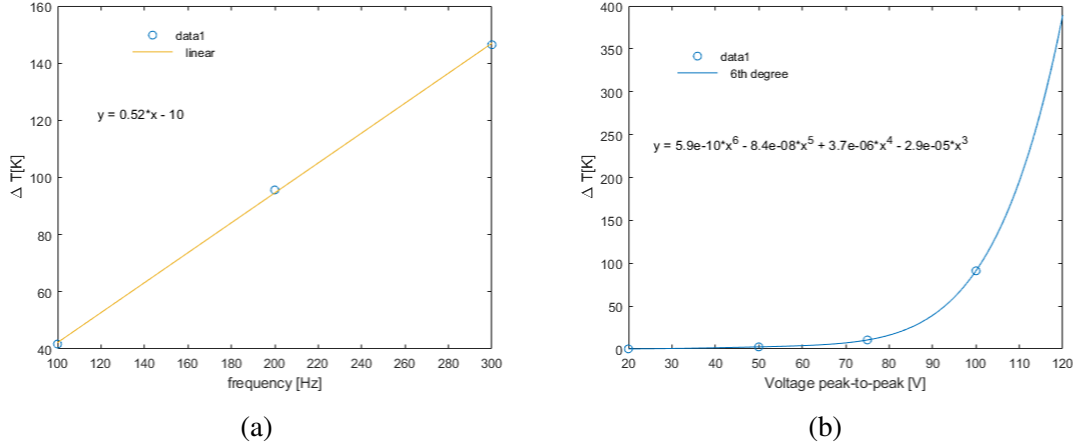


Figure 5.22: (a) Temperature rise of piezo driven by a $V_{pp} = 100$ V sine wave with different frequencies. (b) Temperature rise of piezo driven by a 100 Hz sine wave at different voltages.

100 Hz and 50 $V_{pp} = V$ the temperature rise was 2.49 K. Thus it was expected that at 100 Hz and $V_{pp} = 100$ V the temperature rise would be roughly 20 K taking into account the rise of capacitance and dissipation factor with respect to temperature. Instead, a temperature rise of 91 K from 19 K was observed which is 4.5 times the value expected. With this larger temperature rise, the PZT piezo actuator cannot operate in bipolar mode (-100 V to 100 V) since it can lead to a failure. Additionally, the large temperature fluctuation leads to elongation and contraction of the piezo. This causes stress on the ceramic which could also reduce the lifetime of the actuator.

To estimate the heat load that the piezo will output as well as the temperature rise, a modification to Eq. 5.11 is needed. The 4.5 discrepancy will be explained in later sections and methods to improve heat dissipation will be presented in section 5.3. In the next section, the self-heating model will be presented which gives an equation to predict the temperature rise.

5.2.5 Self-heating Generation Model

The temperature of the piezo as a function of time can be modeled with a 1-D self-heating equation based on the first law of thermodynamics [93], [94]. The behavior of the temperature rise for different voltages and frequencies show that the rise is proportional to $(1 - e^{-t/\tau})$ as shown above. Additionally, this model can be used to estimate the internal heat generation of the piezo when an empirical formula is not known [95]. For this derivation a uniform temperature distribution and

isotropic material is being assumed, the equation then can be written as

$$\dot{Q}_G - \dot{Q}_d = mC_p dT/dt \quad (5.12)$$

where \dot{Q}_G is the internal heat generation due to dielectric losses and \dot{Q}_d is the heat dissipation; m is the mass; and C_p is the specific heat capacity of PZT. At low electric field (voltage) the heat generation can be approximated by Eq. 5.11 but at large voltages this equation no longer holds. Alternatively, Eq. 5.12 can be used to fit the data and obtain the heat dissipation from the fit of the temperature rise. In order to solve Eq. 5.12 it is assumed that the specific heat capacity of the piezo as well as the dielectric losses are not dependent on temperature. As shown earlier, this is not true but can be taken as a rough approximation.

The heat dissipation for the piezo is modeled by

$$\dot{Q}_d = R_{Th}(T - T_o) \quad (5.13)$$

where R_{Th} is the modified heat transfer coefficient which is assumed to be independent of T ; T_o is the initial piezo temperature; and T is the temperature of the piezo. The modified heat transfer coefficient is defined as $R_{Th} = h_{eff}A$ where h_{eff} is the effective heat transfer coefficient seen by the piezo and A is the area where the heat is transferred. Solving Eq. 5.12 yields

$$T = T_o + T_\infty(1 - e^{-t/\tau}) \quad (5.14)$$

$$\tau = mC_p/R_{Th} \quad (5.15)$$

$$T_\infty = (\dot{Q}_G)/R_{Th} \quad (5.16)$$

where Eq. 5.15 is the time constant and Eq. 5.16 is the steady state temperature reached after a long time. The heat generated by the piezo (\dot{Q}_G) can be obtained by Eq. 5.15 and 5.16. In order to obtain R_{Th} to solve for \dot{Q}_G the heat capacity of PZT at the steady state temperature T_∞ is used.

5.2.6 Piezo Heat Generation Model Comparison

The dielectric heating comparison from Eq. 5.11 and the value from the fit from equation 5.14 was done for a sine waveform with different frequencies and voltages. The results of a fit from Eq. 5.14

is shown in Fig. 5.23, this is the temperature rise for the trial with a sine wave of 100 Hz at $V_{pp}=100$ V which produced the largest temperature rise. The temperature rise from the initial temperature value was of 91 K, the results shows that the temperature rise has a good fit from Eq. 5.14.

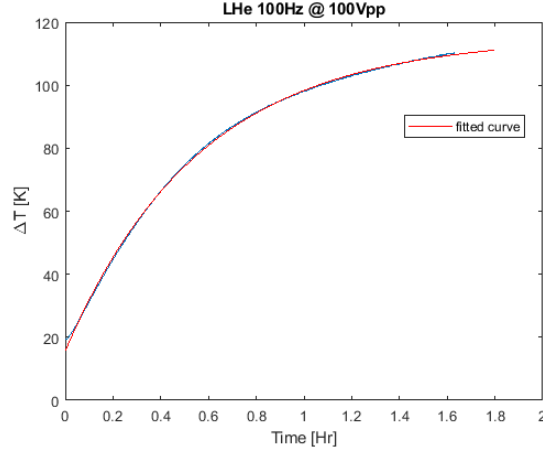


Figure 5.23: Fit of Eq. 5.14 for temperature rise of piezo driven by $V_{pp}=100$ V at 100 Hz sine wave.

Table 5.4: Power generated by the piezo calculated from Eq. 5.11 and power generated by the piezo obtained from the fit of Eq. 5.14 at the steady state.

| \dot{Q}_G (Eq. 5.11) [mW] | \dot{Q}_G (Fit Eq. 5.14) [mW] | f [Hz] | V_{pp} [V] |
|-----------------------------|---------------------------------|----------|--------------|
| 27.9 | 29.6 | 300 | 50 |
| 20.7 | 20.5 | 100 | 75 |
| 112.8 | 191.3 | 100 | 100 |

The results for various fits are shown in Table 5.4. Note that the dielectric heating is calculated at the maximum temperature. The dielectric heating \dot{Q}_G below 75 V calculated from Eq. 5.11 at the steady state temperature is similar to the dielectric heating obtained from the fit of Eq. 5.14. At voltages larger than 75 V the values start to deviate. This is due to the large temperature changes of the piezo, in this case the capacitance C and dissipation factor $\tan \delta$. Additionally, C and $\tan \delta$ also increase with respect to the voltage applied [96].

5.2.7 Heating Effects Due to the Driving Waveform

During this experiment all of the waveforms used to drive the piezo were sinusoidal. Additionally, the duty cycle was 100% for all the waveforms. In a linac with pulse operation, the RF pulse has a small duty cycle (2%) during which the beam is accelerated. The cavity must be kept on resonance during the flat top operation. Although the RF pulse has a small duty cycle, the piezoelectric actuator must operate both before and after the flattop region in order to decrease the overall power and to keep the cavity on resonance. Due to this, the piezoelectric actuator has a larger duty cycle than the RF pulse. Depending on the frequency of the beam and the RF duty cycle the piezoelectric actuator can have a duty cycle of 50% to 90% [51]. Additionally, during operation, the signal required to tune the cavity frequency will be composed of a sum of sinusoids to compensate multiple modes which will also alter the heating of the piezo. Three different waveforms were used to study the heating of the piezoelectric actuator; a sine wave, a triangular wave, and a square waveform with 100 Hz at $V_{pp}=50$ V were used. The results of these trials are shown in Fig. 5.24a. The square wave had the largest temperature increase of $\Delta T = 13.20$ K, followed by the triangular waveform with $\Delta T = 3.73$ K, and the sine wave with $\Delta T = 2.47$ K.

The different temperature rises can be explained by the harmonics of the square and triangular waveform whereas the sine waveform only has one harmonic. In the case of the square and triangular wave, only the odd harmonics of the fundamental frequency are produced. The frequency spectrum of the three different spectra is shown in Fig. 5.24b. The fundamental frequency for all the waveforms was 100 Hz and with a sampling rate of 10,000 kHz based on a MATLAB simulation of the waveforms. The amplitude was normalized for all waveforms, the results of the frequency spectra show that the square waveform had the largest peak at 100 Hz as well as a higher noise floor frequency level compared to the two other waveforms. The harmonics were also larger in amplitude compared to the triangular waveform. The heating of the piezoelectric actuator depends linearly on frequency as given by Eq. 5.11, this shows that the higher noise frequency level, as well as the larger harmonic amplitudes, contributed more to heating compared with the sine and triangular waveforms.

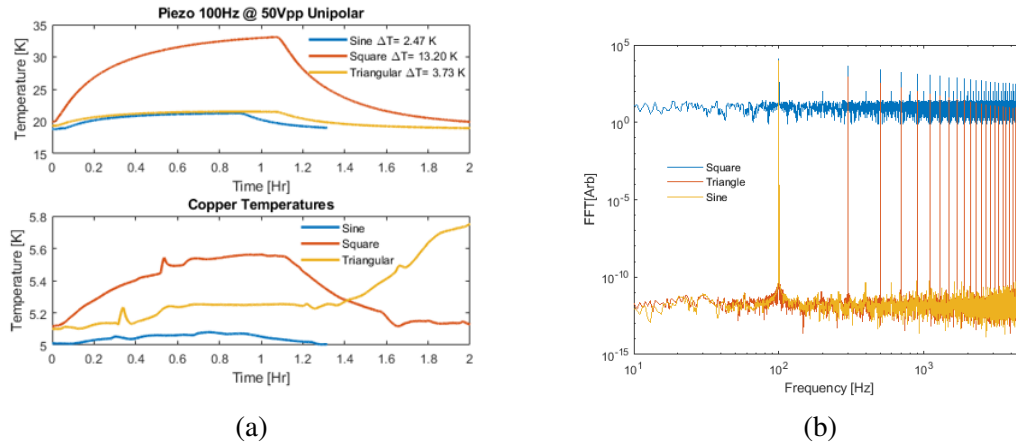


Figure 5.24: (a) Piezoelectric actuator being driven with 3 different waveforms with the same peak-to-peak voltage and frequency. The square wave gives the largest temperature rise followed by the triangular wave and lastly the sine wave. In the case of the copper temperature for the triangular waveform a helium liquid level drop caused an increase in temperature. (b) Frequency spectrum of the three different waveforms with fundamental frequency of 100 Hz.

The resonance control algorithm used during pulsed mode or CW mode of the cavity does not contain only one frequency to drive the piezo. Multiple filters are used to cancel out the effects of detuning, the majority of the noise terms are under 100 Hz for CW operation. In the case of pulse mode, the RF pulse can excite the mechanical modes of the cavity. For the $\beta_G = 0.92$ 650 MHz cavity the first longitudinal mode occurs at 215 Hz with the largest detuning compared to other modes. To get an accurate representation of the heating under these conditions a waveform consisting of the sum of three sine waves with frequencies of 25 Hz, 50 Hz, and 100 Hz was used in the initial trial with liquid nitrogen. The voltage peak-to-peak for this trial was 100 V and each of the sine waves was given equal weight. The results of the heating for a single tone of frequency 50 Hz and 100 Hz were also measured for comparison to the tones waveform composed of three different frequencies. The temperature rise for each of these trials is shown in Fig. 5.25a. The largest temperature increase was 105 K from a drive of 100 Hz, and the 50 Hz drive produced an increase of 27 K. When the tones signal was used to drive the piezoelectric actuator the temperature increase was 15 K which was lower than the drive for the 100 Hz and 50 Hz. The resulting sum of sinusoids shows that the period of the waveform is 0.04 s which is 25 Hz. Although, each of the sine waves were given equal weight the resulting wave of the sum show that the 25 Hz is more

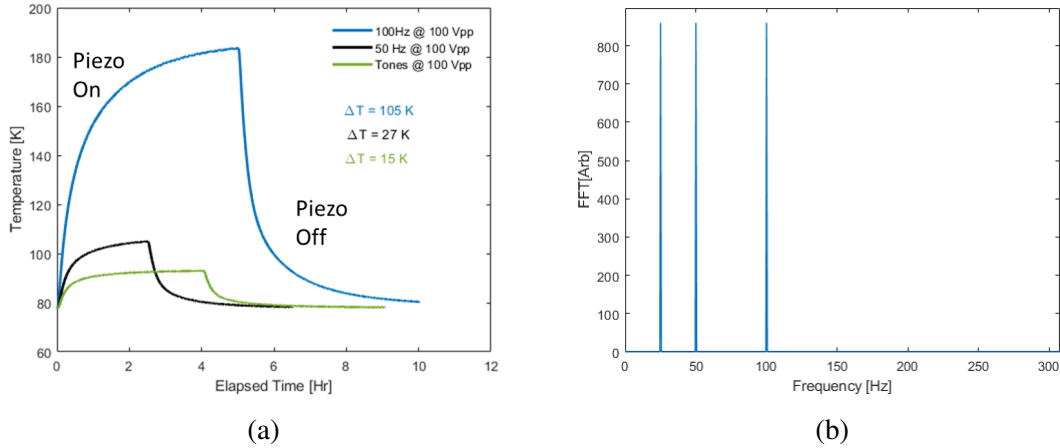


Figure 5.25: (a) Piezoelectric actuator being driven with 3 different waveforms all at $V_{pp} = 100V$. The tones waveform is composed of the sum of three sinusoids with frequency of 25 Hz, 50 Hz, and 100 Hz. The amplitude of each of the sum is equal and their sum is equal to the $V_{pp} = 100V$. (b) Frequency spectrum of the tones waveform, each of the frequencies was given equal weight.

dominant. This helps explain why the temperature increase was smaller than for the 100 Hz and 50 Hz. Therefore, it is not enough to analyze the frequency of the spectrum signal but also analyze the period of the waveform (if it has one) to get an accurate estimate of the temperature rise due to the driving signal.

5.2.8 Effects of Heating on Resonance Control

The main goal of the piezoelectric actuator is to control the frequency of the cavity to minimize the RF power used. It is shown that the high voltage operation causes large temperature increases. The stroke of the actuator depends on the temperature, at room temperature the value at 100V is $34\ \mu m$. Since the stroke is related to the capacitance it can be seen from Fig. 5.21 that the value from room temperature to 20K is reduced to 20 % of the original value. It is, therefore, necessary to take into account this change in displacement stroke with respect to temperature. The results from the geophone shown in Fig. 5.26 demonstrate that the stroke also increases with temperature. The figure shows two signals, one with the piezoelectric actuator driven by a 100 Hz sine wave at $V_{pp} = 100\text{ V}$ and the other with no driving waveform which shows the noise floor. The noise detected from the geophone is due to outside vibrations, the main source is from the vacuum pump.

The signal taken from the geophone uses a 5 s interval and the average of the amplitude from this interval is taken. The geophone is calibrated to convert the voltage signal into the velocity at which the geophone is moving due to the stimulation from the piezo. The increase in voltage (which gives the velocity from which the movement can be obtained) of the piezoelectric actuator follows the same behavior observed from the temperature rise. Therefore, the displacement stroke can also be modeled with Eq. 5.14 but instead of temperature the stroke is used.

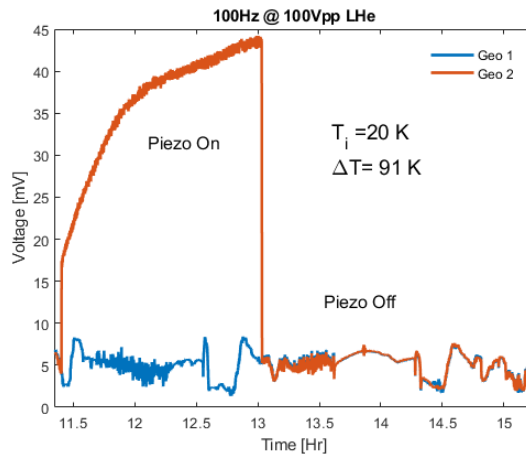


Figure 5.26: Voltage of geophone during the trial at 100 Hz at $V_{pp}= 100$ V. The voltage of signal from the geophone can be relate to its velocity from the stimulation from the piezo.

Modeling the piezo stroke will be beneficial since the piezo stroke can be increased 2.58 times with a temperature increase of 91 K as shown in Fig. 5.26. A 2.58 increase in stroke needs to be taken into account in the resonance control algorithm since a larger stroke will increase the detuning from the piezo. The frequency shift of the piezoelectric actuator in the $\beta_G = 0.92$ 650 MHz cavity cooled down to 2 K at 100 V is -1.97 kHz. If the piezoelectric actuator is driven at 100 Hz and $V_{pp}= 100$ V the temperature will increase. This will increase the nominal frequency shift from -1.97 Hz to -5.08 kHz in one and a half hours. If this is not taken into account the control algorithm can become unstable and strongly overcompensate the microphonic noise. The algorithm must then take into account this temperature increase and properly drive the piezoelectric actuator to not overcompensate.

5.2.9 Heating Effects From Unipolar and Bipolar Operation

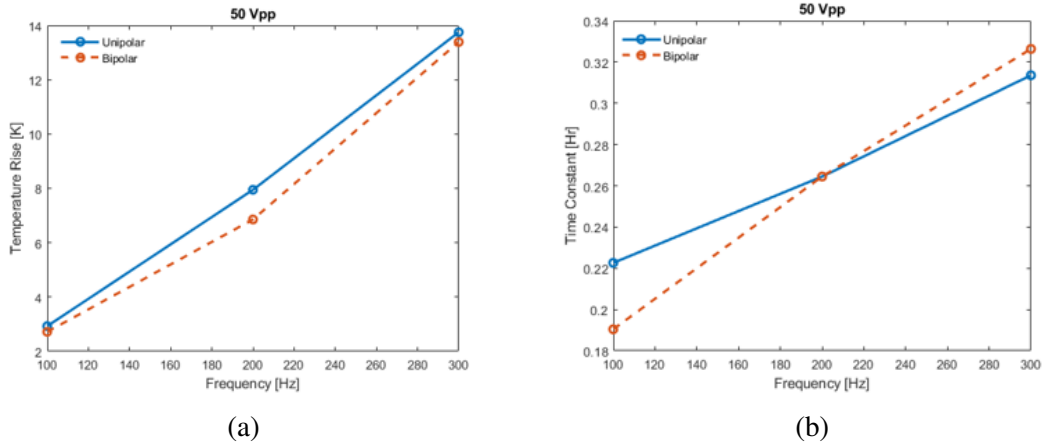


Figure 5.27: (a) Temperature rise at $V_{pp}= 50$ V in both unipolar and bipolar mode, the results are consistent with each other.(b) The time constant from for each of the trials are similar.

The stroke of the actuator depends on temperature, as it cools down the stroke also goes down. An alternative to increasing the stroke by raising the temperature is to use the piezo in the bipolar mode. During the bipolar operation, the piezoelectric actuator can be driven in the range of -100 V to 100 V doubling the piezo stroke. The piezoelectric actuator can only work in the bipolar mode if it reaches a temperature threshold which occurs for PZT at 77 K. At this temperature the piezoelectric material undergoes a ferroelectric phase transition which increases the coercive field of the material. The coercive field is the field needed to polarize the piezoelectric material. When the piezoelectric actuator is warm, the coercive field is small and going into the negative voltage regime can result in depolarization. Thus, below 77 K the piezoelectric actuator can operate in both positive and negative voltages. The results from a study in Ref. [97] show that the permittivity of PZT is larger for bipolar operation than unipolar. Since the heating equation depends on the permittivity of the ceramic it is expected that the heating between these two different modes of operation should be different. The results of this study are shown in Fig. 5.27a.

The voltage operation for these trials was $V_{pp}= 50$ V with the range being from -25 V to 25 V. The results show that there is not a significant change in temperature rise and the time constant for each of the trials. In the results from [97] the peak-to-peak voltage used was 100 V, therefore the

results presented are not at the same level. Another trial at $V_{pp} = 100$ V is needed to verify that the heating of the two modes is similar or different at higher voltages.

5.3 Improvements to Heat Mitigation of Piezoelectric Actuators

In the experiments conducted at high voltage piezo operation up to $V_{pp} = 100$ V the temperature rise was not in agreement with Eq. 5.11 where the temperature rise with respect to piezo driving voltage was not observed to be quadratic. The temperature rise instead follows a trend of a higher-order polynomial with respect to the driving voltage. In this section, it is shown that the heat dissipation improves with a novel design of a PZT actuator. The results of this experiment are presented with an actuator made from PZT with a heat sink attached. Additionally, an actuator made from lithium niobate $LiNbO_3$ is tested for the first time for applications for resonance control of SRF cavities.

5.3.1 Novel Piezoelectric Actuator Design

To prevent the piezo from reaching large temperature fluctuations a collaboration between Physik Instrumente (PI), the manufacturer of PZT piezos, and FNAL was started to develop a piezo actuator with a high heat dissipation factor. When operated in the cryomodule setting the standard PICMA piezo has only two contacts through which heat can flow. These are the top and bottom points where the piezo makes contact with the cavity and tuner. Before making contact with the cavity and tuner the piezo has ceramic balls (Silicon Nitride) to prevent shearing forces on the piezo. These ceramic balls have a low thermal conductivity so heat flow is not efficient. In the first trial with the standard PICMA piezo actuator design, these ceramic balls were not taken into account. The setup up was modified to accommodate the piezos with the ceramic balls to replicate the same configuration in the cryomodule.

The conventional methods of cooling a piezo ceramic such as using oil or forced air were not pursued due to the piezo's location in an insulating vacuum. The best method for heat dissipation was to use a heat sink attached to the actuator. The design of the new piezo consists of placing

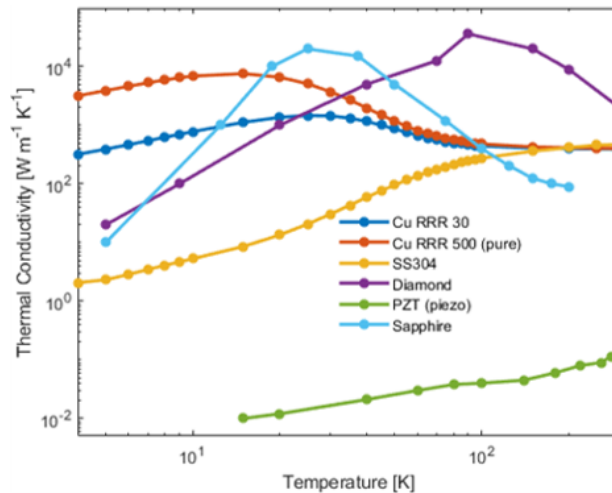


Figure 5.28: Thermal conductivities of different materials which are used in the piezo actuator.

a high thermal conductivity material in contact with the piezo ceramic. Figure 5.28 shows the thermal conductivity for several materials including the values for PZT with respect to temperature. The temperature of the piezo actuator will be in the range of 10 K to 20 K when cooled to 2 K with the cavity. The materials with high thermal conductivity in that range are copper, diamond, and sapphire. Copper foam is used to make contact with the ceramic and the outer encasing of the piezo actuator. Since the piezo ceramic will be operated at high voltage, aluminum nitride is used as a buffer between the connections of the copper foam in the ceramic and outer actuator encapsulation (see Fig. 5.30). Aluminum nitride has similar properties to sapphire, it has high thermal conductivity and small electrical conductivity.

The design copper foam piezo actuator is shown in Fig. 5.29 along with the standard PICMA design to contrast the designs. In this design, the encapsulation of the piezo has two copper plates and the inside has copper foam with a dielectric material as an interface between the copper foam and the ceramic. A copper heat sink is attached to the piezo encapsulation. To attach the heat sink the cylinder shape was changed to a rectangular one. Additionally, the encapsulation was optimized for heat transfer and include a preload integrated with the housing (see Fig. 5.30). This copper foam piezo design has 4 paths ways in which heat can flow compared to the standard PICMA design which only has two. Additionally, the encapsulation is kept at the liquid helium temperature since

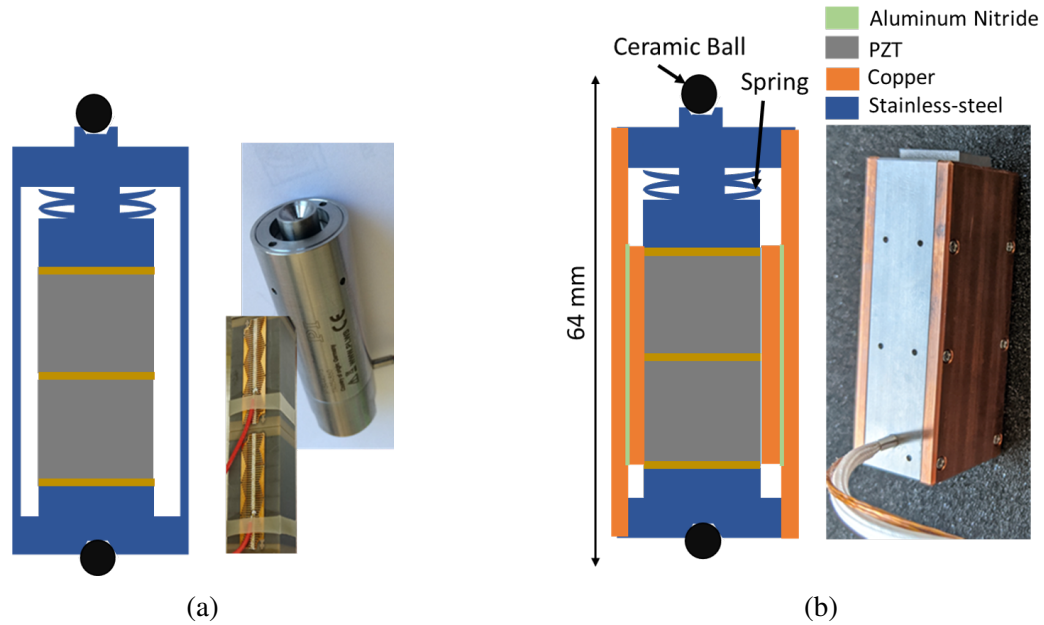


Figure 5.29: (a) Cross-section of standard piezo design with only two contact points. The encapsulation is also shown. (b) New copper foam design with copper plates used to contact the copper foam. Encapsulation of the new design is shown.

the copper braid is connected to the rod in the liquid helium.

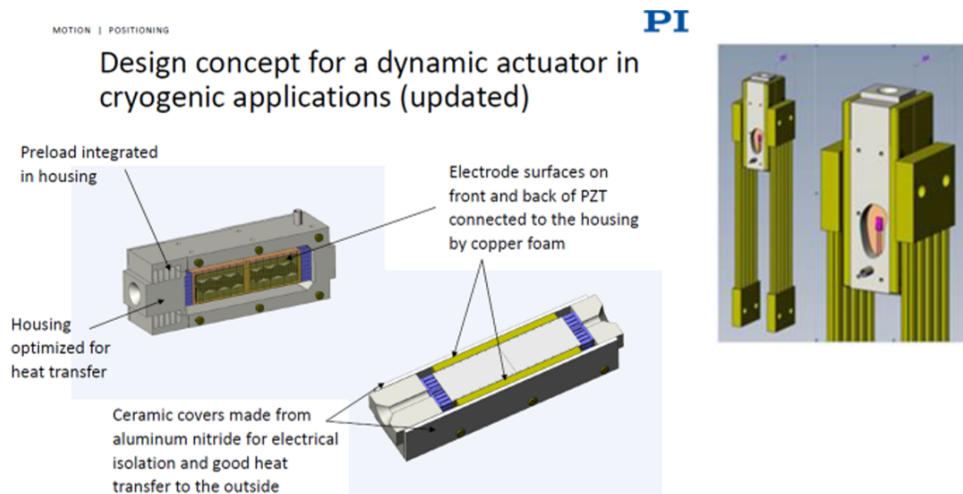


Figure 5.30: Design model of the copper foam piezo actuator design.

Testing of the heat dissipation for the copper foam piezo actuator design was done with two piezos of the same model as shown in Fig. 5.31. Changes were made to the previous setup to accommodate the copper foam actuators and to also take into account the effect of the silicon

nitride balls since they have low thermal conductivity. In this setup, two heat sinks were used compared to one in the previous setup and two C-brackets (see Fig. 5.31 (b)) to hold the piezos. The same number of temperature sensors and two accelerometers were used. The results of this new piezo design compared to the standard PICMA design will be compared in the following sections.

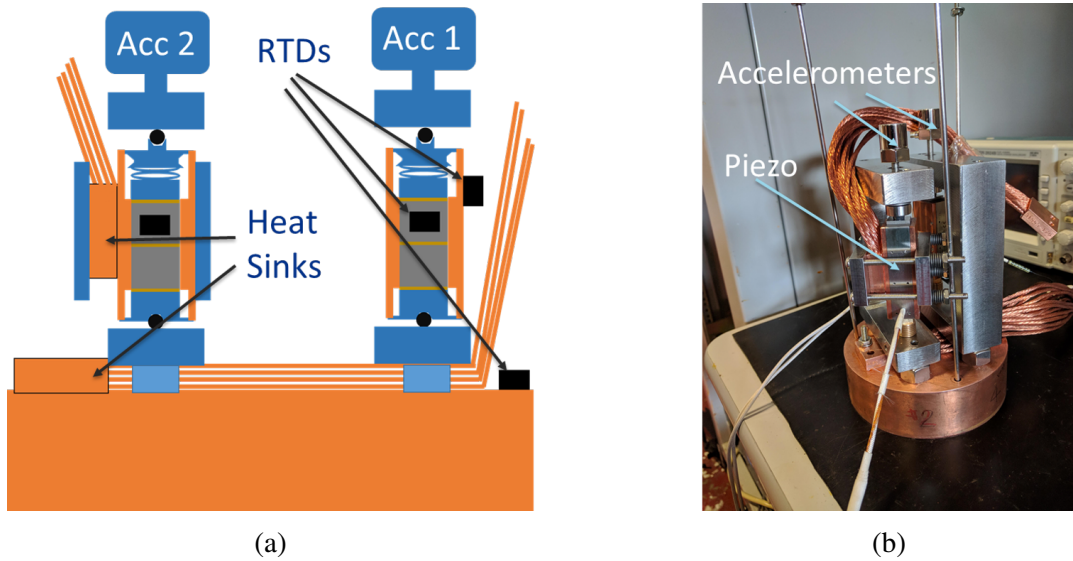


Figure 5.31: (a) Schematic of piezo setup, this setup up uses two heat sinks where one is attached directly to the piezo. (b) Actual piezo setup.

5.3.1.1 Cryogenic Tests Results

The copper foam piezo design was tested when cooled to 77 K and later to 4 K. In this iteration one of the copper foam design piezos has a heat sink attached while the other does not. The comparison of the new piezo design with the standard PICMA design results obtained from an earlier section is summarized from plots like in Fig. 5.32 where the voltage and frequency of the driving waveform is varied. The results are shown in Tables 5.5 and 5.6. The ceramic material used is PZT which is used for both the standard PICMA design and the copper foam design. The table gives the temperature rise of the piezo ΔT and also the time constants of the temperature rise τ_R and decay τ_D after the voltage was turned off. The time constants were obtained by fitting the temperature rise and decay. The temperature rise of the piezo can be related to the dielectric heating (\dot{Q}_G) shown in the self-heating section to the heat transfer coefficient R_{Th} as \dot{Q}_G/R_{Th} . If the heat generation

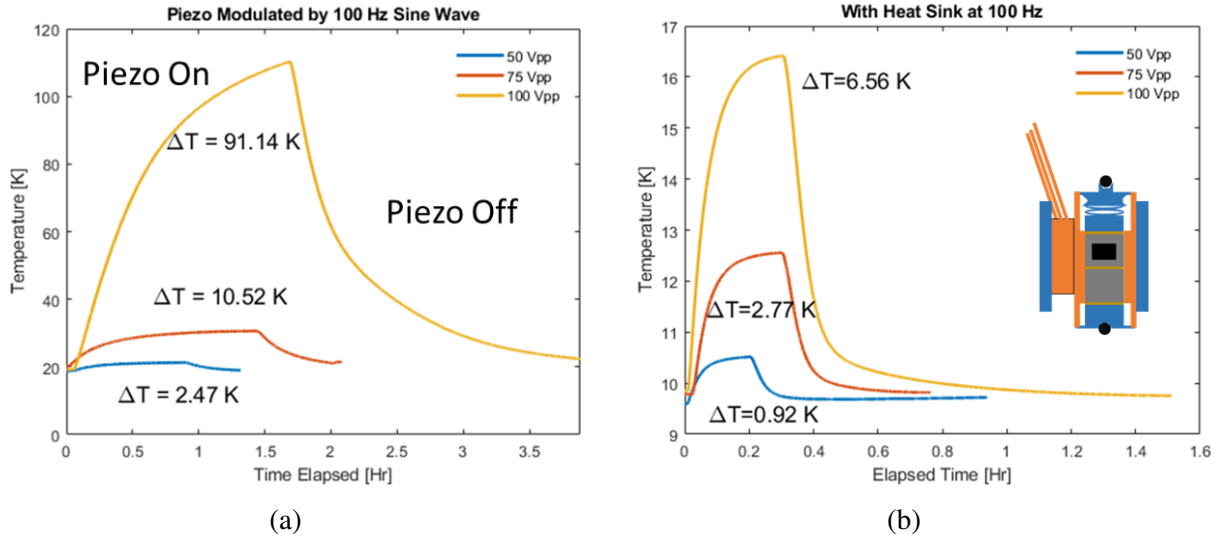


Figure 5.32: The piezos were cooled with liquid helium. (a) The standard PICMA design piezo modulated with 100 Hz sine wave with varying voltages. (b) Piezo with heat sink modulated with a 100 Hz sine wave with varying voltages. The temperature rise is smaller in the new design.

is kept the same then a smaller temperature increase indicates an increase in the heat transfer coefficient which is expected from the new design. Additionally, a larger heat transfer prevents the piezo from creating positive thermal feedback. The time constants are inversely proportional heat transfer coefficient, thus an increase in the heat transfer coefficient will result in a smaller time constant.

Table 5.5: Comparison of temperature rise between the standard PICMA design piezo with the copper foam piezo with a heat sink for a 100 Hz sine wave.

| Initial Temp | Standard PICMA Design | | | | Cu Foam Design | | |
|--------------|-----------------------|----------------|---------------|---------------|----------------|---------------|---------------|
| | Voltage [V] | ΔT [K] | τ_R [Hr] | τ_D [Hr] | ΔT [K] | τ_R [Hr] | τ_D [Hr] |
| 77 K | 50 | 6 | .60 | .41 | 2.01 | .08 | .08 |
| | 100 | 105 | 1.11 | .52 | 18.92 | .09 | .09 |
| 4 K | 50 | 2.47 | .20 | .13 | .92 | .05 | .04 |
| | 75 | 10.52 | .29 | .20 | 2.77 | .05 | .06 |
| | 100 | 91.14 | .43 | .48 | 6.56 | .06 | .08 |

The heating of a single stack at 77 K of the standard PICMA design piezo stimulated at 100 Hz and voltage of $V_{pp} = 100$ V resulted in a temperature increase of 105 K on the ceramic. The same modulation was done to the copper foam piezo with a heat sink with both stacks active, the

temperature rise was 18.92 K, demonstrating that the heat sink and the new design improve heat dissipation by a factor of 11. For comparison the temperature rise was divided by two since both stacks were operated in the copper foam design. The copper foam design piezo without a heat sink had a ceramic temperature increase of 41.73 K with the same modulation. The heat dissipation of the copper foam piezo without a heat sink improved by 3.75 times compared to the standard PICMA design. The piezos will operate when the cavity is cooled to 2 K and the temperature of the piezos will be around 10 to 20 K. The same tests performed at 77 K were performed when the piezos were cooled with liquid helium. The results are shown in Table 5.5, the heat dissipation improves by a factor of 14 when comparing the standard PICMA design to the copper foam with a heat sink. The copper foam design without the heat sinks improves the heat dissipation by a factor of 6 compared to the standard PICMA design. The copper foam design with and without the heat sink shows excellent heat dissipation improvement in both 77 K and 4 K environments. The results demonstrate that the copper foam piezo can be operated in bipolar mode when cooled with liquid helium to increase the stroke without reaching the 77 K threshold.

Table 5.6: Comparison of the standard PICMA design piezo with the copper foam piezo design without the heat sink.

| | Standard PICMA Design | | Cu Foam W/O Heat Sink | |
|-----------------------|-----------------------|--------|-----------------------|--------|
| Initial Temp | 20 K | 77K | 14 K | 77 K |
| T_{max}^{Cer} [K] | 110.37 | 183.49 | 28.57 | 119.84 |
| T_{max}^{Shell} [K] | 70.68 | 130.73 | 20.71 | 96.39 |
| τ_R^{Shell} [Hr] | .52 | 1.46 | .16 | .49 |
| τ_D^{Shell} [Hr] | .53 | .98 | .226 | .58 |

The copper foam design demonstrates that thermal equilibrium is reached faster compared to the standard PICMA design. At thermal equilibrium, the heat generation Q_G and the heat dissipation \dot{Q}_D are the same. At 77 K with a driving waveform of 100 Hz at $V_{pp}= 100$ V, the piezo with the heat sink reaches thermal equilibrium within half-hour while the standard PICMA design takes 5 hours

with modulation of 100 Hz at $V_{pp}=100$ V. This demonstrates that the positive thermal feedback from poor heat transfer is thwarted with the copper foam design. The faster thermal equilibrium is due to an increase of the heat transfer, this results in a smaller time constant τ . The results for the copper foam design with and without the heat sink at both 4 K and 77 K operation are shown in Tables 5.5 and 5.6. The temperature difference between the sensor on the ceramic (T_{max}^{Cer}) and the one on the capsule shell (T_{max}^{Shell}) is another proxy for calculating the heat transfer improvement. A small temperature difference between the capsule shell and the piezoceramic indicates that there is good heat flow. For the standard PICMA design cooled with liquid helium and operated at 100 Hz at $V_{pp}=100$ V the temperature difference from the inside to the outside encapsulation is 40 K. Under the same operation, the copper foam piezo with the heat sink had a temperature difference is 8 K. A smaller time constant from the temperature rise of the piezo and a smaller temperature difference from the ceramic to the piezo encapsulation show that the thermal heat transfer improved.

The large dielectric heating observed in the standard PICMA design was due to the positive thermal feedback of the piezo. The copper foam piezo with a heat sink matches the expected temperature rise from the dielectric heating formula \dot{Q}_G for modulation below $V_{pp}=75$ V. At higher voltage, there is a deviation but not as large compared to the standard PICMA design result which was 4.5 times larger than the dielectric heating formula. The piezo temperature increase during liquid helium operation and with a driving waveform of 100 Hz at $V_{pp}=50$ V was 0.92 K. Comparing this to the operation at 100 Hz and $V_{pp}=100$ V the temperature increase is 6.56 K compared to the expected 3.68 K. This difference is due to the increase in permittivity of the ceramic at high voltage [97]. This also contributed to the standard PICMA design but the permittivity and dissipation factor increase with temperature contributing more to the heating.

5.3.2 Lithium Niobate Measurements

The piezo heat dissipation can be improved by changing the design and adding a heat sink as shown in the previous section. Another way to minimize dielectric heating is by using a different piezo material with a smaller dissipation factor and constant dielectric properties with respect to the

driving voltage. Lithium niobate ($LiNbO_3$) exhibits a small permittivity and dissipation factor as shown in Table 5.3. The piezo was developed by PI and it is a single crystal as opposed to two stacks glued together as in the PZT design. The measurements for the lithium niobate material $LiNbO_3$ were done with the same setup as shown in Fig. 5.31. A temperature sensor was attached to the metal encasing of the $LiNbO_3$ piezo to infer the temperature inside. This piezo did not include a sensor directly attached to the crystal compared to the PZT design. This material can operate in bipolar mode reaching a maximum of $V_{pp}= 1000$ V at any temperature. It is also a ferroelectric like PZT but exhibits a smaller hysteresis. The maximum stroke displacement is $3 \mu m$ at room temperature from -500 V to 500 V. This is 12 times smaller than the stroke produced by the PZT piezo which is $36 \mu m$ at room temperature for the same length. Note that this is comparing two stacks of PZT glued together to be the same length as the $LiNbO_3$ piezo.

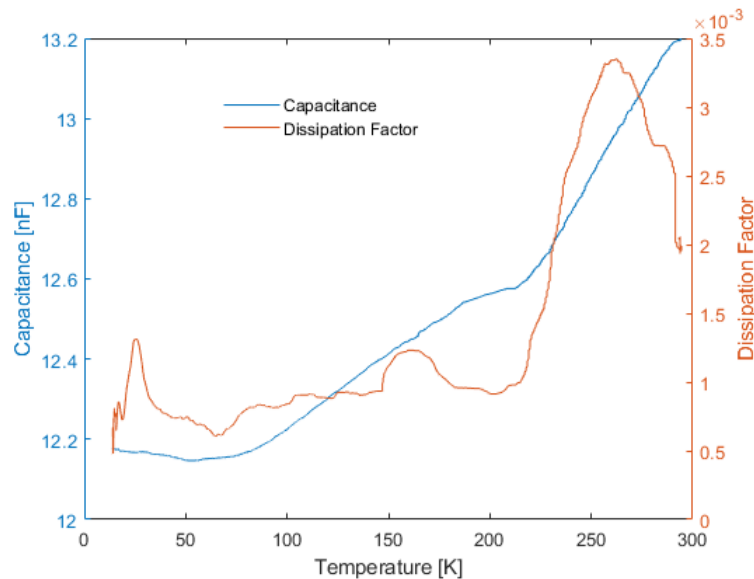


Figure 5.33: The capacitance and dissipation factor are measured with an LCR for the lithium niobate piezo at 1 kHz at $V_{pp}= 1$ V.

The capacitance and dissipation factor were measured with the LCR meter with $V_{pp}= 1$ V at 1 kHz during the cooldown of the setup. The results are shown in Fig. 5.33. The capacitance is 13.2 nF and the dissipation factor is estimated to be about 3×10^{-3} at room temperature. At a temperature of 12 K, the capacitance is 150 times smaller than the PZT and the dissipation factor is 28 times smaller compared to the PZT value. These small values indicate that the power dissipation

will be small. Additionally, the capacitance only changes to 92 percent of the capacitance at 293 K when cooled to 12 K. The capacitance of the PZT changes by 27 percent for the same temperature change. As discussed earlier the capacitance and stroke size are proportional, thus it is expected that the $LiNbO_3$ piezo will only decrease stroke to 92 percent of the room temperature value.

5.3.2.1 Cryogenic Tests Results

The lithium niobate piezo was first cooled down with liquid nitrogen to reach a temperature of 77 K. Using the dielectric heating equation 5.11 the power generated by the piezo is estimated to be on the order of μW with driving voltage of $V_{pp} = 500$ V and at 200 Hz. The results from stimulating the piezo at $V_{pp} = 500$ V and at 200 Hz yielded no temperature increase on the metal shell of the piezo encapsulation as shown in Fig. 5.34 below. This is due to the small heat generated from the piezo. It is possible that the temperature on the crystal might have gone up but only the temperature on the outside of the encapsulation was measured. Further testing at higher voltages was left for the cooldown to 4 K.

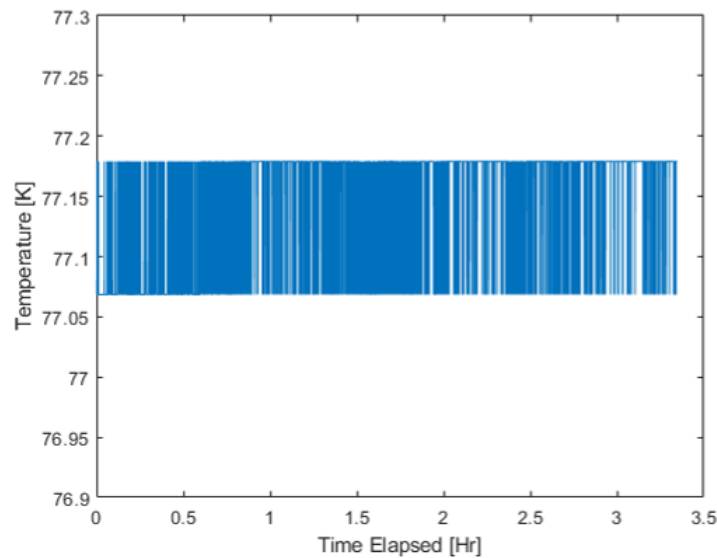


Figure 5.34: Temperature increase of the piezo being driven by a 200 Hz sine wave at 500 V_{pp} while cooled at 77K. No significant temperature rise was observed.

The $LiNbO_3$ piezo was cool down further with liquid helium to reach a temperature of 10 K. The voltage was increased to $V_{pp} = 1000$ V with a sine wave of 200 Hz since the temperature rise

was small for smaller voltage. In this case the temperature on the outside of the capsule increased by 0.1 K. The temperature rise is small and thus shows that $NbLiO_3$ material is an alternative to PZT albeit with a smaller stroke size. The stroke of the PZT piezo with both stacks at a temperature of 12 K will be reduced to $9.72 \mu m$ at 100 V. At 1000 V and at 12 K the stroke of the $NbLiO_3$ piezo is reduced to $2.76 \mu m$.

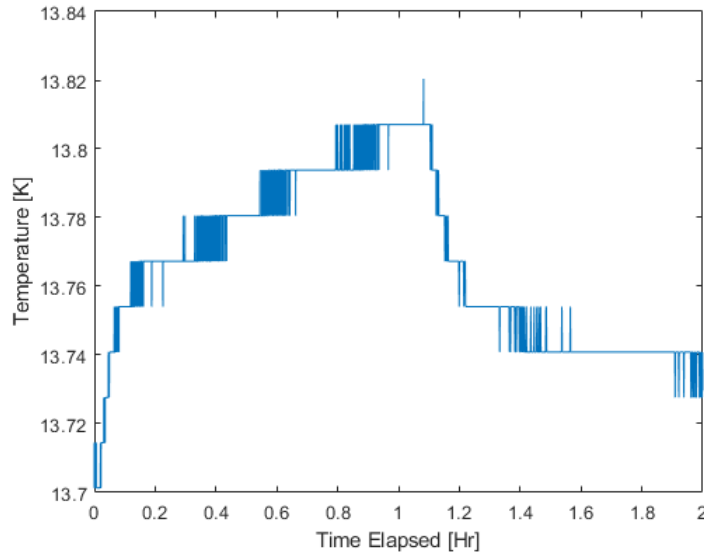


Figure 5.35: The piezo was cooled with liquid helium. The modulation at 200 Hz at $V_{pp} = 1000$ V resulted in a 0.1 K in temperature on the outside encapsulation.

5.4 Summary of Chapter

Microphonics are still present in the cavity detuning even after passive mitigation techniques are implemented as shown in Chapter 4. A cavity tuner is used for active compensation on the remaining microphonics. The tuner is also used to bring the cavity to the operational frequency after cool down and to protect the cavity during pressure tests in the production phase. For the PIP-II project, the first double-level tuner was built and tested for the 650 MHz cavities at room temperature and at 2 K installed on a dressed cavity. A large tuner stiffness is required to minimize the effects of helium pressure variation and LFD. A discrepancy between the tuner stiffness measured with the prototype tuner and tuner stiffness calculated with an ANSYS simulation was found. This was due to inaccurate tuner deformations in the ANSYS model. Measurements of

the deformation of the prototype tuner were conducted on the prototype tuner mounted on a mock cavity. These measurements helped develop a more accurate tuner deformation model used for the ANSYS simulations. As a result, an accurate tuner deformation model helped improve the design which yielded an increase of tuner stiffness from 20 kN/mm to 40 kN/mm.

The second tuner design was tested on a dressed cavity at room temperature and at 2 K in the cryostat. The piezo frequency tuning sensitivity was measured at -19.7 Hz/V. The piezo can operate at -120 V to 120 V, this gives a frequency range of compensation of 4.7 kHz. For the slow tuner component, the motor frequency motor sensitivity was measured at -0.57 Hz/step. This gives a compression range of the cavity of 114 kHz. This measurement demonstrated that this tuner will be able to compensate for microphonics and have enough range to bring the cavity to resonance after cool down.

The piezoelectric properties of actuators for operation in a CW linac are found in the scientific literature. This chapter provided results for piezo actuators operated at a high voltage which are need for high gradient pulsed linacs. This work led to the discovery of a deviation from the dielectric heating formula found in the scientific literature. The reason for the large deviation was due to an increase in the capacitance and dissipation factor with respect to voltage. Positive thermal feedback also contributed to the heating. It was discovered the thermal feedback only occurs when piezo is driven with voltage amplitude greater than 50 % of nominal voltage. A time-dependent temperature model was developed to estimate the heating and the thermal properties of the piezo. This model can be used to estimate the heat load of the piezo on the cavity.

A novel piezoelectric actuator design was developed and tested yielding a reduction of heating by a factor of 14 at liquid helium temperatures. This new design also succeeded in stopping the positive thermal feedback. Since the temperature rise is small for the PZT copper foam piezo design with a heat sink the piezo can be operated in bipolar mode (-120 V to 120 V). In this operation mode, the piezo can provide a larger displacement stroke compared to the unipolar mode (-20 to 120 V). The piezoelectric material with no copper foam undergoes expansion and contraction during large temperature fluctuations on the order of 100 K. These contractions cause stress on the

ceramic, by preventing large temperature fluctuations due to heating the PZT copper foam design improves the lifetime. The properties of an actuator made from the lithium niobite piezo ceramic were studied for use in SRF cavity resonance control for the first time. The lithium niobate piezo ceramic actuator shows no heating but with a compromise of a smaller displacement stroke.

CHAPTER 6

RESONANCE CONTROL

During operation at 2 K, an SRF cavity will experience microphonics which will cause frequency detuning. The effects of microphonics were described in Chapters 4 and 2. When a cavity experiences frequency detuning more RF power must be used to maintain the nominal accelerating gradient. In low beam intensity linacs, a smaller RF power source is used to accelerate the beam. Microphonics are suppressed by using a tuner with a piezoelectric actuator. The reliability of the piezo actuator and the design of the tuner are discussed in Chapter 5. To prepare, cool down, and maintain the SRF cavity at 2 K requires a significant amount of resources. Therefore, a single cell elliptical copper cavity at room temperature was used to implement the hardware and develop a resonance control system. This approach accelerates the optimization of the control algorithm since no wait time is needed for an SRF cavity. The algorithm developed from this study can then be implemented in an SRF cavity at 2 K since the response of piezo control is the same. In the copper cavity section, the implementation of the two algorithms the proportional-integral (PI) control as well as the least means square algorithm (LMS) will be discussed. These algorithms can suppress microphonics and thus save RF power which will lower the cost of operation in a linac.

6.1 Resonance Control on a Copper Cavity

The resonance control algorithms and hardware were implemented in a 1.3 GHz single cell copper cavity shown in Fig. 6.1. The copper cavity was held together with four aluminum plates with threaded rods. In one of the plates, the thread was removed so that it could move freely with the piezo displacement. At the ends two piezo are attached, one piezo is used for resonance control and the other is used to drive noise and simulate microphonics. The hardware for the data acquisition is similar to the one used for transfer function measurement discussed in Chapter 3. The phase detector AD8302 again is used to measure the phase between the input forward and transmitted output power of the cavity. The phase of the forward and transmitted power can then be related to

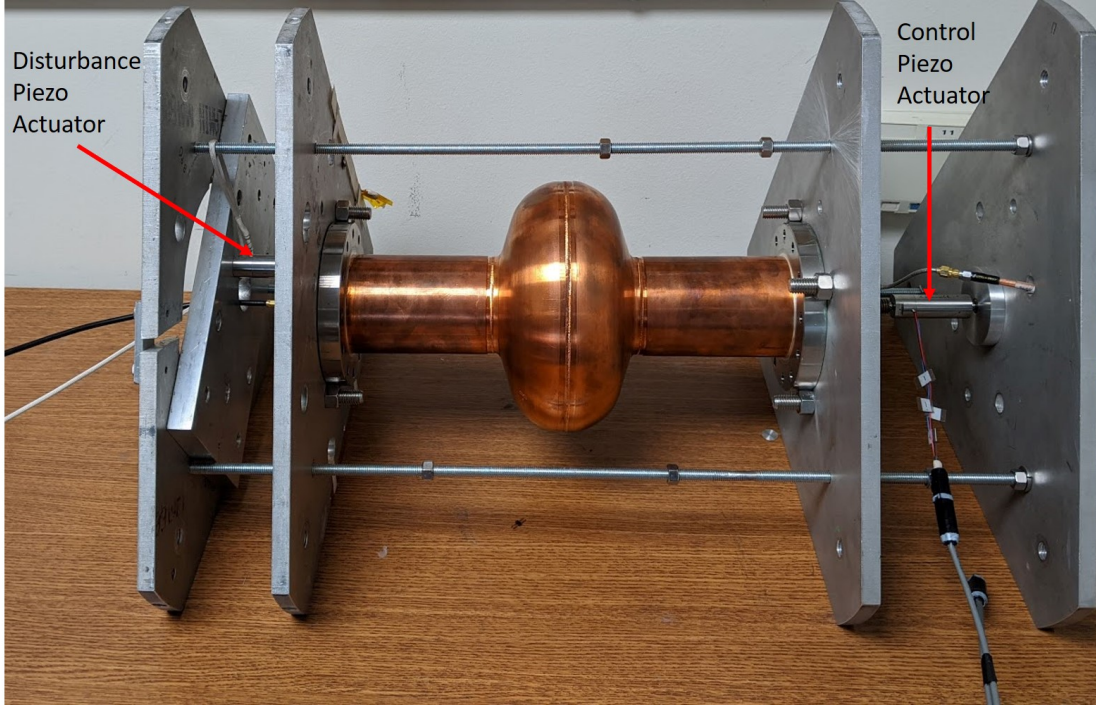


Figure 6.1: Setup of a single cell copper cavity for resonance control. The left side is driven by a piezo simulating the microphonics disturbance and the right side is driven by a piezo for compensation.

the frequency offset of the cavity by

$$\Delta f = \frac{f_0}{2Q_L} \tan(\phi) \quad (6.1)$$

where ϕ is the phase difference of the forward and transmitted power. The loaded Q_L is measured from the resonance curve of the cavity with a network analyzer. The cavity is driven by a master oscillator (MO) where the forward power is routed into the dual directional coupler, this signal along with the other signals that are needed for resonance control are shown in Fig. 6.2. From the dual directional coupler, the reflected power is measured in the LabVIEW program. At resonance, the reflected power is minimum, when the resonance of the cavity changes with respect to the MO the reverse power will increase. The phase between the forward (P_f) and transmitted power (P_t) from the phase detector are used to calculate the frequency shift of the cavity. The control algorithm is implemented in the National Instruments(NI) field-programmable gate array (FPGA) 7833R, the output is the control signal which goes into the piezo amplifier. An FPGA is used since

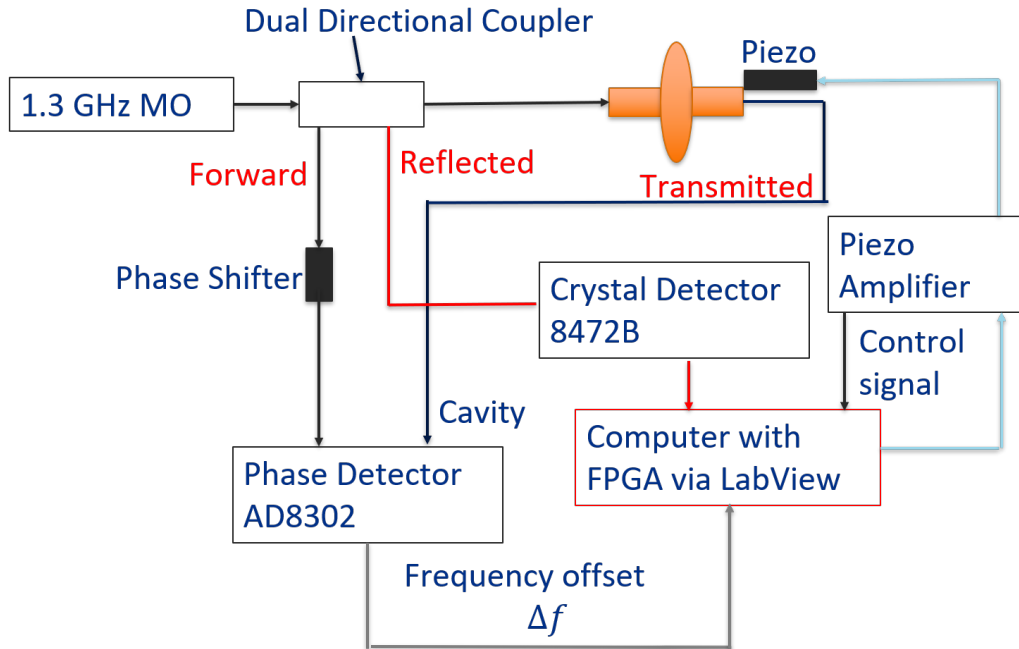


Figure 6.2: Resonance control algorithm setup, a master oscillator (MO) is used to drive the cavity. The forward and reverse power are measured from the dual directional coupler. The envelope of the reverse power is measured with a crystal detector.

the resonance control requires calculations in real-time without lagging which can occur in a CPU computer.

The copper cavity at room temperature has a thermal frequency sensitivity of 22 kHz/K and resonance control piezo has a frequency detuning sensitivity of 140 Hz/V. The testing is conducted at room temperature therefore the piezo is limited to a voltage range -20 V to 120 V. The bandwidth of the cavity in this setup at room temperature is 72 kHz and the resonant frequency is 1293.800 MHz. The mechanical modes of the cavity (transfer function) are determined similarly as discussed in Chapter 3. The piezo is driven by a sine wave with a frequency sweep from 1 to 750 Hz with each frequency lasting 2 seconds and one second off before moving to the next frequency value. During this frequency sweep the cavity frequency detuning is recorded, the results are shown in Fig. 6.3 (a). The cavity frequency detuning shows that when the driving frequency of the piezo is above 450 Hz the response increases. The cavity detuning goes from 500 Hz from piezo driving frequencies below 450 Hz to 9000 Hz cavity frequency detuning with a piezo driving frequency of 550 Hz. The

system's linearity was also checked and is shown in Fig. 6.3(b). This figure shows the spectrogram of the driving piezo frequency and cavity detuning. The diagonal line on the spectrogram shows detune frequency and driving piezo frequency. Adjacent to the diagonal line are two fainter lines with different slopes which are the harmonics of the system. This result demonstrates that the system can be approximated as linear since the adjacent lines are faint.

The longitudinal mechanical modes of this cavity system are 550 Hz, 625 Hz, and 700 Hz. These frequencies have a broad bandwidth spanning 100 Hz such as in the 550 Hz mode. In a 2 K testing environment, the main microphonics vibrations coupling to the cavity occur below 100 Hz, if this cavity setup was cooled to 2 K, then no microphonic noise sources would couple to the mechanical modes. It is still possible for other noise stemming from white noise or harmonics of the cavity-tuner system to couple to higher frequency vibration modes. In these studies, only vibrations below 100 Hz will be induced. This is based on the results from Chapter 4 which specified that all main contributions to detuning stemmed from vibrations below 100 Hz.

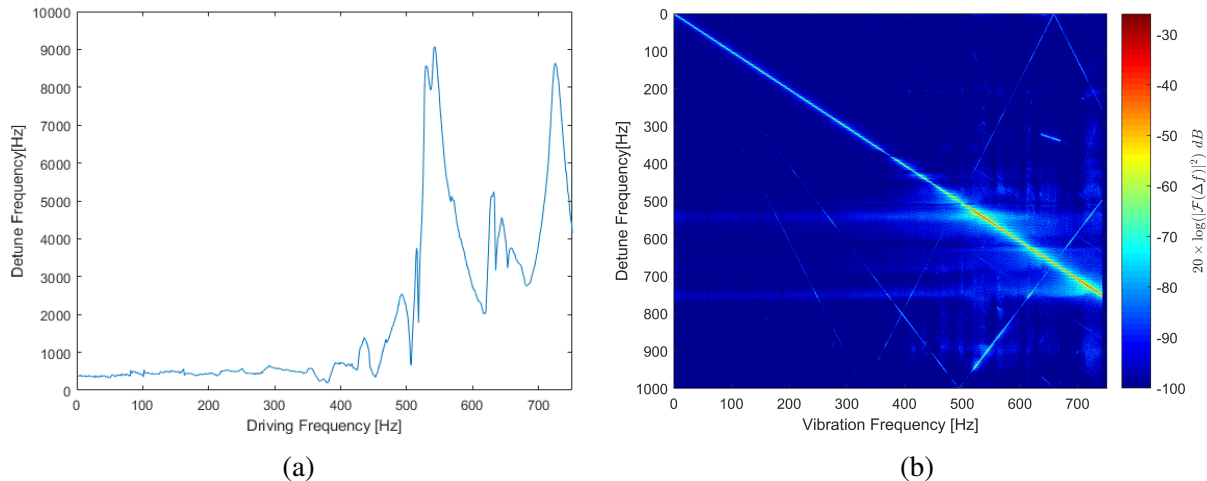


Figure 6.3: (a) Transfer function of copper cavity. (b) The harmonics of the system arise when the transfer function is taken. The main diagonal line is due to the stimulation of the piezo and the adjacent lines are the harmonics.

6.1.1 Resonance Control Algorithm

The implementation of the resonance control algorithm on the copper cavity setup was done using the disturbance piezo as a microphonics source and another piezo to correct for the vibration. Two algorithms were implemented, the proportional-integral (PI) and the least mean square algorithm (LMS). The PI control loop is a feedback control system while the LMS algorithm is a feedforward control system. The PI control loop is the most widely used control algorithm due to its simplicity and ease of implementation on hardware. The LMS algorithm is more sophisticated than the PI control loop but compared to other "intelligent" control algorithms it uses fewer hardware resources in the FPGA. Due to the limited memory and slices on the NI FPGA 7833R only these two algorithms were implemented.

The PI loop was tested by changing the cavity frequency from the MO (see Fig. 6.1). The implementation of the PI loop resulted in compensation for slow variations but it did not damp vibrations frequencies above 5 Hz. The higher frequency vibrations are damped with the LMS algorithm. The LMS algorithm can adapt to an amplitude and phase change of a sinusoidal vibration. The results shown in this section provide proof that the algorithms can be tested in a cryomodule environment.

6.1.2 PI Loop Control

The PI control was implemented in the FPGA to control temperature variations in real-time which are slow varying, taking hours for any noticeable frequency shift to be measured. The cavity frequency with respect to temperature is shown in Fig. 6.4. Large frequency shifts on the order of 30 kHz can be observed throughout the day. The PI control algorithm was first tested by shifting the MO driving frequency from the cavity frequency and then applying the PI loop control with different gains shown in Fig. 6.5. The integral control gain (K_i) is solely responsible for getting the cavity frequency to zero. As K_i increases the time to convergence to zero detuning gets smaller. At $K_i = 15$ it takes the PI control 5 s to get the cavity detuning to 0 Hz. Larger K_i values can be used to reach the 0 Hz detuning faster, there is a limit on this value ($K_i \approx 100$) since it can cause

instability. The proportional gain (K_p) does not affect reaching the setpoint faster together with K_i .

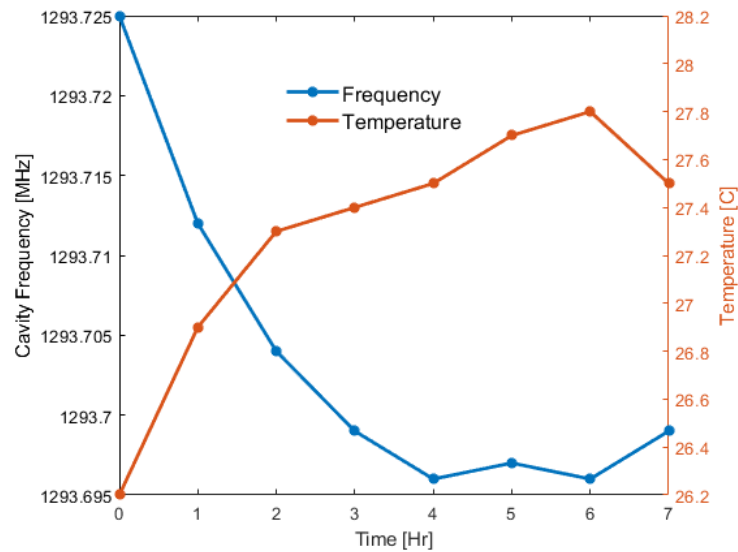


Figure 6.4: Temperature and frequency variation of the copper cavity.

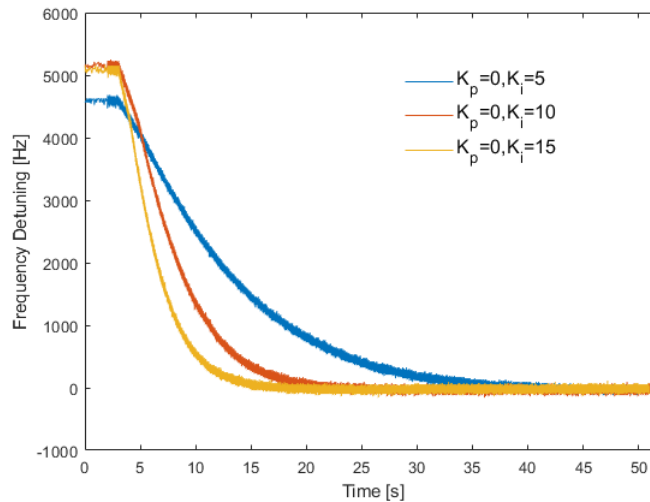


Figure 6.5: Compensation with integral gain only with frequency offset in the cavity.

In the cryomodule environment, the slow varying effects from helium pressure fluctuations on the cavity frequency can then be compensated with the PI loop control as shown above. The microphonics in the cryomodule also exhibit narrowband sinusoidal frequency. The PI loop control was used to control a 10 Hz vibration from the disturbance piezo. To cancel this frequency, the control needs to have destructive interference with the deformation of the disturbance piezo. The

integral control alone did not produce any damping of the vibration and very large gains (K_i 100 or more) are needed to reproduce the vibration signal. The proportional control reproduced the vibration signal from the cavity frequency with smaller gain values ($K_p = 1$ to 10). To have destructive interference the cavity frequency detuning and the control signal must have a phase of 0 degrees. A positive voltage (squeezing of the cavity) decreases the cavity detuning and negative voltage (relaxation of the cavity) increases the cavity detuning. The measurements taken with an oscilloscope shown in Fig. 6.6 demonstrate that with the current setup the frequency detuning signal and control signal are in phase. The phase between these two signals was swept but the best results for damping the 10 Hz vibration were obtained with a phase of 0 between the two signals. At 180 degrees the frequency detuning became worse since the interaction produce constructive interference.

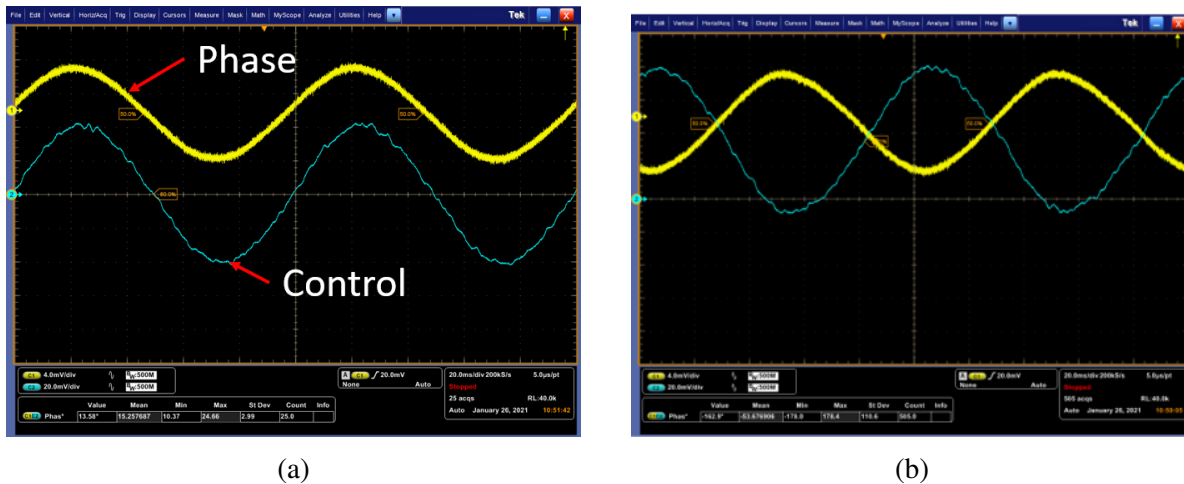


Figure 6.6: (a) Signal of the phase detector and control signal. The phase between them is close to 0 degrees. (b) A phase shift of 180 degrees was also implemented but the frequency detuning got worse.

The proportional K_p gain was increased until an instability was reached. The result of the highest proportional gain $K_p = 45$ attainable for the PI loop on the cavity detuning is shown in Fig. 6.7. With this proportional gain, the 10 Hz vibration begins to dampen, this can be seen in the cavity frequency detuning and on the histogram for the duration of the capture. An FFT of the cavity detuning shows that the PI loop gets rid of low vibration frequency noise as shown in Fig. 6.8(a) which can be attributed to the integral control. The 10 Hz peak bandwidth also gets

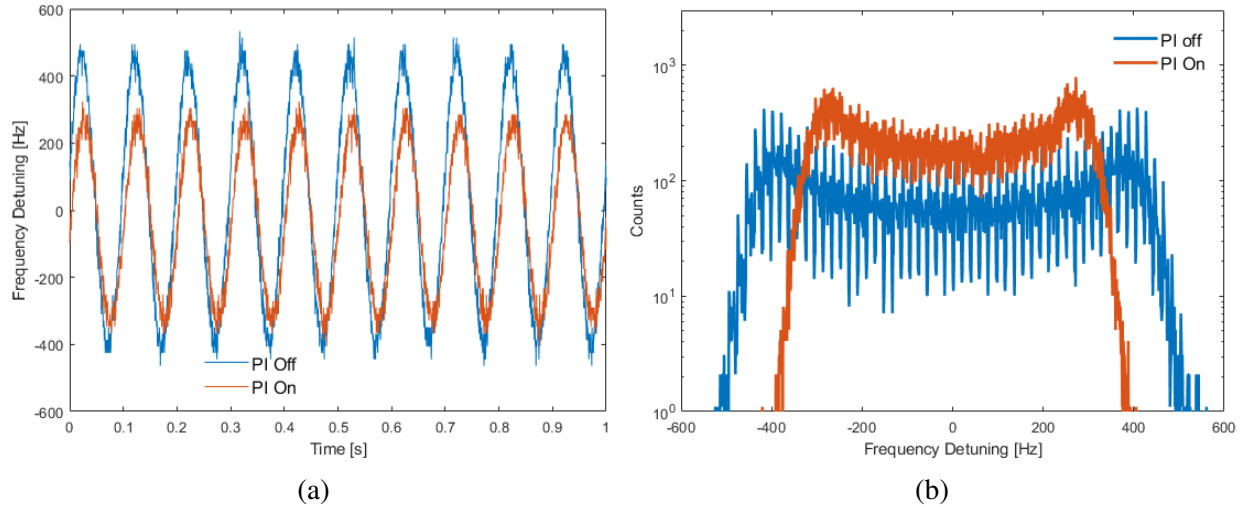


Figure 6.7: (a) Time series signal of the cavity frequency detuning with a 10 Hz vibration from the disturbance piezo. A proportional gain $K_p = 45$ and integral gain of $K_I = 15$ was used to dampen the 10 Hz vibration. (b) Histogram of the peak to peak values of the cavity detuning.

reduced but the peak is unchanged, likewise, the peaks of higher frequencies are not reduced. The integrated RMS cavity detuning is shown in Fig. 6.8(b), this value is equal to the RMS value and the main contributions of the spectra are shown as a jump of the curve. The integrated RMS value also gives the base noise frequency of the cavity. The RMS detuning is reduced from 270 Hz without the PI loop to 210 Hz with the PI loop. After a proportional gain of $K_p = 45$, the system reaches an instability. This instability arises due to the amplification of Gaussian white noise which is present in the frequency detuning signal. The Gaussian white noise stems from the phase detector. In the case of the integral control, the time step is 10^{-4} so this would need a large gain to start seeing the same effects as the proportional control. This amplification of the Gaussian white causes the system to couple to one of the cavity's mechanical modes, in this case, a mode around 750 Hz. This mode then becomes dominant and is still present even after a digital 4th-order Butterworth low pass filter is placed before the control output at a cut-off frequency of 300 Hz.

The PI control is limited to slow varying vibration frequencies and not apt for vibrations higher than 5 Hz due to instabilities in the control system. The PI loop amplifies noise and therefore cannot be used in this setup. Additionally, if the vibration changes in amplitude or phase the system will not be able to react quickly enough.

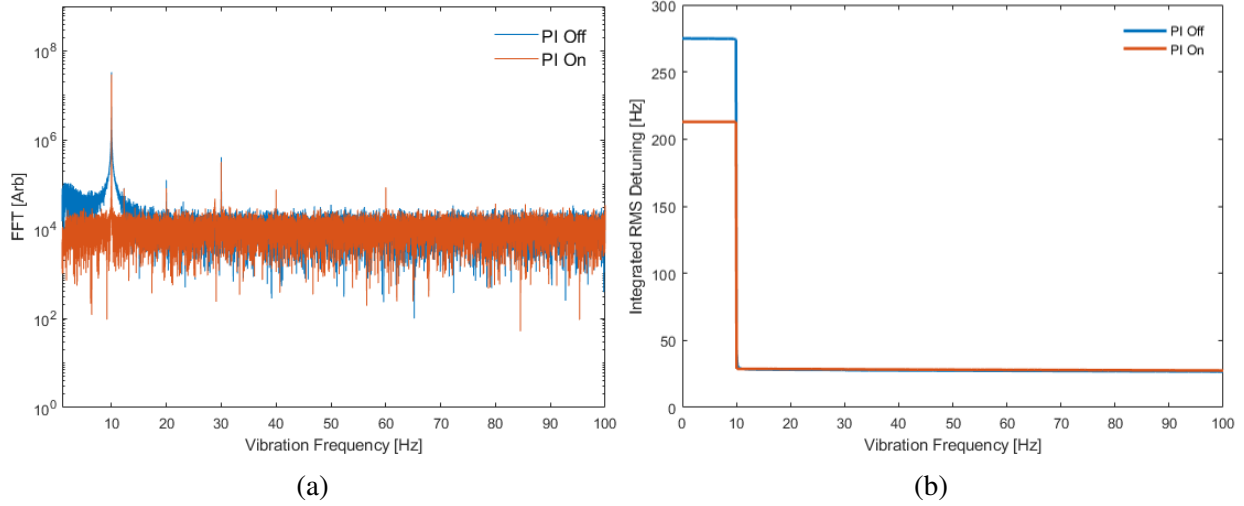


Figure 6.8: (a) FFT of cavity detuning with PI algorithm on and off, the gains were $K_p = 45$ and $K_I = 15$. (b) Integrated RMS frequency detuning with PI algorithm on and off.

6.1.3 LMS Theory

The least mean square (LMS) algorithm was used to overcome the limitation of the PI loop algorithm. The LMS algorithm is formulated using another algorithm which is known as the steepest-descent algorithm. A function $J(\mathbf{w})$ that is continuously differentiable with respect to an unknown weight vector \mathbf{w} will have an optimal solution \mathbf{w}_0 that satisfies [98]:

$$J(\mathbf{w}_0) \leq J(\mathbf{w}) \quad (6.2)$$

for all \mathbf{w} . The algorithm then consists of an iterative process where an initial guess $\mathbf{w}(0)$ generates a sequence of weight vectors $\mathbf{w}(1)$ and so on which reduces the function J . This is summarized as

$$J(\mathbf{w}(k+1)) < J(\mathbf{w}(k)) \quad (6.3)$$

where k is the iteration variable, this means that the updated weight vector will give a smaller value of J compared to the old value. In the steepest descent algorithm, the weight vector is updated by subtracting the old value by the gradient of the function that needs to be minimized. For this algorithm to be used the J function has to be differentiable with respect to the weight vector \mathbf{w} . The steepest-descent algorithm then is given by

$$\mathbf{w}(k+1) = \mathbf{w}(k) - \frac{1}{2}\mu\nabla_{\mathbf{w}}(J(\mathbf{w})) \quad (6.4)$$

where the gradient vector is with respect to \mathbf{w} and negative sign to denote the descent. The parameter μ is known as the learning rate and is generally small to reduce the amplification of noise. The LMS algorithm defines the function and how to take the gradient of that function. In this case, the function J is error squared which in this setup is the frequency measure from the cavity, $J = (\Delta f)^2$.

The schematic for the LMS algorithm for a resonant cavity is shown Fig. 6.9. The algorithm generally is implemented by using a reference signal and using a finite impulse filter (FIR) as shown in Refs. [99] and [53]. This approach generally takes up a significant amount of resources on the FPGA hardware, an algorithm that uses fewer resources is implemented in this thesis. The algorithm implemented in this thesis assumes that the microphonics noise spectrum can be approximated by a sum of sinusoids which was done by Refs.[100], [101], and [73]. The microphonics signal is then approximated by

$$m(t) = \sum_{i=1}^{\infty} A_i \sin(\omega_i t + \theta_i) \quad (6.5)$$

Likewise the control signal should be of the same form:

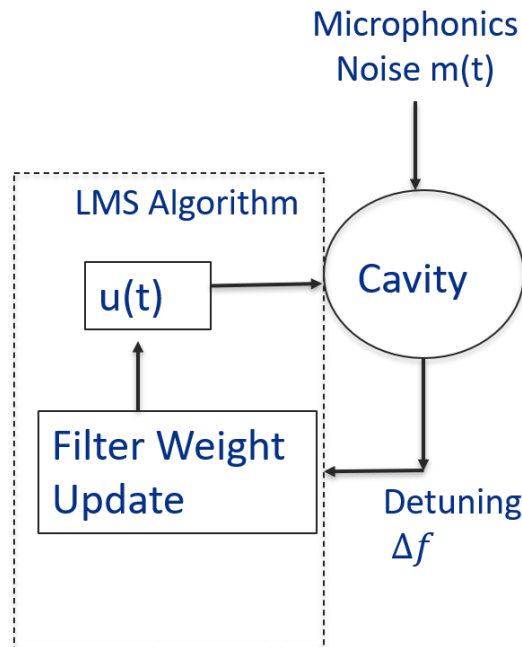


Figure 6.9: LMS algorithm schematic, the control $u(t)$ has a filter weight update based on the frequency shift of the cavity.

$$u(t) = \sum_{i=1}^N B_i \sin(\omega_i t + \phi_i) \quad (6.6)$$

To have destructive interference between these two signals the phase and amplitude should match. This of course can be done manually, but the LMS algorithm can adapt to these changes. To implement in the FPGA the in-phase(I) and quadrature (Q) method is used which is derived from trigonometric properties of the sine function yielding:

$$u_i = w_{1,i} \sin(\omega_i t) + w_{2,i} \cos(\omega_i t) \quad (6.7)$$

where the parameters $w_{1,i}$ and $w_{2,i}$ are linear and orthogonal. These parameters change the amplitude and the phase of the control signal. The parameters can be updated iteratively via the LMS algorithm yielding the equations

$$w_{1,i}[k+1] = w_{1,i}[k] + \mu_i \Delta f[k] \sin(\omega_i k - \phi_i) \quad (6.8)$$

$$w_{2,i}[k+1] = w_{2,i}[k] + \mu_i \Delta f[k] \cos(\omega_i k - \phi_i) \quad (6.9)$$

where k is the discrete-time sample and Δf is the frequency measured from the phase detector. This algorithm was implemented in the FPGA and the calculations were done in real-time. The only parameters that must be selected before the operation of the algorithm are the noise frequency ω_i which can be obtained from the microphonics spectrum, the phase of the system ϕ_i , and the learning rate μ .

The damping of the 10 Hz source was done with the LMS algorithm, the learning rate μ was changed to see the effects on the vibration source. In general, the value must be small to minimize the amplification of the noise from the detuning signal. The results with different learning rates are shown in Fig. 6.10 demonstrating that the larger the learning rate value the faster the response and the quicker the damping occurs. Note that for the $\mu = 0.01$ value the cavity frequency detuning experiences an overshoot due to the large amplitude from the control. At $\mu = 0.001$ the vibration is damped in 20 s while at $\mu = 0.01$ it takes 10 s. To prevent cavity detuning overshoot, the learning rate will be kept at $\mu = 0.001$. A 500 μ V Gaussian white noise was added to the driving signal of the disturbance piezo to simulate the environment in the cryomodule. This is equivalent to .07 Hz

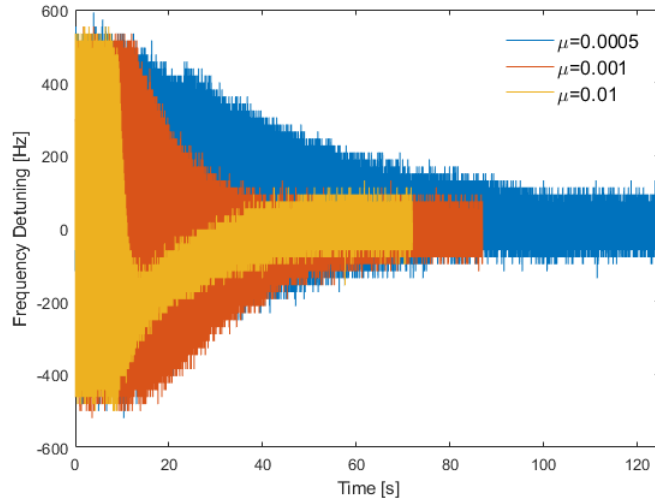


Figure 6.10: Cavity detuning with a 10 Hz vibration is damped with different learning rates μ . The large the μ value the faster the damping of the 10 Hz occurs.

of frequency detuning, note that a higher Gaussian white noise was not used due to issues with the piezo. The PI loop and the LMS algorithm were tested with this noise level for a 10 Hz vibration. The LMS algorithm completely damps the 10 Hz vibration and does not give rise to the higher frequency instability, the results are shown in Fig. 6.11.

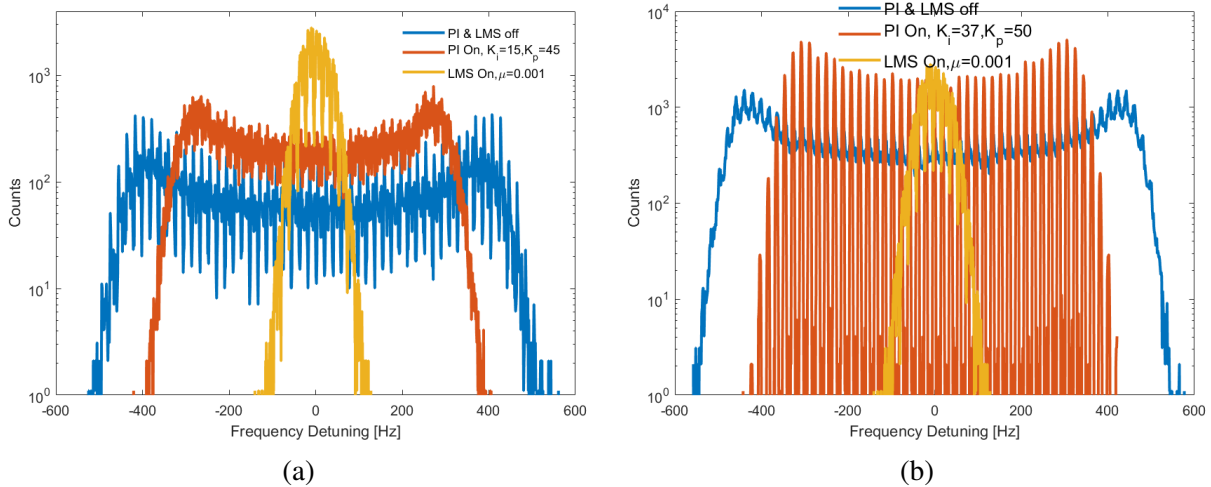


Figure 6.11: (a) Control using PI and LMS algorithms with no white noise added to the disturbance piezo. (b) Control using PI and LMS algorithms with white noise on the disturbance piezo.

The adaptation to phase and amplitude of the vibration noise was done by changing these parameters of the disturbance piezo voltage. The 10 Hz vibration in the disturbance piezo voltage

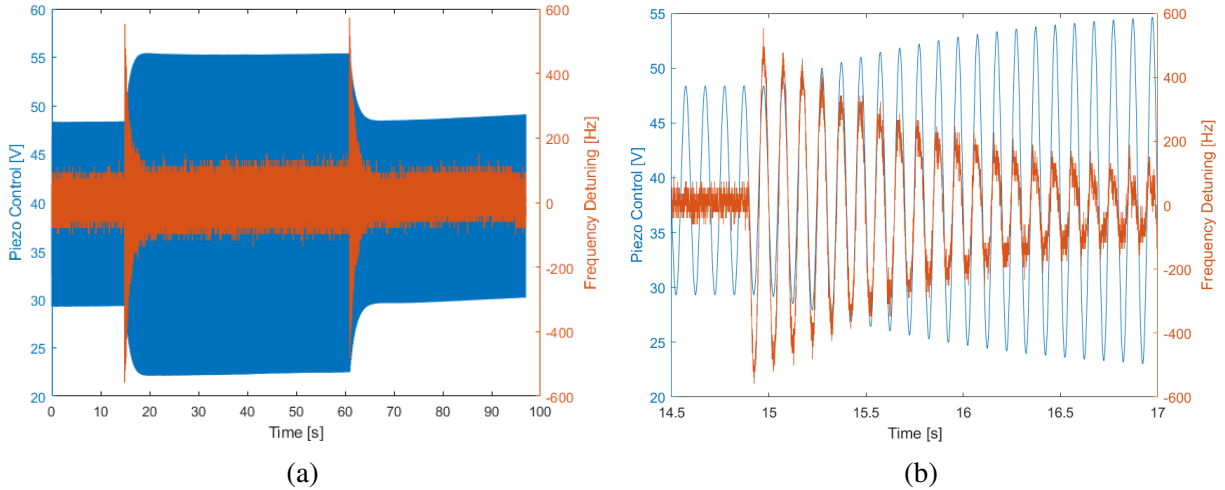


Figure 6.12: (a) Piezo control voltage (left) and cavity frequency detuning (right). The disturbance piezo voltage is doubled changing the cavity frequency detuning. (b) A closer look at the point where the piezo disturbance signal is doubled, the piezo control signal adapts to this change by increasing the voltage.

was doubled and the LMS algorithm adapted to this change which is shown in Fig. 6.12 (a). The learning rate used for this trial was $\mu = 0.001$, note that if a higher value was used the phase signal would reach nominal value faster. The piezo control signal is also doubled as shown in Fig. 6.12(b) which shows the amplitude at a time at the time of change close to 15 s. Note that the time of convergence to damp the vibration is shorter (2s) than the earlier trial which varied the learning rate. This is because the weight vector w already has information on the vibration. Similarly, the phase of the disturbance piezo signal was changed from 0 degrees to 180 degrees, the LMS algorithm also adapted to this change shown in Fig. 6.13 (a). The piezo control signal changed the phase also and can be seen in Fig. 6.13 (b). The convergence time for the phase change is longer at 4 s. The adaptation to both amplitude and phase from the vibration noise shows that the algorithm will work well in the cryomodule environment. No instability was reached during this trial.

When the cavity is located in the cryostat or the cryomodule it will experience several narrow bandwidth sinusoidal vibrations. The LMS algorithm needs to dampen each of these vibration disturbances without each control interfering with one another. A 10 and 80 Hz vibration was driven by the disturbance piezo to check the adaptability to two different frequencies. Adaptation for two different frequencies requires 4 weight vector w_i and two different input frequencies ω_i .

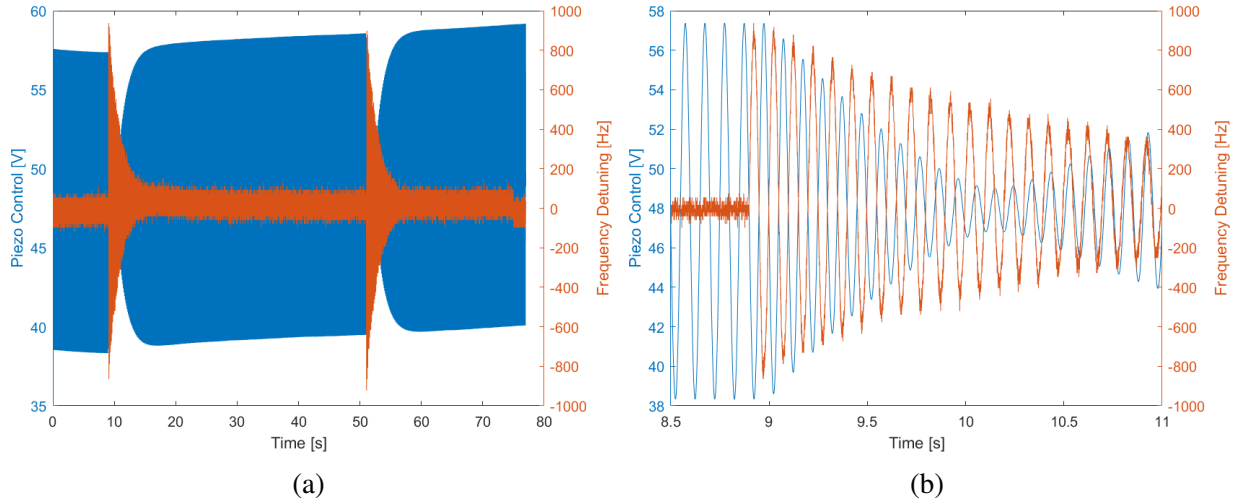


Figure 6.13: a) Piezo control and cavity detuning signal, the disturbance piezo signal phase is changed from 0 to 180 degrees. (b) A closer look at the control signal shows that the phase also changes to adapt and dampen the vibration.

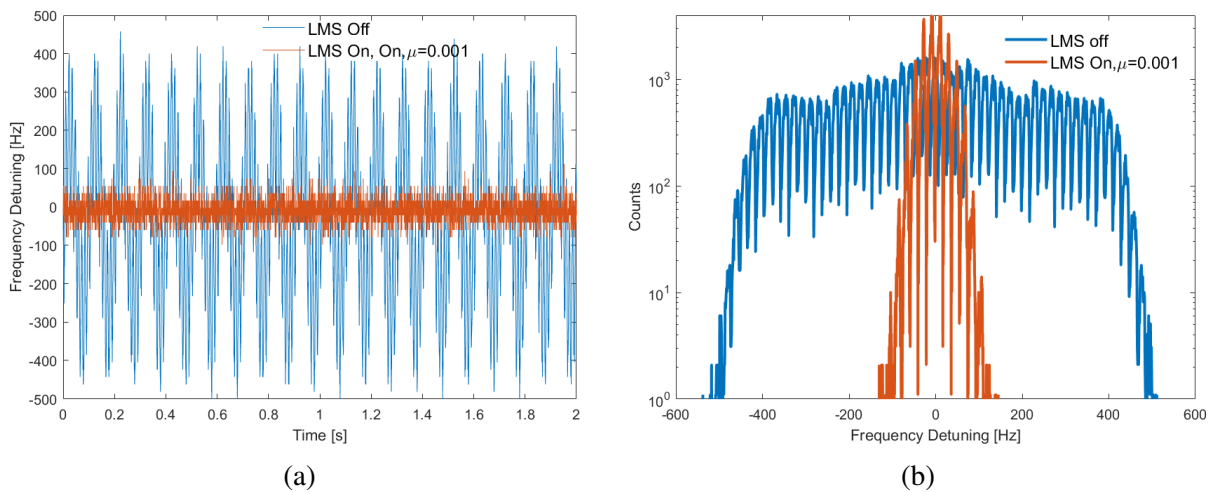


Figure 6.14: (a) Cavity frequency detuning with the LMS algorithm turn on and off with 10 and 80 Hz vibrations. (b) Histogram cavity frequency detuning with the LMS algorithm on and off.

The learning rate used for both of these two responses was $\mu = 0.001$. The cavity frequency detuning results are shown in Fig. 6.14. After the LMS algorithm was turned on, cavity frequency detuning shows the base detuning. The 10 and 80 Hz signal are completely damped, the results for the entire capture is shown in the integrated RMS detuning Fig. 6.15. During the damping of these two frequencies, no instability was observed. The successful implementation and suppression of two vibration sources demonstrate that the LMS algorithm control won't interfere with one another.

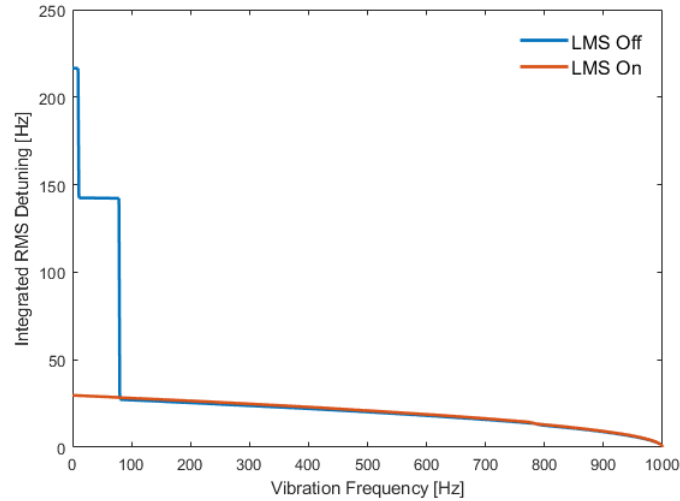


Figure 6.15: Integrated RMS cavity frequency detuning with the LMS algorithm on or off. The vibrations damped are 10 and 80 Hz.

6.1.4 Stability of Control Algorithm

The stability of the algorithm can be studied by studying the control signal and checking for harmonics that can couple to the cavity's mechanical modes. The effects on the control signal at the monitor of the piezo amplifier were recorded to probe the differences between both the PI loop and the LMS algorithm. To prevent coupling to one of the mechanical modes of the cavity the output control was passed through a 4th-order Butterworth low-pass filter with a cut-off frequency of 300 Hz. The control signal for the PI loop shown in Fig. 6.16(a) shows that the drop-off of the frequency level spectrum at 300 Hz. The spectrum below 300 Hz is one order of magnitude higher than the spectrum above 300 Hz. There are also several peaks below 300 Hz which are high but are not large enough to overtake the 10 Hz driving signal of the control. In the case of the LMS control signal the frequency level drop off is much steeper as shown in Fig. 6.16(b). There are harmonics of 10 Hz but the main 10 Hz peak is several orders of magnitude higher than the others. The magnitude of the learning rate does not increase the level of harmonics observed in the control spectrum as shown in Fig. 6.17. Although the higher-order harmonics level is small it should be observed to prevent coupling to the higher frequency mechanical modes of the cavity.

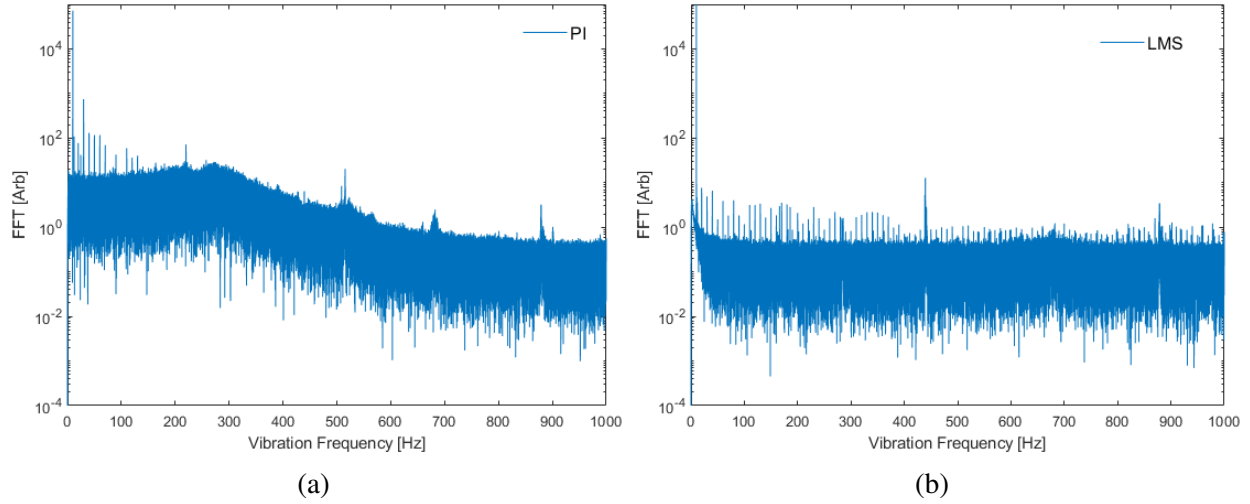


Figure 6.16: (a) Control signal for the PI loop control at $K_p = 37$ and $K_I = 50$ for 10 Hz vibration (b) Control signal with LMS algorithm on for a 10 Hz vibration.

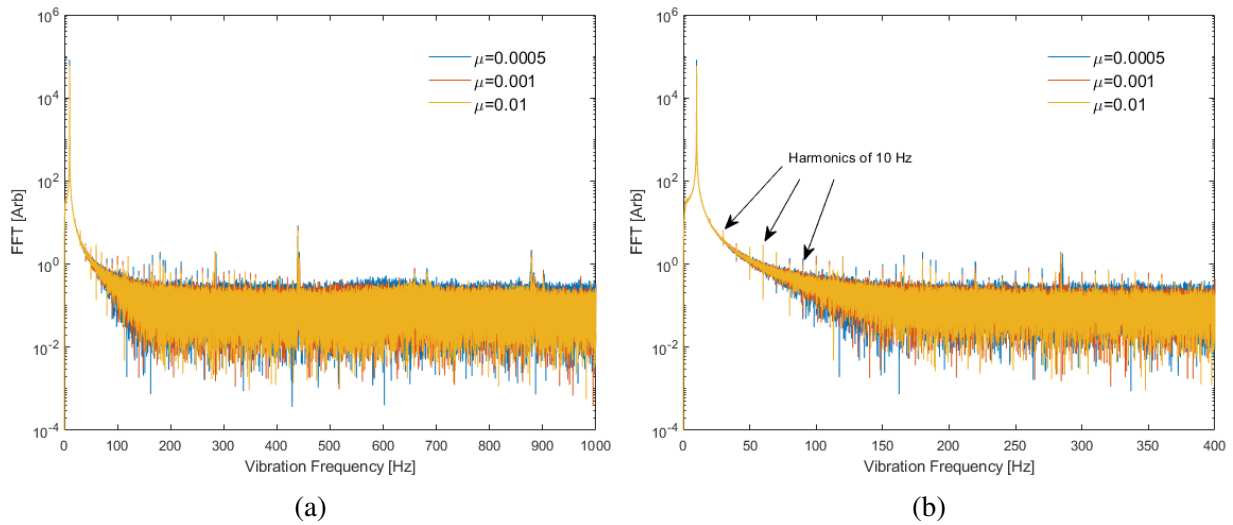


Figure 6.17: (a) LMS control with different learning rates μ . (b) Zoom in showing vibration harmonics from the 10 Hz.

6.1.5 Limitations of Piezo Actuators

The limitation of the piezo actuator tuner is that it can only compress the cavity longitudinally. Therefore, this setup will be most effective at controlling longitudinal modes. It was shown in Chapter 3 that the longitudinal modes produce the largest frequency detuning response. The frequency detuning response from the longitudinal modes is 2 to 3 times larger than the transverse modes. From Chapter 4, it was also shown that the majority of vibrations occur below 100 Hz.

In this region based on the warm transfer function measurement the response is constant. In a constant response this tuner will be able to compensate for vibrations that couple to the cavity. The mechanical modes of the cavity are different when the RF coupler and other ancillaries are installed as show in Refs. [102] and [53]. There is one transverse mode that is attributed to the RF coupler cavity mode. The response again is small but the piezo control can damp it as shown in [102]. This tuner will be most effective when a vibration coupling to the cavity is longitudinal or the response from the vibration is constant. The tuner does not completely damp the transverse modes but these mode do not cause large detuning.

6.2 Summary of Chapter

Active microphonics compensation requires the use of a piezoelectric actuator installed in a tuner. The results from Chapter 4 demonstrate that up to 70 % of vibration sources in the cavities operated in CW are below 100 Hz. It is expected that this behavior will be also observed in future CW linacs such as for the PIP-II project. The resonance control algorithm was optimized using a warm cavity and a modified tuner due to the significant resource required to bring an SRF cavity to 2 K. The algorithms were implemented in an FPGA using LabVIEW. A PI loop was used to compensate for slow varying vibrations (less than 5 Hz). The successful PI loop implementation at room temperature demonstrates that this algorithm should be able to control the liquid helium pressure variation experienced by the cavity at 2 K. The PI loop will also damp other slow varying vibrations. For vibrations above 5 Hz, the LMS algorithm was used. Two sinusoidal vibrations with white Gaussian noise added were suppressed using the LMS algorithm. The algorithm showed rapid damping of these vibrations. This algorithm can be used in the cryomodule setting. By damping these vibrations, RF power will be saved, and the linac will be able to operate without interruptions due to microphonics.

CHAPTER 7

CONCLUSION

During beam operation, the linac must provide continuous beam delivery to the target or for particle-on-particle collisions for experiments. For low beam intensity linacs in CW operation, the power needed to provide energy to the beam, depending on the particle being accelerated, is on the order of 10-50 kW. This results in a large loaded quality factor yielding a narrow cavity bandwidth ranging from 10 Hz to 50 Hz. The power source used for operation will add a buffer of 10-30 kW for microphonics or other instabilities in the RF feedback loops to maintain constant accelerating. If the microphonics vibration leads to a detuning of the cavity greater than the available power buffer, the cavity will not be operational, leading to linac downtime. The mechanism that produces microphonics and how to damp them were presented in this thesis.

A lumped-circuit model was presented to study the cavity behavior under microphonics in Chapter 2. This model also included a method to estimate the width of the hysteresis instability that occurs in narrowband high gradient linacs. Future work can expand this model to include the behavior of the cavity when quenching and with the beam. The code can later be transferred to an FPGA for more realistic simulations of hardware configurations to aid corrections. In Chapter 3 the mechanical modes of a 650 MHz cavity were measured for the first time. This information was used to model the behavior of the cavity with the lumped-circuit model. Future work can be done to improve the time of acquisition of the transfer function by using a frequency chirp instead of a sine wave. This could cut the time of measurement in half.

In Chapter 4, passive mitigation techniques were implemented to reduce the cavity frequency detuning by a factor of 4. Despite these passive mitigation techniques, the cavities still experience frequency detuning due to microphonics. The frequency detuning of 96 cavities along with multiple cryogenic parameters was analyzed for 12 cryomodules for the LCLS-II project. The results demonstrate that cryogenic parameters can strongly affect cavity frequency detuning. Helium pressure variation is the main frequency detuning contribution for vibrations below 10 Hz. On

average, 70 % of vibrations contributing to frequency detuning are below 100 Hz. These results provide a set point for cavity design to prevent mechanical modes under 100 Hz. Future studies such as a simulation of superfluid helium with a heat load are needed to check quantum turbulence.

Chapter 5 introduces the development of a new double lever tuner for the PIP-II 650 MHz elliptical cavities. The same tuner can be used for 644 MHz cavities being developed for the FRIB energy upgrade. The measurements of the tuner on a mock cavity improved the ANSYS simulations. These simulations led to a doubling of the tuner stiffness from 20 kN/mm to 40 kN/mm by changing the location of the piezos and modifying the tuner arms. In addition to improving the stiffness of the tuner, the dielectric heating of the piezo at high voltage was also studied for application SC cavities operating in a pulsed mode. This work led to a discovery of a deviation from the dielectric heating formula found in scientific literature. The culprit behind the large deviation is the capacitance and dissipation factor; these values increased with respect to voltage. Positive thermal feedback also contributed to the heating; the feedback only occurs when a voltage greater than 50 V is used in the PICMA piezo. A time-dependent temperature model was developed to estimate the heating and thermal properties of the piezo. This model can be used to estimate the heat load of the piezo on the cavity.

To mitigate the effects of this runaway heating, a novel piezoelectric actuator design with improved cooling was developed and tested yielding a reduction of heating by a factor of 14 at liquid helium temperatures. This new design also succeeded in stopping the positive thermal feedback. The properties of lithium niobate piezo for use in SRF cavity resonance control was tested for the first time. Lithium niobate shows no heating but with a compromise of a smaller stroke. The improvements in heat dissipation allow the piezo to operate in bipolar mode doubling the stroke. A smaller temperature rise will result in smaller piezo strain. This will result in an improved lifetime of the piezoelectric material. Future work can be done to further optimize different piezoelectric materials which have a large stroke but produce little heat dissipation. Additionally, other high thermal conductivity materials such as sapphire or diamond can be used in contact with the ceramic to reduce the need for a heat sink.

Chapter 6 describes two resonance control algorithms implemented in an FPGA using LabVIEW. A PI loop was used to compensate for slow varying vibrations (less than 5 Hz). The successful PI loop implementation at room temperature demonstrates that this algorithm will be able to control the liquid helium pressure variation experienced by the cavity at 2 K. The PI loop will also damp other slow varying vibrations. For vibrations above 5 Hz, the LMS algorithm was used. Two sinusoidal vibrations with white Gaussian noise added were suppressed using the LMS algorithm. To mitigate non-linear and stochastic vibrations a higher performance FPGA is needed. Future work will target non-linear and stochastic vibrations of the cavity.

APPENDIX

A.1 Linear and Non-linear Harmonic Oscillator

The damped harmonic oscillator has the form:

$$\ddot{x} + 2\alpha\dot{x} + \omega_o^2x = 0 \quad (1)$$

There are three general cases for which the equation above can be solved, one is for the weak damping ($\omega_o^2 > \alpha^2$), the critical damped case ($\omega_o^2 = \alpha^2$), and lastly the strong damped case ($\omega_o^2 < \alpha^2$). The harmonic oscillator will be solved with weak damping which is what is observed for a cavity. The solution to the weak damped harmonic oscillator is given by

$$x_c(t) = Ae^{-\alpha t} \cos(\omega_1 t - \phi) \quad (2)$$

where $\omega_1 = \sqrt{\omega_o^2 - \alpha^2}$, A and ϕ are set by the initial conditions. The solution shows that the motion of the harmonic oscillator decays and is also sinusoidal. Note that measuring the decay of the system will give the damping value. The driven harmonic oscillator is given by

$$\ddot{x} + 2\alpha\dot{x} + \omega_o^2x = D \cos(\omega t) \quad (3)$$

The particular solution for this equation is

$$x_p(t) = D \cos(\omega t - \gamma)$$

plugging $x_p(t)$ into Eq. 3 and after some algebra the phase (γ) and amplitude (D) can be obtained as

$$\tan(\gamma) = \frac{2\omega\alpha}{\omega_o^2 - \omega^2} \quad (4)$$

$$D = \frac{A}{\sqrt{(\omega_o^2 - \omega^2)^2 + 4\omega^2\alpha^2}} \quad (5)$$

The general solution to Eq 3 is the sum of particular solution and complementary solution $x(t) = x_c + x_p$. After a long time, the transient effects from x_c dampen and only x_p is present. The amplitude D and phase (γ) of the particular solution are frequency dependent as shown in Fig. .1. As the driving frequency deviates from the natural frequency of the system the amplitude

and phase change. During operation the cavity's natural frequency changes due to deformations caused by vibration noise. This causes a decrease in the accelerating gradient of the cavity. The degree of damping in an oscillating system can be defined in terms of the quality factor

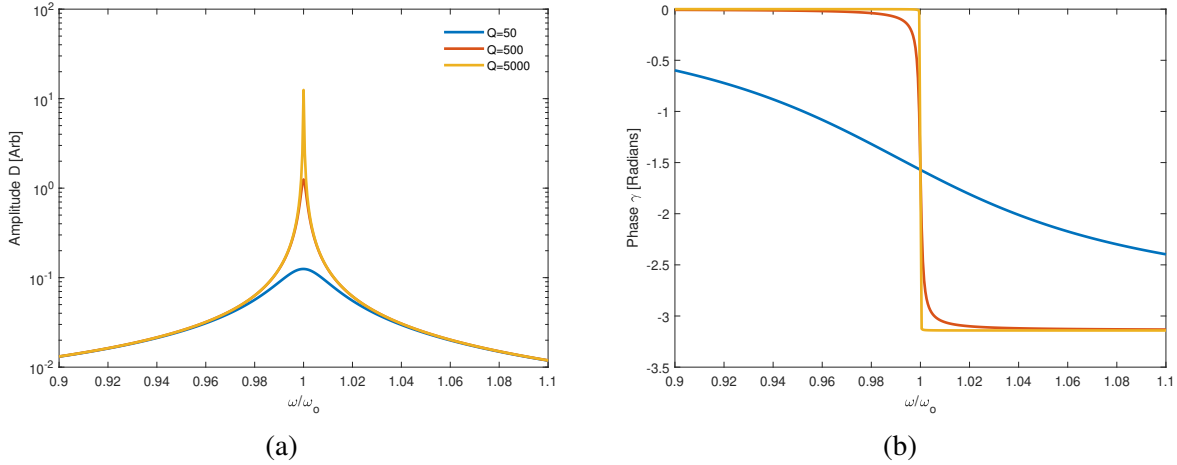


Figure .1: The amplitude and phase of the harmonic oscillator with different Q values. (a) Amplitude of the harmonic oscillator with respect to the driving frequency. (b) Phase of the harmonic oscillator with respect to the driving frequency.

Q. The quality factor is defined as the ratio of the energy stored to the energy loss per cycle ($Q = 2\pi \frac{\text{energy stored}}{\text{energy dissipated per cycle}}$). For a damped harmonic oscillator this becomes $Q = \frac{\omega_R}{2\alpha}$ where $\omega_R = \sqrt{\omega_0^2 - 2\alpha^2}$ is the frequency where the amplitude D is maximum ($\frac{dD}{d\omega} = 0$). Large damping in the system results in large energy loss yielding a small Q. For a system with small damping, the energy loss is small yielding a large Q. The intrinsic quality factor Q_o factor is a figure of merit of SRF cavities which can be as high as 10^{11} due to the small resistance.

For a weakly damped oscillator the Q can be related to the bandwidth ($\Delta\omega$) of the resonance curve as $Q = \frac{\omega_0}{\Delta\omega}$. As the quality factor of the system increases the bandwidth of resonance decreases. A smaller bandwidth results in a more challenging operation for a harmonic oscillator. During beam operation, the bandwidth of the cavity will be determined by the loaded quality factor which includes all losses in the system. For a low beam intensity linac, this can range from 10 to 50 Hz. The behavior of the cavity with detuning can thus be characterized by the amplitude and phase of the resonance curves.

A.2 Duffing Equation

The resonance curve of a cavity is expected to be in the linear regime similar to Fig. .1. Experimental data demonstrate that cavities experience a non-linear resonance curve [Tesla]. This type of resonance curve is observed in the Duffing equation which describes the behavior of a non-linear harmonic oscillator. The resonance curve behavior is shown in Fig. .2 which is characterized by two different frequency sweeps. If the driving frequency Ω is increasing the amplitude will jump up at a frequency known as the jump-up frequency Ω_u and if it's moving down the amplitude will jump down at the jump-down frequency Ω_d . In this region of the resonance curve the amplitude is multivalued, where the driving frequency can give rise to two different amplitudes. Only one of the branches results in stable operation while the other branch cannot be maintained due to instability. In an SRF cavity, the width of this hysteresis is given by the frequency offset caused by the accelerating gradient $\Delta f = k_L E_{acc}^2$. This frequency shift is known as Lorentz force detuning (LFD). The analytical form of the jump-up and jump-down frequencies will be derived.

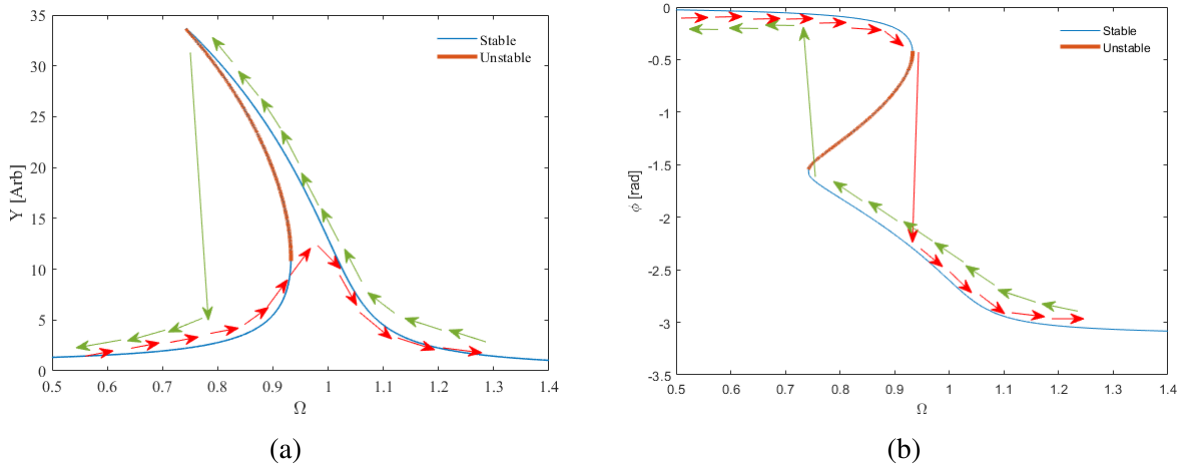


Figure .2: (a) Amplitude plot of Duffing equation with instability hysteresis. The x-axis is given by the normalized frequency Ω . (b) Phase plot with instability hysteresis.

The Duffing Equation describes a non-linear 1D harmonic oscillator given by

$$m\ddot{x} + c\dot{x} + k_1x + k_2x^3 = F\cos(\omega t) \quad (6)$$

where m is the mass, c is the damping coefficient, and a spring with a cubic non-linear restoring

force $k_1x + k_3x^3$ which is excited by a driving force of $F\cos(\omega t)$. If $k_3 > 0$ the spring is said to be hardening and if $k_3 < 0$ the spring is becoming softer. The duffing equation does not have an analytical solution but can be solved numerically. The goal of studying the Duffing Equation is to obtain the resonance curve and the jump resonance frequencies. This can be done using the Harmonic Balance Method (HBM) which is discussed by M.J. Brennan et al. [103]. In the following the main results of the paper will be shown as well as the results from plots derived from the formulas.

For convenience the Duffing Equation is written in non-dimensional form as

$$\ddot{y} + 2\alpha\dot{y} + y + \beta y^3 = \cos(\Omega\tau) \quad (7)$$

where

$$y = \frac{x}{x_o}, \beta = \frac{k_3x_o^2}{k_1}, \alpha = \frac{c}{2m\omega_o}, \omega^2 = \frac{k_1}{m}, \tau = \omega_o t, \Omega = \frac{\omega}{\omega_o}$$

with $x_o = F/k_1|_{k_3=0, \omega=0}$. Applying the HBM and assuming a solution of the form $y = Y\cos(\Omega\tau + \phi)$ yields the frequency amplitude relationship detailed in [103]

$$\left(\frac{3}{4}\beta Y^3 + (1 - \Omega^2)Y\right)^2 + (2\alpha\Omega Y)^2 = 1 \quad (8)$$

Solving for Ω in Eq. 8 and assuming that damping is small such that $\alpha^2 \ll 1$ leads to two positive solutions

$$\Omega_{1,2} \approx \sqrt{1 + \frac{3}{4}\beta Y^2 \pm \sqrt{\frac{1}{Y^2} - 4\alpha^2(1 + \frac{3}{4}\beta Y^2)}} \quad (9)$$

and the phase is given by

$$\tan \phi = -\frac{2\alpha Y \Omega}{\frac{3}{4}\beta Y^3 + (1 - \Omega^2)Y} \quad (10)$$

These equations yield real values of Ω provided that terms in the square roots are positive. Equations 9 and 10 are used to make Fig. .3 with a damping ratio of $\alpha = 0.02$. The plot shows the resonance curves for a softening spring ($k_3 < 0$ and $\beta = -$) which are left leaning, a linear system with ($\beta = 0$), and a hardening spring ($k_3 > 0$ and $\beta = +$). Fig. .3 shows that for a softening spring system the amplitude of the system increases as β decreases compared to the linear system. In the

case of the hardening system the amplitude decreases as β increases. The jump-up and jump-down frequencies are also affected by the size and sign of β .

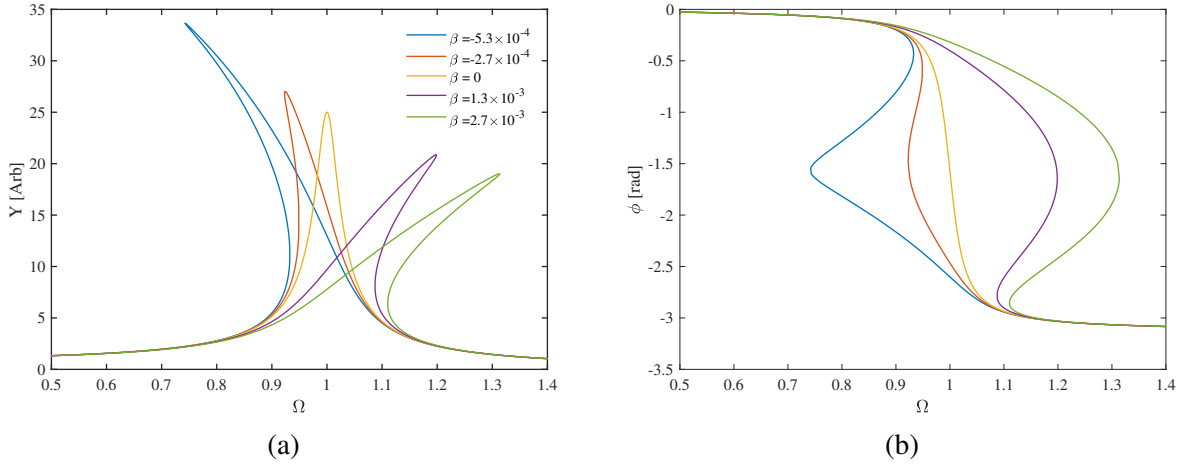


Figure .3: The Amplitude and frequency response of the Duffing oscillator is shown with a damping coefficient of $\alpha = 0.02$. The left leaning curves show a softening spring system with β being negative and the right leaning curves show a hardening system with β . (a) Amplitude of the resonance curve for the Duffing oscillator. (b) Phase of the Duffing oscillator.

The normalized jump-up and jump-down frequencies and amplitudes are calculated using HBM in [103]. The jump-up frequency is given by

$$\Omega_u = 1 \pm \frac{1}{2} \left(\frac{3}{2} \right)^{4/3} |\beta|^{1/3} \quad (11)$$

where the - denotes the jump-up frequency for a softening system and a + denotes the hardening system. The amplitude at the jump-up frequency is given by

$$Y_u = \left(\frac{2}{3} \right) \frac{1}{|\beta|^{1/3}} \quad (12)$$

which is the same for both the softening and hardening system. The jump-down frequency is given by

$$\Omega_d \approx \frac{1}{\sqrt{2}} \left(1 + \left(1 + \frac{3\beta}{4\alpha^2} \right) \right)^{1/2} \quad (13)$$

which is the same for both the softening and hardening system. The amplitude at this frequency which is the maximum is the same for both cases given by

$$Y_d \approx \left(\frac{2}{2\beta} \left(\left(1 + \frac{3\beta}{4\alpha^2} \right)^{1/2} - 1 \right) \right)^{1/2} \quad (14)$$

With these set of equation the jump frequencies can be calculated and the hysteresis obtained. The jump frequencies are used to estimate the region of operation for a pulsed low beam intensity linac if no tuner is available. One last important property of the Duffing equation is that it can exhibit chaos making it very sensitive to initial conditions. The system can be classified to exhibit chaos by generating a Poincare map, a more detail discussion of chaos for the Duffing equation is done by Ref. [104].

BIBLIOGRAPHY

BIBLIOGRAPHY

- [1] A. Seryi. *Unifying Physics of Accelerators, Lasers and Plasma*. CRC Press, July 29, 2015. 284 pp.
- [2] G. Ising. *Prinzip einer Methode zur Herstellung von Kanalstrahlen hoher Voltzahl*. Ark. Mat. Astron. Fys. Pages: 1 Volume: 18. 1924. URL: <https://cds.cern.ch/record/433984>.
- [3] R. Wideröe. “Über ein neues Prinzip zur Herstellung hoher Spannungen”. In: *Archiv f. Elektrotechnik* 21.4 (July 1, 1928), pp. 387–406. DOI: 10.1007/BF01656341.
- [4] T. P. Wangler. *RF Linear Accelerators*. Google-Books-ID: 5EO4_nyndUMC. John Wiley & Sons, Mar. 3, 2008. 476 pp.
- [5] H. Padamsee, J. Knobloch, and T. Hays. *RF Superconductivity for Accelerators, 2nd Edition* | Wiley. Wiley.com. URL: <https://www.wiley.com/en-us/RF+Superconductivity+for+Accelerators%2C+2nd+Edition-p-9783527408429>.
- [6] P. Ostroumov and F. Gerigk. “Superconducting Hadron Linacs”. In: *Rev. Accl. Sci. Tech.* 06 (Jan. 2013), pp. 171–196. DOI: 10.1142/S1793626813300089.
- [7] N. W. Ashcroft and N. D. Mermin. *Solid State Physics*. Holt, Rinehart and Winston, 1976. 868 pp.
- [8] C. Buchal, F. Pobell, R. M. Mueller, et al. “Superconductivity of Rhodium at Ultralow Temperatures”. In: *Phys. Rev. Lett.* 50.1 (Jan. 3, 1983). Publisher: American Physical Society, pp. 64–67. DOI: 10.1103/PhysRevLett.50.64.
- [9] M. Kostrzewa, K. M. Szczeńśniak, A. P. Durajski, et al. “From LaH10 to room-temperature superconductors”. In: *Sci Rep* 10.1 (Dec. 2020), p. 1592. DOI: 10.1038/s41598-020-58065-9.
- [10] C. Kittel, K. Charles, H. Kroemer, et al. *Thermal Physics*. Google-Books-ID: c0R79nyOoNMC. Macmillan, Jan. 15, 1980. 500 pp.
- [11] F. London, H. London, and F. A. Lindemann. “The electromagnetic equations of the supraconductor”. In: *Proceedings of the Royal Society of London. Series A - Mathematical and Physical Sciences* 149.866 (Mar. 1, 1935). Publisher: Royal Society, pp. 71–88. DOI: 10.1098/rspa.1935.0048.
- [12] C. J. Gorter and H. Casimir. “On supraconductivity I”. In: *Physica* 1.1 (Jan. 1, 1934), pp. 306–320. DOI: 10.1016/S0031-8914(34)90037-9.

- [13] J. Bardeen, L. N. Cooper, and J. R. Schrieffer. “Theory of Superconductivity”. In: *Phys. Rev.* 108.5 (Dec. 1, 1957), pp. 1175–1204. DOI: 10.1103/PhysRev.108.1175.
- [14] A. Gurevich. “Superconducting Radio-Frequency Fundamentals for Particle Accelerators”. In: *Reviews of Accelerator Science and Technology* (Jan. 27, 2013). Publisher: World Scientific Publishing Company. DOI: 10.1142/S1793626812300058.
- [15] A. Romanenko, A. Grassellino, O. Melnychuk, et al. “Dependence of the residual surface resistance of superconducting radio frequency cavities on the cooling dynamics around T_c ”. In: *Journal of Applied Physics* 115.18 (May 14, 2014), p. 184903. DOI: 10.1063/1.4875655.
- [16] V. L. Ginzburg and L. D. Landau. “On the Theory of Superconductivity”. In: *On Superconductivity and Superfluidity: A Scientific Autobiography*. Ed. by V. L. Ginzburg. Berlin, Heidelberg: Springer, 2009, pp. 113–137. DOI: 10.1007/978-3-540-68008-6_4.
- [17] S. Posen and D. L. Hall. “Nb₃Sn superconducting radiofrequency cavities: fabrication, results, properties, and prospects”. In: *Supercond. Sci. Technol.* 30.3 (Mar. 1, 2017), p. 033004. DOI: 10.1088/1361-6668/30/3/033004.
- [18] J. Stohr. *Linac Coherent Light Source II (LCLS-II) Conceptual Design Report*. SLAC-R-978. SLAC National Accelerator Lab., Menlo Park, CA (United States), Nov. 16, 2011. DOI: <https://doi.org/10.2172/1029479>.
- [19] M. Ball, A. Burov, B. Chase, et al. *The PIP-II Conceptual Design Report*. FERMILAB-DESIGN-2017-01; FERMILAB-TM-2649-AD-APC. Argonne National Lab. (ANL), Argonne, IL (United States); Fermi National Accelerator Lab. (FNAL), Batavia, IL (United States), Mar. 1, 2017. DOI: <https://doi.org/10.2172/1346823>.
- [20] P. U. Kolb. “The TRIUMF nine-cell SRF cavity for ARIEL”. PhD thesis. University of British Columbia, 2016. DOI: 10.14288/1.0300057.
- [21] L. Cardman, R. Ent, N. Isgur, et al. *The Science Driving the 12 GeV Upgrade of CEBAF*. JLAB-R-2001-01. Thomas Jefferson National Accelerator Facility (TJNAF), Newport News, VA (United States), Feb. 1, 2011.
- [22] P. Ostroumov, C. Contreras, A. Plastun, et al. “Elliptical superconducting RF cavities for FRIB energy upgrade”. In: *Nuclear Instruments and Methods in Physics Research Section A: Accelerators, Spectrometers, Detectors and Associated Equipment* 888 (Apr. 2018), pp. 53–63. DOI: 10.1016/j.nima.2018.01.001.
- [23] M. Altarelli, ed. *XFEL, the European X-ray free-electron laser: technical design report*. OCLC: 254657183. Hamburg: DESY XFEL Project Group [u.a.], 2006. 630 pp.

- [24] S. Peggs and European Spallation Source. *ESS technical design report*. OCLC: 940713856. Lund: European Spallation Source (ESS), 2013.
- [25] S. Henderson, W. Abraham, A. Aleksandrov, et al. “The Spallation Neutron Source accelerator system design”. In: *Nuclear Instruments and Methods in Physics Research Section A: Accelerators, Spectrometers, Detectors and Associated Equipment* 763 (Nov. 2014), pp. 610–673. DOI: 10.1016/j.nima.2014.03.067.
- [26] T. Behnke, J. E. Brau, B. Foster, et al. *The International Linear Collider Technical Design Report - Volume 1: Executive Summary*. ILC-REPORT-2013-040, ANL-HEP-TR-13-20, 1347945. June 26, 2013, ILC-REPORT-2013-040, ANL-HEP-TR-13-20, 1347945. DOI: 10.2172/1347945.
- [27] R. Paparella, C. Albrecht, S. Barbanotti, et al. “Analysis of the Production, Installation and Commissioning of the European-XFEL Frequency Tuners”. In: *Proceedings of the 18th Int. Conf. on RF Superconductivity SRF2017* (2018). In collab. with S. RW (Ed.) Volker. Artwork Size: 5 pages, 0.465 MB ISBN: 9783954501915 Medium: PDF Publisher: JACoW, Geneva, Switzerland, 5 pages, 0.465 MB. DOI: 10.18429/JACOW-SRF2017-MOPB076.
- [28] J. Wei et al. “FRIB Accelerator Status and Challenges”. In: *Proc. 26th Linear Accelerator Conf. (LINAC’12)* (Tel Aviv, Israel). JACoW Publishing, Sept. 2012, pp. 417–421.
- [29] N. R. Council. *Nuclear Physics: Exploring the Heart of Matter*. June 26, 2012. DOI: 10.17226/13438.
- [30] F. S. Community. “FRIB 400 The Scientific Case for the 400 MeV/u Energy Upgrade of FRIB”.
- [31] E. U. Condon. “Forced Oscillations in Cavity Resonators”. In: *JOURNAL OF APPLIED PHYSICS* 12 (1941), p. 5.
- [32] H. A. Bethe. “Theory of Diffraction by Small Holes”. In: *Phys. Rev.* 66.7 (Oct. 1, 1944), pp. 163–182. DOI: 10.1103/PhysRev.66.163.
- [33] J. C. Slater. “Microwave Electronics”. In: *Rev. Mod. Phys.* 18.4 (Oct. 1, 1946). Publisher: American Physical Society, pp. 441–512. DOI: 10.1103/RevModPhys.18.441.
- [34] T. Schilcher. “Vector Sum Control of Pulsed Accelerating Fields in Lorentz Force Detuned Superconducting Cavities”. PhD thesis. University of Hamburg.
- [35] T. Czarski, K. Pozniak, R. Romaniuk, et al. “TESLA cavity modeling and digital implementation in FPGA technology for control system development”. In: *Nuclear Instruments and Methods in Physics Research Section A: Accelerators, Spectrometers, Detectors and Associated Equipment* 556.2 (Jan. 2006), pp. 565–576. DOI: 10.1016/j.nima.2005.10.122.

- [36] C. Serrano, L. Doolittle, and V. Vytlá. “Cryomodule-on-Chip Simulation Engine”. In: *Proceedings of the 16th Int. Conf. on Accelerator and Large Experimental Control Systems ICALEPCS2017* (2018). DOI: 10.18429/JACOW-ICALEPCS2017-TUAPL06.
- [37] P. Echevarria, E. Aldekoa, J. Jugo, et al. “Superconducting radio-frequency virtual cavity for control algorithms debugging”. In: *Review of Scientific Instruments* 89.8 (Aug. 2018), p. 084706. DOI: 10.1063/1.5041079.
- [38] F. Qiu, S. Michizono, T. Miura, et al. “Real-time cavity simulator-based low-level radio-frequency test bench and applications for accelerators”. In: *Phys. Rev. Accel. Beams* 21.3 (Mar. 16, 2018), p. 032003. DOI: 10.1103/PhysRevAccelBeams.21.032003.
- [39] E. Häbel and J. Tückmantel. *Electromagnetic surface forces in RF cavities*. CERN-AT-RF-INT-91-99. CM-P00058119, Dec. 11, 1991.
- [40] *Lorentz force detuning | ILC Newslines*. URL: <http://newslines.linearcollider.org/2011/07/07/achieving-cavity-resonance/lorentz-force-detuning-2/>.
- [41] M. Karliner, V. Shapiro, and I. Shekhtman. “Instability in the Walls of a Cavity Due to Ponderomotive Forces of the Electromagnetic Field”. In: *Soviet Physics-Technical Physics* 11.11 (1967).
- [42] V. E. Shapiro. “Ponderomotive Effects of Electromagnetic Radiation”. In: *Soviet Physics JETP* 28.2 (1969).
- [43] D. Schulze. “Mechanical Instabilities of a Superconducting Helical Structure due to Radiation Pressure”. In: *Proc. 1970 Linear Accelerator Conf. (LINAC’70)* (Batavia, IL, USA). JACoW Publishing, Sept. 1970, pp. 359–370.
- [44] J. R. Delayen. “Ponderomotive instabilities and microphonics—a tutorial”. In: *Physica C: Superconductivity*. Proceedings of the 12th International Workshop on RF Superconductivity 441.1 (July 15, 2006), pp. 1–6. DOI: 10.1016/j.physc.2006.03.050.
- [45] M. Karliner, V. Petrov, and I. Shekhtman. “Vibration of the Walls of a Cavity Resonator Under Ponderomotive Forces in the Presence of Feedback”. In: *Soviet Physics-Technical Physics* 14.8 (1970).
- [46] L. D. Landau and E. M. Lifshitz. *Mechanics: Volume 1*. Elsevier, Jan. 29, 1982. 199 pp.
- [47] T. Saeki et al. “Initial Studies of 9-Cell High-Gradient Superconducting Cavities at KEK”. In: *Proc. 23rd Linear Accelerator Conf. (LINAC’06)* (Knoxville, TN, USA). JACoW Publishing, Aug. 2006.

- [48] O. Melnychuk, A. Grassellino, and A. Romanenko. “Error analysis for intrinsic quality factor measurement in superconducting radio frequency resonators”. In: *Review of Scientific Instruments* 85.12 (Dec. 2014), p. 124705. doi: 10.1063/1.4903868.
- [49] J. Holzbauer, C. Contreras, Y. Pischalnikov, et al. “Improved RF measurements of SRF cavity quality factors”. In: *Nuclear Instruments and Methods in Physics Research Section A: Accelerators, Spectrometers, Detectors and Associated Equipment* 913 (Jan. 2019), pp. 7–14. doi: 10.1016/j.nima.2018.09.155.
- [50] D. Frolov. “Intrinsic quality factor extraction of multi-port cavity with arbitrary coupling”. In: *Review of Scientific Instruments* 92.1 (Jan. 1, 2021), p. 014704. doi: 10.1063/5.0014471.
- [51] W. Schappert. “Resonance Control for Future Linear Accelerators”. In: *Proc. 28th Linear Accelerator Conf. (LINAC’16)* (East Lansing, MI, USA). <https://doi.org/10.18429/JACoW-LINAC2016-TU2A03>. JACoW Publishing, Sept. 2016, pp. 363–367. doi: doi : 10.18429/JACoW-LINAC2016-TU2A03.
- [52] J. P. Edelen, B. E. Chase, E. Cullerton, et al. “Low Level RF Control for the PIP-II Injector Test RFQ”. In: *Proc. North American Particle Accelerator Conf. (NAPAC’16)* (Chicago, IL, USA). <https://doi.org/10.18429/JACoW-NAPAC2016-TUPOA18>. JACoW Publishing, Oct. 2016, pp. 323–325. doi: doi : 10.18429/JACoW-NAPAC2016-TUPOA18.
- [53] A. Neumann, W. Anders, O. Kugeler, et al. “Analysis and active compensation of microphonics in continuous wave narrow-bandwidth superconducting cavities”. In: *Phys. Rev. ST Accel. Beams* 13.8 (Aug. 4, 2010), p. 082001. doi: 10.1103/PhysRevSTAB.13.082001.
- [54] A. Sun, H. Wang, and G. Wu. “Effect of the Tuner on the Field Flatness of SNS Superconducting RF Cavities”. In: *Proc. 22nd Linear Accelerator Conf. (LINAC’04)* (Lübeck, Germany). JACoW Publishing, Aug. 2004.
- [55] D. E. Nagle, E. A. Knapp, and B. C. Knapp. “Coupled Resonator Model for Standing Wave Accelerator Tanks”. In: *Review of Scientific Instruments* 38.11 (Nov. 1967), pp. 1583–1587. doi: 10.1063/1.1720608.
- [56] P. Schmuser. “Tuning of Multi-cell Cavities Using bead-pull Measurements”. In: SRF92.
- [57] H. Wang and J. Guo. “Bead-pulling Measurement Principle and Technique Used for the SRF Cavities at JLab”. In: (), p. 41.
- [58] H. Jiang, D. Baars, A. Zamiri, et al. “Mechanical Properties of High RRR Niobium With Different Texture”. In: *IEEE Transactions on Applied Superconductivity* 17.2 (June 2007). Conference Name: IEEE Transactions on Applied Superconductivity, pp. 1291–1294. doi: 10.1109/TASC.2007.898463.

- [59] *COMSOL: Multiphysics*. COMSOL. URL: <https://www.comsol.com/>.
- [60] V. Shemelin and P. Carriere. “Frequency control in the process of a multicell superconducting cavity production”. In: *Review of Scientific Instruments* 83.4 (Apr. 2012), p. 043304. DOI: 10.1063/1.4705985.
- [61] *AD8302.pdf*. URL: <https://www.analog.com/media/cn/technical-documentation/data-sheets/AD8302.pdf>.
- [62] *373861d.pdf*. URL: <https://www.ni.com/pdf/manuals/373861d.pdf>.
- [63] R. Donnelly and C. Barenghi. “The Observed Properties of Liquid Helium at the Saturated Vapor Pressure”. In: *Journal of Physical and Chemical Reference Data* 27.6 (Nov. 1998), pp. 1217–1274. DOI: 10.1063/1.556028.
- [64] M. Paoletti and D. P. Lathrop. “Quantum Turbulence”. In: *Annu. Rev. Condens. Matter Phys.* 2.1 (Mar. 2011), pp. 213–234. DOI: 10.1146/annurev-conmatphys-062910-140533.
- [65] E. Harms, C. Contreras-Martinez, E. Cullerton, et al. “Experience With LCLS-II Cryomodule Testing at Fermilab”. In: *Proceedings of the 19th International Conference on RF Superconductivity SRF2019* (2019). DOI: 10.18429/JACOW-SRF2019-THP060.
- [66] G. Huang et al. “High Precision RF Control for the LCLS-II”. In: *Proc. North American Particle Accelerator Conf. (NAPAC’16)* (Chicago, IL, USA). <https://doi.org/10.18429/JACoW-NAPAC2016-FRA2IO02>. JACoW Publishing, Oct. 2016, pp. 1292–1296. DOI: doi : 10.18429/JACoW-NAPAC2016-FRA2IO02.
- [67] B. J. Hansen, O. Al Atassi, R. Bossert, et al. “Effects of thermal acoustic oscillations on LCLS-II cryomodule testing”. In: *IOP Conf. Ser.: Mater. Sci. Eng.* 278 (Dec. 2017), p. 012188. DOI: 10.1088/1757-899X/278/1/012188.
- [68] N. Rott. “Damped and thermally driven acoustic oscillations in wide and narrow tubes”. In: *Journal of Applied Mathematics and Physics (ZAMP)* 20.2 (Mar. 1969), pp. 230–243. DOI: 10.1007/BF01595562.
- [69] N. Rott. “Thermally driven acoustic oscillations. Part II: Stability limit for helium”. In: *Journal of Applied Mathematics and Physics (ZAMP)* 24.1 (Jan. 1973), pp. 54–72. DOI: 10.1007/BF01593998.
- [70] J. Holzbauer, B. Chase, J. Einstein-Curtis, et al. “Passive Microphonics Mitigation during LCLS-II Cryomodule Testing at Fermilab”. In: *Proceedings of the 9th Int. Particle Accelerator Conf. IPAC2018* (2018). DOI: 10.18429/JACOW-IPAC2018-WEPML001.

- [71] T. T. Arkan et al. “LCLS-II Cryomodules Production at Fermilab”. In: (Apr. 2018). <https://doi.org/10.18429/JACoW-IPAC2018-WPEMK010>, pp. 2652–2655. DOI: doi:10.18429/JACoW-IPAC2018-WPEMK010.
- [72] T. T. Arkan et al. “LCLS-II Cryomodules Production Experience and Lessons Learned at Fermilab”. In: (June 2019). <https://doi.org/10.18429/JACoW-SRF2019-TUP101>, pp. 709–714. DOI: doi:10.18429/JACoW-SRF2019-TUP101.
- [73] N. Banerjee, G. Hoffstaetter, M. Liepe, et al. “Active suppression of microphonics detuning in high Q L cavities”. In: *Phys. Rev. Accel. Beams* 22.5 (May 9, 2019), p. 052002. DOI: 10.1103/PhysRevAccelBeams.22.052002.
- [74] Y. M. Pischalnikov, B. Hartman, J. P. Holzbauer, et al. “Reliability of the LCLS II SRF Cavity Tuner”. In: *Proc. 17th Int. Conf. RF Superconductivity (SRF’15)* (Whistler, Canada). JACoW Publishing, Sept. 2015, pp. 1267–1271.
- [75] S. Y. Kazakov, S. V. Shchelkunov, V. P. Yakovlev, et al. “Fast ferroelectric phase shifters for energy recovery linacs”. In: *Phys. Rev. ST Accel. Beams* 13.11 (Nov. 24, 2010), p. 113501. DOI: 10.1103/PhysRevSTAB.13.113501.
- [76] I. V. Gonin et al. “650 MHz Elliptical Superconducting RF Cavities for PIP-II Project”. In: *Proc. 28th Linear Accelerator Conf. (LINAC’16)* (East Lansing, MI, USA). JACoW Publishing, Sept. 2016, pp. 943–945. DOI: doi:10.18429/JACoW-LINAC2016-THPLR041.
- [77] C. Contreras-Martinez, E. Borissov, S. Cheban, et al. “Dynamic Tuner Development for Medium β Superconducting Elliptical Cavities”. In: vol. IPAC2018. 2018. DOI: 10.18429/JACoW-IPAC2018-THPAL034.
- [78] Y. Pischalnikov, S. Chandrasekaran, S. Cheban, et al. “Performance of the 650 MHz SRF Cavity Tuner for PIP II Project”. In: vol. SRF2019. 2019. DOI: 10.18429/JACoW-SRF2019-TUP083.
- [79] Y. Pischalnikov, S. Cheban, and J. Yun. “Design of 650 MHz Tuner for PIP-II Project”. In: vol. IPAC2018. 2018. DOI: 10.18429/JACoW-IPAC2018-WPEML002.
- [80] “Results of Accelerated Life Testing of LCLS-II Cavity Tuner Motor”. In: *Proceedings of the 18th Int. Conf. on RF Superconductivity SRF2017* (2018), 5 pages, 1.493 MB. DOI: 10.18429/JACoW-SRF2017-MOPB110.
- [81] P. (I. L.P. *PICMA® Technology*. URL: <https://www.pi-usa.us/en/apps-tech/technology/piezo-technology/picma/>.
- [82] M. Fouaidy, G. Martinet, N. Hammoudi, et al. “Radiation hardness tests of piezoelectric actuators with fast neutrons at liquid helium temperature”. In: (), p. 21.

- [83] W. Schappert and Y. M. Pischalnikov. “Adaptive Compensation for Lorentz Force Detuning in Superconducting RF Cavities”. In: *Proc. 15th Int. Conf. RF Superconductivity (SRF’11)* (Chicago, IL, USA). JACoW Publishing, July 2011, pp. 940–942.
- [84] Y. Pishchalnikov, E. Borissov, T. Khabiboulline, et al. *Tests of a tuner for a 325 MHz SRF spoke resonator*. FERMILAB-CONF-11-100-TD. Fermi National Accelerator Lab. (FNAL), Batavia, IL (United States), Mar. 1, 2011.
- [85] M. Liepe, W. Moeller, and S. Simrock. “Dynamic Lorentz force compensation with a fast piezoelectric tuner”. In: *PACS2001. Proceedings of the 2001 Particle Accelerator Conference (Cat. No.01CH37268)*. PACS2001. Proceedings of the 2001 Particle Accelerator Conference (Cat. No.01CH37268). Vol. 2. June 2001, 1074–1076 vol.2. doi: 10.1109/PAC.2001.986582.
- [86] M. Grecki, A. Bosotti, R. Paparella, et al. “Piezo characterization, tests and operation at FLASH”. In: (), p. 29.
- [87] K. Uchino. *Ferroelectric Devices 2nd Edition*. 2nd. USA: CRC Press, Inc., 2009. 367 pp.
- [88] S. Rupitsch. *Piezoelectric Sensors and Actuators: Fundamentals and Applications*. Topics in Mining, Metallurgy and Materials Engineering. Berlin, Heidelberg: Springer Berlin Heidelberg, 2019. doi: 10.1007/978-3-662-57534-5.
- [89] A. W. Warner, M. Onoe, and G. A. Coquin. “Determination of Elastic and Piezoelectric Constants for Crystals in Class (3m)”. In: *The Journal of the Acoustical Society of America* 42.6 (1967). _eprint: <https://doi.org/10.1121/1.1910709>, pp. 1223–1231. doi: 10.1121/1.1910709.
- [90] P. Pertsch, S. Richter, D. Kopsch, et al. “Reliability of Piezoelectric Multilayer Actuators”. In: *Actuator 2006* (2006), p. 3.
- [91] S. Yarlagadda, M. Chan, H. Lee, et al. “Low Temperature Thermal Conductivity, Heat Capacity, and Heat Generation of PZT”. In: *Journal of Intelligent Material Systems and Structures* 6.6 (Nov. 1995), pp. 757–764. doi: 10.1177/1045389X9500600603.
- [92] krn5. *CST Studio Suite 3D EM simulation and analysis software*. URL: <https://www.3ds.com/products-services/simulia/products/cst-studio-suite/>.
- [93] K. Uchino and S. Hirose. “Loss mechanisms in piezoelectrics: how to measure different losses separately”. In: *IEEE Trans. Ultrason., Ferroelect., Freq. Contr.* 48.1 (Jan. 2001), pp. 307–321. doi: 10.1109/58.896144.
- [94] M. S. Senousy, R. K. N. D. Rajapakse, D. Mumford, et al. “Self-heat generation in piezoelectric stack actuators used in fuel injectors”. In: *Smart Mater. Struct.* 18.4 (Apr. 1, 2009), p. 045008. doi: 10.1088/0964-1726/18/4/045008.

- [95] M. Fouaidy, G. Martinet, N. Hammoudi, et al. “Full Characterization at Low Temperature of Piezoelectric Actuators Used for SRF Cavities Active Tuning”. In: *Proceedings of the 2005 Particle Accelerator Conference*. 2005 Particle Accelerator Conference. Knoxville, TN, USA: IEEE, 2005, pp. 728–730. DOI: 10.1109/PAC.2005.1590542.
- [96] D. Hall and P. Stevenson. “High field dielectric behaviour of ferroelectric ceramics”. In: *Ferroelectrics* 228.1 (May 1999), pp. 139–158. DOI: 10.1080/00150199908226132.
- [97] Q. M. Zhang, H. Wang, and J. Zhao. “Effect of Driving Field and Temperature on the Response Behavior of Ferroelectric Actuator and Sensor Materials”. In: *Journal of Intelligent Material Systems and Structures* 6.1 (Jan. 1, 1995). Publisher: SAGE Publications Ltd STM, pp. 84–93. DOI: 10.1177/1045389X9500600111.
- [98] S. Haykin. *Adaptive Filter Theory : International Edition*. Pearson Education Limited, May 28, 2014. 913 pp.
- [99] R. Carcagno, L. Bellantoni, T. Berenc, et al. “Microphonics Detuning Compensation in 3.9 GHz Superconducting RF Cavities”. In: *Proc. 11th Workshop RF Superconductivity (SRF’03)* (Lübeck, Germany). JACoW Publishing, Sept. 2003, pp. 726–729.
- [100] T. Kandil. “Adaptive Feedforward Cancellation of Sinusoidal Disturbances in Superconducting Radio Frequency Cavities”. MA thesis. Michigan State University, 1993, p. 70.
- [101] R. Rybaniec, K. Przygoda, W. Cichalewski, et al. “FPGA-Based RF and Piezocontrollers for SRF Cavities in CW Mode”. In: *IEEE Trans. Nucl. Sci.* 64.6 (June 2017), pp. 1382–1388. DOI: 10.1109/TNS.2017.2687981.
- [102] J. Holzbauer, B. Chase, L. Doolittle, et al. “Active Microphonics Compensation for LCLS-II”. In: *Proceedings of the 9th Int. Particle Accelerator Conf. IPAC2018* (2018). DOI: 10.18429/JACOW-IPAC2018-WEPML007.
- [103] M. J. Brennan, I. Kovacic, A. Carrella, et al. “On the jump-up and jump-down frequencies of the Duffing oscillator”. In: *Journal of Sound and Vibration* 318.4 (Dec. 23, 2008), pp. 1250–1261. DOI: 10.1016/j.jsv.2008.04.032.
- [104] I. Kovacic and M. J. Brennan, eds. *The Duffing Equation: Nonlinear Oscillators and their Behaviour*. Chichester, UK: John Wiley & Sons, Ltd, Mar. 25, 2011. DOI: 10.1002/9780470977859.

ProQuest Number: 28498572

INFORMATION TO ALL USERS

The quality and completeness of this reproduction is dependent on the quality and completeness of the copy made available to ProQuest.



Distributed by ProQuest LLC (2021).

Copyright of the Dissertation is held by the Author unless otherwise noted.

This work may be used in accordance with the terms of the Creative Commons license or other rights statement, as indicated in the copyright statement or in the metadata associated with this work. Unless otherwise specified in the copyright statement or the metadata, all rights are reserved by the copyright holder.

This work is protected against unauthorized copying under Title 17, United States Code and other applicable copyright laws.

Microform Edition where available © ProQuest LLC. No reproduction or digitization of the Microform Edition is authorized without permission of ProQuest LLC.

ProQuest LLC
789 East Eisenhower Parkway
P.O. Box 1346
Ann Arbor, MI 48106 - 1346 USA